27/8-23-77 to NTIS
25 cy

312

TREE-NUREG-1107

for U.S. Nuclear Regulatory Commission

FRAP-S2: A COMPUTER CODE FOR THE STEADY STATE ANALYSIS OF OXIDE FUEL RODS

JOHN A. DEARIEN GARY A. BERNA
MICHAEL P. BOHN DENNIS R. COLEMAN
E. THOMAS LAATS

July 1977

MASTER

EG&G Idaho, Inc.

IDAHO NATIONAL ENGINEERING LABORATORY

ENERGY RESEARCH AND DEVELOPMENT ADMINISTRATION

IDAHO OPERATIONS OFFICE UNDER CONTRACT EY-76-C-07-1570

Printed in the United States of America
Available from
National Technical Information Service
U.S. Department of Commerce
5285 Port Royal Road
Springfield, Virginia 22161
Price: Printed Copy $9.25; Microfiche $3.00

"The NRC will make available data tapes and operational computer codes on research programs dealing with postulated loss-of-coolant accidents in light water reactors. Persons requesting this information must reimburse the NRC contractors for their expenses in preparing copies of the data tapes and the operational computer codes. Requests should be submitted to the Research Applications Branch, Office of Nuclear Regulatory Research, Nuclear Regulatory Commission, Washington, D.C. 20555."

TREE-NUREG-1107

FRAP-S2: A COMPUTER CODE FOR THE STEADY STATE ANALYSIS OF OXIDE FUEL RODS

Approved:

John A. Dearien

J. A. Dearien, Manager
FARAD Branch

J. G. Crocker, Manager
Thermal Fuels Behavior Division

DISTRIBUTION OF THIS DOCUMENT IS UNLIMITED

TREE-NUREG-1107

Distributed Under Category:
NRC-4
Water Reactor Safety Research
Analysis Development

FRAP-S2: A COMPUTER CODE FOR THE STEADY-STATE ANALYSIS OF OXIDE FUEL RODS

by

John A. Dearien
Gary A. Berna
Michael P. Bohn
Dennis R. Coleman
E. Thomas Laats

EG&G IDAHO, INC.

July 1977

PREPARED FOR THE
U.S. NUCLEAR REGULATORY COMMISSION
AND
ENERGY RESEARCH AND DEVELOPMENT ADMINISTRATION
IDAHO OPERATIONS OFFICE
UNDER CONTRACT NO. EY-76-C-07-1570

ABSTRACT

This document describes the Fuel Rod Analysis Program - Steady State code (FRAP-S) and the verification of FRAP-S as a fuel rod analysis tool.

FRAP-S2 (Fuel Rod Analysis Program - Steady State, Version 2) is a FORTRAN IV computer code which can be used to solve for the long term burnup response of a light water reactor fuel rod. The coupled effects of fuel and cladding deformation, temperature distribution, internal gas accumulation, and pressure and material property on the behavior of the fuel rod are considered. Fission gas generation and release are calculated as a function of burnup. The cladding deformation model includes multiaxial elasto-plastic analysis and considers creep.

FRAP-S2 is a modular code with each major computational subcode isolated within the code and coupled to the main code by subroutine calls and data transfer through argument lists. A major purpose of FRAP-S2 arises because it can be coupled to versions of the transient fuel rod code FRAP-T. FRAP-S2 generates a set of initial conditions used by FRAP-T to initiate analysis of transient accidents such as loss-of-coolant (LOCA), power coolant mismatch (PCM) and reactivity initiated accidents (RIA).

A material property subcode, MATPRO, which is used to provide gas, fuel, and cladding properties to the FRAP-S computational subcodes is coupled to FRAP-S2. No material properties need to be supplied by the code user.

FRAP-S2 has been evaluated by making extensive comparisons between predictions of the code and experimental data. Comparisons of predicted and experimental results are presented for a range of FRAP-S2 calculated parameters.

The code is presently programmed and running on the IBM 360/75 and CDC 7600 computers.

SUMMARY

FRAP-S is a FORTRAN IV computer code developed to describe the steady state behavior of nuclear fuel rods during long-term burnup conditions. FRAP-S includes the coupled effect of thermal, mechanical, internal gas, and material properties response in the analysis of fuel rod behavior. This code is part of a continuing development program by the Nuclear Regulatory Commission designed to produce analytical tools for accurate prediction of nuclear reactor system behavior during normal and abnormal operating conditions. The code described in this document (FRAP-S-MOD002) is the second in a series of fuel rod codes planned for periodic release, with each succeeding version incorporating the most recent advancements that have been made in fuel rod response analysis models. The code is presently programmed and running on the IBM-360/75 and CDC 7600 computers. A transient fuel rod analysis code, FRAP-T, is being developed at the Idaho National Engineering Laboratory to accept history dependent initial conditions from FRAP-S to initiate an off-normal transient. Both codes are being developed with common subcodes and compatible input-output features.

FRAP-S2 is a modular code. Each type of computation, such as the internal gas pressure computation, is performed by an analytical model programmed in a separate subcode or subroutine. This configuration is designed to allow maximum flexibility in developing and modifying the code with minimum impact on the unmodified portion of the code.

A major subcode of FRAP-S2 is MATPRO. This subcode is composed of modular function subprograms and subroutines which define the material properties required by the computational subcodes of FRAP-S2. Each function subprogram or subroutine defines only one material property.

The developmental process of FRAP-S2 includes a verification effort designed to test the analytical capability of the code.

Experimental data on fuel rod response variables such as centerline temperature and cladding deformation are compared with FRAP-S2 calculated values.

This document describes the FRAP-S2 code and the verification of the FRAP-S2 code, and is configured as two individual reports bound in one document for user convenience. Each report is relatively independent with regard to subject matter, references, and style of writing. The MATPRO subcode is referenced in Appendix E of Report I.

REPORT I

FRAP-S2 -- ANALYTICAL MODELS AND INPUT MANUAL

John A. Dearien
Gary A. Berna
Michael P. Bohn
Dennis R. Coleman

CONTENTS

FIGURES

TABLES

FRAP-S2: A COMPUTER CODE FOR THE STEADY-STATE ANALYSIS OF OXIDE FUEL RODS

REPORT I -- FRAP-S2 -- ANALYTICAL MODELS AND INPUT MANUAL

I. INTRODUCTION

FRAP-S2 (Fuel Rod Analysis Program-Steady State, Version 2) is a FORTRAN IV computer code developed to describe the steady state and long-term burnup response of oxide fuel rods in light water reactors (LWR). In addition, the code is designed to generate parametric data required as initial conditions for transient accident analysis using versions of the transient analysis code -- FRAP-T[1]. This effort is part of a safety analysis code improvement program being sponsored by the Office of Water Reactor Safety Research of the Nuclear Regulatory Commission (NRC).

The code described in this report (FRAP-S MOD 002) is the second of a series of steady state fuel rod codes planned for release at intervals with each succeeding version incorporating the most recent advancements made in fuel rod response analysis models.

FRAP-S is a modular code with each type of computation and analytical model, such as internal gas pressure, contained in a separate module or subroutine. This configuration is designed to allow maximum versatility in development and to permit modification of a module without impacting the unmodified portion of the code.

A major subcode of FRAP-S2 is MATPRO[4], see Appendix E. This subcode is comprised of modular function subprograms and subroutines which define the material properties required by the computational subcodes of FRAP-S2. Each function subprogram or subroutine defines a single material property.

The FRAP-S2 developmental process includes a verification effort designed to test the analytical capability of the code. Fuel rod response parameters, such as centerline temperature and cladding deformation as predicted by FRAP-S2, are compared with experimental data, see Report II.

This document describes the FRAP-S2 code, the models used in the code, and examples of code input and output. Section II describes the purpose of the code and the general methods by which the objectives are achieved. Sections III and IV cover the analytical and correlative models, respectively. Section V describes the computational flow of the code and presents a detailed flow diagram of the code for clarity. Appendices contain a user input manual (Appendix A), a FRAP-S example problem (Appendix B), a problem illustrating the FRAP-S link to FRAP-T (Appendix C), and a description of the configuration control procedure used at EG&G Idaho, Inc. to document analytical codes (Appendix D).

II. PROGRAM SUMMARY DESCRIPTION

The FRAP-S code is being developed to predict the behavior of fuel rods during long-term irradiation and to calculate initial conditions for transient accident analyses performed using the FRAP-T code. The program calculates the interrelated effects of fuel and cladding temperature, rod internal pressure, fuel and cladding deformation, release of fission product gases, fuel swelling, cladding thermal growth, cladding corrosion, and crud deposition as a function of time and specific power. Calculations can be performed for rods which are expected to experience varying axial power distributions as well as rod power level changes with time and/or burnup or changes in core system conditions. Parametric fuel rod design studies can be performed by varying as-fabricated rod dimensions or specifications. Printout for up to 15 axial rod increments and for 69 power/time steps can be obtained for each case.

1. RESPONSE MODELS

FRAP-S2 contains models which calculate the following quantities as a function of irradiation time:

(1) Coolant bulk and cladding axial temperature distribution

(2) Temperature distribution in the fuel pellets at eleven radial nodes and up to 15 axial increments

(3) Zircaloy cladding corrosion and hydriding at each axial increment in either a boiling water reactor (BWR) or pressurized water reactor (PWR) environment

(4) Fuel swelling, densification, and thermal expansion at each axial increment and radial node

(5) Cladding irradiation-induced growth at each axial increment

(6) Elastic-plastic pellet-cladding interaction and contact pressure at each axial increment

(7) Pellet to cladding gap and fuel crack gas composition and thermal conductivity

(8) Cladding stresses and strains at each axial increment including zircaloy cladding creep

(9) Krypton, xenon, and helium generation at each pellet node

(10) Total fuel rod gas release and internal rod pressure through summation of the release in each axial increment and calculation of the plenum, dish, gap, and crack void volumes and temperatures.

2. PROGRAMMING FEATURES

FRAP-S2 incorporates certain programming features which influence its application to providing transient code initial conditions that are dependent on prior operating history.

(1) Creep rates are applied over the time step after the code has converged on the power of that time step.

(2) With respect to fuel cladding properties, as well as input and output routines, the degree of modularization in FRAP-S2 is equivalent to that exhibited by versions of FRAP-T. The MATPRO material properties subcode is called repeatedly by both codes.

(3) Some of the other submodels in the code representing physical mechanisms such as gas release and void volume calculations

are called by the control program but the interface is currently functional rather than modular in nature. The calling sequence uses a large common block to pass information to and from the subroutines. A similar situation exists for the fuel swelling model which is called from subroutine TEMP. TEMP incorporates the analytical fuel rod temperature calculation, as well as convergence control, and models for corrosion and cladding stress.

(4) Where common mechanisms exist, the same physical models, such as fuel thermal expansion and gap conductance, are used in FRAP-S and FRAP-T.

Current plans are to increase use of modular programming in FRAP-S and improve consistency of physical models between the FRAP-S and FRAP-T.

3. OPERATIONAL FEATURES

As an indication of how FRAP-S2 operated, the input features and calculational procedures are given below.

3.1 Input Data Required

The input required for running the FRAP-S code is that collection of data necessary to describe the fuel rod geometry, core thermal and hydraulic conditions, and the expected irradiation history, namely:

(1) Fuel rod geometry (initial cold dimensions):

(a) Cladding material

(b) Cladding outside diameter

(c) Cladding inside diameter

(d) Pellet diameter

(e) Percent of UO_2 theoretical density

(f) UO_2 enrichment

(g) Fuel stack length

(h) Cold pellet height

(i) Dish depth

(j) Dish spherical radius

(k) Cold plenum length

(l) Hold-down spring (coil) diameter

(m) Hold-down spring wire diameter

(n) Total number of spring turns.

(2) Core thermal and hydraulic conditions:

(a) Primary loop system pressure

(b) Coolant mass flow rate

(c) Hydraulic diameter

(d) Core inlet water temperature.

(3) Rod power:

(a) Axial power distribution as a function of time

(b) Rod average heat flux or power as a function of time.

3.2 Calculation Procedure

The FRAP-S2 code iteratively calculates the interrelated effects of fuel and cladding temperature, rod internal pressure, fuel and cladding elastic-plastic deformation, release of fission product gases, fuel swelling and densification, cladding thermal expansion and irradiation-induced growth, cladding corrosion, and crud deposition as functions of time and specific power.

The fuel rod power history is approximated by a series of steady state power levels with instantaneous jumps from one power level to another. The length of the rod is divided into a number of axial segments, each assumed to operate at an average set of conditions over its length. The axial flux (power) shape is input and may be varied as a function of time. Fuel and cladding temperatures, fuel swelling, densification, thermal expansion, cladding thermal and irradiation induced growth, cladding stresses and strains, and fission gas releases are calculated separately for each axial segment. The fission gas release and fuel and cladding deformations are then integrated over the length of the fuel rod and added to previous power step values to obtain the rod internal pressure. This pressure is fed back into the fuel and cladding elastic and plastic deflection calculations in subsequent iterations. For purposes of evaluating thermal expansion, fuel swelling, densification, and fission gas release, within each axial increment, the fuel pellet is divided into ten equal-volume concentric rings with each ring assumed to be at its average temperature.

A detailed coverage of the numerical solution procedure is presented in Section V with program flow diagrams and subroutine interactions.

4. FRAP-S/FRAP-T LINK

One of the primary reasons for developing FRAP-S is to provide a computational tool which is compatible with the transient accident analysis code FRAP-T[1]. For realistic evaluation of fuel rod response during a reactor accident transient such as a loss-of-coolant accident (LOCA), a realistic set of initial conditions, based on a real or hypothetical reactor history, is required to initiate the transient analysis. Consistent computational models in the two codes are required for a smooth transition between the predictions of the two codes at initiation of the transient. The sample problem described in Appendix C shows the result of small discrepancies between similar models in FRAP-S and FRAP-T. These discrepancies presently are being removed in the development process.

The link between FRAP-S2 and FRAP-T is accomplished by having FRAP-S2 generate a magnetic tape containing FRAP-S2 calculated information in the format of a FRAP-T restart tape.

The following data are stored on tape and passed to FRAP-T as initial conditions for each axial node specified:

(1) Gap pressure (vector)

(2) Fuel rod outside diameter (vector)

(3) Radial gap thickness (vector)

(4) Crack volume per unit length (vector)

(5) Interfacial pressure (vector)

(6) Rod surface heat flux (vector)

(7) Fuel outside radius (vector)

(8) Axial cladding strain (vector)

(9) Radial cladding strain (vector)

(10) Length change of fuel stack

(11) Area of the top pellet

(12) Length change of the cladding

(13) Total moles of gas in the rod

(14) Temperature distribution (vector)

(15) Node location (vector)

(16) Fuel displacement due only to swelling (vector)

(17) Cladding creep strain (vector)

(18) Cold gap thickness

(19) Mole fractions of fuel rod gases.

III. DESCRIPTION OF ANALYTICAL MODELS

The major analytical models of FRAP-S2 describe fuel rod behavior in the following response regimes:

(1) Fuel rod temperature

(2) Fuel rod internal gas pressure

(3) Cladding deformation

(4) Fuel deformation

(5) Fuel-cladding interaction.

The equations and models used to describe these response regimes are covered in this section. Each subsection first lists the assumptions and then describes the models. Asterisks (*) mark those assumptions representing known model simplifications for which tasks presently are under way to develop more advanced models.

1. FUEL ROD TEMPERATURE

The fuel rod temperature distribution calculation involves models which yield film, crud, and cladding oxide temperature drops; gap temperature drop; coolant temperature; cladding temperature; and the fuel temperature.

1.1 Assumptions

The calculation of the fuel rod temperature distribution is based on the following assumptions:

(1) No axial heat conduction

(2) No circumferential heat conduction *

(3) Steady state boundary conditions during each time step

(4) Gamma heating effects are negligible.

1.2 Fuel Rod Surface Temperature

The fuel rod surface temperature is calculated by first finding the coolant temperature and then summing the temperature drops due to film and crud.

1.2.1 Coolant Conditions. FRAP-S2 performs a single, closed channel coolant temperature calculation at each axial node along the rod. Bulk temperatures at these positions are determined according to the following expression:

$$T_b(z) = T_{in} + \int_0^z \left[4q''(z) / (C_p G D_e) \right] dz \tag{1}$$

where

$T_b(z)$ = bulk coolant temperature at axial position

T_{in} = inlet coolant temperature

$q''(z)$ = rod surface heat flux at axial position

C_p = heat capacity of the coolant

G = coolant mass flow rate

D_e = unit flow channel heated diameter.

The rod surface temperature at axial elevation z is taken as the minimum value between the following expressions:

$$T_w(z) = T_b(z) + \Delta T_f(z) + \Delta T_c(z) \tag{2}$$

$$T_w(z) = T_{sat} + \Delta T_{J.L.} \tag{3}$$

where

$T_w(z)$ = rod surface temperature at z (°F)

$\Delta T_f(z)$ = forced convection film temperature drop at z (°F)

$\Delta T_c(z)$ = crud temperature drop (°F)

T_{sat} = coolant saturation temperature (°F)

$\Delta T_{J.L.}$ = nucleate boiling temperature drop (°F).

The forced convection temperature drop across the coolant film layer at the surface of the rod is based on the expression

$$\Delta T_f(z) = q''(z)/h_f \tag{4}$$

where h_f is the Dittus-Boelter[5] film conductance; and

$$h_f = (0.023k/D_e) \quad R_e^{0.8} P_r^{0.4} \tag{5}$$

and

$$\Delta T_c = q''(z) \frac{\delta_c}{k_c}$$

where

δ_c = crud thickness

k_c = crud thermal conductivity (0.5 Btu/hr-ft-°F)

R_e = Reynolds number

P_r = Prandtl number.

The nucleate boiling temperature drop is based on the Jens-Lottes[6] formulation:

$$\Delta T_{J.L.}(z) = 60\ [q''(z)/10^6]^{0.25}/e^{(P/900)} \qquad (6)$$

where

P = system pressure (psia).

No additional temperature rise occurs due to crud deposition because the coolant is assumed to boil through the crud blanket.

In the case of zircaloy clad rods, the rod surface temperature applies to the ZrO_2 surface temperature.

1.2.2 <u>ZrO_2 Temperature Drop</u>. For zircaloy clad rods, the temperature drop across the zirconium oxide layer at axial station z is determined by the expression

$$\Delta T_{ZrO_2}(z) = q''(z)\ \delta_{ZrO_2}(z)/k_{ZrO_2} \tag{7}$$

where

$\delta_{ZrO_2}(z)$ = oxide thickness at axial position (ft)

k_{ZrO_2} = oxide thermal conductivity (Btu/hr-ft-°F)

1.3 Cladding Temperature Drop

The cladding temperature drop for an axial location is calculated according to the expression

$$\Delta T_{clad} = q''(z)\ R_o\ \ell n\ (R_o/R_i)/k_{clad}(T) \tag{8}$$

where

R_o = cladding outside radius (ft)

R_i = cladding inside radius (ft)

$k_{clad}(T)$ = temperature and material dependent thermal conductivity of the cladding (Btu/hr-ft-°F).

1.4 Gas Gap Temperature Drop

FRAP-S2 contains two different gap conductance models. The first is based on a cracked pellet geometry[7] and the second is a modification of the Ross and Stoute[8] model.

1.4.1 Cracked Pellet Model.

Assumptions:

(1) Nonuniform geometry of the open gap between the fuel and cladding

(2) Both plastic and elastic deformation occur at the fuel and cladding contact points when the gap is closed.

A gap conductance model was developed for use in the FRAP codes which models the cracked pellet geometry of the open gap between the fuel and cladding as well as the contact conductance when the gap is closed. The model has been compared with experimental data to determine the correct value of the various constants. This section presents an abridged treatment of the cracked pellet gap conductance model (see Reference 4 for more detail).

(1) Open Gap. If the fuel and cladding are not in contact an eccentric cladding-fuel geometry is assumed. The fraction of the pellet circumference in contact with the cladding is considered to be governed by the equations

$$F = \frac{1}{a_1 \left[\frac{100\ \Delta D}{D_F}\right]^{a_2} + a_3} + a_4 \qquad (9)$$

and

$$\frac{1}{a_3} + a_4 = 1 \qquad (10)$$

where

F = fraction of pellet in contact with the cladding

ΔD = diametral gap (in.)

D_F = hot diameter of the fuel pellet (in.)

a_1, a_2, a_3, and a_4 = empirical constants determined from data.

The constant a_4 represents the minimum fraction of pellet-cladding contact for large diametral gaps. The form of Equations (9) and (10) permits a very large fraction of pellet-cladding contact for a small calculated diametral gap. The justification for this form of the equations is that the cracks (radial and circumferential) that form in the fuel pellets will not close appreciably until the gas gap is closed. Thus the actual gas gap will close before the calculated gap. The calculated gap is the equivalent annular gap.

Heat transfer across the gas gap is considered to occur by conduction through the gas in the open gap plus zero pressure contact conductance times that fraction of the gap circumference with pellet-cladding contact. Radiation heat transfer across the open gap is assumed negligible, since reasonable gaps are always small and thus sufficiently large temperature differences between the fuel and cladding do not exist. Heat transfer across the gas gap is therefore calculated from the equation

$$h_{gap} = (1 - F)\, h_1 + F\, h_2 \qquad (11)$$

where

h_{gap} = net gap conductance (Btu/hr-ft^2-°F)

h_1 = open gap conductance (Btu/hr-ft^2-°F)

h_2 = zero pressure contact conductance (Btu/hr-ft^2-°F).

The open gap conductance is determined from equations

$$h_1 = \frac{k_{mix}}{\Delta r' + \delta} \qquad (12)$$

and

$$\Delta r' = \left(r_1^2 - \frac{r_1^2 - r_2^2}{1 - F} \right)^{1/2} \qquad (13)$$

where

k_{mix} = thermal conductivity of gas mixture (Btu/hr-ft-°F)

$\Delta r'$ = average radial gap thickness of eccentric gas gap (ft)

δ = root mean square of the fuel cladding surface roughness

A value of 14.4×10^{-6} ft is normally used

r_1 = hot calculated inside radius of cladding (ft)

r_2 = hot calculated radius of fuel (ft).

(2) Closed Gap. When the fuel and cladding are in contact, the theory of thermal contact conductance for ceramic fuel elements developed by Jacobs and Todreas[9], is used. The governing equation for contact conductance is

$$h_{gap} = C_1 \, p^n + \frac{k_{mix}}{\delta} \qquad (14)$$

where

h_{gap} = net gap conductance (Btu/hr-ft^2-°F)

C_1 = 0.475 for stainless steel cladding and 0.600 for zircaloy-2 and zircaloy-4 cladding

p = pellet-cladding contact pressure (psi)

n = 1 for $0 \leq P \leq 1000$ (psi) and 0.5 for $p \geq 1000$ (psi).

The value of the exponent, n, is governed by the material behavior at the interface of the fuel and cladding contact points. An exponent of 1 is consistent with the Ross and Stoute[8] theory of contact conductance only if the surface peaks of one of the materials are flowing plastically. If the contact points of both materials are behaving elastically the correct value for the exponent, n, is approximately 0.5. The experimental results of Fenech and Rohsenow[10] support this value and also indicate that for metal-ceramic pairs the transition pressure from elastic to plastic flow is approximately 1000 psi. The parameter k_{mix}/δ accounts for the heat conduction through the gas in the gaps between contact points.

1.4.2 Ross and Stoute Model.

Assumptions:

(1) Uniform geometry of the open gap between the fuel and cladding

(2) Elastic cladding deformation at the points of fuel and cladding contact after the gap is closed.

(1) Open Gap. If the fuel and cladding are not in contact, heat is transferred across the gas gap by conduction through the gas and radiation. Heat transfer across the gas gap is considered to be governed by the equation

$$h_g = \frac{K_g}{t_g + (g_1 + g_2)} + h_r \qquad (15)$$

where

h_g = gap conductance

K_g = conductivity of gas in gas gap

t_g = gap thickness

g_1 = temperature jump distance at cladding inside surface

g_2 = temperature jump distance at fuel outside surface

h_r = radiant heat transfer conductance.

Radiant heat transfer conductance is computed using the following equation:

$$h_r = \sigma F_e (T_f^2 + T_c^2)(T_f + T_c) \qquad (16)$$

where

h_r = radiant heat transfer conductance

σ = Stefan-Boltzman constant

F_e = emissivity factor

T_f = temperature of outside surface of fuel

T_c = temperature of inside surface of cladding.

The emissivity factor is computed by the equation

$$F_e = [\frac{1}{e_f} + \frac{r_f}{r_c} (\frac{1}{e_c} - 1)]^{-1} \qquad (17)$$

where

F_e = emissivity factor

e_f = emissivity of fuel surface

e_c = emissivity of cladding inside surface

r_f = outside radius of fuel

r_c = inside radius of cladding.

The temperature jump distance is computed by an empirically derived equation presented in the GAPCON code report[3]. The equation is

$$g_1 + g_2 = 5.448 [\frac{\mu}{p} (\frac{T}{M})^{1/2}] \qquad (18)$$

where

$g_1 + g_2$ = jump distance (cm)

μ = viscosity of gas (gm/cm-sec)

P = pressure of gas (psi)

T = temperature of gas (K)

M = molecular weight of gas.

(2) Closed Gap. If the fuel and cladding are in contact, the GAPCON code equation for contact conductance is used. This equation agrees with gap conductance data presented by Ross and Stoute[8]. The equation is

$$h_g = \frac{K_m P_i}{a_o R^{0.5} H} + \frac{K_g}{c(R_f+R_c) + (g_1 + g_2)} + h_r \qquad (19)$$

where

h_g = gap conductance (cal/sec-cm^2-°C)

K_m = $\frac{2k_f k_c}{k_f+k_c}$

k_f = fuel conductivity (cal/sec-cm-°C)

k_c = cladding conductivity (cal/sec-cm-°C)

P_i = interfacial pressure between fuel and cladding (psi)

a_o = a constant -- 0.5 cm$^{1/2}$

R = $\frac{(R_f^2 + R_c^2)^{1/2}}{2}$

R_c = arithmetic mean roughness height of cladding (cm)

R_f = arithmetic mean roughness height of fuel (cm)

H = Meyer-Hardness of cladding (psi).

The coefficient c in Equation (19) is computed by the empirical equation

$$c = 1.98\ e^{-0.00125\ P_i} \qquad (20)$$

where

P_i = interfacial pressure between fuel and cladding (kg/cm^2).

1.5 Pellet Heat Conduction

The pellet temperature distribution is calculated using one of two models. The first relies on results generated by the depletion code LASER, whereas the second makes use of flux depression.

1.5.1 Pellet Temperature Distribution with LASER.

The heat transfer formulation in FRAP-S2 is based on a nonlinear least squares fit of LASER[11] generated radial power distribution data. The model accounts for the spatial effects of isotopic production on pellet self-shielding characteristics at any burnup and power level for both PWR and BWR plutonium or uranium enriched spectrums. The radial power depression has been obtained for typical commercial fuel enrichments by making use of the results from the depletion code LASER.

From a heat balance across a differential annular ring

$$\theta\left(k + \frac{dk}{dr}\,dr\right)(r + dr)\left.\frac{dT}{dr}\right|_{r + dr} - \theta kr\left.\frac{dT}{dr}\right|_{r} + q'''(r)rdr = 0 \qquad (21)$$

where the terms are defined in Figure 1. After rearrangement of Equation (21), omission of higher order terms, and integration we obtain:

$$kr\,\frac{dT}{dr} = -\int_{0}^{r} rq'''(r)dr. \qquad (22)$$

A second integration, from the pellet surface, a, to some point, r, gives:

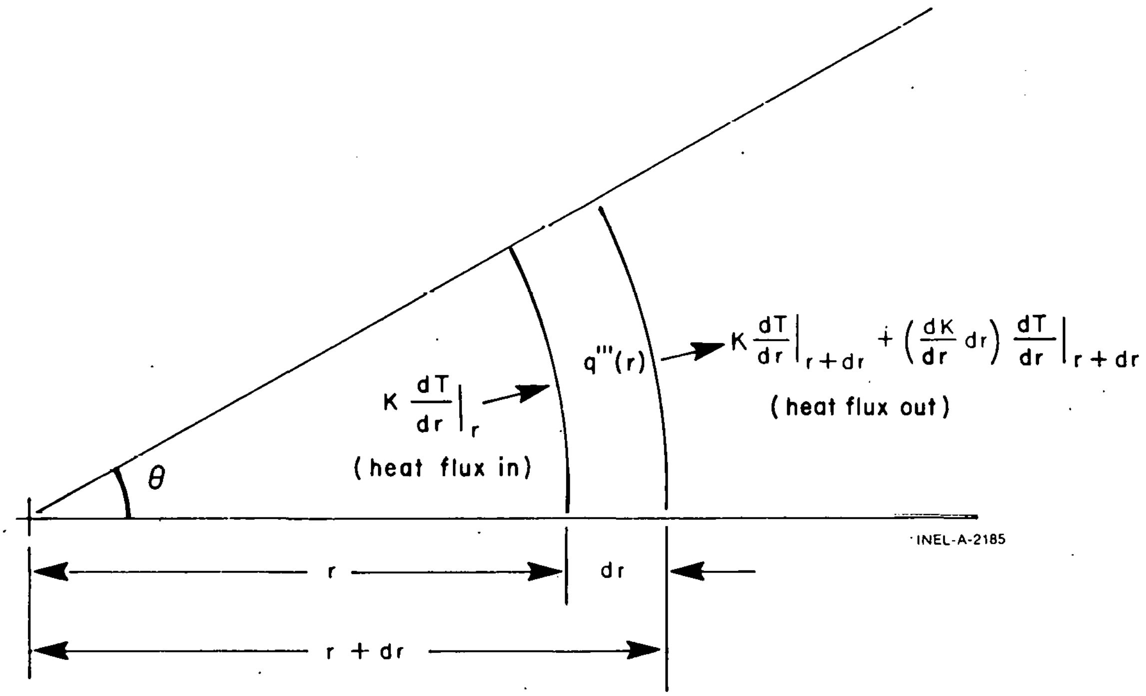

Fig. 1 Heat conduction in fuel rod.

$$\int_{T_a}^{T_r} k(T)dT = \int_r^a \left[\int_0^r q'''(r)rdr\right] dr/r. \tag{23}$$

From a least square surface fit of the LASER code output we obtain values of P_1, P_2, and P_3.

$$q'''(r) = P_1R^{P_2} + P_3 \tag{24}$$

where the P's are some function of time and enrichment and R is a fractional radius.

The heat generation distribution of Equation (24) can be normalized as follows:

$$q'''(r) = \frac{q'}{12\pi a^2 \, q_L'''} \left[P_1\left(\frac{r}{a}\right)^{P_2} + P_3\right] \tag{25}$$

where

$q'''(r)$ = radially dependent energy generation (kW/in.^{3})

q' = average local power (kW/ft)

a = pellet radius (in.)

q'''_l = LASER average heat generation rate (kW/in.^{3})

= 7.7316069 for PWR
= 4.4353724 for BWR
} for typical commercial rods

P_1, P_2, and P_3 = factors generated from LASER output which vary with time and enrichment.

Then substitution of Equation (25) into Equation (23) results in

$$\int_{T_a}^{T_r} k(t)dt = \frac{q'}{12\pi a q_L'''} \int_r^a \left\{ \int_0^r \left[P_1 (r/a)^{P_2} + P_3 \right] rdr \right\} dr/r \qquad (26)$$

and integrating twice,

$$\int_{T_a}^{T_r} k(t)dt = \frac{q'}{12\pi a q_L'''} \int_r^a \left[\frac{P_1 r^{P_2+2}}{(P_2+2)a^{P_2}} + \frac{1}{2} P_3 r^2 \right] dr/r \qquad (27)$$

$$\int_{T_a}^{T_r} k(t)dt = \frac{q'}{\pi a^2 q_L'''} \left[\frac{P_1 a^{P_2+2}}{(P_2+2)^2 a^{P_2}} + \frac{1}{4} P_3 a^2 - \frac{P_1 r^{P_2+2}}{(P_2+2)^2 a^{P}} - \frac{1}{4} P_3 r^2 \right] . \qquad (28)$$

The FRAP-S2 code divides the pellet into ten equal area rings, with boundaries numbered 1 at the surface and 11 at the center. The fractional radius R can, therefore, be written as

$$R_L = \sqrt{(12 - L)/10} \tag{29}$$

$$R_{L+1} = \sqrt{(11 - L)/10} \tag{30}$$

where L is the ring boundary number.

To determine the integral of the thermal conductivity across any one FRAP-S pellet ring, Equation (28) is written as

$$\int_{T_L}^{T_{L+1}} k(t)dt = \frac{q'}{\pi q_L'''} \left[\frac{P_1 R_L^{P_2+2}}{(P_2+2)^2} + \frac{1}{4} P_3 R_L^2 - \frac{P_1 R_{L+1}^{P_2+2}}{(P_2+2)^2} - \frac{1}{4} P_3 R_{L+1}^2 \right] \tag{31}$$

where R_L and R_{L+1} are defined in Equations (29) and (30). Note that $r_L = a * R_L$.

The value of $\int kdT$ to any point r in the pellet is calculated by summing each ring $\int kdT$ calculation of Equation (31), starting from the surface. Then, from an empirical correlation of temperature as a function of $\int kdT$ (polynominal fit of data) the temperature of ring R_L is calculated.

1.5.2 Pellet Temperature Distribution with Flux Depression.

(1) Basic Relationships. The equation for the radial conduction of heat across a circular boundary within a solid cylindrical pellet may be written

$$\int_0^r P(r)\, 2\pi r dr + 2\pi r k(dT/dr) = 0 \tag{32}$$

where

r = the radius of the circle

$P(r)$ = the volumetric heat generation rate at radius r

T = the temperature

k = the pellet thermal conductivity, a function of T.

The average value of $P(r)$ is given by the equation

$$\bar{P} = \int_0^a P(r)\ 2\pi r dr / \int_0^a 2\pi r dr = (2/a^2) \int_0^a P(r) r dr \qquad (33)$$

where a is the pellet radius.

The relationship between the thermal heat rating q', the surface heat flux q'', and $\overline{P}$ is given by the equation

$$q' = \pi a^2 \bar{P} = 2\pi a q''. \qquad (34)$$

The value of $P(r)$ at the center of the pellet is designated P_0, i.e.

$$P_0 = P(r) \Big|_{r=0}. \qquad (35)$$

The surface and center temperatures of the pellet are T_s and T_c, respectively.

(2) Uniform Heat Generation. Consider the case of uniform heat generation. For this case Equations (33) and (35) give

$$P(r) = \bar{P} = P_0. \qquad (36)$$

Substituting Equation (37) in Equation (32) and carrying out the integration gives

$$P_o r^2/2 + rk(dT/dr) = 0. \tag{37}$$

Separating variables and integrating from r = r to r = a gives

$$(P_o/4)(a^2-r^2) = \int_{T_s}^{T} kdT. \tag{38}$$

Using Equations (34) and (37), Equation (39) becomes

$$(q'/4\pi)(1-\rho^2) = \int_{T_s}^{T} kdT \tag{39}$$

where ρ is the dimensionless radius given by the equation

$$\rho = r/a. \tag{40}$$

At the center of the pellet, $\rho = 0$ and $T = T_c$ in which case Equation (39) becomes

$$q'/4\pi = \int_{T_s}^{T_c} kdT. \tag{41}$$

An expression for radius as a function of temperature within the pellet may be found by solving Equation (39) for ρ:

$$\rho = [1 - (4\pi/q')\int_{T_s}^{T} kdT]^{1/2}. \tag{42}$$

(3) Nonuniform Heat Generation (Diffusion Theory). Due to self-shielding effects, the power generation within an enriched fuel pellet will not be uniform. The following equation is obtained from simple diffusion theory.

$$P(r) = AI_0(\kappa r) \tag{43}$$

where

A = a constant

I_0 = the zero order modified Bessel function of the first kind

κ = the reciprocal of the thermal diffusion length in the fuel.

The value of κ depends upon the fuel density and enrichment. A plot indicates that for UO_2 of 95% theoretical density, κ varies from 2 to 3 cm^{-1} for enrichment values of 2.5 to 6% U-235. Substituting Equation (43) in Equation (35) leads to $A = P_0$ since $I_0(0) = 1$. Equation (43) can thus be written

$$P(r) = P_0 I_0(\kappa r). \tag{44}$$

Substituting Equation (44) in Equation (33) gives

$$\bar{P} = 2P_0[I_1(\kappa a)]/(\kappa a) \tag{45}$$

where I_1 is the first order modified Bessel function of the first kind. Substituting Equation (44) in Equation (32) and carrying out the integration gives

$$P_0 r[I_1(\kappa r)]/\kappa + rk(dT/dr) = 0. \tag{46}$$

Separating variables and integrating from r = r to r = a gives

$$(P_0/\kappa^2)[I_0(\kappa a)-I_0(\kappa r)] = \int_{T_s}^{T} kdT. \tag{47}$$

Using Equations (34) and (45), Equation (47) becomes

$$(q'/4\pi)\ \left\{2[I_0(\kappa a)-I_0(\kappa r)]\right\} / \left\{\kappa a[I_1(\kappa a)]\right\} = \int_{T_s}^{T_c} kdT. \tag{48}$$

At the center of the pellet r = 0 and $T = T_c$ in which case Equation (48) becomes

$$(q'/4\pi)\ \left(2[I_0(\kappa a)-1]/\left\{\kappa a[I_1(\kappa a)]\right\}\right) = \int_{T_s}^{T_c} kdT. \tag{49}$$

The expression multiplying q'/4π in this equation is called f. Since f is less than 1, a comparison of Equations (41) and (49) indicates that the thermal heat rating associated with given fuel surface and center temperatures is greater for nonuniform heat generation given by Equation (44) than for uniform heat generation given by Equation (36), the ratio of the two heat ratings being f. Thus, nonuniform heat generation decreases the effect of the thermal heat rating on fuel temperature and consequently f is termed the flux depression factor.

(4) Nonuniform Heat Generation (Parabolic Approximation). As was shown above, a tedious calculation procedure is required to obtain the radial temperature distribution for the nonuniform heat generation relationship given by Equation (44). Equation (44) can be approximated very well by the relation

$$P(r) = P_0[1 + 0.27(\kappa r)^2]. \tag{50}$$

In order to obtain a better fit for any particular problem, the following equation is proposed:

$$P(r) = P_o[1 + B(r/a)^2] \qquad (51)$$

where B will be determined as a function of f only.

Equation (51) is in agreement with the results of a fission distribution analysis obtained using several digital computer programs. Substituting Equation (51) in Equation (33) gives

$$\bar{P} = P_o(1+B/2). \qquad (52)$$

Substituting Equation (51) in Equation (32) and carrying out the integration gives

$$(p_o r^2/2)[1 + (B/2)(r/a)^2] + rk(dT/dr) = 0.$$

Separating variables and integrating from r = r to r = a gives

$$(P_o/4)(a^2-r^2)[1 + B(a^2+r^2)/(4a^2)] = \int_{T_s}^{T} kdT. \qquad (53)$$

Using Equations (34), (40), and (52), Equation (53) becomes

$$(q'/4\pi)(1-\rho^2)[B(1+\rho^2) + 4]/(2B+4) = \int_{T_s}^{T} kdT. \qquad (54)$$

At the center of the pellet, $\rho = 0$ and $T = T_c$, in which case Equation (54) becomes

$$(q'/4\pi)[(B+4)/(2B+4)] = \int_{T_s}^{T_c} kdT. \qquad (55)$$

Solving for B gives

$$B = 4(1-f)(2f-1). \qquad (56)$$

Substituting in Equation (54) gives

$$(q'/4\pi)(1-\rho^2)[f + (1-f)\rho^2] = \int_{T_s}^{T} kdT. \tag{57}$$

Equation (57) is a quadratic equation in ρ^2 which when solved for ρ gives

$$\rho = 1-2f + \left\{[q' - 16\pi(1-f) \int_{T_s}^{T} kdT]/q'\right\}^{1/2} /[2(1-f)]^{1/2}. \tag{58}$$

Equation (58) enables solving for ρ in terms of T directly. Note that for f = 1, Equation (58) reduces to $\rho = [0/0]^{1/2}$. Applying L'Hospital's rule to Equation (28) results in Equation (42).

1.6 Stored Energy

The stored energy in the fuel rod is calculated by summing the energy of each pellet ring calculated at that ring temperature in the same manner as one of the methods used in GAPCON-THERMAL-1[3].

$$E = \frac{\sum_{i=1}^{N} m_i \int_{298°C}^{T_i} C_p(T)dT}{m} \tag{59}$$

where

E = stored energy

m_i = mass of ring segment i

T_i = temperature of ring segment i

$C_p(T)$ = heat capacity

m = mass of the axial segment

N = number of annular rings (10 maximum).

2. FUEL ROD INTERNAL GAS PRESSURE

2.1 Assumptions

The static fuel rod internal pressure model is based on the following assumptions:

(1) Perfect gas law holds (PV = NRT)

(2) Gas pressure is constant throughout the fuel rod

(3) Gas in the fuel rod cracks is at the fuel average temperature.

2.2 Static Fuel Rod Internal Pressure

Fuel rod internal gas pressure is computed by the equation:

$$p_g = \frac{M_g R}{\frac{V_P}{T_P} + \sum_{n=1}^{N} \left(\pi \frac{(r_{cn}^2 - r_{fn}^2)\Delta z_n}{T_{G_n}} + \frac{V_c \Delta z_n}{T_c} \right)} \qquad (60)$$

where

P_g = internal fuel rod pressure

M_g = moles of gas in fuel rod

R = universal gas constant

V_p = plenum volume (defined by plenum volume model)

n = axial node number

T_p = temperature of gas in plenum

N = number of axial nodes into which fuel rod is divided for numerical solution

r_{cn} = radius of inside surface of fuel at axial node n

r_{fn} = radius of outside surface of fuel at axial node n

T_{G_n} = temperature of gas in gas gap at axial node n

Δz_n = fuel rod length associated with axial node n

V_c = fuel crack volume per unit length

T_c = temperature of the crack volume.

2.3 Plenum Gas Temperature

The plenum gas temperature is calculated based on energy transfer between the top of the pellet stack and the plenum gas, between the coolant channel and the plenum gas, and between the spring and the plenum gas. The three contributions are discussed in the following.

Natural convection from the top of the fuel stack is calculated based on heat transfer coefficients from McAdams[12] for laminar or turbulent natural convection from flat plates.

$$Nu = C(GrPr)^m \tag{61}$$

where

Nu = the Nusselt number

Gr_f = the Grashof number

Pr_f = the Prandtl number

and for

$GrPr \leq 2.0 \times 10^7$ $C = 0.54$ and $m = 0.25$

or

$GrPr > 2.0 \times 10^7$ $C = 0.14$ and $m = 0.33$.

The heat transfer coefficient is calculated from

$$h_p = \frac{k\ Nu}{D} \tag{62}$$

where

h_p = the heat transfer coefficient from the top of the pellet stack to the plenum gas (Btu/hr-ft-°F)

Nu = Nusselt number as found above

D = inside diameter of the cladding of the top node (ft)

k = conductivity of the plenum gas (Btu/hr-ft^2-°F).

The overall effective conductivity from the coolant to the plenum is found as follows:

$$U_c = \frac{1.0}{\dfrac{1}{\frac{D\ h_f}{2}} + \dfrac{\ln\left(\frac{D_o}{D_I}\right)}{k_{Clad}} + \dfrac{1.0}{D_o\ (1.0 + \alpha\Delta T)\ h_{DB}}} \tag{63}$$

where

U_c = overall effective conductivity from the coolant to the plenum gas (Btu/hr-ft-°F)

D = hot state inside cladding diameter (ft)

h_f = cladding inside surface film coefficient (Btu/hr-ft-°F)

D_o = cold state outside cladding diameter (ft)

D_I = cold state inside cladding diameter (ft)

k_{clad} = cladding thermal conductivity (Btu/hr-ft^2-°F)

α = coefficient of thermal expansion of the cladding (ft/ft-°F)

ΔT = temperature difference between cladding average temperature and datum temperature (°F)

h_{DB} = heat transfer coefficient between the coolant and the cladding (Btu/hr-ft-°F).

Gamma heating in the hold-down spring is calculated at a volumetric rate of 1.146 Btu/hr-ft^3 for every Btu/hr-ft^2 of rod average heat flux

$$Q_{sp} = 1.146 \, \dot{q}'' \, V_s \qquad (64)$$

where

Q_{sp} = energy generated in the spring (Btu/hr)

$\dot{q}''$ = average heat flux of the rod (Btu/hr-ft)

V_s = volume of the spring (ft^3).

The plenum temperature is then approximated from the following equation:

$$T_{plen} = \frac{Q_{sp} + U_c \frac{V_p}{D^2} T_{BLK} + T_{pa} h_p \pi D^2/4}{U_c \frac{V_p}{D^2} + \frac{h_p \pi D^2}{4}} \qquad (65)$$

where

Q_{sp}, U_c, D, and h_p are previously described

and

T_{plen} = plenum temperature (°F)

V_p = volume of the plenum (ft^3)

T_{BLK} = bulk coolant temperature at the top axial increment (°F)

T_{pa} = temperature associated with the insulator or top pellet (°F).

2.4 Pellet Dish Volume

The volume between pellets is calculated and included as part of the overall volume in the internal pressure model. The interpellet volume is calculated at each time step as the difference between the cold pellet geometry and the hot pellet operating geometry.

Figure 2 shows: (A) a cold pellet interface configuration; and (B) an exaggerated hot pellet interface configuration. The volume available for expansion of internal fill gas is defined by the cross hatched areas (A and B) in the figure.

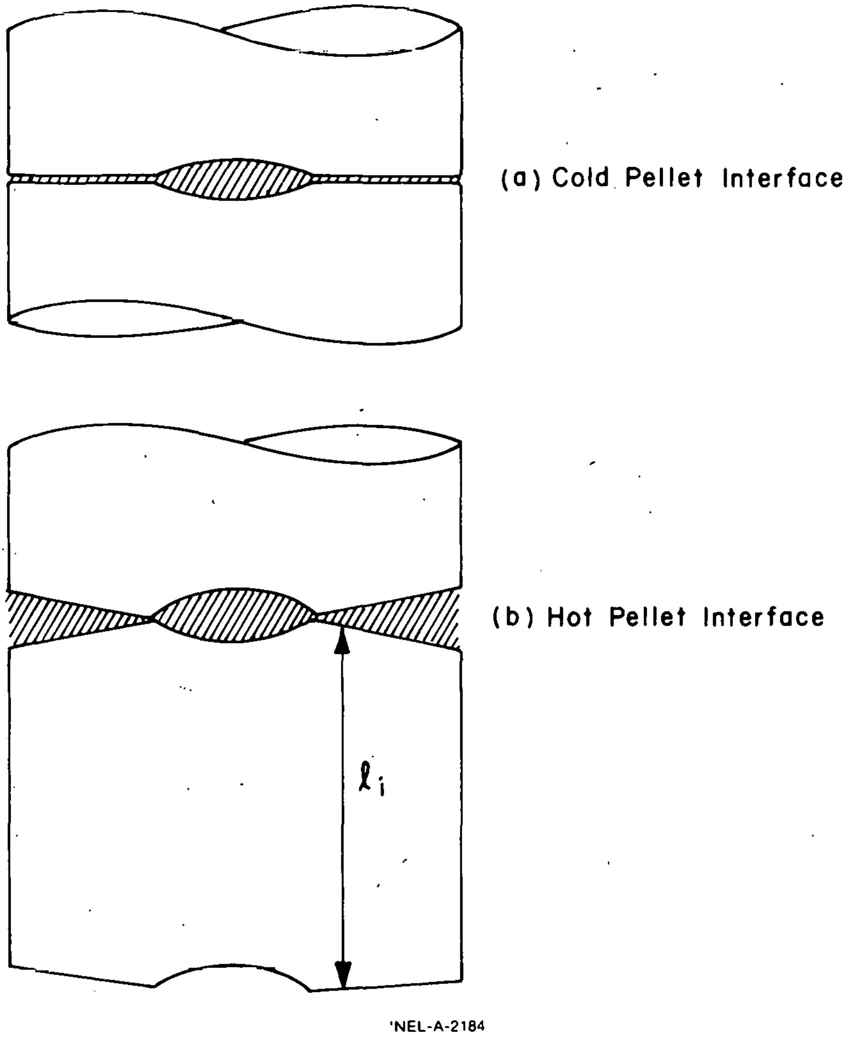

Fig. 2 Pellet expansion.

3. CLADDING DEFORMATION

3.1 Assumptions

The cladding deformation model is based upon the following assumptions:

(1) Incremental theory of plasticity

(2) Prandtl-Reuss flow rule

(3) Isotropic work-hardening

(4) Thin wall cladding (stress, strain, and temperature are uniform through cladding thickness)

(5) If fuel and cladding are in contact, no slippage occurs at fuel-cladding interface

(6) Bending strains and stresses in cladding are insignificant

(7) Axisymmetric loading and deformation of cladding.

This section describes the models which perform the mechanical analysis of the cladding. The models analyze the elastic and plastic deformation of the cladding due to thermal and pressure loadings, as well as loads due to mechanical interaction between the cladding and the fuel pellets.

Fuel Rod and Cladding Analysis Subcode (FRACAS) consists of a set of individual subroutines, each of which is independent of the others. Hence, the model contained in each subroutine can be modified or replaced without requiring changes in any other part of the subcode.

Deformation and stresses in the cladding in the open gap regime are computed in subroutine CLADF. The model considered is that of a thin cylindrical shell with specified internal and external pressures and a prescribed uniform temperature.

Calculations for the closed gap regime are made in subroutine COUPLE. The model considered is a thin cylindrical shell with prescribed external pressure and a prescribed radial displacement of its inside surface. The prescribed displacement is obtained from the fuel displacement models contained in FRAP-S. Further, since no slip is assumed to take place when the fuel and cladding are in contact, the axial expansion of the fuel is transmitted directly to the cladding, and hence, the change in axial strain in the shell is also prescribed.

Calculations for the trapped stack regime are made in subroutine STACK. The model considered is a thin cylindrical shell with prescribed internal and external pressures and a prescribed total change in length of the cylinder. In contrast to CLADF and COUPLE, which solve for the stresses and strains at only one axial location at a time, subroutine STACK simultaneously solves for the stresses and strains in all axial nodes which are being strained axially by the trapped stack of fuel pellets.

The decision as to whether or not the gap is open or closed, and whether to call COUPLE, STACK or CLADF is made in the executive subroutine, FCMI, (Fuel-Clad Mechanical Interaction). This is the only subroutine which must be called to initiate the fuel-clad interaction analysis. At the completion of this analysis, FCMI returns either a new gap size or a new interface pressure between fuel and clad for use in the next iteration of the thermal calculations.

In each of COUPLE, STACK, and CLADF, either an elastic-plastic (time-independent) solution or a creep-stress relaxation (time-dependent) solution is obtained, depending on the value of an input flag.

For the plasticity calculations, two additional subroutines, STRAIN and STRESS, compute changes in yield stress with work-hardening, given a uniaxial stress-strain curve. This stress-strain curve will be obtained from the material properties package subcode, MATPRO[4]. Subroutine STRAIN computes the effective total strain and new effective plastic strain given a value of effective stress and the effective plastic strain at the end of the last loading increment. Subroutine STRESS computes the effective stress given an increment of plastic strain and the effective plastic strain at the end of the last loading increment. Depending on the work-hardened value of yield stress, loading can be either elastic or plastic, while unloading is constrained to occur elastically. (Isotropic work-hardening is assumed in these calculations.)

For the creep and stress relaxation analysis, the creep rate (at the appropriate stress and temperature) is obtained from subroutine CREPR, while the creep-stress corresponding to a given creep rate is obtained from subroutine CREEP. The creep calculations are based on the so-called "equation of state" approach in which the numerical calculations closely parallel those in the incremental plasticity calculations.

Section 3.2 of this report presents a discussion of the general problem of elastic-plastic analysis in biaxial stress fields. It will be indicated there how the formulation of the problem naturally leads to the Method of Successive Substitutions as a means of obtaining a solution to the coupled, nonlinear elastic-plastic continuum equations. Section 3.3 describes the general multiaxial creep-stress relaxation problem, and describes the method of extending an elastic-plastic incremental solution to consider creep deformation. Section 3.4 describes the individual subroutines and specific equations which are solved.

3.2 General Considerations in Elasto-Plastic Analysis

Problems involving elastic-plastic deformation and multiaxial states of stress involve a number of questions which do not need to be considered in a uniaxial problem. In the following, an attempt is made to briefly outline the structure of incremental plasticity, and to outline the Method of Successive Substitutions (also called the Method of Successive Elastic Solutions) which has been used so successfully in treating multiaxial elastic-plastic problems[13].

In a problem involving only uniaxial stress σ_1, the strain ϵ_1 is related to the stress by an experimentally determined stress-strain curve as shown in Figure 3, and Hooke's law is taken as

$$\epsilon_1 = \frac{\sigma_1}{E} + \epsilon_1^P + \int \alpha \, dT$$

where ϵ_1^P is the plastic strain. The onset of yielding occurs at the yield stress, which can be determined directly from Figure 3. Given a load (stress) history, the resulting deformation can be determined in a

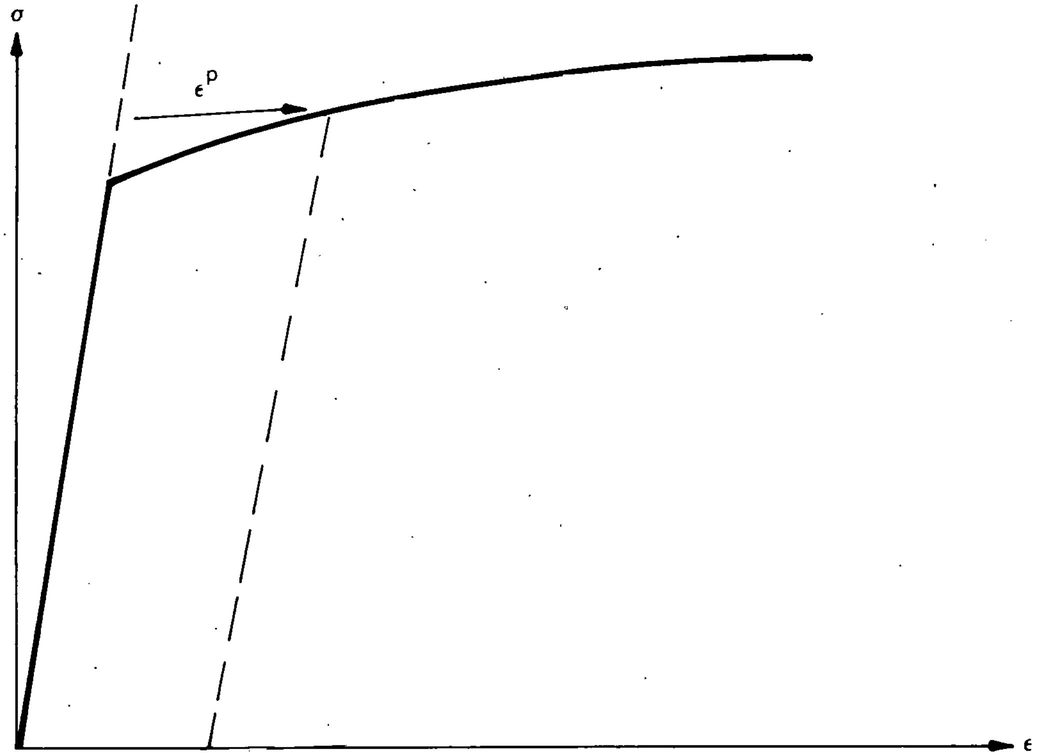

INEL-A-2183

Fig. 3 Typical isothermal stress-strain curve.

simple fashion. Increase of yield stress with work-hardening is easily computed directly from Figure 3.

In a problem involving multiaxial states of stress, however, the situation is not so clear cut. Here one must have a method of relating the onset of plastic deformation to the results of a uniaxial test, and further, when plastic deformation occurs, one must have some means of determining how much plastic deformation has occurred, and how it is distributed among the individual components of strain. These two complications are taken into account by use of the so-called "Yield Function" and "Flow Rule", respectively.

A considerable wealth of experimental evidence exists on the onset of yielding in a multiaxial stress state. The bulk of this evidence supports the von Mises yield criteria, which assert that yielding occurs when the stress state is such that:

$$0.5 \left[(\sigma_1 - \sigma_2)^2 + (\sigma_2 - \sigma_3)^2 + (\sigma_3 - \sigma_1)^2 \right] = \sigma_y^2 \qquad (66)$$

where σ_i are the principal stresses, and σ_y is the yield stress as determined in a uniaxial stress-strain test. The square root of the left-hand side of this equation is referred to as the effective stress, σ_e, and this effective stress is one commonly used type of yield function.

To determine how the yield stress changes with permanent deformation, it is hypothesized that the yield stress is a function of the effective plastic strain, ε^P. An increment of effective plastic strain is determined at each loadstep and ε^P is defined as the sum of all increments incurred:

$$\varepsilon^P \triangleq \int d\varepsilon^P . \qquad (67)$$

Each increment of effective plastic strain is related to the individual plastic strain components by

$$d\varepsilon^P = \sqrt{\frac{2}{3}} \left[(d\varepsilon_1^P - d\varepsilon_2^P)^2 + (d\varepsilon_2^P - d\varepsilon_3^P)^2 + (d\varepsilon_3^P - d\varepsilon_1^P)^2 \right]^{1/2} \qquad (68)$$

where the $d\varepsilon_i^P$ are the plastic strain components in principal coordinates. It is a well known experimental result that at pressures on the order of the yield stress, plastic deformation occurs with no change in volume. This implies that

$$d\varepsilon_1^P + d\varepsilon_2^P + d\varepsilon_3^P = 0 \qquad (69)$$

and hence in a uniaxial test with $\sigma_1 = \sigma$, $\sigma_2 = \sigma_3 = 0$, the plastic strain increments are

$$d\varepsilon_2^P = d\varepsilon_3^P = -1/2 \, d\varepsilon_1^P$$

so that in a uniaxial test, Equations (66) and (68) reduce to

$$\sigma_e = \sigma$$

$$d\varepsilon^P = d\varepsilon_1^P. \tag{70}$$

Thus, when it is assumed that the yield stress is a function of the total effective plastic strain (called the Strain-Hardening Hypothesis), the functional relationship between yield stress and plastic strain can be taken directly from a uniaxial stress-strain curve by virtue of Equation (70).

The relationship between the magnitudes of the plastic strain increments and the effective plastic strain increment is provided by the Prandtl-Reuss Flow Rule:

$$d\varepsilon_i^P = \frac{3}{2}\frac{d\varepsilon^P}{\sigma_e} S_i \qquad i = 1, 3 \tag{71}$$

where S_i are the deviatoric stress components (in principal coordinates) defined by

$$S_i = \sigma_i - \frac{1}{3}(\sigma_1 + \sigma_2 + \sigma_3) \qquad i = 1, 3. \tag{72}$$

Equation (71) embodies the fundamental observation of plastic deformation that the plastic strain increments are proportional to the deviatoric stresses. It may be shown[13] that the constant of proportionality is determined by the choice of the yield function. Direct substitution shows that Equations (67), (69), (70), (71), and (72) are consistent with one another.

Once the plastic strain increments have been determined for a given loadstep, the total strains are determined from a generalized form of Hooke's law given by:

$$
\begin{aligned}
\varepsilon_1 &= \frac{1}{E}\left[\sigma_1 - \nu(\sigma_2 + \sigma_3)\right] + \varepsilon_1^P + d\varepsilon_1^P + \int \alpha_1 dT \\
\varepsilon_2 &= \frac{1}{E}\left[\sigma_2 - \nu(\sigma_1 + \sigma_3)\right] + \varepsilon_2^P + d\varepsilon_2^P + \int \alpha_2 dT \qquad (73) \\
\varepsilon_3 &= \frac{1}{E}\left[\sigma_3 - \nu(\sigma_2 + \sigma_1)\right] + \varepsilon_3^P + d\varepsilon_3^P + \int \alpha_3 dT
\end{aligned}
$$

in which ε_1^P, ε_2^P, and ε_3^P are the total plastic strain components at the end of the previous load increment and ν is Poisson's ratio.

The remaining continuum field equations of equilibrium, strain displacement, and strain compatibility are unchanged. The complete set of governing equations is presented in Table I, written in terms of rectangular Cartesian coordinates and employing the usual indicial notation in which a repeated Latin index implies summation. This set of equations is augmented by an experimentally determined uniaxial stress-strain relation.

3.2.1 Method of Solution. When the problem under consideration is statically determinate, so that the stresses can be found from equilibrium conditions alone, the resulting plastic deformation can easily be determined. However, when the problem is statically indeterminate, and the stresses and deformation must be found simultaneously, then the full set of plasticity equations proves to be quite formidable even in the case of simple loadings and geometries.

One numerical procedure which as been used with considerable success is the Method of Successive Substitutions. This can be applied to any problem for which an elastic solution can be obtained, either in closed form or numerically. A full discussion of this technique including a number of technologically useful examples is contained in Reference 13.

TABLE I

SUMMARY OF GOVERNING EQUATIONS

Equilibrium

$$\sigma_{ji,j} + \rho f_i = 0$$

where

σ = stress tensor

ρ = mass density

f_i = components of body force per unit mass

Stress-Strain

$$\varepsilon_{ij} = \frac{1+\nu}{E} \sigma_{ij} - \delta_{ij} \left(\frac{\nu}{E} \sigma_{kk} - \int \alpha dT\right) + \varepsilon^P_{ij} + d\varepsilon^P_{ij}$$

Strain Displacement

$$\varepsilon_{ij} = \frac{1}{2} (u_{i,j} + u_{j,i})$$

Compatibility

$$\varepsilon_{ij,k\ell} + \varepsilon_{k\ell,ij} - \varepsilon_{ik,j\ell} - \varepsilon_{j\ell,ik} = 0$$

Definitions used in Plasicity

$$\sigma_e \triangleq \sqrt{\frac{3}{2} S_{ij} S_{ij}}$$

$$S_{ij} \triangleq \sigma_{ij} - \frac{1}{3} \sigma_{kk}$$

$$d\varepsilon^P \triangleq \sqrt{\frac{2}{3} d\varepsilon^P_{ij} d\varepsilon^P_{ij}}$$

Prandtl-Reuss Flow Rule

$$d\varepsilon^P_{ij} = \frac{3}{2} \frac{d\varepsilon^P}{\sigma_e} S_{ij}$$

Briefly, the method involves breaking the loading path up into a number of small increments. (For example, in the present application, the loads are external pressure, temperature, and either internal pressure of prescribed displacement or the inside surface of the cladding. These loads all vary during the operating history of the fuel rod.) For each new increment of the loading, the solution to all the plasticity equations listed in Table I is obtained as follows:

First, an initial estimate of the plastic strain increments $d\varepsilon^P_{ij}$ is made. Based on these values, the equations of Equilibrium, Hooke's law, Strain-Displacement and compatibility are solved as for any elastic problem. From the stresses so obtained, the deviatoric stresses S_{ij} may be computed. This represents one path in the computational scheme.

Independently, using the assumed $d\varepsilon^P_{ij}$ values, the increment of effective plastic strain $d\varepsilon^P$ may be computed, and from this and the stress-strain curve, a value of the effective stress σ_e is obtained.

Finally, a new estimate of the plastic strain increments is obtained from the Prandtl-Reuss Flow Rule:

$$d\varepsilon^P_{ij} = \frac{3}{2} \frac{d\varepsilon^P}{\sigma_e} S_{ij}$$

and the entire process is continued until the $d\varepsilon^P_{ij}$ converge. A schematic of the iteration scheme is shown in Figure 4.

The mechanism by which improved estimates of $d\varepsilon^P_{ij}$ are obtained results from the fact that the effective stress obtained from $d\varepsilon^P$ and the stress-strain curve will not be equal to the effective stress which would be obtained from the stresses from the elastic solution. They will only agree when convergence is obtained.

The question of convergence is one that cannot, in general, be answered a priori. However, it can be shown[13] that convergence will be obtained for sufficiently small load increments. Furthermore, lack

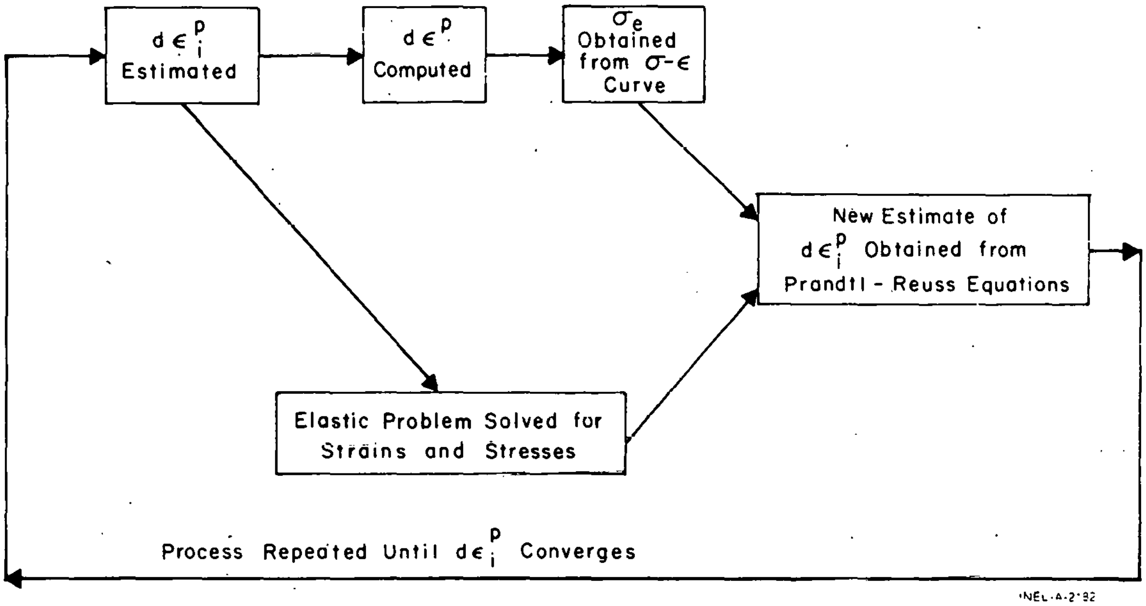

Fig. 4 Schematic of the method of successive elastic routines.

of convergence can usually be traced to the flatness of the stress-strain curve in the plastic region. Problems with convergence are accentuated when the material is at high temperatures (approximately 1200°F and above for zircaloy), due to the fact that work-hardening effects decrease with temperature.

3.2.2 Modified Iteration Scheme. To avoid (or at least minimize) such convergence problems, an alternate iteration scheme was devised by Mendelson and his co-workers. This scheme is based on the von Mises yield function and the Prandtl-Reuss flow rule, so no new hypotheses or assumptions are involved. The iteration scheme is essentially the same as the Prandtl-Reuss iteration scheme described above, except that the iterated variables σ_e and $d\varepsilon_{ij}^P$ (which are related by the highly nonlinear stress-strain law) are replaced by a new pair of variables which are related to $d\varepsilon^P$ in a more nearly linear fashion. The new variables are ε_{et}, the equivalent modified total strain, and ε'_{ij}, the modified deviator strains, and in terms of these new variables, the Prandtl-Reuss flow rule becomes

$$d\varepsilon_{ij}^P = \frac{d\varepsilon^P}{\varepsilon_{et}} e'_{ij} . \qquad (74)$$

Thus, ε_{et} plays the role of σ_e, and ε'_{ij} replaces the deviator stresses S_{ij}. At each step in the iteration, ε_{et} is calculated from the strains obtained from the pseudoelastic solution based on the previous values of the plastic strain increments, and then $d\varepsilon^P$ is related to ε_{et} via the uniaxial stress-strain curve by the expression

$$d\varepsilon^P = \frac{\varepsilon_{ct} - \frac{2}{3}\left(\frac{1+\nu}{E}\right)\sigma_e^{old}}{1 + \frac{2}{3}\left(\frac{1+\nu}{E}\right)\left(\frac{d\sigma_e}{d\varepsilon^P}\right)_{old}} \tag{75}$$

in which σ_e^{old} is the value of the effective stress at the end of the last converged loadstep, and $\left(\frac{d\sigma_e}{d\varepsilon^P}\right)_{old}$ is the slope of the stress-plastic strain curve at the end of the last converged loadstep. Since $\left(\frac{d\sigma_e}{d\varepsilon^P}\right)_{old}$ is usually at least an order of magnitude smaller than the elastic modulus E, it can be seen that the denominator in Equation (75) is nearly unity, and thus $d\varepsilon^P$ is very nearly linearly related to ε_{et}. Thus, the convergence difficulties associated with the nonlinearity of the stress-strain curve can be avoided.

Only the appropriate equations which are used in this Plastic Strain-Total Strain iteration scheme will be given here. The full derivation is presented in Mendelson's book[13], Sections 7-9 and 9-1. The modified strains are obtained from

$$\varepsilon'_{ij} = \varepsilon^e_{ij} + d\varepsilon^P_{ij} \tag{76}$$

in which ε^e_{ij} are the elastic strains defined by

$$\varepsilon^e_{ij} = \frac{1+\nu}{E}\sigma_{ij} - \frac{\nu}{E}\sigma_{kk}\,\delta_{ij}. \tag{77}$$

The modified deviator strains are then obtained from Equation (76) as

$$e'_{ij} = e^e_{ij} + d\varepsilon^P_{ij} \tag{78}$$

where e^e_{ij} are the elastic deviator strains, and the fact that $d\varepsilon^P_{ii} = 0$ has been used. The equivalent modified total strain is defined as

$$\varepsilon_{et} \triangleq \sqrt{\frac{2}{3}} \left[(\varepsilon'_{11} - \varepsilon'_{22})^2 + (\varepsilon'_{22} - \varepsilon'_{33})^2 + (\varepsilon'_{33} - \varepsilon'_{11})^2 + 6(\varepsilon'_{12})^2 + 6(\varepsilon'_{23})^2 + 6(\varepsilon'_{31})^2 \right]^{1/2}. \quad (79)$$

A schematic outline of the Plastic Strain-Total Strain iteration scheme is shown in Figure 5. The similarity with the previous iteration scheme based directly on the Prandtl-Reuss flow relations is evident.

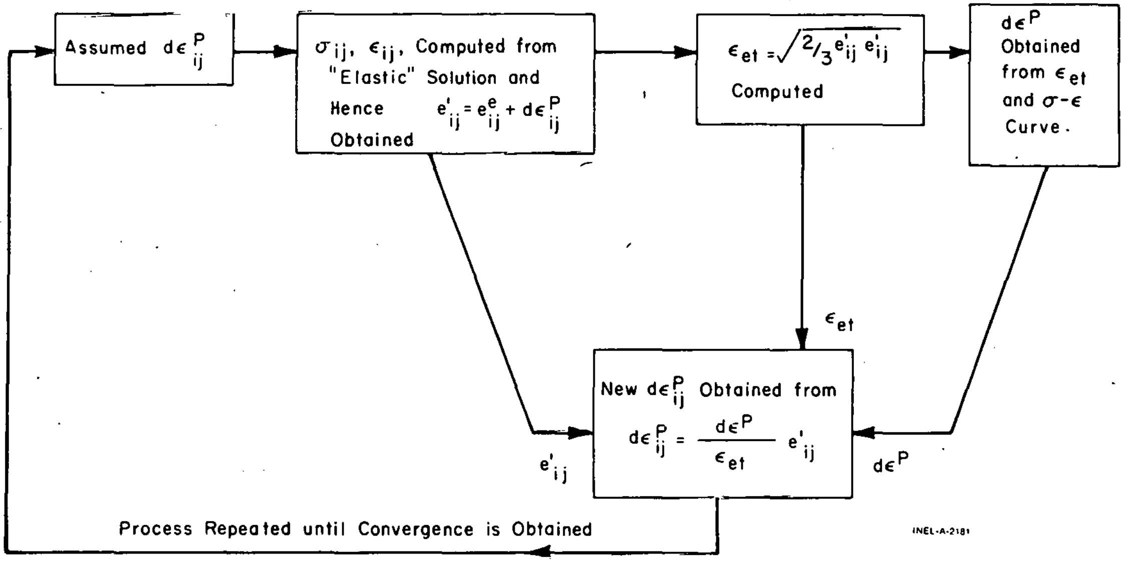

Fig. 5 Flow chart for plastic strain-total strain iteration scheme.

At the start of each loadstep calculation, initial values of $d\varepsilon^P_{ij}$ are assumed. Using these values, the pseudoelastic equations are solved for new stresses and strains. From the strains so calculated ε_{et} and ε'_{ij} are obtained. Then, using the uniaxial stress-strain curve, a value of $d\varepsilon^P$ corresponding to ε_{et} is obtained using Equation (75). Finally, new estimates of $d\varepsilon^P_{ij}$ are obtained from the modified flow rule

$$d\varepsilon^P_{ij} = \frac{d\varepsilon^P}{\varepsilon_{et}} e_{ij}$$

and the process is repeated until convergence is obtained.

This modified iteration procedure differs from the previous iteration scheme in one important aspect. In the previous scheme, if one of the nodes at which the plastic strains are being sought is actually only strained elastically, then in the course of the iteration process, the plastic strain increments will approach zero, and the correct elastic solution will be obtained automatically. In the modified iteration scheme, however, the iteration process will not converge to the appropriate elastic solution, but will, in fact, generally diverge in this case. Thus, at each step in the iteration process it is necessary to compute the effective stress and compare it with the current, work-hardened yield stress. If the yield stress has not been exceeded, then the plastic strain increments are set to zero.

Not only will the modified iteration scheme described above permit convergent plasticity calculations for higher temperatures and larger loadsteps, it also converges much more rapidly than the previous iteration scheme. Hence, the modified iteration scheme is utilized in all the (time-dependent) plasticity calculations.

3.3 General Considerations in Creep-Stress Relaxation Analysis

3.3.1 Uniaxial Behavior. Creep can broadly be defined as the inelastic time-dependent change in stress and strain in a body under constant load. For most common structural metals, high temperatures are required. Shown in Figure 6 are typical creep curves taken on a uniaxial specimen at constant stress for zircaloy-2 at 300°C taken from a correlation by Ibrahim[14].

Two features are notable. First, doubling the stress more than doubles the strain. Second, the strain rate decreases as time goes on. A typical uniaxial creep test taken to failure is shown in Figure 7. From time $t = 0$ to $t = t_1$, the creep rate (slope of ε versus t) is continually decreasing. This is called the period of primary, or transient creep. From time t_1 to t_2, the creep rate is approximately constant (although it does depend on the stress level, temperature, radiation

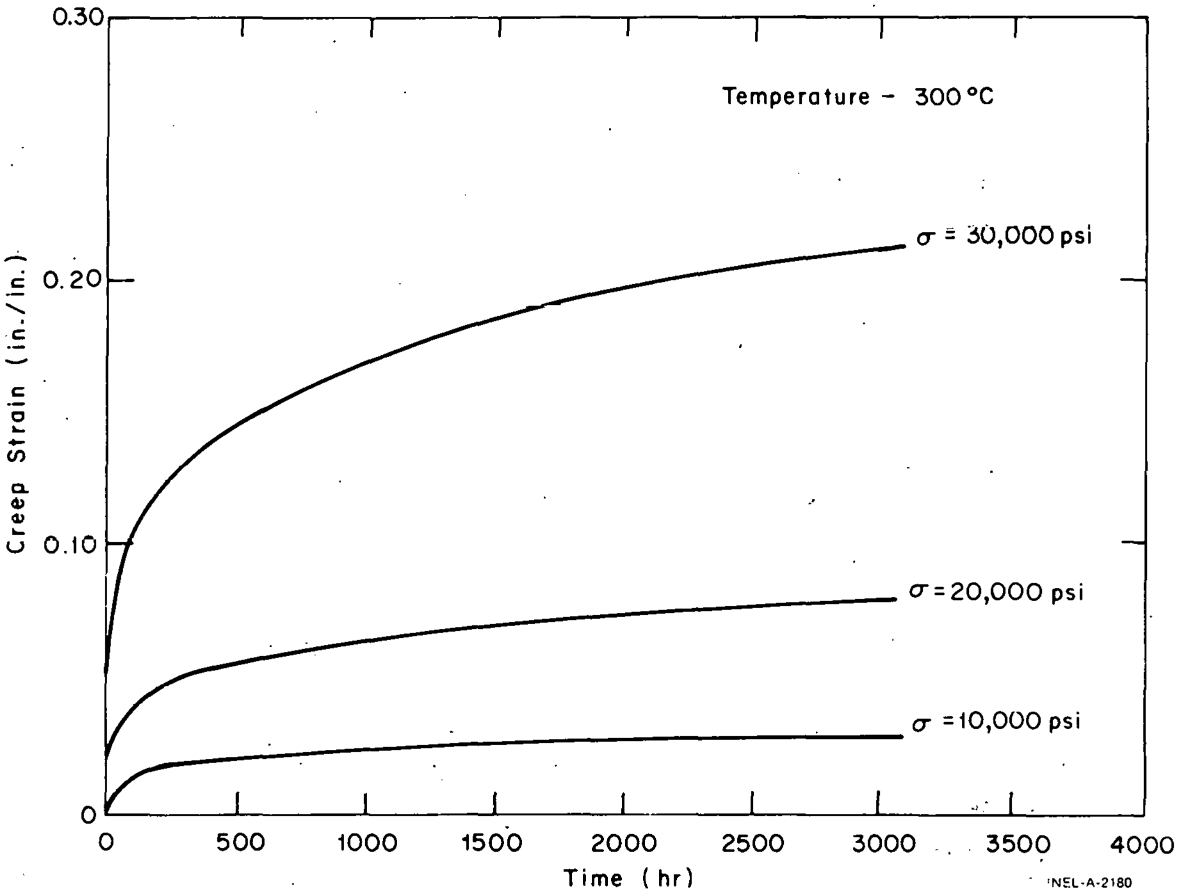

Fig. 6 Creep curves for zircaloy-2 at 300 C (572°F) (correlations from Ibrahim, Reference 14).

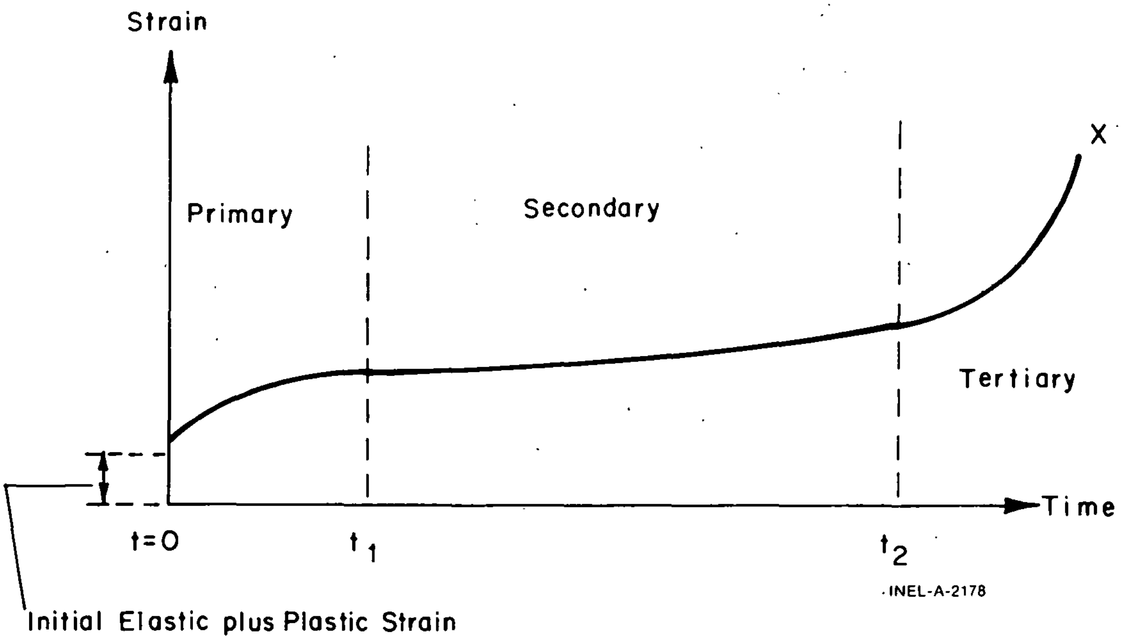

Fig. 7 Typical creep test taken to failure.

flux, etc.). The region of constant creep rate is called the region of secondary or steady state creep.

The final region is one in which the creep rate begins increasing and is called the region of tertiary creep. In this region, the specimen usually exhibits cracks or other nonuniform deformation, and hence, the usual continuum theory is not applicable. Thus, in a structural analysis, attention is restricted to the primary and secondary stages of creep.

One approximation that is often used in creep analysis is to consider only the steady state portion of creep, so that the creep rate is independent of time. This considerably simplifies any such analysis. However, as can be seen from Figure 6, the creep strain incurred during the period of transient creep cannot be neglected in comparison to the creep incurred during the period of steady state creep (at least for hold times of less than 3000 hours) so that both transient and secondary creep must be included. This consideration is especially important when comparisons are to be made between code predictions and laboratory experiments which are usually of limited duration compared to anticipated service life.

The strains induced during creep are permanent, and it is a basic assumption of creep analysis that the constitutive law can be written:

$$\varepsilon_1 = \frac{1}{E}\left[\sigma_1 - \nu(\sigma_2 + \sigma_3)\right] + \varepsilon_1^P + \varepsilon_1^C + d\varepsilon_1^C \qquad (80)$$

where

ε_1^P = accumulated plastic strain

ε_1^C = accumulated creep strain

$d\varepsilon_1^C$ = increment of creep strain.

Although both plastic strains and creep strains are permanent, there is a fundamental difference between plasticity, which does not depend on time, and creep which is explicitly time-dependent. That is, the magnitude of the plastic strains resulting from the application of a sequence of loads to a body does not depend on the time intervals between the applications of the individual loads. The magnitude of the resulting creep strain, however, is greatly affected by the time history of the application of the loads.

Since creep is explicitly a time-dependent process, it would be most appropriate to use a theory in which the time rates of strain are related to the rates of stress, i.e., a visco-elastic theory. And, in fact, there are simple, linear rheological models available which can qualitatively reproduce all the effects observed in a uniaxial creep test. However, as pointed out in regard to Figure 6, the creep response of metals is a nonlinear function of stress. Hence, a nonlinear theory of visco-elasticity would have to be used to accurately predict creep strains. While such a nonlinear theory does exist (in the Frechet Expansion Theorem), its implementation is currently beyond the scope of present day computers. Further, the theory requires experimental data which do not exist to date, and which would be relatively difficult to obtain. Thus, the use of a nonlinear visco-elastic theory is not within the current state of the art. For a further discussion of this, reference is made to C. E. Pugh et al[15].

3.3.2 The Equation of State Approach. A workable alternative to a visco-elastic creep analysis is to use the so-called "equation of state" approach. Here, analytical expressions are fit to the experimental uniaxial creep strain versus time curves measured at constant applied stress, giving the functional relation:

$$\varepsilon = f(\sigma, t, T, R) \tag{81}$$

where

σ = applied constant stress

t = time

T = temperature

R = irradiation flux parameter.

The creep strain rate is obtained analytically by differentiating Equation (81) to obtain

$$\dot{\varepsilon} = g(\sigma,t,T,R). \tag{82}$$

Now it must be kept in mind that Equations (81) and (82) are strictly valid for constant stress only. To extend their use to problems involving continuously varying stress, certain assumptions must be made. Consider the two creep curves in Figure 8 obtained at two different stress levels. Suppose that creep strain has been accumulating at stress σ_1 until time t_1, and then the stress is changed to σ_2. The question to be answered is: at what point on the $\sigma = \sigma_2$ creep curve do we start our calculations for further creep analysis? One of two hypotheses is commonly made:

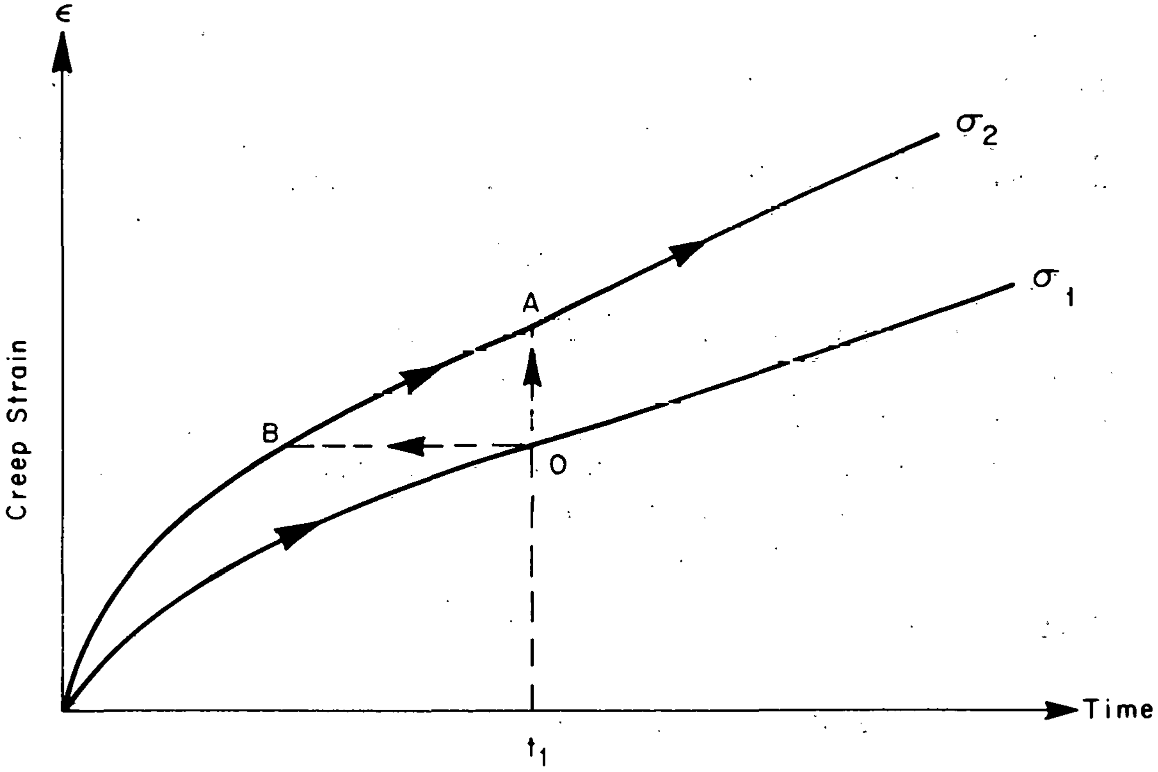

INEL-A-2179

Fig. 8 Time hardening and strain hardening hypotheses for creep with varying stress.

(1) Time-hardening Hypothesis: Here it is assumed that it is the elapsed time which is the determining factor, so that in making the transition from stress σ_1 to σ_2, one moves from point 0 to point A in Figure 8. Hence, creep strain rates are determined directly from Equation (82).

(2) The Strain-hardening Hypothesis: Here it is assumed that it is the accumulated creep strain which is the determining factor. Thus, one moves from point 0 to point B in Figure 8. Analytically, this is accomplished by eliminating time, t, from Equation (82) by use of Equation (81) to obtain

$$\dot{\varepsilon} = h(\sigma, \varepsilon, T, R) \tag{83}$$

and thus the subsequent creep strain rates are determined by the accumulated creep strain.

In general, experimental data agree better with analytical predictions based on the strain-hardening assumption, so this is the assumption which is incorporated into the FRACAS subcode. This is in accordance with the recommendations of Reference 15.

When the creep function, Equation (81), is a complicated function of its arguments, it is often not possible to eliminate time analytically between Equations (81) and (82). In these cases it is necessary to perform the elimination of time numerically. This can be done for arbitrary functional forms of Equations (81) and (82) and thus, complete generality can be maintained. However, this is achieved at the cost of having to solve a pair of highly nonlinear, coupled algebraic equations at each step of the creep iteration scheme, which is a time consuming procedure.

In order to optimize the computation time for creep calculations in FRACAS, the following procedure is utilized. It is assumed that the creep law, Equation (81), is such that time can be explicitly evaluated so as to obtain Equation (83), and that Equation (83) is available to

FRACAS from a subroutine denoted CREPR. Secondly, it is assumed that Equation (83) can be written in the form

$$\sigma = \sigma\,(\varepsilon,\varepsilon,T) \tag{84}$$

and that this equation is available to FRACAS from a subroutine denoted CREEP. In the majority of cases, subroutine CREEP will use an iteration scheme to obtain σ given $\dot{\varepsilon}$ and ε, but this can usually be done very efficiently. For use in the FRAP codes, subroutine CREPR is obtained from the material properties subcode MATPRO. Subroutine CREEP uses the analytic expression for creep rate from MATPRO and the method of successive substitutions. This results in minimizing the creep calculation time.

3.3.3 <u>Extension to Multiaxial Creep Problems</u>. All of the foregoing discussion is applied to uniaxial loading behavior only. To extend this to creep and stress relaxation in multiaxial states of stress, we proceed in a fashion similar to that used in plasticity, and introduce an effective creep strain increment defined by

$$d\varepsilon^{c} \triangleq \sqrt{\frac{2}{3}\, d\varepsilon^{c}_{ij}\; d\varepsilon^{c}_{ij}} \tag{85}$$

which is, of course, directly analogous to the effective plastic strain defined for the plasticity calculations. Then the effective creep strain rate is computed from

$$\dot{\varepsilon}^{c} = \frac{d\varepsilon^{c}}{dt} = \frac{1}{\Delta t}\;\sqrt{\frac{2}{3}\, d\varepsilon^{c}_{ij}\; d\varepsilon^{c}_{ij}}\,. \tag{86}$$

The same effective stress is utilized:

$$\sigma_{e} \triangleq \sqrt{\frac{3}{2}\,\sigma_{ij}\sigma_{ij}}\,.$$

It is then assumed that the effective stress, σ_e, and the effective creep strain rate, $\dot{\varepsilon}^{c}$, are related by the uniaxial creep strain function, Equation (83). For any given problem, the equilibrium and kinematic equations are identical with those used in the plasticity calculations.

The external loading (temperatures, pressures, displacements etc.,) are assumed to be applied stepwise. At each time that these loads are incremented, a (time-independent) plasticity solution is obtained as described in the previous sections. The time periods in between (at constant load) are subdivided into a number of small time increments, Δt, and a creep analysis is performed. For each time increment, Δt, the Method of Successive Elastic Solutions is applied in the usual fashion, except that the effective stress, σ_e, is obtained from the uniaxial creep curve at the iterated value of the effective creep rate, $\dot{\varepsilon}^c$, instead of from the uniaxial stress-strain curve. Thus, for each time increment, Δt, the creep solution is obtained as follows:

(1) Assume the creep strain increments, $d\varepsilon^c_{ij}$

(2) Compute the effective creep strain rate

$$\dot{\varepsilon}^c = \frac{1}{\Delta t} \sqrt{\frac{2}{3} d\varepsilon^c_{ij} d\varepsilon^c_{ij}}$$

(3) Obtain the effective stress from the uniaxial creep curve, using the strain-hardening hypothesis

$$\sigma_e = h(\dot{\varepsilon}^c, \varepsilon^c, T, R)$$

where ε^c is the total accumulated effective creep strain, including $d\varepsilon^c = \dot{\varepsilon}^c \Delta t$ incurred during the current time increment

(4) Obtain the deviator stresses from the elastic solution, with Hooke's law taken as

$$\varepsilon_{11} = \frac{1}{E} \left[\sigma_{11} - \nu(\sigma_{22} + \sigma_{33})\right] + \varepsilon^P_{11} + \varepsilon^c_{11} + d\varepsilon^c_{11}$$

$$\varepsilon_{12} = \frac{1+\nu}{E} \sigma_{12} + \varepsilon^P_{12} + \varepsilon^c_{12} + d\varepsilon^c_{12}$$

etc.

where

ε^P_{ij} = accumulated plastic strains at end of last load step

ε^c_{ij} = accumulated creep strains at end of last Δt time increment

$d\varepsilon_{ij}^{c}$ = increments of creep strain during current Δt time increment

(5) Obtain new estimates of the creep strain increments from the Prandtl-Reuss flow rule:

$$d\varepsilon_{ij}^{c} = \frac{3}{2} \frac{\dot{\varepsilon}^{c}\Delta t}{\sigma_e} S_{ij}.$$

(6) Repeat until convergence.

3.4 Description of Individual Subroutines

The package of subroutines which perform the Fuel-Clad Mechanical Interaction analysis consists of four main subroutines. FCMI is the executive subroutine, and it calls either COUPLE, STACK, or CLADF as appropriate. STRESS and STRAIN are called by either CLADF, STACK, or COUPLE to obtain the necessary mechanical properties. Subroutine CLOSE is an interpolation routine called by FCMI to locate the point at which the gap closes for each node. These subroutines are described in detail below.

3.4.1 Subroutine FCMI. Subroutine FCMI performs the basic function of determining whether or not the fuel pellets and the cladding are in contact. The radial expansion of the fuel is obtained from models contained externally to the fuel-clad interaction subroutines, and is passed to FCMI in the calling sequence. Stress effects on the fuel expansion are known to be small relative to thermal expansion and swelling, and so the fuel expansion is uncoupled from the cladding deformation. (Stress induced creep is important, however, and is being considered separately.)

The decision as to whether or not the fuel is in contact with the cladding is made by comparing the radial displacement of the fuel with the radial displacement which would occur in the cladding due to the prescribed external (coolant) pressure and the prescribed internal (fission gas) pressure. Both of these values are passed to FCMI through the calling sequence. This free cladding radial displacement is obtained in CLADF. Then, if

$$u_r^{fuel} \geq u_r^{clad} + \delta \tag{87}$$

where δ is the initial (as-fabricated) gap between the fuel and the cladding, the fuel is determined to be in contact with the cladding. The as-fabricated gap δ is a constant which does not change throughout the loading history of the rod. The loading history enters into this decision by virtue of the permanent plastic cladding strains which are used in the CLADF solution, and which are updated at each call to CLADF or COUPLE. These plastic strains (and total effective plastic strain ε^P) are stored in the main calling program, and are passed to FCMI through the calling sequence.

If the fuel and cladding displacements are such that Equation (87) is not satisfied, the gap has not closed during the current loadstep, and the solution obtained by CLADF is the appropriate solution. The current value of the gap is computed and passed back to the main calling program. The plastic strain values may be changed in the solution obtained by CLADF if additional plastic straining has occurred.

If Equation (87) is satisfied, however, the fuel and cladding are in contact during the current loading step. If the gap was open at the end of the last loadstep, then subroutine CLOSE is called. This routine linearly interpolates between the current load values and the last load values to determine exactly when the gap closed. For that portion of the loadstep in which the gap is open, subroutine CLADF is called. For the remaining portion of the loadstep, in which the cladding and the fuel are in contact, radial continuity at the contact interface requires that

$$u_r^{clad} = u_r^{fuel} - \delta \tag{88}$$

while in the axial direction it is assumed that no-slip occurs between the fuel and the cladding. Since a thin shell theory is used for the cladding, it is assumed that the strain induced in the cladding by the axial expansion of the fuel is taken up entirely by straining of the middle surface of the cladding.

It must be noted that only the additional strain which occurs in the fuel after lock-up has occurred is transferred to the cladding. Thus, if $\varepsilon_{z,o}^{clad}$ is the axial strain in the clad just prior to contact and $\varepsilon_{z,o}^{fuel}$ is the corresponding axial strain in the fuel, then the no-slip condition in the axial direction becomes

$$\varepsilon_{z}^{clad} - \varepsilon_{z,o}^{clad} = \varepsilon_{z}^{fuel} - \varepsilon_{z,o}^{fuel} . \tag{89}$$

The values of the prestrains $\varepsilon_{z,o}^{fuel}$ and $\varepsilon_{z,o}^{clad}$ are set equal to the values of the strains which existed in the fuel and the clad at the last load increment during which the gap was open. These values are stored in the main calling program, and passed to FCMI in the calling sequence. They are updated at the end of any load increment during which the gap closes.

After u_{r}^{clad} and ε_{z}^{clad} have been computed in FCMI, they are passed to subroutine COUPLE, which considers a thin cylindrical shell with prescribed axial strain, external pressure, and prescribed radial displacement of its inside surface. After the solution to this problem is obtained in COUPLE, subroutine FCMI passes a value of the interface pressure back to the main calling program, along with new plastic strains and stresses.

After all the nodes in the fuel rod have been examined for open or closed gaps as described above, all those nodes with open gaps are re-examined to consider axial compatibility. This is necessary because in the course of normal power histories it is possible for gaps to exist between the fuel pellets. The gaps can, in the case of collapsible cladding, give rise to local high strain concentrations. As a means of following the generation and development of such axial gaps, models are included in FCMI to consider the behavior of the cladding in the situations depicted in Figure 9a or Figure 9b. In both of these figures, nodes J* and J-1 are nodes which have been determined to be in firm contact with the cladding. Nodes J to J*-1 are nodes which have been determined not to be in contact with the cladding.

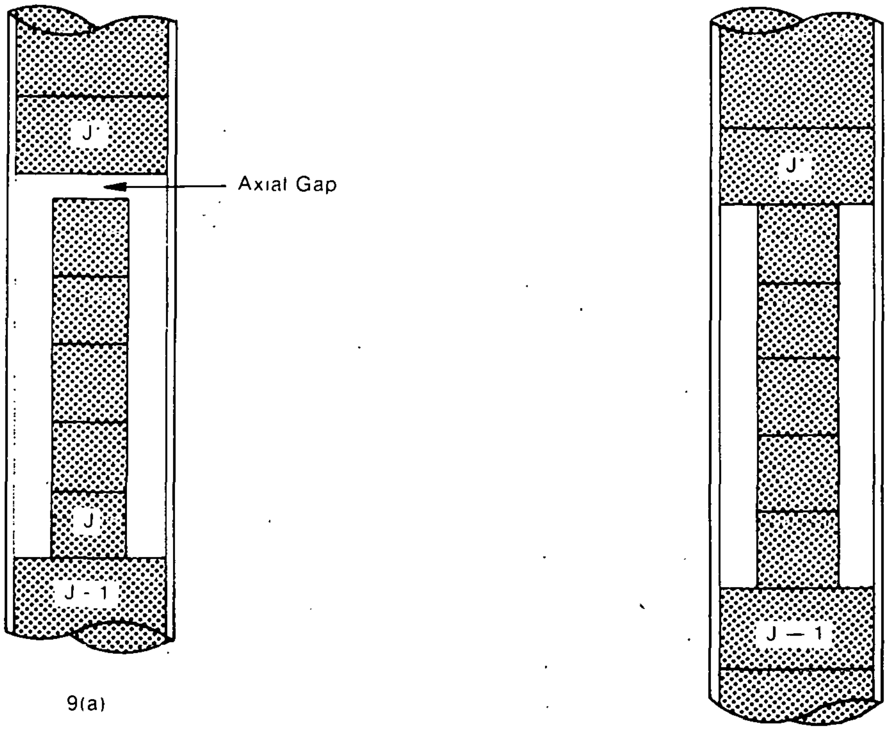

9(a)

9(b)

INEL-A-2168

Fig. 9 Axial gap and trapped stack configurations.

Figure 9a depicts the case where, due to the pressure differences and thermal expansion, the length of the enclosed column of pellets is less than the length of the cladding, and hence, an axial gap exists. For the case of vertical fuel rods, the gap will occur at the top of the uppermost pellet. In this situation, the deformation of the cladding is determined by the internal (fission gas) and external (coolant) pressures, and the axial temperature distribution in the cladding.

By contrast, it can happen that the axial expansion of the column of fuel pellets is great enough so that no gap can exist, and in fact, the expansion of the fuel pellets trapped between nodes J-1 and J* actually stretches the cladding axially, as depicted in Figure 9b. This situation is denoted as the "Trapped Stack" regime.

Models for the determination of the elastic-plastic deformation of the cladding for the two regimes discussed above are contained in the two subroutines CLADF and STACK, which are described in detail later in this report. In the following, the assumptions and logic used to determine which deformation regime is appropriate are discussed.

Consider the situation shown in Figure 9a, wherein nodes J* and J-1 have been determined to be in firm contact. Nodes J through J*-1 are nodes with open radial gaps, and thus, for these nodes, the fuel is not in contact with the cladding. Let $\xi^{K}(i)$ denote the axial gap between node i and node i + 1 at the end of the loadstep k. (It is assumed that there is never any gap between the lowest pellet and the bottom of the fuel rod.) Then, at the start of loadstep k + 1, it is assumed that all the fuel pellets consolidate at the bottom of the stack, so that all axial gaps are zero except the gap between the top node in the free stack and the next locked node J*, that is

$$\begin{cases} \xi^{k+1}(J^*-1) = \sum\limits_{i=j-1}^{J^*-1} \xi^{k}(i) \\ \\ \xi^{k+1}(i) = 0 \quad \text{for} \quad i = j-1 \text{ to } J^*-2. \end{cases}$$

The change in length of the stack of fuel pellets is determined from the prescribed axial fuel strains, using

$$\Delta\ell^{k+1}_{fuel} = \sum_{i=j}^{J^*-1} \left(\varepsilon^{k+1}_{z,fuel} - \varepsilon^{k}_{z,fuel} \right) dz(i) \qquad (90)$$

where the summation is taken over all nodes in the stack, and the superscript indicates the loadstep number.

The length of the trapped cladding can now be computed assuming that the fuel and cladding do interact, and that changes in the length of the trapped cladding are determined by changes in the length of the stack of fuel pellets. The trapped cladding length, assuming axial interaction, is given by

$$\ell^{(k+1)}_{clad} = \ell^{(k)}_{clad} + \Delta\ell^{(k+1)}_{fuel} - \xi^{k+1}(J^*-1) \qquad (91)$$

where

$\ell_{clad}^{(k)}$ = length of trapped cladding at the end of the last loadstep

$\Delta\ell_{fuel}^{(k+1)}$ = change in length of column of fuel pellets during current loadstep

$\xi^{k+1}(j^*-1)$ = axial gap between column of fuel pellets and upper end of trapped cladding.

The trapped cladding length computed above is compared with the length that the cladding would assume due to the internal and external pressures and temperature gradients acting alone, as in the absence of axial fuel-cladding interaction. This free length can be obtained from the strains computed by subroutine CLADF, using

$$\ell_{free}^{(k+1)} = \sum_{i=j}^{J^*-1} \left[1 + \varepsilon_{z,CLADF}^{(k+1)} \right] dz(i). \tag{92}$$

The decision as to whether or not fuel-cladding axial interaction takes place can now be made. If the length that the cladding would assume under the action of pressure and thermal gradients alone is greater than the length the cladding would assume due to axial interaction, then no axial interaction is possible and, in general, an axial gap will exist. Otherwise, axial interaction must have taken place. The two cases are considered separately.

Case A:

If $\ell_{free}^{(k+1)} > \ell_{clad}^{(k+1)}$, then a gap has opened between the fuel pellet stack and the cladding and the stresses and strains are set equal to those computed in CLADF. The new axial gap (at the top of the fuel pellet stack) can be computed from

$$\xi^{k+1}(J^*-1) = \xi^{k}(j^*-1) + \Delta\ell_{clad}^{(k+1)} - \Delta\ell_{fuel}^{(k+1)} \tag{93}$$

in which $\Delta\ell_{clad}^{(k+1)}$ is the change in length of the trapped cladding during the current loadstep, and is obtained from

$$\Delta\ell_{clad}^{(k+1)} = \ell_{free}^{(k+1)} - \ell^{(k)} \tag{94}$$

where $\ell^{(k)}$ is the length of the trapped cladding at the end of the last loadstep. The axial gaps between all other axial nodes in the stack of fuel pellets (including the gap beneath the lowest pellet in the stack) are set equal to zero.

Case B:

If $\ell_{clad}^{(k+1)} > \ell_{free}^{(k+1)}$, then axial interaction has taken place and no axial gap will exist. The change in length of the trapped cladding is determined by the preexisting axial gap and the change in the fuel pellet stack length via

$$\Delta\ell_{clad}^{(k+1)} = \Delta\ell_{fuel}^{(k+1)} - \xi^{k}(J^{*}-1) \tag{95}$$

This quantity is then passed to subroutine STACK, after which all the axial gaps in the fuel stack are set equal to zero.

Finally, if the stack of pellets with open radial gaps occurs at the top of the fuel rod, then the solution obtained in CLADF is the appropriate solution, and all axial gaps are set to zero. This is done since it is assumed that there is always a plenum volume containing a hold-down spring at the top of the fuel rod, and hence that the uppermost pellet can never contact the top of the fuel rod cladding.

3.4.2 Subroutine CLADF. This subroutine considers a thin cylindrical shell loaded by both internal and external pressures. Axisymmetric loading and deformation are assumed. Loading is also restricted to be uniform in the axial direction, and no bending is considered. The geometry and coordinates are shown in Figure 10. The displacements of the midplane of the shell are u and w in the radial and axial directions respectively.

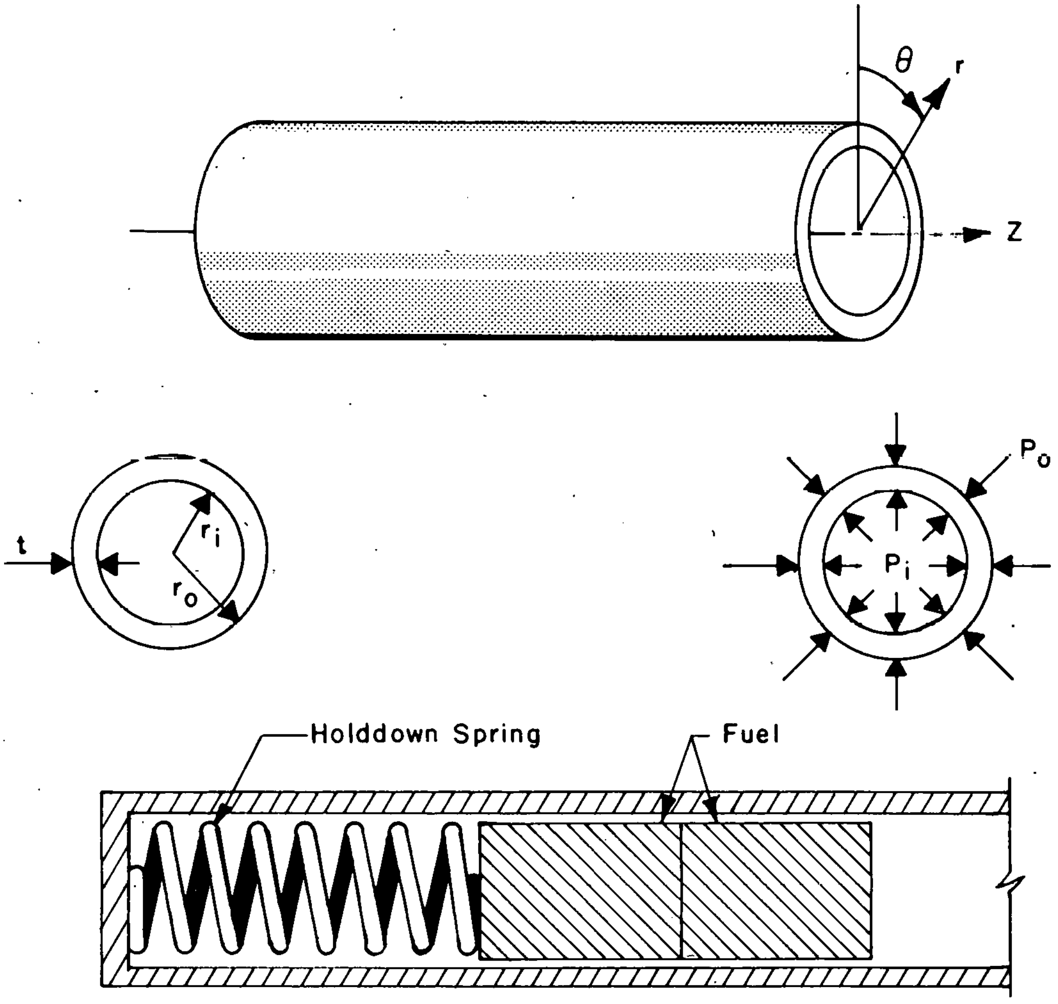

Fig. 10 Fuel rod geometry and coordinates.

Then, as is well known, the equilibrium equations simplify considerably, and are identically satisfied by

$$\sigma_\theta = \frac{r_i P_i - r_o P_o}{t} \tag{96}$$

$$\sigma_z = \frac{r_i^2 P_i - r_o^2 P_o}{r_o^2 - r_i^2}. \tag{97}$$

For membrane shell theory[16], the strains are related to the midplane displacements by

$$\varepsilon_z = \frac{\partial w}{\partial z} \tag{98}$$

$$\varepsilon_\theta = \frac{u}{\bar{r}} \tag{99}$$

where $\bar{r}$ is the radius of the midplane. Strain across the thickness of the shell will be allowed. In shell theory, since the radial stress can be neglected, and since the hoop stress, σ_r, and axial stress, σ_z, are uniform across the thickness when bending is not considered, the radial strain is due only to Poisson's effect, and is uniform across the thickness. (Normally, radial strains are not considered in a shell theory, but when plastic deformations are to be considered, plastic radial strains must be included.)

The stress-strain relations are written in the incremental form:

$$\varepsilon_\theta = \frac{1}{E}\left[\sigma_\theta - \nu\sigma_z\right] + \varepsilon_\theta^P + d\varepsilon_\theta^P + \int_{T_o}^{T} \alpha_\theta dT \tag{100}$$

$$\varepsilon_z = \frac{1}{E}\left[\sigma_z - \nu\sigma_\theta\right] + \varepsilon_z^P + d\varepsilon_z^P + \int_{T_o}^{T} \alpha_z dT \tag{101}$$

$$\varepsilon_r = -\frac{\nu}{E}\left[\sigma_\theta + \sigma_z\right] + \varepsilon_r^P + d\varepsilon_r^P + \int_{T_o}^{T} \alpha_r dT \tag{102}$$

where

T_o = strain-free reference temperature

$\alpha_\theta, \alpha_z, \alpha_r$ = coefficients of thermal expansion

T = current average clad temperature.

The terms ε_θ^P, ε_z^P, and ε_r^P are the plastic strains at the end of the last load increment, and $d\varepsilon_\theta^P$, $d\varepsilon_r^P$, and $d\varepsilon_z^P$ are the additional plastic strain increments which occur due to the new load increment.

As discussed in Section 3.2, the magnitudes of the additional plastic strain increments are determined by the effective stress and the Prandtl-Reuss flow rule, namely:

$$\sigma_e = \frac{1}{\sqrt{2}} \left[(\sigma_\theta - \sigma_z)^2 + (\sigma_z)^2 + (\sigma_\theta)^2 \right]^{1/2} \tag{103}$$

$$\begin{aligned} d\varepsilon_\theta^P &= \frac{3}{2} \frac{S_\theta}{\sigma_e} d\varepsilon^P \\ d\varepsilon_z^P &= \frac{3}{2} \frac{S_z}{\sigma_e} d\varepsilon^P \\ d\varepsilon_r^P &= - d\varepsilon_\theta^P - d\varepsilon_z^P \end{aligned} \tag{104}$$

$$\begin{aligned} S_\theta &= \sigma_\theta - \frac{1}{3} (\sigma_\theta + \sigma_z) \\ S_z &= \sigma_z - \frac{1}{3} (\sigma_\theta + \sigma_z) \\ S_r &= -\frac{1}{3} (\sigma_\theta + \sigma_z). \end{aligned} \tag{105}$$

The solution in CLADF proceeds as follows. At the end of the last load increment the plastic strain components ε_r^P, ε_θ^P, and ε_z^P, are known, and also the total effective plastic strain, ε^P, is known.

The loading is now incremented with new values of P_i, P_o, and T prescribed. The new stresses can be determined immediately from Equations (96) and (97), and a new value of effective stress is obtained from Equation (103).

The increment of effective plastic strain, $d\varepsilon^P$, which results from the current increment of loading can now be determined from the uniaxial stress-strain curve at the new value of σ_e, as shown in Figure 11. (The new elastic loading curve depends on the value of ε^P.) This computation is performed by subroutine STRAIN.

Once $d\varepsilon^P$ is determined, the individual plastic strain components are found from Equations (104), and the total strain components are obtained from Equations (100) through (102).

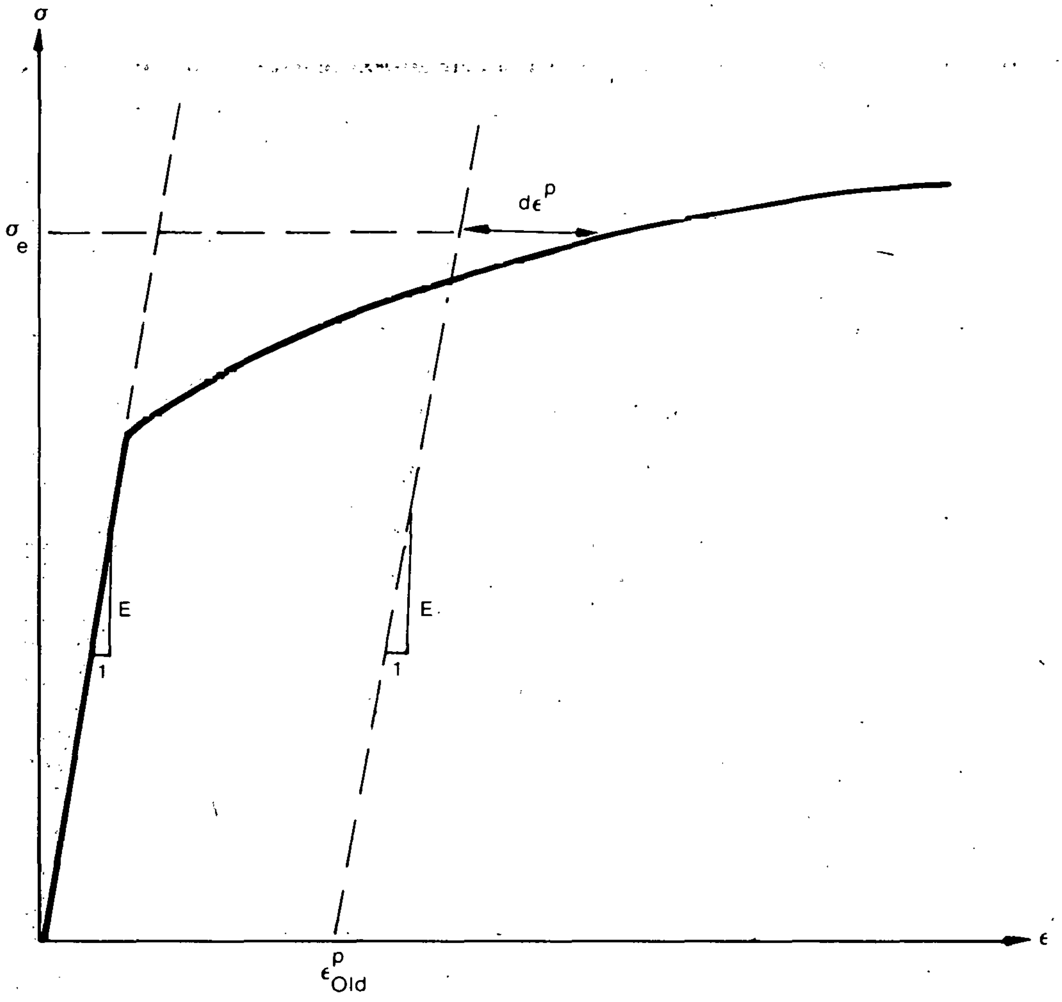

Fig. 11 Calculation of effective stress σ_e from $d\varepsilon^P$.

The displacement of the inside surface of the shell must be determined so that a new gap width can be computed. The radial displacement of the inside surface is given by

$$u(r_i) = \bar{r}\ \varepsilon_\theta - \frac{t}{2}\ \varepsilon_r \tag{106}$$

where the first term is the radial displacement of midplane [from Equation (99)] and ε_r is the uniform strain across the thickness, t.

The final step performed by CLADF prior to returning control to FCMI is to add the plastic strain increments to the previous plastic strain values as in

$$(\varepsilon_\theta^P)_{new} = (\varepsilon_\theta^P)_{old} + d\varepsilon_\theta^P$$

$$(\varepsilon_z^P)_{new} = (\varepsilon_z^P)_{old} + d\varepsilon_z^P$$

$$(\varepsilon_r^P)_{new} = (\varepsilon_r^P)_{old} + d\varepsilon_r^P$$

$$(\varepsilon^P)_{new} = (\varepsilon^P)_{old} + d\varepsilon^P$$

and these values are returned to FCMI for use at the next load increment.

Thus, all the stresses and strains can be computed directly since, in this case, the stresses are determinate. In the case of the driven cladding displacement, the stresses depend on the displacement, and such a straightforward solution is not possible.

3.4.3 Subroutine COUPLE.

This subroutine considers the problem of a cylindrical shell for which the radial displacement of the inside surface and axial strain are prescribed. Here the stresses cannot be computed directly since the pressure at the inside surface (the interface pressure) must be determined as part of the solution.

As in CLADF, the displacement at the inside surface is given by

$$u(r_i) = u - \frac{t}{2} \varepsilon_r$$

where u is the radial displacement of the midplane. From Equation (73), $u = \bar{r}\, \varepsilon_\theta$ and hence:

$$u(r_i) = \bar{r}\, \varepsilon_\theta - \frac{t}{2} \varepsilon_r. \tag{107}$$

Thus, prescribing the displacement of the inside surface of the shell is equivalent to a constraining relation between ε_θ and ε_r. As before, Hooke's law is taken in the form

$$\varepsilon_\theta = \frac{1}{E}\left(\sigma_\theta - \nu\,\sigma_z\right) + \varepsilon_\theta^P + d\varepsilon_\theta^P + \int_{T_o}^{T} \alpha_\theta dT \qquad (108)$$

$$\varepsilon_z = \frac{1}{E}\left(\sigma_z - \nu\,\alpha_\theta\right) + \varepsilon_z^P + d\varepsilon_z^P + \int_{T_o}^{T} \alpha_z dT \qquad (109)$$

$$\varepsilon_r = -\frac{\nu}{E}\left(\sigma_\theta + \sigma_z\right) + \varepsilon_r^P + d\varepsilon_r^P + \int_{T_o}^{T} \alpha_r dT. \qquad (110)$$

Using Equations (107) and (110) in Equation (108) yields a relation between the stresses σ_θ, σ_z, and the prescribed displacement $u(r_i)$:

$$\frac{u(r_i)}{\bar{r}} + \frac{1}{2}\frac{t}{\bar{r}}\left(\varepsilon_r^P + d\varepsilon_r^P + \int_{T_o}^{T} \alpha_r dT\right)$$

$$- \left(\varepsilon_\theta^P + d\varepsilon_\theta^P + \int_{T_o}^{T} \alpha_\theta dT\right) = \frac{1}{E}\left[\left(1 + \frac{\nu}{2}\frac{t}{\bar{r}}\right)\sigma_\theta \qquad (111)\right.$$

$$\left. + \nu\left(\frac{1}{2}\frac{t}{\bar{r}} - 1\right)\sigma_z\right].$$

Equations (109) and (111) are now a pair of simultaneous algebraic equations for the stresses σ_θ and σ_z, which may be written as

$$\begin{bmatrix} A_{11} & A_{12} \\ A_{21} & A_{22} \end{bmatrix} \begin{bmatrix} \sigma_\theta \\ \sigma_z \end{bmatrix} = \begin{bmatrix} B_1 \\ B_2 \end{bmatrix}$$

where

$$A_{11} = 1 + \frac{\nu}{2}\frac{t}{\bar{r}}$$

$$A_{12} = \nu \left(\frac{1}{2}\frac{t}{\bar{r}} - 1\right)$$

$$A_{21} = -\nu$$

$$A_{22} = 1$$

$$B_1 = E\,\frac{u(r_i)}{\bar{r}} + \frac{E}{2}\frac{t}{\bar{r}}\left[\varepsilon_r^P + d\varepsilon_r^P + \int_{T_o}^{T} \alpha_r dT\right]$$

$$- E\left[\varepsilon_\theta^P + d\varepsilon_\theta^P + \int_{T_o}^{T} \alpha_\theta dT\right]$$

$$B_2 = E\,\varepsilon_z - E\left[\varepsilon_z^P + d\varepsilon_z^P + \int_{T_o}^{T} \alpha_z dT\right].$$

Then the stresses can be written explicitly as

$$\sigma_\theta = \frac{B_1 A_{22} - B_2 A_{12}}{A_{11} A_{22} - A_{12} A_{21}} \qquad (112)$$

$$\sigma_z = \frac{B_2 A_{11} - B_1 A_{21}}{A_{11} A_{22} - A_{12} A_{21}}. \qquad (113)$$

These equations relate the stresses to $u(r_i)$ and ε_z which are prescribed and to $d\varepsilon_\theta^P$, $d\varepsilon_z^P$, and $d\varepsilon_r^P$, which are to be determined. The remaining equations which must be satisfied are

$$\varepsilon_{et} = \sqrt{\frac{2}{3}}\left[(\varepsilon_\theta' - \varepsilon_z')^2 + (\varepsilon_z' - \varepsilon_r')^2 + (\varepsilon_r' - \varepsilon_\theta')^2\right]^{1/2}. \qquad (114)$$

The modified Prandtl-Reuss flow equations are

$$d\varepsilon_\theta^P = \frac{d\varepsilon^P}{\varepsilon_{et}} \varepsilon_\theta'$$

$$d\varepsilon_z^P = \frac{d\varepsilon^P}{\varepsilon_{et}} \varepsilon_r' \qquad (115)$$

$$d\varepsilon_r^P = -d\varepsilon_\theta^P - d\varepsilon_z^P$$

in which ε_θ' and ε_r' are the modified deviator strains defined by Equation (76). The equivalent modified total strain ε_{et} is related to the plastic strain increment $d\varepsilon^P$ using Equation (79) and the uniaxial stress-strain law. Equations (112) through (115) must be simultaneously satisfied for each loading increment.

As discussed in Section 3.1, a straightforward numerical solution to these equations can be obtained via the Method of Successive Substitutions. Here, one initially assumes arbitrary values for the increments of plastic strain, and uses Equations (111) through (115) to obtain improved estimates of the plastic strain components. The steps performed by COUPLE for each increment of load are as follows:

(1) Values of $d\varepsilon_\theta^P$, $d\varepsilon_z^P$, and $d\varepsilon_r^P$ are assumed

(2) From Hooke's law, using the assumed plastic strain increments and the prescribed values of $u(r_i)$ and ε_z, values for the stresses can be obtained from Equations (111) and (112)

(3) From the pseudoelastic solution in Step 2, compute the modified strains and modified deviator strains, and hence obtain ε_{et} from Equation (114)

(4) Obtain $d\varepsilon^P$ from ε_{et} and the uniaxial stress-strain curve

(5) Compute new values of the plastic strain increments using the modified Prandtl-Reuss equations

(6) The old and new values of $d\varepsilon_\theta^P$, $d\varepsilon_z^P$, and $d\varepsilon_r^P$ are compared and the process continued until convergence is obtained

(7) Once convergence has been obtained, the interface pressure is computed from Equation (65):

$$P_{int} = \frac{t\ \sigma_\theta + r_o\ P_o}{r_i} . \qquad (116)$$

When steps 1 through 7 have been accomplished, the solution is complete, provided that the interface pressure is not less than the local gas pressure.

Due to unequal amounts of plastic straining in the hoop and axial direction, however, it often happens on unloading that the interface pressure as obtained in Step 7 is less than the gas pressure even though the gap has not opened. When this situation occurs, the frictional locking mechanism which is assumed to constrain the cladding axial deformation to equal the fuel axial deformation can no longer act. The axial strain and stress adjust themselves so that the interface pressure just equals the gas pressure, at which point the axial strain is again locked. Thus, on further unloading, the axial strain and the hoop and axial stresses continually readjust themselves so as to maintain the interface pressure equal to the gas pressure until the gap opens. Because the unloading occurs elastically, a solution for this portion of the fuel-cladding interaction problem can be obtained directly as follows.

Since the external pressure and the interface pressure are known, the hoop stress is obtained from Equation (65) as:

$$\sigma_\theta = \frac{r_i\ P_{int} - r_o\ P_o}{t}. \qquad (117)$$

From Equation (43) we can write:

$$\varepsilon_\theta = \frac{u_r^{\text{fuel}} - \delta + t/2\ \varepsilon_r}{\bar{r}}. \tag{118}$$

Substituting ε_θ and ε_r as given by Equations (108) and (110) into Equation (118) gives an explicit equation for σ_z as:

$$\nu\ r_i\ \sigma_z = (\bar{r} + \nu\ t/2)\ \sigma_\theta + \bar{r}\ E \left[\int \alpha_\theta dT + \varepsilon_\theta^P\right]$$

$$- \frac{t}{2} E \left[\int \alpha_r dT + \varepsilon_r^P\right] - E\ u(r_i) \tag{119}$$

in which σ_θ is known from Equation (117). With σ_z and σ_θ known, the strains may be computed from Hooke's law, Equations (108) through (110). This set of equations is included in subroutine COUPLE and is automatically invoked when a value of P_{int} less than the local gas pressure is computed.

As in CLADF, the last step performed by COUPLE before returning control to FCMI is to set the plastic strain components and total effective strain ε^P equal to their new values by adding in the computed increments $d\varepsilon_i^P$ and $d\varepsilon^P$.

3.4.4 Subroutine STACK. Subroutine STACK is called when one or more fuel pellet nodes are trapped between the lower end of the cladding and a pellet in firm contact with the cladding, as shown in Figure 12. In this case the axial expansion of the fuel will be imparted to the cladding even though the cladding and fuel are not in radial contact.

The total change in length of the trapped cladding is computed in FCMI, and passed to STACK in the calling sequence. For each axial node in the trapped cladding, the axial strain is given by

$$\varepsilon_z(i) = \frac{1}{E(i)} \left[\sigma_z - \nu\ (i)\ \sigma_\theta(i)\right] + \varepsilon_z^P(i) + d\varepsilon_z^P(i) + \int_{T_0}^{T(i)} \alpha_z dT \tag{120}$$

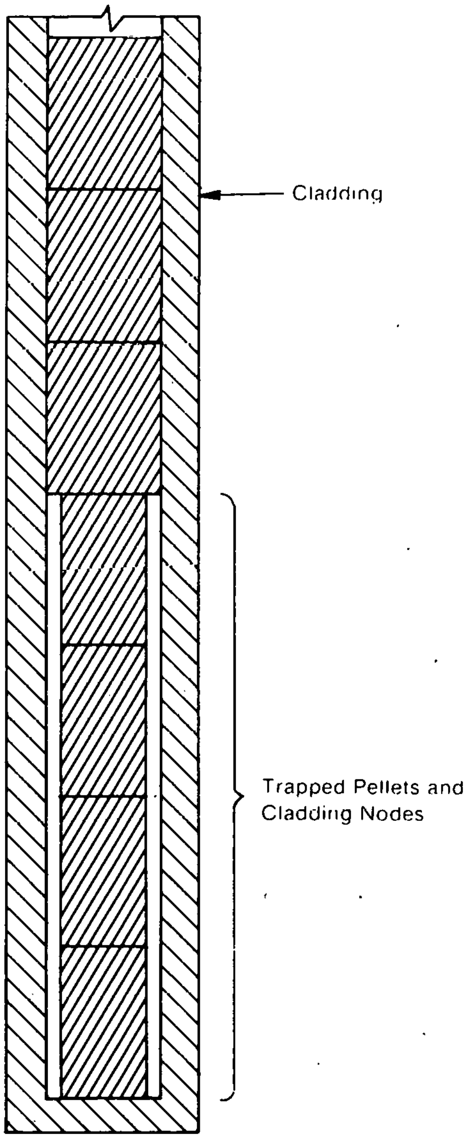

Fig. 12 Schematic of trapped stack.

in which i denotes the axial node number. Axial force equilibrium requires that σ_z be the same in each node. Since the total length change is prescribed, one can write

$$\Delta \ell = \sum_{i=1}^{n} \left[\varepsilon_z(i) - \varepsilon_z^0(i) \right] dz(i)$$

in which dz(i) are the axial cladding node lengths, and $\varepsilon_z^0(i)$ are the axial strains in the cladding at the end of the last loadstep. Inserting Equation (120) in the above equation yields

$$\sigma_z = \left[\sum_{i=1}^{N} \frac{E(i)}{dz(i)} \right] \left\{ \Delta\ell + \sum_{i=1}^{N} dz(i) \left[\frac{\nu(i)\ \sigma_\theta(i)}{E(i)} + \varepsilon_z^0(i) - \varepsilon_z^P(i) - d\varepsilon_z^P(i) - \int_{T_0}^{T(i)} \alpha_z dT \right] \right\} . \tag{121}$$

For each node, the plasticity equations are

$$\varepsilon_{et}(i) = \sqrt{\frac{2}{3}} \left\{ \left[\varepsilon_z'(i) - \varepsilon_r'(i) \right]^2 + \left[\varepsilon'_r(i) - \varepsilon_\theta'(i) \right]^2 + \left[\varepsilon_\theta'(i) - \varepsilon_z'(i) \right]^2 \right\}^{1/2} \tag{122}$$

$$e_j'(i) = e_j^e(i) + d\varepsilon_j^P(i) \qquad j = r,\ \theta,\ z \tag{123}$$

and the modified Prandtl-Reuss equations:

$$\left\{ \begin{aligned} d\varepsilon_z^P(i) &= \frac{d\varepsilon^P(i)}{\varepsilon_{et}(i)}\ e_z'(i) \\ d\varepsilon_\theta^P(i) &= \frac{d\varepsilon^P(i)}{\varepsilon_{et}(i)}\ e_\theta'(i) \\ d\varepsilon_r^P(i) &= -d\varepsilon_\theta^P(i) - d\varepsilon_z^P(i). \end{aligned} \right. \tag{124}$$

Equations (121) through (124) must be simultaneously satisfied for all the trapped axial cladding nodes. And since the nodes may have different temperatures, different stress-strain curves are used at different nodes.

As before, the Method of Successive Elastic Solutions is used. In contrast to subroutine COUPLE, however, the method is applied simultaneously to several axial nodes. Because more than one node is being considered, an additional possibility arises.

This is the possibility that, due to the axial stretching and Poisson's effect, some (or all) of the cladding nodes may come into contact with the fuel pellets, although contact would not occur due to internal and external pressures alone. In this case, the hoop stress in Equation (122) is no longer given by Equation (65), but now depends on σ_z and the radial displacement of the fuel. While contact occurs, however, radial compatibility as expressed in Equation (76) requires that

$$\bar{r}\varepsilon_\theta(i) - 0.5\ t\ \varepsilon_r(i) = u_r(f)^{\text{fuel}} - \delta.$$

Substituting for $\varepsilon_\theta(i)$ and $\varepsilon_r(i)$ from Hooke's law, Equations (96) and (98), there results a single equation relating $\sigma_\theta(i)$ at each node to the axial stress σ_z, which can be solved for $\sigma_\theta(i)$ explicitly to obtain

$$\begin{aligned}
\left[\frac{\bar{r}}{E(i)} + \frac{0.5\nu(i)\ t}{E(i)}\right] \sigma_\theta(i) &= u_r(i)^{\text{fuel}} - \delta \\
&- \bar{r}\left[\frac{-\nu(i)}{E(i)}\ \sigma_z + \varepsilon_\theta^P(i) + d\varepsilon_\theta^P(i) + \int_{T_0}^{T(i)} \alpha_\theta dT\right] \\
&+ \frac{t}{2}\left[\frac{-\nu(i)}{E(i)}\ \sigma_z + \varepsilon_r^P(i) + d\varepsilon_r^P(i) + \int_{T_0}^{T(i)} \alpha_r dT\right]
\end{aligned} \qquad (125)$$

which applies at each node where contact has occurred. Finally, Equation (125) is used to eliminate $\sigma_\theta(i)$ from Equation (124) for those nodes at which contact has occurred. Thus, we obtain an equation for σ_z involving summations over all nodes not in contact plus summations over all nodes, denoted j*, where contact has occurred. This equation, solved explicitly for σ_z, is shown below:

$$
\begin{aligned}
&\left\{ \sum_{i} \frac{dz(i)}{E(i)} - \sum_{i-j^*} \frac{dz(i)\ \nu(i)}{E(i)} \left[\frac{(\bar{r}-0.5t)\ \nu(i)}{\bar{r}+0.5t\ \nu(i)} \right] \right\} \sigma_z \\
&= \delta\ell + \sum_{i} \varepsilon_z^{o}(i)\ dz(i) \\
&- \sum_{i} \left[\varepsilon_z^{P}(i) + d\varepsilon_z^{P}(i) + \int_{T_o}^{T(i)} \alpha_z dT \right] dz(i) \\
&+ \sum_{i\neq j^*} \frac{\nu(i)}{E(i)} \left[\frac{P_i(i)r_i - P_o(i)r_o}{r_o - r_i} \right] dz(i) \qquad (126) \\
&+ \sum_{i=j^*} \frac{\nu(i)dz(i)}{r+0.5t\ \nu(i)} \left\{ u_r^{\text{fuel}}(i) - \delta - \bar{r} \left[\varepsilon_\theta^{P}(i) + d\varepsilon_\theta^{P}(i) \right.\right. \\
&\left.\left. + \int_{T_o}^{T(i)} \alpha_\theta dT \right] + 0.5t \left[\varepsilon_r^{P}(i) + d\varepsilon_r^{P}(i) + \int_{T_o}^{T(i)} \alpha_r dT \right] \right\}.
\end{aligned}
$$

This modified equation for σ_z allows for an arbitrary number of contacting nodes, and is solved for σ_z at each step in the iteration for the plastic strain increments. Of course, it is not known a priori which nodes may be in contact.

However, for given values of the plastic strain increments (the iterates in the Method of Successive Elastic Solutions), the governing equations are all linear. Thus, one can solve for σ_z assuming no pellets are in contact, then compute the gaps, and if any negative gaps are found, recompute σ_z with those nodes now assumed to be in contact. This process is repeated until all calculated gaps are either positive or zero. At most, N steps are required since the equations are linear, where N is the number of nodes in the stack.

Thus, in this application, the Method of Successive Elastic Solutions becomes an iteration within an iteration, and one in which the set of variables iterated upon is determined as the solution progresses.

3.4.5 Subroutines STRAIN and STRESS. These two subroutines are called by COUPLE and CLADF to relate stress and plastic strain, taking into consideration the direction of loading and the previous plastic deformation. A typical stress-strain curve is shown in Figure 13. This curve represents the results of a uniaxial stress-strain experiment, and may be interpreted (beyond initial yield) as the locus of work-hardened yield stresses. The equation of the curve is provided by MATPRO[4] at each temperature.

To utilize this information, the usual idealizations of the mechanical behavior of metals are made. Thus, we assume linear elastic behavior until a sharply defined yield stress is reached, after which plastic (irrecoverable) deformation occurs. Unloading from a state of stress beyond the initial yield stress, σ_y^o, is assumed to occur along a straight line having the elastic modulus for its slope. When the (uniaxial) stress is removed completely, a residual plastic strain remains, and this plastic strain completely determines the subsequent yield stress. That is, it is assumed that when the specimen is loaded again, loading will occur along line BA, and no additional plastic deformation will occur until Point A is again reached. Point A is the subsequent yield stress. If $\sigma = f(\varepsilon)$ is the equation of the plastic portion of the stress-strain curve (YAC), then for a given value of plastic strain, the subsequent yield stress is found by solving simultaneously the pair of equations:

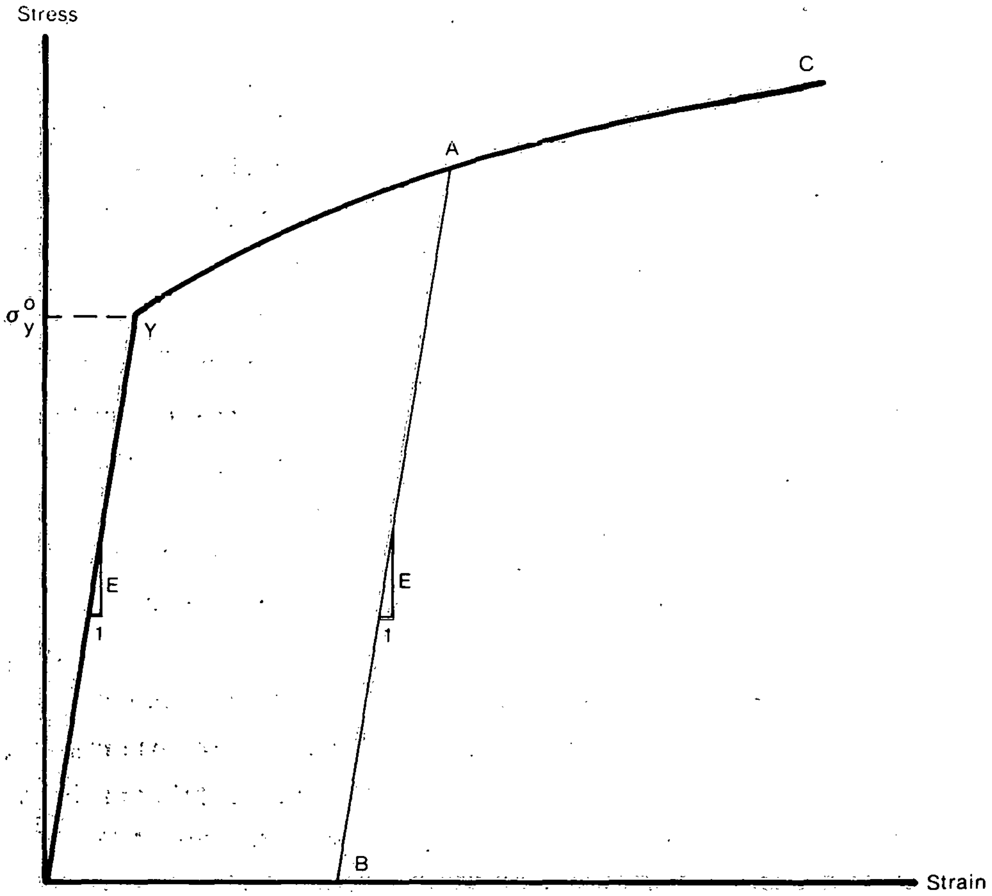

INEL-A-2172

Fig. 13 Idealized σ-ε behavior.

$$\begin{cases} \sigma = f(\varepsilon) \\ \sigma = E(\varepsilon - \varepsilon^P) \end{cases}$$

which may be written as

$$\sigma = f\left(\frac{\sigma}{E} + \varepsilon^P\right).$$

The solution to this nonlinear equation may be computed very efficiently by Newton's Iteration Scheme:

$$\sigma^{(m+1)} = f\left(\frac{\sigma^{(m)}}{E} + \varepsilon^P\right) \qquad m = 0, 1, 2, \ldots \tag{127}$$

The initial iterate $\sigma^{(o)}$ is arbitrary, and without loss of generality, is taken as 5000 psi. It can be proven that, for any monotonically increasing stress-plastic strain relation, the iteration scheme in Equation (127) converges uniformly and absolutely. Furthermore, it converges so rapidly that it is sufficient to perform the iteration no more than 30 times to obtain 8 decimal accuracy. Thus, no convergence or error criteria are necessary in utilizing this scheme.

The computations in STRAIN and STRESS are described below. It is to be noted that STRESS is only called when additional plastic deformation has occurred.

(1) Subroutine STRAIN. Values of plastic strain, ε^P, temperature and stress are passed to STRAIN through the calling sequence.

(a) For given temperature, obtain $\sigma = f(\varepsilon)$ from MATPRO

(b) Obtain yield stress σ_y for given ε^P from Equation (127)

(c) For given value of stress, σ,

(i) if $\sigma \leqq \sigma_y$,

$$\varepsilon = \frac{\sigma}{E} + \varepsilon^P$$

$$\varepsilon^P_{new} = \varepsilon^P_{old}$$

$$d\varepsilon^P = 0$$

(ii) if $\sigma > \sigma_y$,

$$\varepsilon = f(\sigma)$$

$$\varepsilon^P_{new} = \varepsilon - \sigma/E$$

$$d\varepsilon^P = \varepsilon^P_{new} - \varepsilon^P_{old}$$

(d) Return.

(2) Subroutine STRESS. Values of plastic strain, ε^P, temperature and plastic strain increment $d\varepsilon^P$ are passed to STRESS through the calling sequence.

(a) For given temperature, obtain $\sigma = f(\varepsilon)$ from MATPRO

(b) Obtain yield stress σ_y for given ε^P from Equation (127)

(c) Given $d\varepsilon^P$ (see Figure 14)

$$\varepsilon^P_{new} = \varepsilon^P_{old} + d\varepsilon^P$$

Since $d\varepsilon^P > 0$, the new value of stress and strain must lie on the plastic portion of the stress-strain curve $\sigma = f(\varepsilon)$. So σ, ε are obtained by simultaneously solving, as before,

$$\sigma = f(\varepsilon)$$

$$\sigma = E(\varepsilon - \varepsilon^P_{new})$$

(d) Return.

3.4.6 Subroutines CLOSE and GAPT. These two subroutines are called by FCMI when one of the node gaps has closed between two successive loadstep changes. It is assumed that all the applied loads vary linearly between the two loadsteps, so that

$$\begin{aligned} P_c(\lambda) &= P_c(i-1) + \lambda \left[P_c(i) - P_c(i-1)\right] \\ P_g(\lambda) &= P_g(i-1) + \lambda \left[P_g(i) - P_g(i-1)\right] \\ T(\lambda) &= T(i-1) + \lambda \left[T(i) - T(i-1)\right] \\ u_r^{fuel}(\lambda) &= u_r^{fuel}(i-1) + \lambda \left[u_r^{fuel}(i) - u_r^{fuel}(i-1)\right] \end{aligned} \qquad (128)$$

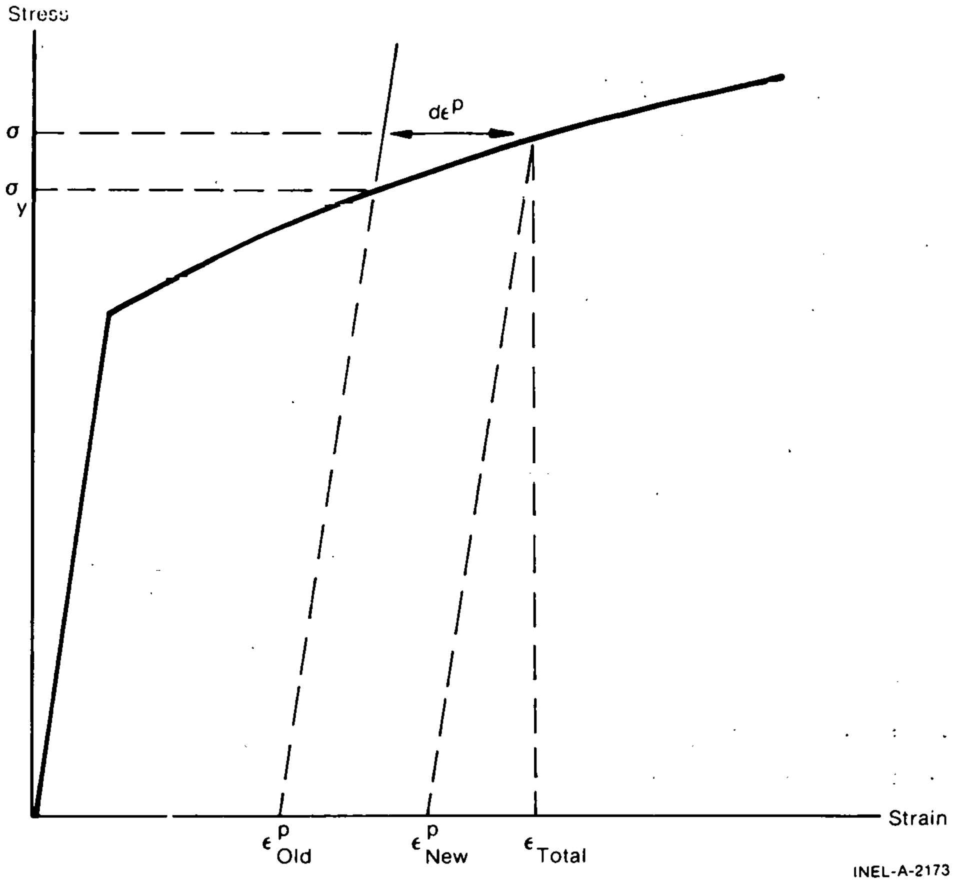

Fig. 14 Computations in subroutine STRESS.

where the index i-1 denotes the last loadstep values, i denotes the current loadstep values and λ varies between zero and unity. Given the old and new loadstep values, subroutine GAPT computes the size of the radial gap for any given value of λ by calling subroutine CLADF, and passing to it the linearly interpolated values computed from Equation (127).

Subroutine CLOSE iterates on λ to find the exact value of λ at which the radial gap closes. The method used is the Modified Newton-Raphson iteration scheme which solves for the roots of the equation:

$$\text{Radial gap} = f(\lambda) = 0$$

by use of the recurrence relation:

$$\lambda^{(m+1)} = \lambda^{(m)} - \frac{f[\lambda^{(m)}]}{g[\lambda^{(m)}, \lambda^{(m-1)}]} \qquad (129)$$

$$g\left[\lambda^{(m)}, \lambda^{(m-1)}\right] = \frac{f[\lambda^{(m)}] - f[\lambda^{(m-1)}]}{\lambda^{(m)} - \lambda^{(m-1)}} \qquad (130)$$

in which $f(\lambda)$ is the gap thickness as a function of the interpolating parameter λ as given by subroutine GAPT. The iteration procedure is performed until

$$|f(\lambda)| < CUT \qquad (131)$$

where CUT is the tolerance value which is currently set (internally) to the value 1.0×10^{-8} inches. If, for any reason, the iteration scheme cannot converge to a gap value less than CUT, an error message is printed out, and the last computed value of λ is returned. However, experience has shown that convergence has always occurred for values of CUT greater than 10^{-10}.

4. FUEL MECHANICAL RESPONSE

Deformation of the fuel is calculated as a function of thermal expansion, irradiation swelling, and densification. The deformation model is described here with irradiation swelling calculations described in Section IV.

4.1 Assumptions

(1) No pellet deformation from stresses induced by fuel-cladding contact or thermal stresses*

(2) No pellet creep under induced stresses*

(3) Free ring thermal expansion.

4.2 Radial Expansion

Radial expansion of the pellet due to temperature, irradiation swelling, and densification is calculated by a free ring expansion model. The governing equation for this model is

$$R_H = \sum_{i-1}^{N} \Delta r_i \left(1+\alpha_{T_i} T_i + \frac{\Delta L}{L} s_i + \frac{\Delta L}{L} d_i\right) \tag{132}$$

where

R_H = hot pellet radius

α_{T_i} = coefficient of thermal expansion of i^{th} radial ring for temperature T_i

T_i = average temperature of i^{th} radial ring

Δr_i = width of i^{th} radial ring

N = number of radial rings

$\frac{\Delta L}{L} s_i$ = swelling strain

$\frac{\Delta L}{L} d_i$ = densification strain.

4.3 Axial Expansion

Axial expansion of the fuel stack is calculated by summing the maximum ring axial expansions of each pellet. Maximum ring axial expansion of each pellet is calculated as the difference between the length of the ring with the maximum overall hot length and the cold length of the pellet.

The calculation of overall ring height includes consideration of the depression of a central dish. The fuel stack length is thus calculated by

$$L_f = \sum_{j=1}^{M} \left(1 + \alpha_{T_i} T_i + \frac{\Delta L}{L} s_i \ell_i + \frac{\Delta L}{L} d_i \ell_i\right) \Delta z_j \qquad (133)$$

where

i is the ring with the maximum axial expansion

and

L_t = hot length of fuel stack

M = number of axial nodes

ℓ_i = length of i^{th} radial ring

Δz_j = node length

T_i, α_{T_i}, N, $\frac{\Delta L}{l} s_i$, and $\frac{\Delta L}{L} d_i$ are defined as above.

4.4 Fuel Crack Volume

As the fuel expands, extensive cracking occurs due to the high thermally-induced stresses. This crack volume is computed as

$$V_c = V_{eg} - V_{TX}$$

where

V_c = crack volume

V_{eg} = volume defined by expanded radial nodes

V_{TX} = volume of thermally expanded fuel

with

$$V_{eg} = \sum_{i=1}^{N} \pi \left(r_i^2 - r_{i-1}^2\right) \ell_i \tag{134}$$

and

$$V_{TX} = \sum_{i=1}^{N} \pi \left(r_{ic}^2 - r_{ic-1}^2\right)\ell_{ic}\left(1 + 3\alpha_i T_i\right) \tag{135}$$

where

ℓ_{ic} = cold length of i^{th} radial ring

r_{ic} = cold radius of i^{th} node.

IV. CORRELATION MODELS

This section on correlation models deals with those fuel rod models which fall somewhere between an analytical model such as cladding deformation and a material property such as thermal conductivity.

These models are usually defined by a mathematical model which reflects a theory of behavior but are quite heavily weighted by experimental data.

Models which require substantial material property data such as cladding creep are covered in greater detail in the material property documentation of MATPRO[4].

1. FISSION GAS PRODUCTION

Given production rates for the major diffusing gases, the burnup dependent total fission gas generated at axial station z is calculated as follows:

$$GPT(z) = \frac{BU(z)\ VR(z)\ 100}{A_v} \left(PR_{krypton} + PR_{helium} + PR_{xenon}\right) \qquad (136)$$

where

$GPT(z)$ = total fission gas produced at z (gm-moles)

$BU(z)$ = burnup at z (fiss/cc)

$VF(z)$ = fuel volume (cc)

A_v = Avogadro's Number

PR_e = Fission gas production rate (atoms/100 fissions) for krypton, xenon, and helium, respectively, 30, 30, and 0.3.

2. FISSION GAS RELEASE

The fission gas release model used in FRAP-S2 considers the release to be determined by escape of gas from the fuel matrix and release of trapped gas from grain boundaries or dislocations. If k^1 represents the portion of fission gas that escapes without being trapped, then

$$dn_1 = k^1 pdt$$

where

dn_i = the moles of gas released directly in time dt

dt = the time increment

and

p = the gas production rate.

If the probability of trapped particle release per unit time is k and the number of moles trapped is C, then the trapped moles released in dt is $dn_2 = k\ C\ dt$. Only a fraction, k, of the gas released from traps reaches the surface, thus the total gas released is $dn = k^1\ k\ c\ dt + k^1\ p\ dt$.

If C is replaced by (p t - n) and integration is performed:

$$n = p \left\{ t - \frac{1 - k^1}{k^1 k} \left[1 - \exp\left(k^1 kt\right) \right] \right\} . \qquad (137)$$

At constant power, the total fractional release is

$$F = n/(pt) = 1 - (1 - k^1) \frac{1 - e^{-Kt}}{Kt} \tag{138}$$

where $K = k^1 k$. The constants, K and k^1, have been evaluated from the available data as functions of fuel temperature and density only in the form

$$K, k^1 = Ae^{(-B/T - Cd + D)} \tag{139}$$

where

T = fuel temperature (°R)

d = fuel density

and for K and k^1 respectively:

A = 0.25, 1

B = 21,410, 12,450

C = 0, 0.333

D = 0, 33.95.

The preceding formulation [Equation (137)] is extended to variable power time histories by assuming reactor operation is described by a series of constant power steps. The number of moles released, Δn_i, during the i^{th} interval is then

$$\Delta n_i = n_i - n_{i-1} = P_i \left\{ \Delta t_i - \frac{1 - k_i^1}{K_i} \left[1 - \exp(-K_i \Delta t_i) \right] \right\} \tag{140}$$
$$+ C_{i-1} \left[1 - \exp(-K_i \Delta t_i) \right] .$$

The first two terms, identical with Equation (137) represent the release during Δt_i, had the initial concentration been zero. The last term is additional release due to previously produced gas. Since the total release from time zero is $\Sigma \Delta n_i$, the fraction of total gas produced which is released is

$$F = \left(\sum_{i-1}^{m} \Delta n_i \right) / \left(\sum_{i-1}^{m} P_i \Delta t_i \right) . \tag{141}$$

3. NITROGEN RELEASE

The release of nitrogen initially present in fuel material from fabrication occurs as a result of a diffusion transport mechanism. From the model proposed by Booth[18], given the assumptions that

(1) The initial concentration of diffusing substance C_0 is assumed to be uniform throughout a sphere of radius a

(2) Transport of material does not occur from the external phase (gaseous nitrogen) back into the initial carrier medium, the following diffusion expression holds:

$$r \frac{\partial C}{\partial t} = D \frac{\partial^2 (Cr)}{\partial r^2} \tag{142}$$

where

r = radial location

C = concentration of diffusing substance

t = time

D = diffusion coefficient

and

$C = 0$ when $r = a$

$C = C_o$ when $t = 0$.

By applying a series solution method, the fractional release of the diffusing substance (nitrogen) can be approximated by the following, based on the value of B.

If

$$B = \pi^2 D_{N_2} (T)t \tag{143}$$

where

D_{N_2} = temperature dependent diffusion coefficient for nitrogen

t = time (sec) from the start of diffusion

then, when $B > 1$, the fraction of nitrogen released as of time t, equals:

$$F_{N_2} = 1 - 6\ e^{-B}/\pi^2 \tag{144}$$

and when $B \leq 1$

$$F_{N_2} = 6 \left[D_{N_2}(T)t/\pi\right]^{0.5} - 3D_{N_2}(T)t. \tag{145}$$

From the experimental data of Ferrari:[19, 20]

$$D_{N_2}(t) = (1x10^{-12})\ e^G \tag{146}$$

where

$$G = 20202\ (1/1673 - 1/T) \qquad (147)$$

and

T is in kelvins.

4. FUEL SWELLING

Early work at the Westinghouse Bettis Atomic Laboratories on UO_2 fuel swelling[21] is probably still the most authoritative. Westinghouse reported that, for temperatures between about 730 and 1400°C, the total volumetric swelling rate is $0.7\%/10^{20}$ fissions/cc with $0.16\%/10^{20}$ fissions/cc outward swelling and the rest accommodated by void until most of the porosity is filled. The fuel was restrained during irradiation. Recently various General Electric Company workers have reported[16,22] volumetric swelling rates ranging from 0.2 to $0.3\%/10^{20}$ fissions/cc for fuel at 1800°C and values of between 0.12 and $0.2\%/10^{20}$ fissions/cc for restrained fuel at temperatures of 1400 and 2200°C. Anselin and Baily[23] have calculated that the solid fission product contribution in UO_2 of theoretical density amounts to a maximum volumetric swelling rate of between 0.13 and $0.54\%/10^{20}$ fissions/cc depending on the extent of irradiation induced lattice vacancy utilization. In short, fuel swelling has been documented to be dependent on temperature, burnup, and fuel density. In light of the Bettis data, a total swelling rate of $0.24\%/10^{20}$ fissions/cc is the driving force in the peripheral region of the fuel below about 800°C. A significant portion of this swelling is accommodated by internal voids (an amount increasing with lower fuel densities) so that the net outward dimensional change can be related to the fuel density as follows:

$$\Delta V/V = 0.24 - e^{A}$$

where

$$\Delta V/V = 0.24 - e^{A} \tag{148}$$

$$\Delta V/V = \%\ \text{Volume increase}/10^{20}\ \text{fissions/cc}$$

and

$$A = 31.916 - 0.3903\ \text{DEN}$$

where

DEN = fuel density (% TD, 87-99%).

Above 800°C, the total volumetric swelling rate is assumed to be about 0.82%/10^{20} fissions/cc. No real volume changes occur, however, until the initial porosity has been saturated with fission products.

Given the fact that in FRAP-S2, a pellet is divided into ten equal area rings, an incremental amount of swelling is calculated at each time step (power level) for each fuel ring. If the temperature of a given fuel ring changes from the low temperature domain to the higher domain, the fuel structure (as indicated by examinations of burned elements), will rapidly change so that the higher temperature swelling characteristics are now applicable.

5. CLADDING CORROSION

The following equations for out-of-pile zircaloy corrosion have been published by A. van der Linde[24].

Pretransition oxidation: $W = 27.1 \times 10^{3}\ t^{0.33} \exp(-5220/T_c)$

Posttransition: $W = 23. \times 10^{8}\ t \exp(-14{,}400/T_c)$

Weight gain at transition: $W_{tr} = 123 \exp(-790/T_c)$

where

W = ZrO_2 weight gain (mg/dm^2)

T_c = oxide - cladding surface interface temperature (K)

t = time (days).

These expressions are similar to equations published by Westinghouse NES and Bettis.

The curves of Figure 15 represent the calculated ZrO_2 weight gain of BWR type fuel rods at various cladding temperatures as a function of time at temperature. The data points are from tests conducted by General Electric Company in the Vallecitos and Big Rock Point BWRs[25-27].

Correct interpretation and correlation of these and other published results is impeded by the wide scatter in the data obtained from different test specimens irradiated under similar conditions and also the disagreement in published oxidation and hydridation rates obtained by different experimentors.

In addition a general lack of understanding of the effect of irradiation on the oxidation and hydridation mechanism makes modeling difficult. For the present, the following tentative assumptions are applied:

(1) Out-of-pile corrosion temperature dependence is valid for in-pile conditions, and

(2) The in-pile time dependence during pretransition and post-transition corrosion modes is accounted for by acceleration factors.

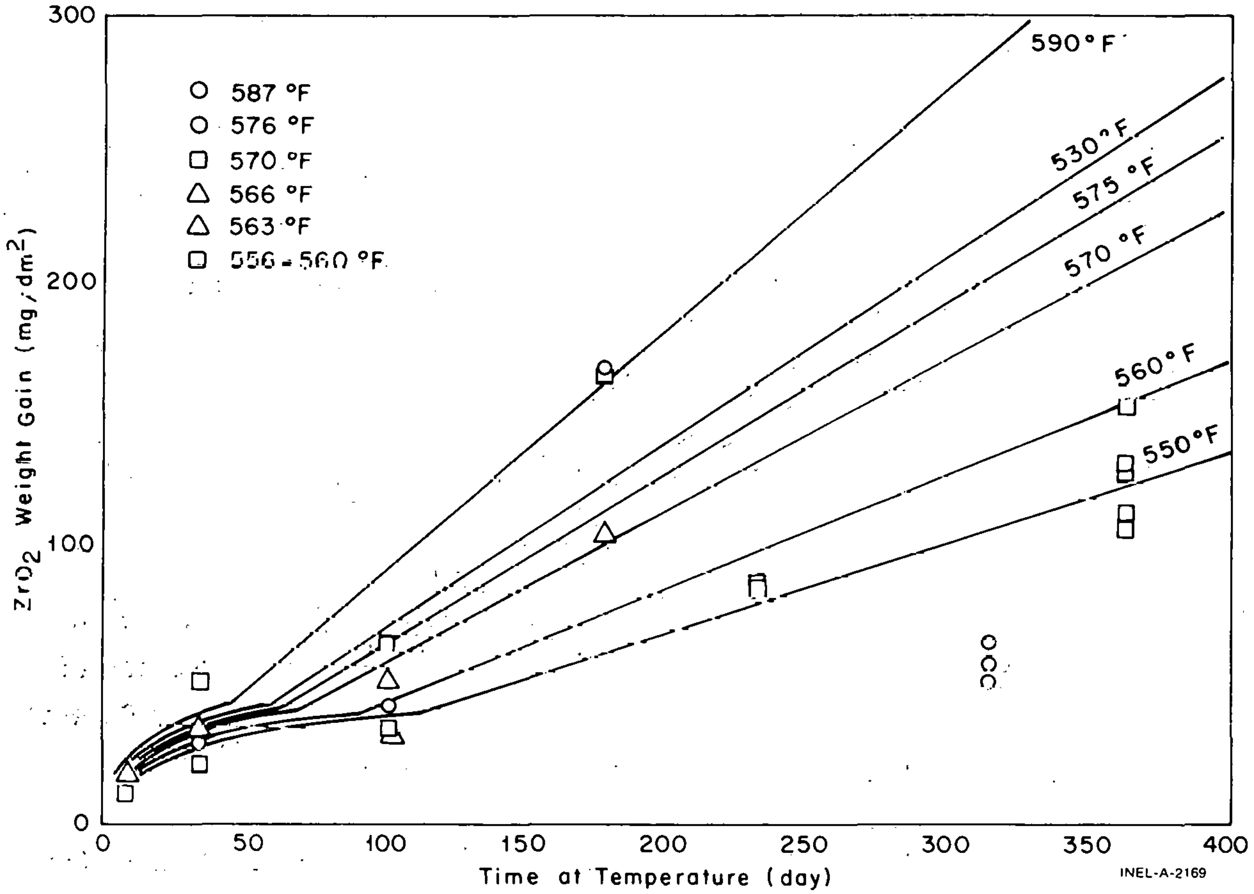

Fig. 15 ZrO_2 weight gain versus time for various temperatures.

A strong irradiation enhancement effect is indicated by the fact that for the calculated values in Figure 15, the initial constants in Equations (114) and (115) were increased by respective factors of 20.77 and 3.88.

For a number of years, General Electric Company has been reporting BWR corrosion data which are a factor of 10 to 15 higher than that which would be predicted by any of the out-of-pile correlations.

For PWR environments, Westinghouse Electric Corporation has claimed no irradiation acceleration of zircaloy corrosion. Recently published Saxton Plutonium Program corrosion data[28,29] show an irradiation acceleration of about a factor of 3. The Saxton data represents the first measurements on high power rods which experienced nucleate boiling throughout high burnup irradiation. The data suggest radiolytic decomposition of the water and attack by transient oxygen, hydrogen, and hydroxide radicals in the steam. Apparently irradiation can accelerate corrosion in a PWR much as it does in a BWR. Figure 16 represents predicted versus measured PWR zircaloy-4 corrosion with a posttransition irradiation acceleration factor of 3 applied to the out-of-pile equation. Although there is considerable scatter, the predictions are good. It is interesting that the Saxton data did not indicate any increase in the hydrogen uptake over what would normally be expected from the out-of-pile correlations.

6. CRUD BUILDUP

Crud thickness is assumed to be one mil unless a value is specified in the input. Flags in the input also determine whether the crud thickness remains constant or varies. If a variable crud thickness is specified, a crud buildup rate of 2.283 x 10^4 mils/hr is assumed. Crud thermal conductivity of 6000 Btu-mils/hr-ft^2-°F is used. This model was obtained as part of the FUEL[2] code.

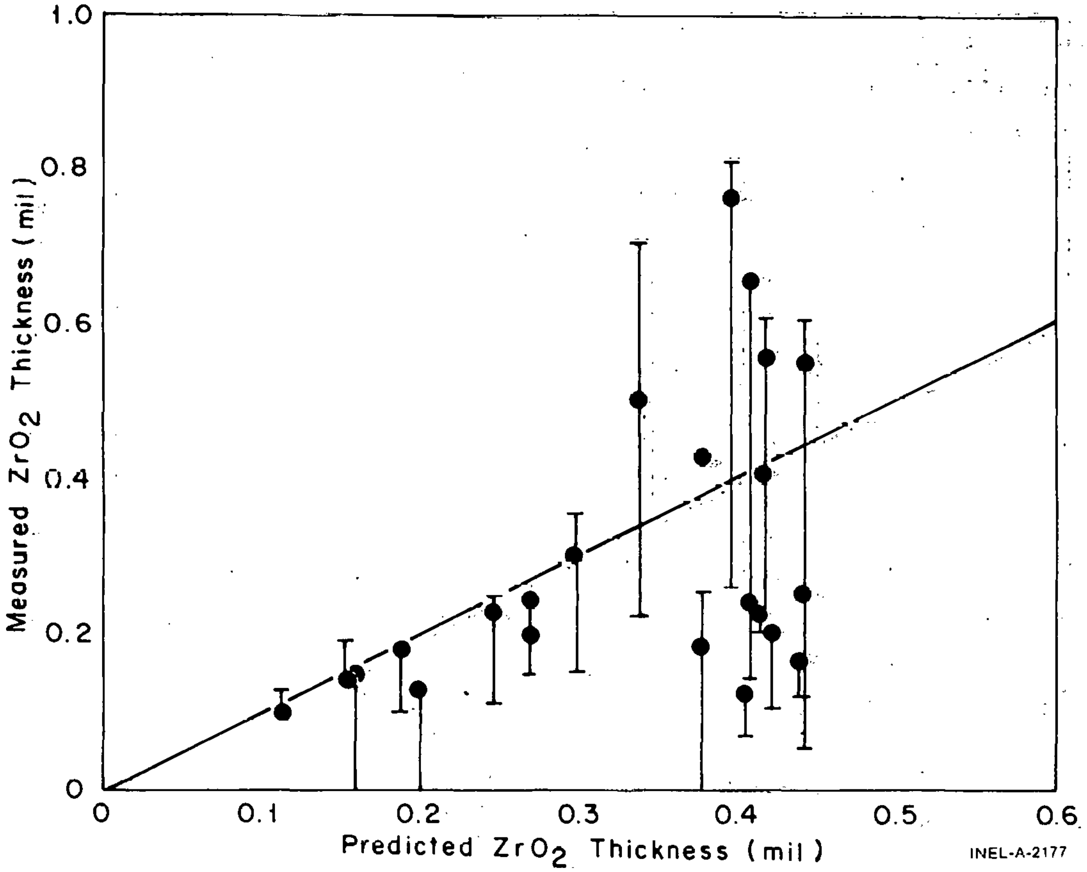

Fig. 16 Measured versus predicted ZrO_2 thickness.

V. NUMERICAL SOLUTION PROCEDURE

This section describes the program numerical sequence and the convergence checks made at various points in FRAP-S2. A flow diagram of the code is given in Table II.

Figure 17 presents a summary of the major interactions dealt with by the FRAP-S code (an arrow from A to B means A affects B). Due to the large number of interaction and feedback between the thermal conditions and the physical behavior of a fuel rod, several iterative processes are nested in the core calculations. The major iterative loops are

(1) At each axial increment the gap and fuel temperatures, the fuel thermal expansion, and the cladding strain, are iterated on until convergence is obtained

(2) At each specified time step the entire rod conditions are recalculated with iterations continued until gas release and rod internal pressure are unchanged.

The code calculations begin with bulk coolant temperatures determined by a one-channel enthalpy rise evaluation. Then, for each given axial segment of the rod, the cladding outside surface temperature is calculated by the Dittus-Boelter[5] formula for subcooled heat transfer or the Jens-Lottes[6] correlation if nucleate boiling is present; a crud temperature rise which is a function of the crud density and thickness, (not considered when nucleate boiling occurs); and an oxide temperature rise. The cladding corrosion rate (oxide thickness) is calculated as an exponential function of the cladding-to-oxide interface temperature, proportional to time at temperature and dependent on material and system conditions (BWR or PWR). The temperature rise across the cladding is calculated as a function of power level and cladding dimensions. The gap conductivity between the pellet surface and the cladding inside diameter is calculated as a function of the composition and pressure of the internal gas mixture and the contact pressure between the fuel and

TABLE II

FRAP-S FLOW DIAGRAM

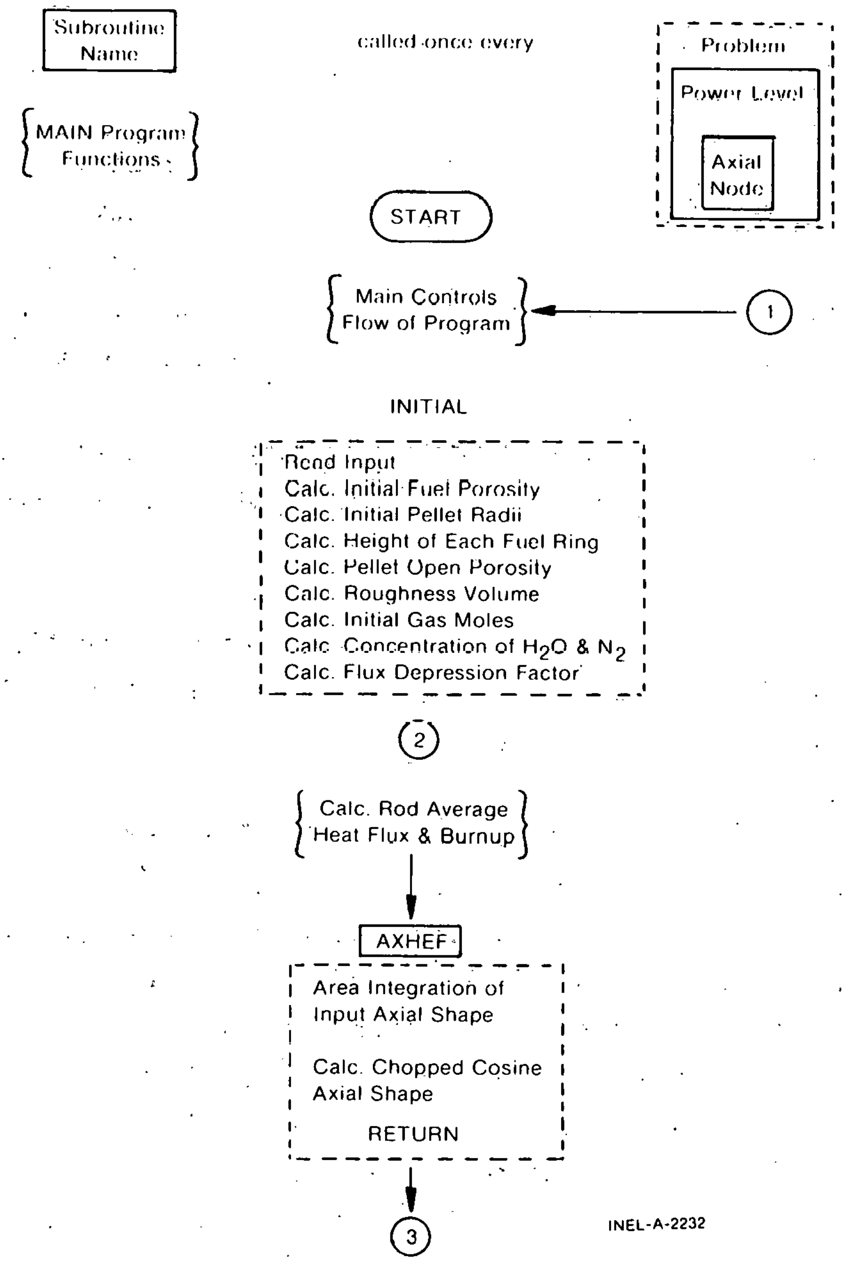

TABLE II (continued)

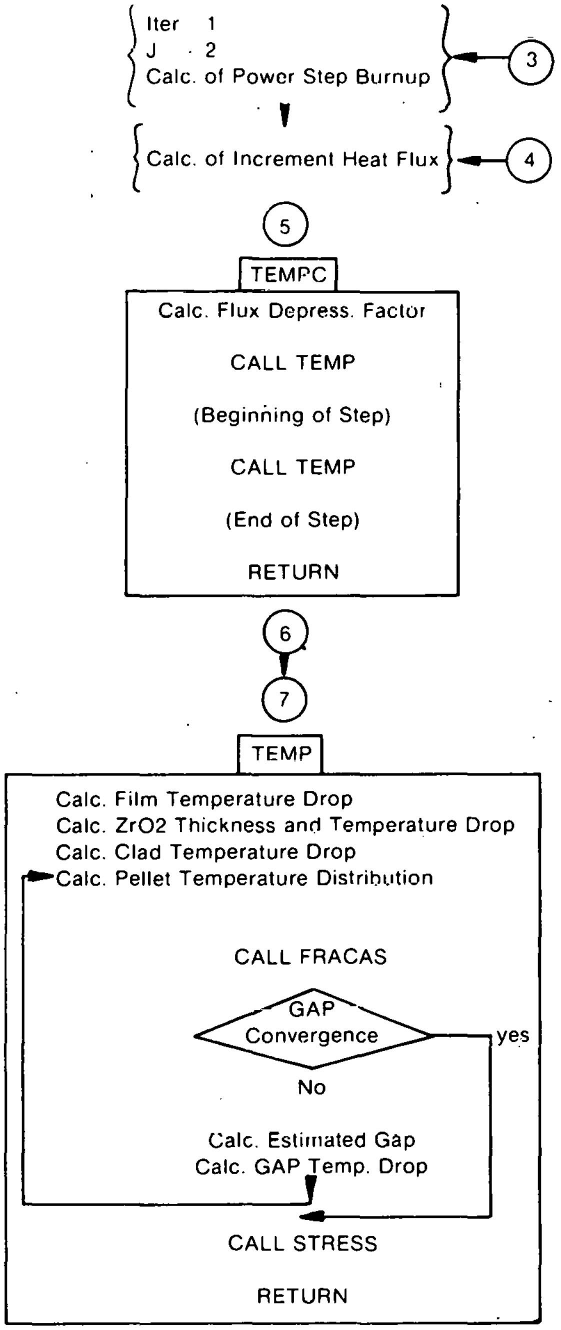

INEL-A-2233

TABLE II (continued)

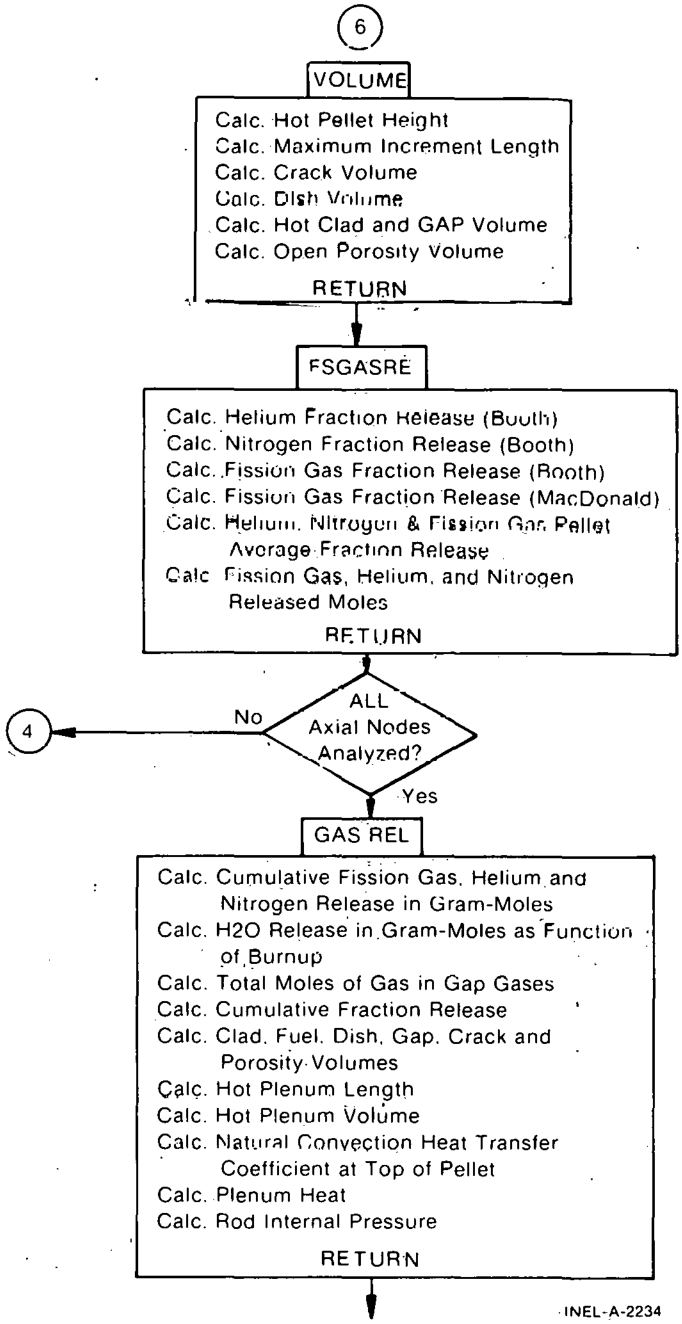

INEL-A-2234

TABLE II (continued)

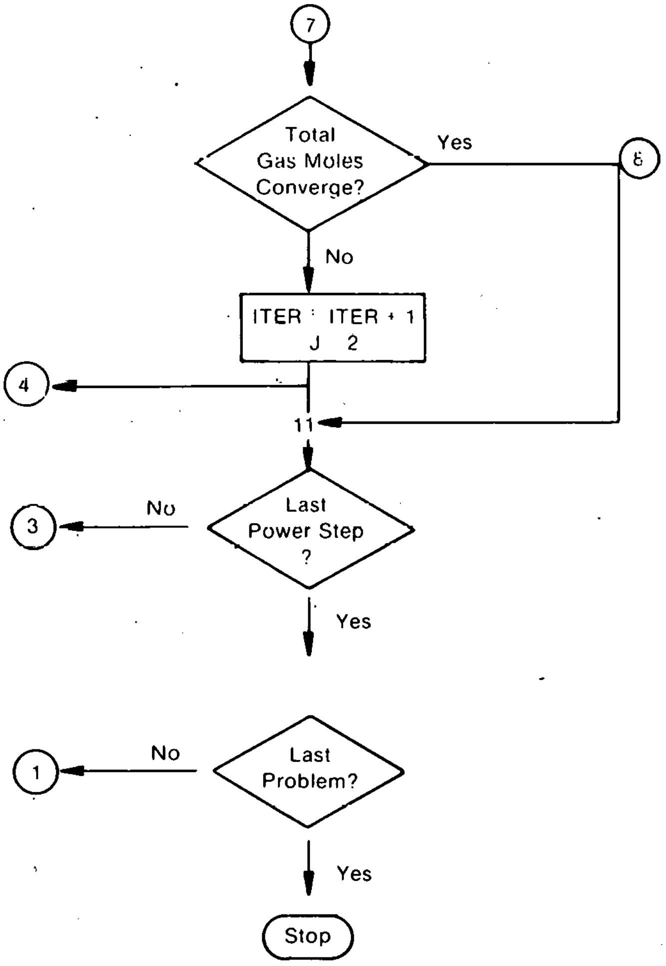

INEL-A-2235

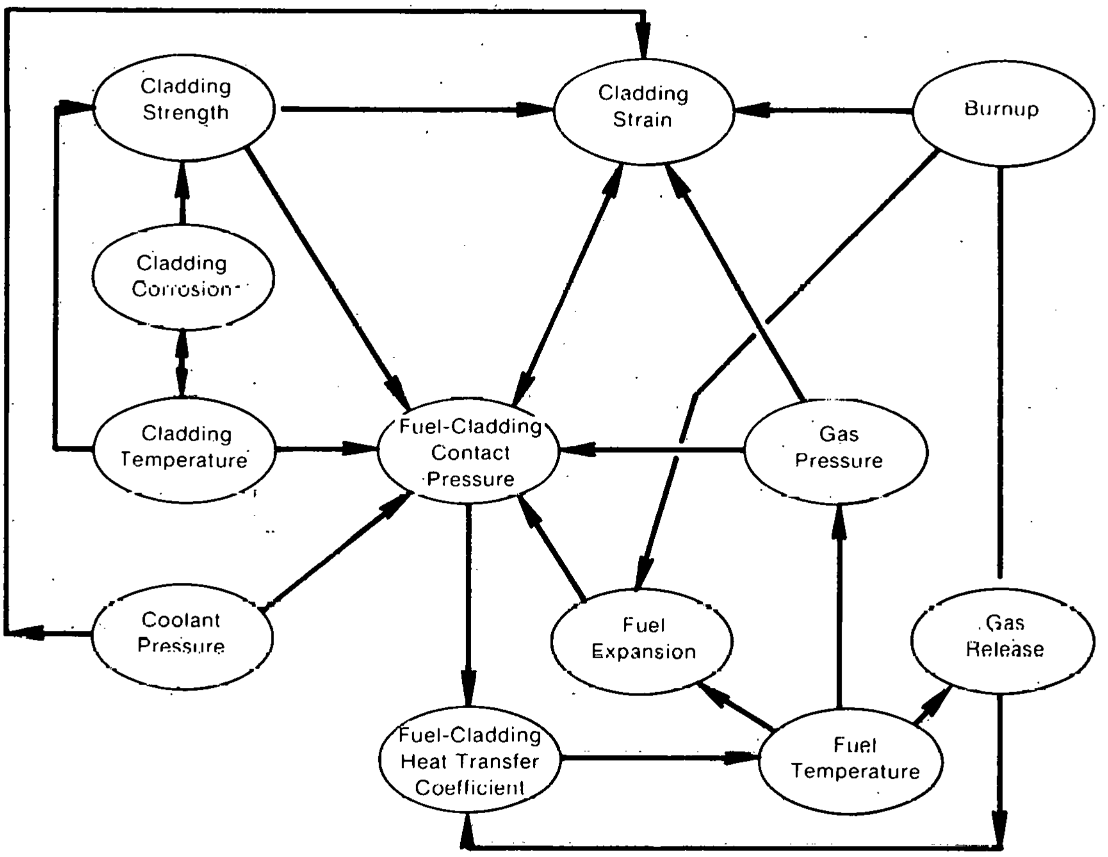

Fig. 17 FRAP-S computational interactions.

cladding. The radial temperature distribution through the pellet is calculated for the 10 rings by the ∫k dT method described by Robertson et al[30].

Burnup dependent pellet radial power distributions, fit to the output of the lattice depletion code LASER[11] are used in calculating the fuel temperature distribution.

After the temperatures in each fuel subvolume are calculated, the fission gas fractional release is calculated using the diffusion-trapping model of Weisman and MacDonald[17]. The quantity of generated fission gases in each fuel subvolume is calculated as a function of fuel burnup (the burnup is calculated for each subvolume from the input power/time and axial flux shapes and from the burnup dependent pellet radial flux depression). The dish, pellet-to-cladding gap, fuel crack, fuel open porosity, and plenum volumes are calculated considering the various fuel and cladding thermal, stress induced, and fission product induced deformation and then, the total fission product gas release and the rod internal pressure is calculated using the ideal gas law by summing the individual axial segment calculated gas releases and void volumes. The plenum temperature calculation considers heat flow from the top of the fuel stack, from the coolant channel, and gamma heating in the hold-down spring.

The new pressure and gas composition are used in the next iteration to recalculate the heat transfer across the pellet to cladding gap. The cladding stresses, strains, and interface pressures or gaps are computed by FRACAS[31]. Zircaloy cladding creep is calculated as described in Section 3. The fuel swelling model is based on the early work at the Bettis Atomic Power Laboratories[21]. The gap and crack gas conductivities are based on the work of Brokaw[32] and Gandhi and Saxena[33]. And, the zircaloy corrosion model is based on the out-of-pile work of van der Linde[24] with the constants adjusted to published in-pile data[25,26,34].

VI. REFERENCES

1. J. A. Dearien et al, FRAP-T2: A Computer Code for the Transient Analysis of Oxide Fuel Rods, TREE-NUREG-1040 (March 1977).

2. Personal Communication with W. I. Schindler, ANC, (June 1974).

3. C. R. Hann, C. E. Beyer, and L. J. Parchen, GAPCON-THERMAL-1: A Computer Program for Calculating the Gap Conductance in Oxide Fuel Pins, BNWL-1778 (September 1973).

4. P. E. MacDonald et al, MATPRO: A Handbook of Materials Properties For Use in the Analysis of Light Water Reactor Fuel Rod Behavior. ANCR-1263, NRC-3 (February 1976).

5. F. W. Dittus and L. M. K. Boelter, "Heat Transfer in Automobile Radiators of the Tubular Type," University of California Publications in Engineering, 2, 13 (1930) pp 443-461.

6. W. H. Jens and P. A. Lottes, Analysis of Heat Transfer, Burnout, Pressure Drop, and Density Data for High-Pressure Water, ANL-4627 (1951).

7. P. E. MacDonald et al, MATPRO-Version 09 - A Handbook of Materials Properties for Use in the Analysis of Light Water Reactor Fuel Rod Behavior, TREE-NUREG-1005, (December 1976).

8. A. M. Ross and R. L. Stoute, Heat Transfer Coefficient Between UO_2 and Zircaloy-2, AECL-1552 (June 1962).

9. C. Jacobs and N. Todreas, "Thermal Contact Conductance in Reactor Fuel Elements," Nuclear Science and Engineering, 50, 3 (March 1973) pp 283-290.

10. H. Fenech and W. M. Rohsenow, "A Prediction of Thermal Conductance of Metallic Surfaces in Contact," Transactions of the ASME, Series C, Journal of Heat Transfer, 85, 1 (February 1963) pp 15-24 (ASME paper 62-HT-32).

11. C. G. Poncelet, LASER - A Depletion Program for Lattice Calculations Based on MUFT and THERMOS, WCAP-6073 (April 1966).

12. W. H. McAdams, Heat Transmission, 3rd ed., New York: McGraw-Hill Book Company, Inc., 1954.

13. A. Mendelson, Plasticity: Theory and Applications, New York: The MacMillan Company, 1968.

14. E. F. Ibrahim, An Equation for Creep of Cold-Worked Zircaloy Pressure Tube Material, AECL-2928 (1965).

15. C. E. Pugh et al, Currently Recommended Constitutive Equations for Inelastic Design Analysis of FFTF Components, ORNL-TM-3602 (September 1973).

16. R. E. Skardahl et al, U.S. Experience on Irradiation Performance of UO_2-PuO_2 Fast Reactor Fuel, CONF 671005 (1970).

17. J. Weisman et al, "Fission Gas Release from UO_2 Fuel Rods with Time Varying Power Histories," ANS Transactions, 12, 2 (November 1969).

18. A. H. Booth, A Method of Calculating Fission Gas Diffusion from UO_2 Fuel and Its Application to the X-2 Loop Test, AECL-496 (CRDC-721), (1957).

19. H. M. Ferrari, "Nitrogen Release from UO_2 Pellets at Elevated Temperatures," Nuclear Science and Engineering, 17, 4 (December 1963).

20. H. M. Ferrari, "Diffusion of Nitrogen in Uranium Dioxide," Journal of Nuclear Materials, 12, 2 (1964).

21. R. C. Daniel et al, Effects of High Burnup on Zircaloy Clad Bulk UO_2 Plate Fuel Element Samples, WAPD-263, (September 1963).

22. C. M. Cox, "The Irradiation Performance of Uranium-Plutonium Oxide Fuel Pins," Nuclear Safety, 10, 5 (October 1969) pp 380-391.

23. F. Anselin and W. F. Baily, "The Role of Fission Products in the Swelling of Irradiated UO_2 and $(U, Pu)O_2$ Fuels," Transactions of the American Nuclear Society, 10, 1 (1967) pp 103-104.

24. A. van der Linde, Calculation of the Safe Lifetime Expectancy of Zirconium Alloy Canning in the Fuel Elements of the NERO Reactor, RCN-41 (1965).

25. R. C. Nelson, The Corrosion of Zircaloy-2 Fuel Element Cladding in a Boiling Water Reactor Environment, GEAP-4089 (1969).

26. H. E. Williamson et al, AEC Fuel Cycle Program Examination of UO_2 Fuel Rods Operated in the VBNR to 10,000 MWd/tU, GEAP-4597 (1965).

27. L. S. Tong and J. Weisman, Thermal Analysis of Pressurized Water Reactors, TID-25635 (1970).

28. W. R. Smalley, Saxton Plutonium Program Semi-Annual Progress Report for the Period Ending June 30, 1969, WCAP 3385-20 (October 1969).

29. W. R. Smalley, Saxton Plutonium Program Semi-Annual Progress Report for the Period Ending December 31, 1969, WCAP 3385-22 (March 1970).

30. J. A. L. Robertson, $\int kdt$ in Fuel Irradiations, CRFD-832 (April 1959).

31. M. P. Bohn, FRACAS -- A Subcode for the Analysis of Fuel Pellet-Cladding Mechanical Interaction, TREE-NUREG-1028 (April 1977).

32. R. S. Brokaw, Alignment Charts for Transport Properties, Viscosity, Thermal Conductivity and Diffusion Coefficients for Nonpolar Gases and Gas Mixtures at Low Density, NASA TR R-81, (1961).

33. J. M. Gandhi and S. C. Saxena, "Correlated Thermal Conductivity Data of Rare Gases and Their Binary Mixtures at Ordinary Pressures," Journal of Chemical and Engineering Data, 13, 3 (1968).

34. H. H. Klepfer and A. S. Melner, Specific Zirconium Alloy Design Program - Final Summary Report, GEAP-10044 (1969).

THIS PAGE
WAS INTENTIONALLY
LEFT BLANK

APPENDIX A

FRAP-S2 INPUT INSTRUCTIONS

THIS PAGE

WAS INTENTIONALLY

LEFT BLANK

APPENDIX A

FRAP-S2 INPUT INSTRUCTIONS

The required input to FRAP-S2 is presented in this appendix. Section I describes the use of NAMELIST[a], the free form input used by FRAP-S2. Section II presents the standard and optional input with a listing of each mnemonic variable, a description of the variable, and any restrictions or options associated with the variable. Section III presents the job control language (JCL) required to run FRAP-S2 and the plot code on the Idaho National Engineering Laboratory (INEL) 360/75. This is followed by the plot subcode input data.

1. NAMELIST INPUT SPECIFICATION

Input data must be in a special form in order to be read using a NAMELIST list. The first character in each record (card) to be read must be blank. The second character in the first record of a group of data records must be a $, immediately followed by the NAMELIST name. For any FRAP-S version this is FRAPS. The NAMELIST name must be followed by a blank and must not contain any embedded blanks. This name is followed by data items separated by commas. (A comma after the last item is optional.) The end of a data group is signaled by $END.

The form of the data items in an input record is:

symbolic name = constant

The symbolic name may be an array element name or a variable name. Subscripts must be integer constants. The constant may be an

---

[a] IBM System/360 and System/370 FORTRAN IV Language, IBM System Reference Library.

integer, real, literal, complex, or logical. (If the constants are logical, they may be in the form T or .TRUE. and F or .FALSE.)

array name - set of constants (separated by commas)

The set of constants consists of constants of the type integer, real, literal, complex, or logical. The number of constants must be less than or equal to the number of elements in the array. Successive occurrences of the same constant can be represented in the form k*constant, where k is a nonzero integer constant specifying the number of times the constant is to occur.

The variable names and array names specified in the input data set must appear in the NAMELIST list, but the order is not significant. A name that has been made equivalent to a name in the input data cannot be substituted for that name in the NAMELIST list. The list can contain names of items in COMMON but must not contain dummy argument names.

Each data record (card) must begin with a blank followed by a complete variable or array name or constant. Embedded blanks are not permitted in names or constants. Trailing blanks after integers and exponents are treated as zeros.

2. INPUT DATA

2.1 Standard Input

The first card which must be included is a job title card. Each standard input card must be supplied unless an optional input card replaces it.

Variable	Description	Restrictions and Options
CPL	Cold plenum length (in., m)	none

Variable	Description	Restrictions and Options
DCI	Diameter of cladding, inside (in., m)	none
DC0	Diameter of cladding, outside (in., m)	none
DE	Equivalent hydraulic diameter (in., m)	none
DEN	Pellet true density (% theoretical density)	none
DISHSD	Dish shoulder width (pellet radius minus dish radius) (in., m)	none
DP	Diameter of pellet (in., m)	none
DSPG	Diameter of spring, outside (in., m)	none
DSPGW	Diameter of spring wire (in., m)	none
ENRCH	Fuel enrichment (w/o U-235) used in flux depression estimate	if omitted, input flux depression (FLXDP)
FGPAV	Initial gas pressure (psia, N/m^2)	none
G0	Mass flow rate ($lb/hr\text{-}ft^2$, $kg/s\text{-}m^2$)	= 0 , cladding surface temperature = TW at all increments. If NSP = 1, input one value for each power step

Variable	Description	Restrictions and Options
HDISH	Height of pellet end dish (in., m)	none
HPIT	Height of pellet (in., m)	none
ICM	Index for cladding material (presently the code does not distinguish between zircaloy-2 and zircaloy-4)	= 2, zircaloy-2 cladding = 4, zircaloy-4 cladding
IDXGAS	Index for initial fill gas	= 1, helium = 2, air = 3, nitrogen = 4, fission gas = 5, argon = 6, user specifies mole fractions of the above (see AMFAIR, etc. in the optional input section). If fission products are input, user should consider input of initial burnup, BUIN
IM	Number of power levels	must equal number of time steps (Maximum of 69)
IQ	Axial power shape index	= 0, shape input = 1, cosine shape
IPLANT	Index for LASER fit of radial power distributions. If IPLANT	= 1, PWR, uranium enriched if ENRCH >6 or

Variable	Description	Restrictions and Options
	is set to zero, FRAP-S2 makes use of the pellet temperature distribution calculation as described in Section 1.5.2	<2 set IPLANT = 0 = 2, BWR, uranium enriched if ENRCH >3.5 or <1.5 set IPLANT = 0 = 3, PWR, plutonium enriched UO_2 if ENRCH >10 or <2 set IPLANT = 0 = -1, user input radial power profile (see RAPOW) = 4, BWR, plutonium enriched UO_2 if ENRCH >6 or <1.5 set IPLANT = 0
JDLPR	Index for axial increments to be output	= 1, and NØPT = 0, peak power increment only ≠ 1, and NØPT = 0, all increments
JN	Number of entries in each set of QF and X tables	omit if IQ = 1. Maximum of 40. If more than one shape JST must be input. Number of values must equal number of axial shapes used.
NT	Number of axial increments	must be odd integer >3, <17

Variable	Description	Restrictions and Options
NUNITS	Units to be input (defaults to SI units)	= 0, SI units are input = 1, British units are input
P2	System pressure (psia, N/m^2)	if NSP = 1, input one value for each power level
QF	Pointwise axial heat flux normalization factors	number of entries must equal JN for each axial shape. $1 \le Q \le 41$ for each shape up to 5 shapes. If more than one shape, normalize all shapes to the average
QMPY	Heat flux at each power ($Btu/hr\text{-}ft^2$) or (kW/ft, W/cm)	= kW/ft or W/cm if first value is less than 100. = $Btu/hr\text{-}ft^2$ if first value is greater than 100. Must be greater than zero however
TIME	Table of accumulated times. (end of step times) Corresponding to QMPY entries (sec) or (hours)	= seconds if first value greater than 17.0 = hours if first value >0.01 hour but, <1.0 hour
TØTL	Fuel stack height (ft, m)	none

Variable	Description	Restrictions and Options
TW	Inlet water temperature (°F, K)	if G0 = 0 TW is clad surface temperature. If NSP = 1, input one value for each power step
VS	Total number of spring turns	none
X	Table of axial stations corresponding to QF entries (ft, m)	number of entries must equal JN for each axial shape. 1 < X < 41 for each shape up to 5 shapes. First value must be 0.0 and last value must be equal to the total length T0TL

The following variables are predefined in the code. It is not necessary to include these cards in the input data deck unless a value other than that listed below is desired. The "additional" factors (i.e., ACOR, etc.) may be used in parametric or scoping studies.

2.2 Optional Input

Variable	Default Value	Description	Restrictions and Options
AC0R	1.0	Additional corrosion buildup factor	≠ 0
AFAL	1.0	Additional thermal expansion factor	≠ 0

Variable	Default Value	Description	Restrictions and Options
AFCR	1.0	Additional creep acceleration factor	≠ 0
AFDN	1.0	Additional densification factor	none
AFGR	1.0	Additional fractional gas release multiplication factor	≠ 0
AFTC	1.0	Additional fuel thermal conductivity multiplication factor	≠ 0
AFSW	1.0	Additional fuel swelling multiplication factor	≠ 0
AMFAIR	0.0	Absolute mole fraction of air	use only if IDXGAS = 6
AMFARG	0.0	Absolute mole fraction of argon	use only if IDXGAS = 6
AMFFG	0.0	Absolute mole fraction of fission gas	use only if IDXGAS = 6
AMFKRY	0.0	Absolute mole fraction of krypton	use only if IDXGAS = 6 and AMFFG = 0.0
AMFXE	0.0	Absolute mole fraction of xenon	use only if IDXGAS = 6 and AMFFG = 0.0

Variable	Default Value	Description	Restrictions and Options
AMFHE	0.0	Absolute mole fraction of helium	use only if IDXGAS = 6
AMFH2	0.0	Absolute mole fraction of hydrogen	use only if IDXGAS = 6
AMFH2O	0.0	Absolute mole fraction of steam	use only if IDXGAS = 6
AMFN2	0.0	Absolute mole fraction of nitrogen	use only if IDXGAS = 6
AMI	0.0	Change in flux depression factor per unit burnup between BUCRIT and end of problem	= 0, constant flux depression factor
AMO	0.0	Change in flux depression factor per unit burnup between zero burnup and BUCRIT	= 0, constant flux depression factor
BETA	1.0	Porosity correction to fuel thermal conductivity	none
BUIN	0.0	Initial fuel burnup (MWd/MtU, MWs/kg)	should include input of fission product mole fractions
BUCRIT	0.0	Burnup at which flux depression factor changes slope (MWd/MtU, MWs/kg)	= 0, AMO not used

Variable	Default Value	Description	Restrictions and Options
CATEXF	0.05	Texture factor (fraction of cladding cells with basal poles parallel to the tube axis)	$0.0 \leq$ CATEXF ≤ 1.0
C0LDWK	0.0	Cold work of the cladding	none
C0MP	0.0	Weight percent of $PU0_2$ in mixed oxide fuel	$0.0 \leq$ C0MP ≤ 100.0
CRDT	1.0	Initial crud thickness (mil, m)	
CRDTR	1.1415525×10^{-4}	Crud buildup rate (mil/hr, m/s)	used only if IC0R = 2
DENG	0.75	Porosity correction to pellet density (%) emersion (true) density to geometric density	none
EX0	1.0	Surface roughness factor in gap conductance calculation	minimum of 1.0
FA	1.0	Nuclear axial hot channel factor (peak/average)	= 1.0, if QF table is normalized to the average, and QMPY = average heat flux. > 1.0, if IQ = 1 and QMPY = peak heat flux.

Variable	Default Value	Description	Restrictions and Options
			> 1.0, if IQ table is normalized to the peak, and QMPY = peak heat flux
FLXDP	0.9999	Initial value of flux depression factor	used only if ENRCH = 0.0 and IPLANT not specified. Must be less than 0.9999 $\text{FLXDP} = \frac{2[I_0(\kappa a)-1]}{\kappa a[I_1(\kappa a)]}$ a = pellet radius (in.) = reciprocal of thermal diffusion length (in.^{-1}) I_0= zero order modified Bessel function (first kind) I_1 = first order modified function (first kind)
FQE	1.0	Heat flux engineering factor	multiplication factor on QMPY values
ICØR	0	Index for crud model	= 0, corrosion model constant crud, no crud temperature drop if boiling. = 1, corrosion model, constant crud, crud temperature drop if boiling.

Variable	Default Value	Description	Restrictions and Options
			= 2, corrosion model, varying crud, crud temperature drop if boiling
JST	IM*1	Indicates type of axial power shape to be used for each time step	IQ must = 0. Must be one type number for each time step, (the first QF and X array is Type 1, the second is Type 2, etc.), maximum of five types. The axial shapes must be normalized to the average
LINKT	2	FRAP-T link index	= 1, link is to FRAP-T1 = 2, link is to FRAP-T2
MDBG	0	Summary power step debug output index	= 0, no debug output = 1, debug output
MØDE	0	Stack calculation selector	= 0, stack calculations are made = 1, stack calculations are not made
NDBG	0	Debug printout index	= 0, normal output = -1, full debug output. To obtain debug output at only one power level set NDBG equal to that power level number

Variable	Default Value	Description	Restrictions and Options
NGAPC	0	Gap conductance model selector	= 0, cracked pellet model = 1, annular gap model
NØPT	3	Printout selector	= 0, full output = 3, short (tabular) output
NREAD	0	FRAP-S restart read index	= 0, no restart = 1, read restart tape
NRESTR	0	FRAP-S restart write index	= 0, no restart write = 1, write FRAP-S restart tape
NRØLL	0	Restart tape rewind index	= 0, rewrites in same storage space = 1, writes a string of restart information for each power step
NSP	0	Varying system parameter	= 0, constant system parameter (P2, TW, GØ) = 1, varying system parameters
NSTART	0	Timestep for start of debug output	$0 \leq$ NSTART $\leq$ IM
NSTØP	0	Timestep for end of debug output	$0 \leq$ NSTØP $\leq$ IM and NSTØP > NSTART

Variable	Default Value	Description	Restrictions and Options
NTAPE	0	FRAP-T restart index	= 0, no restart data stored = 1, restart data stored for FRAP-T use
PPMH20	0	Fuel water content (PPM)	none
PPMN2	15.0	Fuel nitrogen content (PPM)	none
QEND	0.3	Normalized heat flux at top of fuel stack	must be one value for each axial shape. Used to determine heat flow into the plenum
RAP0W	1.0	Normalized radial power profile	IPLANT must be -1. Input eleven values from the fuel surface to the fuel center assuming equal areas between radial nodes
RC	0.0	Pellet core radius (in., m)	none
R0UGHC	4.8×10^{-5}	Arithmetic mean roughness height of cladding (in., m)	none
R0UGHF	8.5×10^{-5}	Arithmetic mean roughness height of fuel (in., m)	none

Variable	Default Value	Description	Restrictions and Options
R0	DC0/24	Cladding outside radius (ft, m)	do not input DC0
R0F	DP/24	Pellet radius (ft, m)	do not input DP
SGAPF	30	Fission gas atoms per 100 fissions	none
TCC	(DC0-DCI)/2	Clad thickness (in., m)	do not input DCI
TSINT	2912	Fuel sintering temperature (°F, K)	none

2.3 Plot Input

The following is the input data for plotting. If no plots are desired, follow the "$END" card of the preceding input with card 1 below. If plots are desired, the "$END" card is followed with first, a full set of plot data, and then a set of plot JCL from SECTION III.

Card No. 1

Columns	Format	Name	Quantity
1 - 5	1	NPLTN0	Number of axial nodes at which plots are desired. If no plots wanted, input the number 0.

Card No. 2 - Specification of axial nodes at which plots are wanted

Columns	Format	Name	Quantity
1 - 5	I	IAPLT(1)	Number of an axial node at which plots are wanted.
6 - 10	I	IAPLT(2)	Number of an axial node at which plots are wanted.

Repeat as necessary for IAPLT(K) (K being an axial node number)

Card No. 3 - Time axis

Columns	Format	Name	Quantity
1 - 10	F	TSTART	Minimum time on time axis (hr, sec).
11 - 20	F	TEND	Maximum time on time axis (hr, sec).
21 - 30	F	AXLT	Length of time axis (in.).
31 - 70	A	LABLT	Label to be given time axis.

Card No. 4 - Cladding surface temperaxis (°F, K)

Columns	Format	Name	Quantity
1 - 10	F	TSMIN	Minimum cladding surface temperature on axis (°F, K).
11 - 20	F	TSMAX	Maximum cladding surface temperature in axis (°F, K).
21 - 30	F	AXLTS	Length of surface temperature axis (in.).
31 - 70	A	LABLTS	Label to be given surface temperature axis.

Card No. 5 - Fuel centerline temperature axis

Columns	Format	Name	Quantity
1 - 10	F	TOLMIN	Minimum fuel centerline temperature on axis (°F, K).
11 - 20	F	TOLMAX	Maximum fuel centerline temperature on axis (°F, K).
21 - 30	F	AXLTMP	Length of centerline temperature axis (in.).
31 - 70	A	LABLTM	Label to be given centerline temperature axis.

Card No. 6 - Gas pressure axis

Columns	Format	Name	Quantity
1 - 10	F	PMIN	Minimum gas gap pressure on axis (psia, N/m^2).

Columns	Format	Name	Quantity
11 - 20	F	PMAX	Maximum gas gap pressure on axis (psia, N/m^2).
21 - 30	F	AXLP	Length of gas gap pressure axis (in.).
31 - 70	A	LABLP	Label to be given gas gap pressure axis.

Card No. 7 - Cladding hoop strain axis

Columns	Format	Name	Quantity
1 - 10	F	EPSMIN	Minimum cladding hoop strain on axis (dimensionless).
11 - 20	F	EPSMAX	Maximum cladding hoop strain on axis (dimensionless).
21 - 30	F	AXLEPS	Length of cladding hoop strain axis (in.).
31 - 70	A	LABLE	Label to be given cladding hoop strain.

Card No. 8 - Fuel axial displacement axis

Columns	Format	Name	Quantity
1 - 10	F	UZFMIN	Minimum fuel axial displacement on axis (ft, m).
11 - 20	F	UZFMAX	Maximum fuel axial displacement on axis (ft, m).

Columns	Format	Name	Quantity
21 - 30	F	AXLUZF	Length of fuel axial displacement axis (in.).
31 - 70	A	LABLUF	Label to be given fuel axial displacement axis.

Card No. 9 - Cladding axial displacement axis

Colums	Format	Name	Quantity
1 - 10	F	UZCMIN	Minimum cladding axial displacement on axis (ft, m).
11 - 20	F	UZCMAX	Maximum cladding axial displacement on axis (ft, m).
21 - 30	F	AXLUZC	Length of cladding axial displacement axis (in.).
31 - 70	A	LABLUC	Label to be given cladding axial displacement axis.

Card No. 10 - Fuel rod power axis

Columns	Format	Name	Quantity
1 - 10	F	PMIN	Minimum linear fuel rod power on axis (kW/ft, W/m).
11 - 20	F	PMAX	Maximum linear fuel rod power on axis (kW/ft, W/m).
21 - 30	F	PLEN	Length of linear fuel rod power axis (in.).

Columns	Format	Name	Quantity
31 - 70	A	PLABL	Label to be given fuel rod power axis.

Card No. 11 - Fuel surface temperature axis

Columns	Format	Name	Quantity
1 - 10	F	TFSMIN	Minimum fuel surface temperature on axis (°F, K).
11 - 20	F	TFSMAX	Maximum fuel surface temperature on axis (°F, K).
21 - 30	F	TFSLEN	Length of fuel surface temperature axis (in.).
31 - 70	A	TFSLAB	Label to be given fuel surface temperature axis.

Card No. 12 - Gap heat transfer coefficient axis

Columns	Format	Name	Quantity
1 - 10	F	HGMIN	Minimum gap heat transfer coefficient on axis (Btu/hr-°F-ft^2, W/m^2-K).
11 - 20	F	HGMAX	Maximum gap heat transfer coefficient on axis (Btu/hr-°F-ft^2, W/m^2-K).
21 - 30	F	HGLEN	Length of gap heat transfer coefficient axis (in.).
31 - 70	A	HGLABL	Label to be given gap heat transfer coefficient axis.

Card No. 13 - Surface heat transfer coefficient axis

Columns	Format	Name	Quantity
1 - 10	F	HSMIN	Minimum surface heat transfer coefficient on axis (Btu/hr-°F-ft^2, W/m^2-K).
11 - 20	F	HSMAX	Maximum surface heat transfer coefficient on axis (Btu/hr-°F-ft^2, W/m^2-K).
21 - 30	F	HSLEN	Length of surface heat transfer coefficient axis (in.).
31 - 70	A	HSLAB	Label to be given surface heat transfer coefficient axis.

Card No. 14 - Average cladding temperature axis

Columns	Format	Name	Quantity
1 - 10	F	TAMIN	Minimum average cladding temperature on axis (°F, K).
11 - 20	F	TAMAX	Maximum average cladding temperature on axis (°F, K).
21 - 30	F	TALEN	Length of average cladding temperature axis (in.).
31 - 70	A	TALABL	Label to be given average cladding temperature axis.

Card No. 15 - Zircaloy-Oxide thickness axis

Columns	Format	Name	Quantity
1 - 10	F	ZOMIN	Minimum ZrO_2 thickness (mil, m).
11 - 20	F	ZOMAX	Maximum ZrO_2 thickness (mil, m).
21 - 30	F	ZOLEN	Length of ZrO_2 thickness (in.).
31 - 70	A	ZOLABL	Label to be given zircaloy-oxide thickness axis.

Card No. 16 - Mole fraction of helium

Columns	Format	Name	Quantity
1 - 10	F	MFMIN	Minimum helium mole fraction on axis.
11 - 20	F	MFMAX	Maximum helium mole fraction on axis.
21 - 30	F	MFLEN	Length of helium mole fraction axis (in.).
31 - 70	A	MFLABL	Label to be given helium mole fraction axis.

Card No. 17 - Plenum temperature axis

Columns	Format	Name	Quantity
1 - 10	F	TPMIN	Minimum plenum temperature on axis (°F or K).
11 - 20	F	TPMAX	Maximum plenum temperature on axis (°F or K).

Columns	Format	Name	Quantity
21 - 30	F	TPLEN	Length of plenum temperature axis (in.).
31 - 70	A	TPLABL	Label to be given plenum temperature axis.

Card No. 18 - Rod gas increase

Columns	Format	Name	Quantity
1 - 10	F	RGMIN	Minimum gas increase on axis (% of initial).
11 - 20	F	RGMAX	Maximum gas increase on axis (% of initial).
21 - 30	F	RGLEN	Length of gas increase axis (in.).
31 - 70	A	RGLABL	Label to be given gas increase axis.

Card No. 19 - Mass flux axis (plot of average mass flux in coolant channels surrounding fuel rod)

Columns	Format	Name	Quantity
1 - 10	F	GMIN	Minimum mass flux on axis (lbm/ft^2-hr or kg/m^2-s).
11 - 20	F	GMAX	Maximum mass flux on axis (lbm/ft^2-hr or kg/m^2-s).
21 - 30	F	GLEN	Length of mass flux axis (in.).
31 - 70	A	GLABL	Label to be given mass flux axis.

Card No. 20 - Fuel stored energy

Columns	Format	Name	Quantity
1 - 10	F	SEMIN	Minimum stored energy on axis (Btu/lbm, Cal/gm).
11 - 20	F	SEMAX	Maximum stored energy on axis (Btu/lbm, Cal/gm).
21 - 30	F	SELEN	Length of quality axis (in.).
31 - 70	A	SELABL	Label to be given quality axis.

Card No. 21 - Coolant pressure axis (plot of average pressure in coolant channel surrounding fuel rod)

Columns	Format	Name	Quantity
1 - 10	F	PCMIN	Minimum pressure on axis (psia or N/m^2).
11 - 20	F	PCMAX	Maximum pressure on axis (psia or N/m^2).
21 - 30	F	PCLEN	Length of pressure axis (in.).
31 - 70	A	PCLABL	Label to be given coolant pressure axis.

Card No. 22 - Gap thickness axis

Columns	Format	Name	Quantity
1 - 10	F	THKMIN	Minimum gap thickness on axis (mil or m).

Columns	Format	Name	Quantity
11 - 20	F	THKMAX	Maximum gap thickness on axis (mil or m).
21 - 30	F	THKLEN	Length of gap thickness axis (in.).
31 - 70	A	THKLAB	Label to be given gap thickness axis.

Card No. 23 - Bulk temperature axis

Columns	Format	Name	Quantity
1 - 10	F	TBMIN	Minimum bulk temperature on axis (°F or K).
11 - 20	F	TBMAX	Maximum bulk temperature on axis (°F or K).
21 - 30	F	TBLEN	Length of bulk temperature axis (in.).
31 - 70	A	TBLAB	Label to be given bulk temperature axis.

3. JOB CONTROL LANGUAGE (JCL)

3.1 JCL Cards for Creating a FRAP-S2 Load Module on the INEL IBM 360/75 Computer

Card No.

1 Job Card

2 // CØR=360,CPU=003,WT=001,SR=T1

```
//STEP1 EXEC FTNHCL,CØSET='X1',MEMB='(X2)',
// DISP='(,CATLG)',UNIT=X3,SPACE='(TRK,(40,05,1),RLSE)',
// CREG=240K,CPGS=290,XREF=XREF
//C.SYSUT2 DD SPACE=(TRK,(40,10)),UNIT=SYSCRA
//C.SYSIN DD DSN='X4',UNIT=TP9ANY,DISP=(ØLD,KEEP),
// VØL=SER=X5
//L.ADD DD DSN =X6,DISP=(ØLD,KEEP)
11/L.SYSIN DD *
INCLUDE ADD (X7)
ENTRY MAIN
```

where

X1 is the data set name assigned to the load module (for example TEMP.GABFRAPS)

X2 is the member name associated with the load module name (for example FRAPS)

X3 is the storage unit on which the load module is to be stored (for example DKTEMP)

X4 is the tape identification name which contains card images of the source deck (for example ANCFRAPS)

X5 is the tape number corresponding to the tape identification name (for example T95246)

X6 is the name of the version of MATPRO, the material properties package (for example MATPRØ03)

X7 is the member name associated with the material properties package load module (for example MATPRO).

3.2 JCL Cards for Executing the Above Created Load Module on the INEL IBM 360/75 Computer.

```
Card No.

1     // Job Card
2     // CØR=360,CPU=Y1,WT=Y2
3     //STEP2 EXEC PGM=X2,REGIØN=360K
4     //STEPLIB DD DSN=X1,DISP=SHR
5     //FT06F001 DD SYSØUT=A,DCB=(RECFM-FBA,LRECL=133,BLKSIZE=1596),
6     // SPACE=(7980,(200,16),RLSE)
7     //FT01F001 DD DSN=Y3,UNIT=Y4,DISP=(,CATLG),
8     // DCB=(BLKSIZE=574,LRECL=104,RECFM=VBS),SPACE=(TRK,(5,5),RLSE)
```

NOTE: Include cards 9 through 12 only if plots are desired.

```
9     //FT17F001 DD DSN=Y5,DISP=(,PASS),UNIT=DKSCRA,
10    // DCB=(BLKSIZE=560,LRECL=56,RECFM=VBS),SPACE=(TRK,(1000,60))
11    //FT18F001 DD DSN=Y6,DISP=(,PASS),UNIT=DKSCRA,
12    // DCB=(BLKSIZE=560,LRECL=56,RECFM=VBS),SPACE=(TRK,(2,1))
13    //FT05F001 DD *
```

INPUT DATA:

where

Y1 is the total computer time required for the job in minutes

Y2 is the total wait time in minutes

Y3 is the name given to the restart data set (for example TEMP.LJSREST1)

Y4 is the storage unit on which the restart data is written (for example DKTEMP)

Y5 is a scratch data set name to be specified by the user (for example &&GAB00017)

Y6 is a scratch data set name to be specified by the user (for example &&GAB00018).

3.3 JCL Cards for Creating the Plot Code Load Module

If plots are desired an executable plot code load module should be available. The following cards are required to compile the plot package for FRAP-S2.

Card No.

```
1     // Job Card
2     // C0R=265,CPU=001,WT=001
3     //S1 EXEC FTNHCL,G0SET='Z1',MEMB='(Z2)',
4     // 0PT=2,DISP='(,CATLG)',UNIT=Z3,CREG=265K,
5     // SPACE='(TRK,(10,10),1),RLSE)',CPGS=100,
6     // XREF=XREF
7     //C.SYSUT2 DD SPACE=(TRK,(40,10)),UNIT=Z4
8     //C.SYSIN DD *
```

SOURCE CARDS:

where

Z1 is the name to be assigned to the load module (for example PL0TFRPS)

Z2 is the member name to be assigned to the compiled load module (for example PL0TCD)

Z3 is the name of the unit on which the load module is to be stored (for example DKTEMP)

Z4 is a scratch space unit (for example SYSCRA).

3.4 JCL Cards for Executing the Above Created Plot Load Module (to follow the plot input cards)

Card No.

```
1     //PL0TSTEP EXEC=Z2,REGI0N=200K
2     //STEPLIB DD DSN=Z1,DISP=(0LD,KEEP)
3     //FT06F001 DD SYS0UT=A,DCB=(RECFM=FRA,LRECL=133,BLKSIZE=1596),
4     // SPACE=(TRK,(2,5))
5     //FT17F001 DD DSN=Y5,DISP=(0LD,DELETE),UNIT=DKSCRA
6     //FT18F001 DD DSN=Y6,DISP=(0LD,DELETE),UNIT=DKSCRA
7     //PL0T DD SYS0UT=(Y,,0003)
8     //FT05F001 DD *
```

where Z1, Z2, Y5, and Y6 are as defined in previous groups of JCL.

THIS PAGE
WAS INTENTIONALLY
LEFT BLANK

APPENDIX B

EXAMPLE PROBLEM INPUT AND OUTPUT

THIS PAGE

WAS INTENTIONALLY

LEFT BLANK

APPENDIX B

EXAMPLE PROBLEM INPUT AND OUTPUT

This section presents the general format used for input to FRAP-S2 and the output format showing the information a user would expect to receive from a run.

(1) Example Problem Input
A set of data for an example problem is presented in Table B-I and B-II.

(2) Example Problem Output

(a) Initial problem parameters and history information appear in the first three pages of output as shown in the first three pages of Table B-III.

(b) A typical set of output information for one axial station is shown in the fourth page of Table B-III.

(c) A power step summary of the entire rod is presented on the fifth page of Table B-III.

(d) A problem summary of information calculated at the peak power axial level along with other information provided at a problem's completion are shown on the seventh and eighth pages of Table B-III.

TABLE B-I

EXAMPLE PROBLEM DATA (PCM-20 PBF ROD)

Coolant Conditions:

mass flux, 1.0 x 10^6 (lbm/hr-ft^2)
inlet temperature, 642 (°F)
hydraulic diameter, 0.348 (in.)
pressure, 2250 (psia)

Fuel Rod Geometry:

fuel stack length, 3.0 (ft)
fuel rod outside diameter, 0.422 (in.)
fuel pellet diameter, 0.366 (in.)
plenum length, 2.0 (in.)

Fuel Initial Conditions:

density, 93.5 (% theoretical density)
pressure, 300 (psia)
enrichment, 35 (%)

Power History:

a power ramp from 5 kW/ft to 10 kW/ft in 10 hours

TABLE B-II

EXAMPLE PROBLEM

FORTRAN CODING FORM

```
                       PBF SINGLE RØD  PCM-20
 $FRAPS
  CPL  =2.0  , QRDTR= 0.0, DCI    = .374, DCØ    =.422, DE    =0.348,
  DEN  =93.5 , DENG = 5.0, DISHSD= .062, DP     =.366, DSPG  =0.355,
  DSPGW=0.04 , ENRCH= 35.0, FGPAV = 300., GØ(1)  =1.E6, HDISH=0.015,
  HPLT =.6545, ICM  =   4, ICØR  =    1, IDXGAS=   1, IM    =    2,
  IPLANT=1   , IQ   =   0, JDLPR =    0, JN(1)  =  19, NT    =    9,
  NTAPE=    0, P2(1)= 2250, NØPT  =    0, TØTL  = 3.0, VS    = 17.0,
  TW(1)= 642., QMPY=5.,10., TIME=.01,10., RØUGHF=8.5E-5, RØUGHC=4.5E-5,
  QF   = 0.62  ,.705  ,.875  ,1.065 ,1.215 ,1.31  ,1.37  ,1.38  ,1.375
       ,1.335 ,1.275 ,1.18  ,1.06  ,0.94  ,0.815 ,0.685 ,0.55  ,0.44  ,0.38 ,
  X    = 0.0   ,.1667 ,.3333 ,0.5   ,.6667 ,.8333 ,1.0   ,1.1667,1.3333,
        1.5   ,1.6667,1.8333,2.0   ,2.1667,2.3333,2.5   ,2.6667,2.8333,3.0,
 $END
```

TABLE B-III

EXAMPLE PROBLEM OUTPUT

```
               FRAP-S MOD 002  VERS 02J* STEADY-STATE FUEL PERFORMANCE CODE*11/29/76*G A BERNA* AEROJET NUCLEAR COMPANY
  RUN DATE IS -  12/18/76                           MAT PRO MODULE MODOC7                                                    PAGE   1
XXXXXXXXXXXXXXXXXXXXXXXXXXXXXXXXXXXXXXXXXXXXXXXXXXXXXXXXXXXXXXXXXXXXXXXXXXXXXXXXXXXXXXXXXXXXXXXXXXXXXXXXXXXXXXXXXXXXXXXXXXXXXXXXX
                                                    PBF SINGLE ROD  PCM-20
       XXXXXXXXXXXXXXXXXXXXXXXXXXXXXXXXXXXXXXXXXXXXXXXXXXXXXXXXXXXXXXXXXXXXXXXXXXXXXXXXXXXXXXXXXXXXXXXXXXXXXXXXXXXXXXXXXXXXX
 ******PWR SYSTEM  U-235 RODS

                                                                          STEP     TIME(HRS)  QMPY(KW/FT)   PZ(PSI)    TW(F)    GO(LBM/HR-FT2)
 CLAD MATERIAL IS ZIRCALOY-4
 CLAD YIELD STRENGTH  (600 F , 588.7 K) = 54200. (PSI)
                                        =  .37369E+09 (N/M**2)
 COLD CLAD O.D. =  .422000(IN)                          .0107188 (M)        1          .90        5.000     2250.0    642.00        1000000.0
 COLD CLAD I.D. =  .374000(IN)                          .0094996 (M)        2        10.00       10.000     2250.0    642.00        1000000.0
 COLD CLAD THICKNESS =  .0240 (IN)                        .00061 (M)        3         0.00        0.000        0.0      0.00              0.0
                                                                            4         0.00        0.000        0.0      0.00              0.0
 COLD DIAMETRAL GAP =  8.0000(MILS)                   .20320E-03 (M)        5         0.00        0.000        0.0      0.00              0.0
                                                                            6         0.00        0.000        0.0      0.00              0.0
 COLD INTERNAL HELIUM PRESSURE =  300.00(PSIA)                              7         0.00        0.000        0.0      0.00              0.0
                               =  .20664E+07 (N/M**2)                       8         0.00        0.000        0.0      0.00              0.0
 COLD PELLET DIAMETER =  .366000(IN)                   .00929642 (M)        9         0.00        0.000        0.0      0.00              0.0
 COLD PELLET LENGTH =    .65455(IN)                     .0166255 (M)       10         0.00        0.000        0.0      0.00              0.0
 PELLET TRUE DENSITY = 93.500(PERCENT)                                     11         0.00        0.000        0.0      0.00              0.0
 ENRICHMENT = 35.0000(WEIGHT PERCENT)                                      12         0.00        0.000        0.0      0.00              0.0
 FUEL STACK HEIGHT =  3.0000(FT)                           .9144 (M)       13         0.00        0.000        0.0      0.00              0.0
 DISH SPHERICAL RADIUS =    .49553(IN)                   .012587 (M)       14         0.00        0.000        0.0      0.00              0.0
 DISH DEPTH =   .01500(IN)                              .0003810 (M)       15         0.00        0.000        0.0      0.00              0.0
 DISH SHOULDER WIDTH =    .06200(IN)                    .0015748 (M)       16         0.00        0.000        0.0      0.00              0.0
 PELLET CORE RADIUS =  0.00000(IN)                      0.000000 (M)       17         0.00        0.000        0.0      0.00              0.0
 COLD FUEL VOLUME =   3.74938(CU.IN.)               .61442E-04 (M**3)      18         0.00        0.000        0.0      0.00              0.0
 DISH VOLUME FRACTION OF FUEL =    .01007                                  19         0.00        0.000        0.0      0.00              0.0
 FUEL ROUGHNESS VOLUME =    .0019(PERCENT)                                 20         0.00        0.000        0.0      0.00              0.0
 FUEL SINTERING TEMP  =2912.0   (F)                       1873.2 (K)       21         0.00        0.000        0.0      0.00              0.0
 COLD PLENUM LENGTH =   2.0000(IN)                       .050800 (M)       22         0.00        0.000        0.0      0.00              0.0
 SPRING DIAMETER =   .35500(IN)                         .0090170 (M)       23         0.00        0.000        0.0      0.00              0.0
 SPRING WIRE DIAMETER =   .04000(IN)                    .0010160 (M)       24         0.00        0.000        0.0      0.00              0.0
 TOTAL SPRING TURNS =  17.00000                                            25         0.00        0.000        0.0      0.00              0.0
 INITIAL BURNUP =  0.             (MWD/MTL)    0.          (MWS/KG)        26         0.00        0.000        0.0      0.00              0.0
 SPRING VOLUME =    .02114(CU.IN.)                  .34644E-06 (M**3)      27         0.00        0.000        0.0      0.00              0.0
 PLENUM VOLUME =    .19858(CU.IN.)                  .32541E-05 (M**3)      28         0.00        0.000        0.0      0.00              0.0
 TOTAL COLD VOID VOLUME =     .41914(CU.IN.)        .68685E-05 (M**3)      29         0.00        0.000        0.0      0.00              0.0
 ARITHMETIC MEAN ROUGHNESS(FUEL)= .0000850(IN)       .00000216 (M)         30         0.00        0.000        0.0      0.00              0.0
 ARITHMETIC MEAN ROUGHNESS(CLAD)= .0000450(IN)       .00000114 (M)         31         0.00        0.000        0.0      0.00              0.0
 CHANNEL EQUIVALENT DIAMETER =   .02900(FT)             .0088392 (M)       32         0.00        0.000        0.0      0.00              0.0
 FISSION GAS ATOMS PER 100 FISSIONS =   30.0                               33         0.00        0.000        0.0      0.00              0.0
 INITIAL WATER CONCENTRATION =    0.00(PPM)                                34         0.00        0.000        0.0      0.00              0.0
 INITIAL NITROGEN CONCENTRATION =    15.00(PPM)                            35         0.00        0.000        0.0      0.00              0.0
                                                                           36         0.00        0.000        0.0      0.00              0.0
 AFCR =  1.0000     AFAL =  1.0000                                         37         0.00        0.000        0.0      0.00              0.0
 AFGR =  1.0000     AFSW =  1.0000                                         38         0.00        0.000        0.0      0.00              0.0
 AFTC =  1.0000     BETA =  1.0000                                         39         0.00        0.000        0.0      0.00              0.0
 EXO  =  1.0000     ACOR =  1.0000                                         40         0.00        0.000        0.0      0.00              0.0
 FA   =  1.0000     FQE  =  1.0000                                         41         0.00        0.000        0.0      0.00              0.0
                                                                           42         0.00        0.000        0.0      0.00              0.0
 FLXDP =   .70319   AMO =  0.00000                                         43         0.00        0.000        0.0      0.00              0.0
 BUCRIT =     0.0   AMI =  0.00000                                         44         0.00        0.000        0.0      0.00              0.0
```

TABLE B-III (continued)

```
             FRAP-S MOD 002  VERS 02J* STEADY-STATE FUEL PERFORMANCE CODE*11/29/76*G A BERNA* AEROJET NUCLEAR COMPANY
  RUN DATE IS -  12/18/76                             MAT PRO MODULE MOD007                                                   PAGE   2
XXXXXXXXXXXXXXXXXXXXXXXXXXXXXXXXXXXXXXXXXXXXXXXXXXXXXXXXXXXXXXXXXXXXXXXXXXXXXXXXXXXXXXXXXXXXXXXXXXXXXXXXXXXXXXXXXXXXXXXXXXXXXXXXXXXX
                                                                  45          0.00      0.000        0.0     0.00           0.0
   ANGI =   .0003358  H2OMI = 0.0000000                           46          0.00      0.000        0.0     0.00           0.0
   IPLANT =  1                                                    47          0.00      0.000        0.0     0.00           0.0
   ICOR =    1                                                    48          0.00      0.000        0.0     0.00           0.0
   CRUD THICKNESS= 1.00 (MILS)    .25400E-04 (M)                  49          0.00      0.000        0.0     0.00           0.0
   CRUD RATE= 0.00 (MILS/C.Y.)                                    50          0.00      0.000        0.0     0.00           0.0
   PCTPRE = 15.0                                                  51          0.00      0.000        0.0     0.00           0.0
   PCTPOST= 35.0                                                  52          0.00      0.000        0.0     0.00           0.0
                                                                  53          0.00      0.000        0.0     0.00           0.0
   BRITISH UNITS ARE USED                                         54          0.00      0.000        0.0     0.00           0.0
   GAP CONDUCTANCE = 0                                            55          0.00      0.000        0.0     0.00           0.0
PLOTS NOT REQUESTED
```

TABLE B-III (continued)

```
               FRAP-S MOD 002  VERS 02J* STEADY-STATE FUEL PERFORMANCE CODE*11/29/76*G A BERNA* AEROJET NUCLEAR COMPANY
  RUN DATE IS -  12/18/76                                      MAT PRO MODULE MOD007                                                          PAGE   3
XXXXXXXXXXXXXXXXXXXXXXXXXXXXXXXXXXXXXXXXXXXXXXXXXXXXXXXXXXXXXXXXXXXXXXXXXXXXXXXXXXXXXXXXXXXXXXXXXXXXXXXXXXXXXXXXXXXXXXXXXXXXXXXXXXXXXXXX
                                               XXXXXXXXXXXXXXX  AXIAL POWER SHAPE INFORMATION  XXXXXXXXXXXXXXX

    AXIAL DISTRIBUTION IS INPUT           ROD AVERAGE POWER IS INPUT            NUMBER OF INCREMENTS =  9
                                                                X'S  IN FEET

                                           XXXXXXXXXXXXXXXXXXXX  INPUT AXIAL SHAPE NUMBER    1  XXXXXXXXXXXXXXXXXXXX

    X( 1)=  0.0000  X( 2)=   .1667  X( 3)=   .3333  X( 4)=   .5000  X( 5)=   .6667  X( 6)=   .8333  X( 7)=  1.0000  X( 8)=  1.1667
  X( 9)=  1.3333  X(10)=  1.5000  X(11)=  1.6667  X(12)=  1.8333  X(13)=  2.0000  X(14)=  2.1667  X(15)=  2.3333  X(16)=  2.5000
  X(17)=  2.6667  X(18)=  2.8333  X(19)=  3.0000  X(
   QF( 1)=   .6200 QF( 2)=   .7050 QF( 3)=   .8750 QF( 4)=  1.0650 QF( 5)=  1.2150 QF( 6)=  1.3100 QF( 7)=  1.3700 QF( 8)=  1.3800
QF( 9)=  1.3750 QF(10)=  1.3350 QF(11)=  1.2750 QF(12)=  1.1800 QF(13)=  1.0600 QF(14)=   .9400 QF(15)=   .8150 QF(16)=   .6850
QF(17)=   .5500 QF(18)=   .4400 QF(19)=   .3800 QF(

  INCREMENT      AXIAL STATION          UNNORMALIZED
                FEET        METERS         HEAT FLUX
      1         .1667       .05080             .7262
      2         .5000       .15240            1.0550
      3         .8333       .25400            1.3013
      4        1.1667       .35560            1.3762
      5        1.5000       .45720            1.3300
      6        1.8333       .55880            1.1737
      7        2.1667       .66040             .9388
      8        2.5000       .76200             .6838
      9        2.8333       .86360             .4525

                                        AVGQL =  1.004167

     NORMALIZED HEAT FLUX AT TOP OF STACK =  .3000


                                   ROD AVE BURNUP AT END OF LIFE (AMWDT) =       21.6
                                   ROD TIME AVE HEAT FLUX (QBAR) =  294952.



                                                      XXXXXXXXXX  INITIAL PLENUM GASES (MOLES)  XXXXXXXXXX

  AIR =  0.             NITROGEN =  0.            ARGON =  0.            FISSION GAS =  0.             HELIUM =   .57931E-02
```

TABLE B-III (continued)

```
             FRAP-S MOD 002  VERS 02J* STEADY-STATE FUEL PERFORMANCE CODE*11/29/76*G A BERNA* AEROJET NUCLEAR COMPANY
  RUN DATE IS -  12/18/76                            MAT PRO MODULE MOD007                                                 PAGE   7
XXXXXXXXXXXXXXXXXXXXXXXXXXXXXXXXXXXXXXXXXXXXXXXXXXXXXXXXXXXXXXXXXXXXXXXXXXXXXXXXXXXXXXXXXXXXXXXXXXXXXXXXXXXXXXXXXXXXXXXXXXXXXXXXXX
 XXXXXXXXXXXXXXXXXXXXXXXXX  AXIAL INCREMENT   4  XXXXXXXXXX  POWER LEVEL  1  XXXXXXXXXX  GAS ITERATION  2  XXXXXXXXXXXXXXXXXXXXX

    START STEP AT     .00 HOURS            17. SECONDS     END STEP AT       .90 HOURS      3240. SECONDS
    POWER DURING STEP  6.883 KW/FT    22581.7 W/M        HEAT FLUX DURING STEP  212579.99 BTU/HR-FT2        .12053E+07 W/M**2
    FLUX DEPRESSION FACTOR  .7032
    BURNUP AT START OF STEP      .00 MWD/MTU     .1234E-02 MWS/KG   BURNUP DURING STEP      1.39 MWD/MTU  .1204E+03 MWS/KG

 XXXXXXXXXXXXXXXXXXXXXXXXXXXXXXXXXXXXXXXXXXXXXXXXXXXXXXX  COOLANT CONDITIONS  XXXXXXXXXXXXXXXXXXXXXXXXXXXXXXXXXXXXXXXXXXXXXXXXX
    INLET TEMP. 642.00 (F)     BULK TEMP.  652.75 (F)    AVERAGE BULK TEMP.  652.75 (F)       COOLANT DENSITY   37.77 (LB/FT3)
                612.04 (K)                 618.01 (K)                        618.01 (K)                         505.1 (KG/M**3)

 XXXXXXXXXXXXXXXXXXXXXXXXXXXXXXXXXXXXXXXXXXXXXX FILM,CRUD AND OXIDE CONDITIONS  XXXXXXXXXXXXXXXXXXXXXXXXXXXXXXXXXXXXXXXXXXXXXXX
         DITTUS-BOELTER FILM COEF.  3267.33 (BTU/HR-FT2-F)  FORCED CONVECTION FILM COEF.   2115.38 (BTU/HR-FT2-F)
                                 .18540E+05 (W/M**2-K)                                   .12004E+05(W/M**2-K)
         DITTUS-BOELTER TEMP. DROP  65.06 (F)    36.15 (K)  FORCED CONVECTION TEMP. DROP  100.49 (F)  55.83 (K)
         JENS-LOTTES TEMP. DROP      3.35 (F)     1.86 (K)
         CRUD THICKNESS  1.0000 (MILS)    .2540E-04 (M)      CRUD TEMPERATURE DROP ,  35.43 (F)   19.68 (K)
  ZR-OXIDE...  SURFACE TEMP.  691.53 (F)   639.55 (K) , THICKNESS  .0000071 (IN)  .1809E-06 (M) , WEIGHT GAIN     2.64 (MGMS/DM2)
         HYDROGEN  2.94 (PPM)     TEMP. DROP .10812 (F)    .0600678 (K)

 XXXXXXXXXXXXXXXXXXXXXXXXXXXXXXXXXXXXXXXXXXXXXXXXXXX CLAD CONDITIONS  XXXXXXXXXXXXXXXXXXXXXXXXXXXXXXXXXXXXXXXXXXXXXXXXXXXXXXXX
  INSIDE DIAM. .37436 (IN)    .0095087 (M)                    VOLUME  .4427 (CU.IN.)       .7255E-05 (CU.M.)
  O.D. TEMP.  691.64 (F)  639.61 (K)          AVG. TEMP.  714.48 (F)  652.30 (K)            I.D. TEMP.  737.32 (F) 664.99 (K)
       HOOP: STRESS -14037. (PSIA)        AXIAL: STRESS  -7738. (PSIA)        RADIAL: STRESS        0.  (PSIA)
                -.96784E+08(N/M**2)                 -.53698E+08 (N/M**2)                    0.          (N/M**2)
             STRAIN  .1077 (PCT)                STRAIN  .1823 (PCT)                 STRAIN       .2675 (PCT)
  BOS EFFECTIVE CREEP STRAIN  0.           AXIAL NODE LENGTH  4.0000 (IN)  .101601 (M)     AXIAL GAP  0.0000 (IN) 0.000000 (M)

 XXXXXXXXXXXXXXXXXXXXXXXXXXXXXXXXXXXXXXXXXXXXXXXXXXX  GAP CONDITIONS  XXXXXXXXXXXXXXXXXXXXXXXXXXXXXXXXXXXXXXXXXXXXXXXXXXXXXXXXX
 DIAMETRAL GAP  5.9242 (MIL) CONDUCTANCE,  2641.(BTU/HR-FT2-F)  AVG. TEMP.  782.93 (F) TEMP. DROP  91.17 (F) VOLUME  .0140IN**3
             .15048E-03 (M)               14985.(W/M**2-K)                  690.33 (K)             50.65 (K)     .2295E-06 M**3
         CONTACT PRESSURE    0.(PSIA)   0.          (N/M**2) GAS CONDUCTIVITY =       .151 (BTU/HR-FT-F)         .262 (W/M-K)

 XXXXXXXXXXXXXXXXXXXXXXXXXXXXXXXXXXXXXXXXXXXXXXXXXXXX  FUEL CONDITIONS  XXXXXXXXXXXXXXXXXXXXXXXXXXXXXXXXXXXXXXXXXXXXXXXXXXXXXXX
 OUTSIDE DIAM.  .36843 (IN)   .009358 (M)                   SURFACE TEMP.  828.49 (F)       715.64 (K)
    STORED ENERGY AT TAVE = 1268.43 (F)  960.05 (K)  IS      77.10 (BTU/LB)        42.84 (CAL/GM)

     RING RADIUS             TEMPERATURE             EXPANSION        SWELLING        POROSITY     DENSIFICATION     GRAIN SIZE
    (IN)       (M)          (F)      (K)               (PCT)            (PCT)          (PCT)           (PCT)         (MICRONS)
0.000000     0.000000     1761.21  1233.82           0.000000           0.00000        0.0000          0.000000           5.00
 .058358      .001482     1652.64  1173.50            .844259           0.00000        2.1667          0.000000           5.00
 .082514      .002096     1547.76  1115.24            .772901           0.00000        2.1667          0.000000           5.00
 .101037      .002566     1446.43  1058.94            .705886           0.00000        2.1667          0.000000           5.00
 .116643      .002963     1348.53  1004.56            .642922           0.00000        2.1667          0.000000           5.00
 .130384      .003312     1253.98   952.03            .583753           0.00000        2.1667          0.000000           5.00
 .142800      .003627     1162.68   901.30            .528145           0.00000        2.1667          0.000000           5.00
 .154211      .003917     1074.56   852.35            .475880           0.00000        2.1667          0.000000           5.00
 .164828      .004187      989.54   805.12            .426755           0.00000        2.1667          0.000000           5.00
 .174794      .004440      907.54   759.56            .380583           0.00000        2.1667          0.000000           5.00
 .184217      .004679      828.49   715.64            .337184           0.00000        2.1667          0.000000           5.00
 VOLUMES,(CU.IN.) ... FUEL    .4245   DISH    .0042    CRACK    .0009   OPEN POROSITY  .0008
         (CU.M. ) ...     .6957E-05        .6817E-07        .1393E-07                 .1243E-07
 NITROGEN CONCENTRATION  .36558E-04 (MOLES)
  RADIUS OF COLUMNAR GRAIN ZONE = 0.000000 (IN)  0.000000 (M)     THRESHOLD TEMP. =3391.2 (F) 2139.4 (K)
  COLUMNAR GRAIN ZONE DENSITY =   .935
```

TABLE B-III (continued)

```
                FRAP-S MOD 002  VERS 02J* STEADY-STATE FUEL PERFORMANCE CODE*11/29/76*G A BERNA* AEROJET NUCLEAR COMPANY
 RUN DATE IS -  12/18/76                                    MAT PRO MODULE MODC07                                                   PAGE  23
XXXXXXXXXXXXXXXXXXXXXXXXXXXXXXXXXXXXXXXXXXXXXXXXXXXXXXXXXXXXXXXXXXXXXXXXXXXXXXXXXXXXXXXXXXXXXXXXXXXXXXXXXXXXXXXXXXXXXXXXXXXXXXXXXXXXXXX
   XXXXXXXXXXXXXXXXXXXXXXXXX     POWER LEVEL   2     XXXXXXXXXXXXXXXXXXXXXXXXX     AXIAL SHAPE NUMBER  1     XXXXXXXXXXXXXXXXXXXX

 BURNUP TO END OF STEP     22. (MWD/MTU)      BURNUP DURING STEP        21.  (MWD/MTU)      ROD AVERAGE HEAT FLUX 308927. (BTU/HR-FT2)
                     .18662E+04.(MWS/KG)                        .17787E+04 (MWS/KG)                                .17530E+07 (W/M)
RAD. + AX. CLAD AVG TEMP   741.35 (F)   667.23 (K) CLAD VOL    .2541 CU.IN.    .416E-05 CU.M. POROS VOL    .0153 CU.IN.   .2525E-06 CU.M.
RAD. + AX. GAP  AVG TEMP   833.73 (F)   718.56 (K) GAP VOL     .1005 CU.IN.    .163E-05 CU.M. DISH VOL     .0374 CU.IN.   .6123E-06 CU.M.
RAD. + AX. FUEL AVG TEMP 1627.82 (F) 1159.72 (K) FUEL VOL   3.8577 CU.IN.    .632E-04 CU.M. ROUGH VOL    .0072 CU.IN.   .1172E-06 CU.M.
AVG. FUEL SURFACE TEMP.    893.14 (F)   751.56 (K) CRACK VOL   .0160 CU.IN.    .263E-06 CU.M.
STACK HEIGHT     36.276 (IN)      .9214 (M)    PCT. INCREASE    .7675      ROD LENGTH    35.070 (IN)      .9162 (M) PCT. INCREASE    .1939

   NITROGEN CONCENTRATION    .28155E-03 (MOLES)  HELIUM PRODUCTION     .16115E-06 (MOLES)  FISSION GAS PRODUCTION    .16115E-04 (MOLES)

   GASES RELEASED --               WATER                       NITROGEN                     HELIUM                   FISSION
                   (MOLES)     0.                             .54256E-04                   .28644E-07               .10312E-05
                (FRACTION)     0.                             .16157E+00                   .17775E+00               .63991E-01

   XXXXXXXXXXXXXXXXXXXXXXXXXXXXXXXXXXXXXXXXXXXXXX    MOLE FRACTIONS OF GAS    XXXXXXXXXXXXXXXXXXXXXXXXXXXXXXXXXXXXXXXXXXXXXX

                   AIR         0.                     HYDROGEN    0.                      WATER          0.
                   ARGON       0.                     HELIUM       .99055E+00             NITROGEN        .92771E-02
                   KRYPTON      .26449E-04            XENON        .14988E-03             FISSION         .17632E-03

   CUMULATIVE QUANTITY OF GAS IN GAP      .58484E-02 (MOLES)

  PLENUM LENGTH                   1.8116 (IN)    .04602 (M)               PLENUM VOLUME                          .1785 CU.IN.      .2925E-05 CU.M.
  GRASHOFF NUMBER OF PLENUM      10011.46                                 HEAT FLOW FROM TOP OF STACK          4.0131 (BTU/HR)     .1175E+01 (W)
  HEAT GENERATED IN SPRING        4.3303 (BTU/HR)   .1268E+01 (W)         PLENUM TEMPERATURE                  695.20 (F)   641.59 (K)
  COOLANT SATURATION TEMP.        652.75 (F)   618.01 (K)                 TOTAL HOT VOID VOLUME                  .3549 CU.IN.      .5815E-05 CU.M.
INTERNAL PRESSURE = (GASMOL)(40.8) /((HPV / TPLEN +460.)    +    SUMDH    +    SUMGP    +    SUMCK    +    SUMRG    +    SUMPOR)
                     .0058484          .1785     695.               .0000185     .0000786     .0000116     .0000057     .0000068       =    865.79

                CLADDING TEMP. IN DEG F  , STRESSES + INTERFACIAL PRESSURE IN PSIA   , + RADIAL GAP IN INCHES
XXXXXXXXXXXXXX  CLAD TEMP., AXIAL - HOOP STRESS,STRAIN,+ PLASTIC STRAIN, GAP WIDTH, AND INTERFACIAL PRESSURE  XXXXXXXXXXXXXX
     J      T CLAD        SIG HOOP        SIG AXIAL        EPS HOOP        EPS AXIAL      EPF HOOP        EPP AXIAL           GAP         PINT
     1    .71784E+03    -.13022E+05    -.73114E+04     .11740E-02     .18551E-02     0.              0.                .24658E-02     0.
     2    .74577E+03    -.13022E+05    -.73114E+04     .13079E-02     .19539E-02     0.              0.                .18634E-02     0.
     3    .76651E+03    -.13022E+05    -.73114E+04     .14099E-02     .20286E-02     0.              0.                .12943E-02     0.
     4    .77280E+03    -.13022E+05    -.73114E+04     .14413E-02     .20516E-02     0.              0.                .11124E-02     0.
     5    .76893E+03    -.13022E+05    -.73114E+04     .14220E-02     .20374E-02     0.              0.                .12246E-02     0.
     6    .75579E+03    -.13022E+05    -.73114E+04     .13568E-02     .19896E-02     0.              0.                .15997E-02     0.
     7    .73593E+03    -.13022E+05    -.73114E+04     .12604E-02     .19190E-02     0.              0.                .20974E-02     0.
     8    .71421E+03    -.13022E+05    -.73114E+04     .11568E-02     .18423E-02     0.              0.                .25309E-02     0.
     9    .69433E+03    -.13022E+05    -.73114E+04     .10636E-02     .17722E-02     0.              0.                .28403E-02     0.
```

TABLE B-III (continued)

```
                FRAP-S MOD 002  VERS 02J* STEADY-STATE FUEL PERFORMANCE CODE*11/29/76*G A BERNA* AEROJET NUCLEAR COMPANY
  RUN DATE IS -  12/18/76                                   MAT PRO MODULE MOD007                                                PAGE  24
XXXXXXXXXXXXXXXXXXXXXXXXXXXXXXXXXXXXXXXXXXXXXXXXXXXXXXXXXXXXXXXXXXXXXXXXXXXXXXXXXXXXXXXXXXXXXXXXXXXXXXXXXXXXXXXXXXXXXXXXXXXXXXXXXXXX

                 CLADDING TEMP. IN DEG F  , STRESSES + INTERFACIAL PRESSURE IN PSIA   , + RADIAL GAP IN INCHES
XXXXXXXXXXXXXX  CLAD TEMP., AXIAL + HOOP STRESS,STRAIN,+ PLASTIC STRAIN, GAP WIDTH, AND INTERFACIAL PRESSURE  XXXXXXXXXXXXXX

    J      T CLAD        SIG HOOP       SIG AXIAL        EPS HOOP        EPS AXIAL       EPP HOOP        EPP AXIAL          GAP           PINT
    1   .71784E+03    -.13022E+05    -.73114E+04     .92372E-03     .18337E-02    -.25025E-03    -.21380E-04     .24128E-02    0.
    2   .74577E+03    -.13022E+05    -.73114E+04     .95050E-03     .19234E-02    -.35743E-03    -.30536E-04     .17876E-02    0.
    3   .76651E+03    -.13022E+05    -.73114E+04     .94905E-03     .19893E-02    -.46090E-03    -.39375E-04     .11965E-02    0.
    4   .77280E+03    -.13022E+05    -.73114E+04     .94432E-03     .20091E-02    -.49700E-03    -.42460E-04     .10070E-02    0.
    5   .76893E+03    -.13022E+05    -.73114E+04     .94749E-03     .19969E-02    -.47447E-03    -.40535E-04     .11240E-02    0.
    6   .75579E+03    -.13022E+05    -.73114E+04     .95223E-03     .19551E-02    -.40457E-03    -.34563E-04     .15139E-02    0.
    7   .73593E+03    -.13022E+05    -.73114E+04     .94454E-03     .18920E-02    -.31583E-03    -.25982E-04     .20304E-02    0.
    8   .71421E+03    -.13022E+05    -.73114E+04     .91816E-03     .18219E-02    -.23862E-03    -.20386E-04     .24803E-02    0.
    9   .69433E+03    -.13022E+05    -.73114E+04     .88070E-03     .17566E-02    -.18291E-03    -.15626E-04     .28015E-02    0.

       CHANGE IN CLADUING LENGTH =    .68713E-01    (IN)      LENGTH CHANGE RELATIVE TO THE FUEL CHANGE =  -.20757E+00 (IN)
                                      .17453E-02    (M)                                                    -.52724E-02 (M)
```

TABLE B-III (continued)

```
             FRAP-S MOD 002  VERS 02J* STEADY-STATE FUEL PERFORMANCE CODE*11/29/76*G A BERNA* AEROJET NUCLEAR COMPANY
  RUN DATE IS -  12/18/76                               MAT PRO MODULE MOD007                                                        PAGE  25
XXXXXXXXXXXXXXXXXXXXXXXXXXXXXXXXXXXXXXXXXXXXXXXXXXXXXXXXXXXXXXXXXXXXXXXXXXXXXXXXXXXXXXXXXXXXXXXXXXXXXXXXXXXXXXXXXXXXXXXXXXXXXXXXXXXXXX
                                             PBF SINGLE ROD  PCM-20
                                    **********  PEAK POWER INCREMENT OUTPUT **********

   TIME  BURNUP POWER  CLAD TEMP (F)   GAP    GAP  FUEL TEMP (F)  CONT.   CLAD STRESS  STRAIN FUEL OD   GAP    FGAS  ZRO2     H2
   HOURS MWD/TU KW/FT  OD.   AVG  ID.  MILS   (F)  OD.  AVG  CEN   PSI    HOOP  AXIAL   PCT    INCH    CONDCT  PSI   MIL     PPM
XXXXXXXX XXXXXX XXXXX XXXXXXXXXXXXXX XXXXXX XXXX XXXXXXXXXXXXXX XXXXX XXXXXXXXXXXXXXXXXXXXX XXXXXXX  XXXXXX  XXXX XXXXX  XXXXXX
 1     1.      1.  6.88 692. 714. 737.   5.92 783. 828.1268.1761.     0. -14037. -7788.  .1077  .36843   2641.  736.    .01     2.9
 2    10.     30. 13.77 728. 773. 817.   3.14 892. 967.2057.3366.     0. -13022. -7311.  .1441  .37135   3247.  866.    .02     7.2
```

TABLE B-III (continued)

```
            FRAP-S MOD 002  VERS 02J* STEADY-STATE FUEL PERFORMANCE CODE*11/29/76*G A BERNA* AEROJET NUCLEAR COMPANY
  RUN DATE IS -  12/18/76                               MAT PRO MODULE MOD007                                                 PAGE  26
XXXXXXXXXXXXXXXXXXXXXXXXXXXXXXXXXXXXXXXXXXXXXXXXXXXXXXXXXXXXXXXXXXXXXXXXXXXXXXXXXXXXXXXXXXXXXXXXXXXXXXXXXXXXXXXXXXXXXXXXXXXXXXXXXXXX

                END OF LIFE STRAIN RANGE (PCT) =     .0751

                FISSION GAS CUMULATIVE FRACTION RELEASE =  .063991

                ZRO2 WEIGHT GAIN , (MG/DM2) =    6.48
```

THIS PAGE

WAS INTENTIONALLY

LEFT BLANK

APPENDIX C

FRAP-S LINK TO FRAP-T

THIS PAGE

WAS INTENTIONALLY

LEFT BLANK

APPENDIX C

FRAP-S LINK TO FRAP-T

A sample problem is presented to show the use of FRAP-S2 results as initial conditions for the transient accident analysis code FRAP-T2.

A typical PWR fuel rod is modeled for FRAP-S2 and an analysis is made for a 2000 hour burnup on the rod. At 2000 hours, the rod is subjected to a full-size break loss-of-coolant accident (LOCA).

Table C-I contains pertinent data on the rod. Figure C-1 shows the response of the fuel rod for the two time scales defining long-term operational behavior and short-term accident response.

The discontinuities evident in Figure C-1 at the transition between normal and accident conditions are due to slight differences in similar models of versions of FRAP-S and FRAP-T. Most of these differences have been removed as part of the continuing development effort of versions of FRAP-S and FRAP-T.

This link capability allows the user to initiate accidents at any time during the operating cycle of a reactor and use a realistic set of initial conditions as input for the accident analysis code.

TABLE C-I

FRAP-S LINK TO FRAP-T EXAMPLE PROBLEM SPECIFICATIONS

(PWR UO_2 ENRICHED)

Coolant Conditions:

mass flux	1.917×10^6 (lbm/ft-ft^2)
pressure	2273 (psia)
inlet temperature	540 (°F)
hydraulic diameter	0.534 (in.)

Rod Geometry:

fuel stack length	12 (ft)
fuel outside diameter	0.366 (in.)
cladding outside diameter	0.422 (in.)
plenum length	7.0 (in.)

Rod Initial Conditions:

internal pressure	600 (psia)
enrichment	3 (%)
density	93.288% theoretical

Power History:

linear ramp from 0.0 kW/ft to 11.08 kW/ft in 50 hours, then held for the remainder of 2000 hours

---

EARLY LINK RESULTS

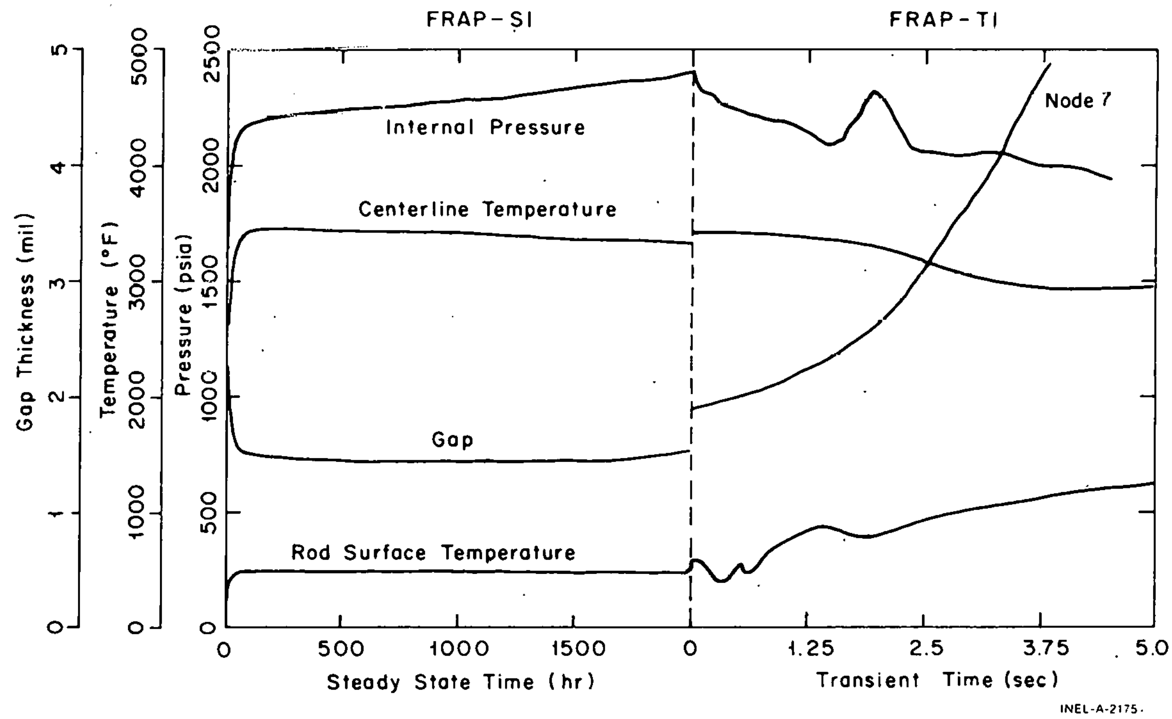

Fig. C-1 Early link results.

THIS PAGE
WAS INTENTIONALLY
LEFT BLANK

APPENDIX D

CONFIGURATION CONTROL PROCEDURE

THIS PAGE

WAS INTENTIONALLY

LEFT BLANK

APPENDIX D

CONFIGURATION CONTROL PROCEDURE

A Configuration Control Procedure (CCP) has been defined to maintain a traceability of results from developing computer codes. During the development process of a computer code, requirements exist for using the code for generating both checkout results and production results, depending on the stage of development.

The Configuration Control Procedure consists of a method by which changes can be made to the code and traceability of results maintained. Any time a modification to the code is made, the following data are taken:

(1) Version of code to which modification was made
(2) Reason for modification
(3) Results affected by modification
(4) Date of modification
(5) Person responsible for modification
(6) The change cards used to modify the original version of the code.

A tape update routine is used to modify the code. This routine requires only those computer cards defining new statements or deleting old statements. These "change cards" are kept on file so any version of the code can be reproduced if necessary.

A new identification number is assigned to the modified version of the code and this new number is programmed into the code where it will be listed at the top of each page of output and on each plot produced by the code.

THIS PAGE

WAS INTENTIONALLY

LEFT BLANK

APPENDIX E

MATERIALS PROPERTIES CORRELATIONS EMPLOYED BY FRAP-S2

THIS PAGE

WAS INTENTIONALLY

LEFT BLANK

APPENDIX E

MATERIALS PROPERTIES CORRELATIONS EMPLOYED BY FRAP-S2

A materials properties subcode is used to provide the computational subcodes of FRAP-S2 with gas, fuel, and cladding properties. Table E-I lists those properties from one of the two references which are used by FRAP-S2 given below.

1. P. E. MacDonald et al, MATPRO - A Handbook of Materials Properties for Use in the Analysis of Light Water Reactor Fuel Rod Behavior, ANCR-1263 (February 1976).

2. P. E. MacDonald et al, MATPRO - Version 09 - A Handbook of Materials Properties for Use in the Analysis of Light Water Reactor Fuel Rod Behavior, TREE-NUREG-1005 (December 1976).

TABLE E-I

PROPERTIES INCLUDED IN MATPRO USED BY FRAP-S2

Property	Subcode	Reference
Fuel Material Properties		
1. Specific Heat Capacity	FCP	2
2. Thermal Conductivity	FTHCON	2
3. Emissivity	FEMISS	2
4. Thermal Expansion	FTHEXP	2
5. Creep Rate	FCREEP	2
6. Densification	FUDENS	2
7. Restructuring	FRESTR	2
Cladding Material Properties		
1. Axial Growth	CAGROW	2
2. Thermal Conductivity and Its Uncertainty	CTHCON	2
3. Zr-Oxide Thermal Conductivity	ZOTCON	2
4. Axial Thermal Expansion	CATHEX	2
5. Diametral Thermal Expansion	CDTHEX	2
6. Elastic Modulus	CELMOD	2
7. Strain versus Stress	CSTRAN	1
8. Stress versus Strain	CSTRES	1
9. Poisson'a Ratio	CPOIR	2
10. Meyer Hardness	CMHARD	2
Gas and Fuel Rod Material Properties		
1. Gas Thermal Conductivity	GTHCON	2
2. Gas Viscosity	GVISCO	2
3. Gap Heat Transfer	GAPHTR	2
4. Physical Properties	PHYPRO	2

REPORT II

REPORT II

FRAP-S2 MODEL VERIFICATION

Dennis R. Coleman
E. Tom Laats

ACKNOWLEDGMENTS

Acknowledgment is given to N. L. Hampton and N. R. Scofield for assistance in data processing and report preparation. Acknowledgment is given also to G. A. Berna for providing model development support.

CONTENTS

FIGURES

TABLES

FRAP-S2: A COMPUTER CODE FOR THE STEADY STATE ANALYSIS OF OXIDE FUEL RODS

REPORT II -- FRAP-S2 -- MODEL VERIFICATION

I. SUMMARY AND CONCLUSIONS

Results for several types of data comparisons as well as typical design analyses are reported to evaluate capabilities of FRAP-S2[1][a]. The model comprises a revised version of a steady state Fuel Rod Analysis Program under development as a supporting tool for reactor safety analysis. Primary application is in supplying initial conditions for the transient response model, FRAP-T[2].

Comparisons between code predictions and experimental results were made for general categories of fuel behavior relating to rod thermal, pressure, deformation, and surface conditions. Results indicate that FRAP-S2 is most applicable to analysis of moderate operating conditions more associated with core average rods as opposed to lead power rods. It is felt that the verification effort described in this document will contribute to a broader physical basis for the model and a more extended range of applicability. Specific results are summarized in the following paragraphs.

1. ANALYTICAL COMPARISON

Standard Design Runs for core average rod pressurized water reactor (PWR) and boiling water reactor (BWR) conditions provided a basis for comparisons between FRAP-S2 and FRAP-S1[3]. Use of lower cladding creep rates, together with consideration of fuel densification, contributed to

---

[a] MOD 002 Version 002 MATPRO MOD 007.

FRAP-S2 obtaining lower cladding strain and higher fuel temperature, gas release, rod internal pressure, and gap size compared with FRAP-S1. FRAP-S2 predicts the same amounts of cladding corrosion and hydrogen uptake when compared with FRAP-S1. Based on physical expectations and interpretation of data comparison results, the higher fuel temperature obtained by FRAP-S2 is felt to be justifiable for pressurized rods and somewhat conservative for unpressurized rods.

2. DATA COMPARISON

2.1 Thermal

Comparing measured and predicted fuel central temperature showed that FRAP-S2 generally overestimates the effects of power and burnup for the unpressurized rods by between 10 and 30% up to 2000°C. The fact that fuel temperature was at the same time underpredicted for 6 out of 8 helium prepressurized rods indicates that calculated influence of effective gas conductivity on heat transfer remains too strong. A corollary to this result would indicate some tendency to underestimate fuel cracking. Consistent gas composition trends were identified in results of gap conductance comparisons. Better representation of contact gap conductance by the model supports the overall evidence that gap closure mechanics remains a key modeling limitation. Relative thermal model agreement versus gap size and fuel density indicates that fuel cracking may be underpredicted for moderate gaps (1 to 2%) and at low fuel densities ($\leq$93%). Extent of incipient fuel melting (<30% fractional radius) is overestimated by the model due to built-in coarse nodalization. Larger melt radii results again show better model capability for closed gap conditions.

2.2 Pressure

Consistent with FRAP-S1[3] verification results, fission gas release data comparisons continue to suggest the need for some mechanistic treatment of gas disposition effects on release probability. The assumption of instantaneous release kinetics causes the gas release fraction to be overpredicted by a factor of 2 to 20 for moderate burnup (<15,000 MWd/t) load follow conditions, especially if fuel temperatures in the range of highest release sensitivity (1400 to 2400°C) are calculated. Results indicate that the assumption of purely temperature dependent gas release used by the model is better applied at the higher burnups (>25,000 MWd/t) associated with buildup of interconnected fuel porosity. The steady state fuel heatup effect on rod internal pressure is better represented for rods with relatively large plenum volume fraction (>4%). Prior to occurrence of significant fission gas release, calculated pressure is within ±20% of the data up to 2200 psia. Pressure overprediction for burnup rods with plenums corresponds to a combination of overpredicting both fuel temperature and instantaneous fission gas release. Pressure underprediction for burnup rods without plenums is more governed by the assumption that fuel surface temperature applies to active length void volumes.

2.3 Deformation

Fuel stack axial expansion during steady state heatup is better represented by the model at fuel temperatures below those associated with the onset of pellet-cladding mechanical interaction (PCMI) (1000 to 1300°C) and initiation of fuel plastic deformation (1500 to 1700°C). Calculated axial fuel stack expansion is within 50% of the data. Stack shortening for rods accumulating burnup is underestimated by 20 to 80% for cases exhibiting PCMI in addition to fuel densification. For rods operated without extended PCMI, data comparison agreement for cladding collapse is dominated by measurement scatter, lower calculated creep rate, and the tendency to overpredict gas release. The generally observed underprediction of cladding permanent axial and circumferential deformation by 20 to 120% corresponds to underprediction of the extent of PCMI using an annular gap closure assumption. Once gap closure was calculated, cladding deformation was overpredicted by a factor of 1.5 to 4. This overprediction is associated with lack of fuel mechanical deformation, particularly at fuel temperature >1800°C.

2.4 Surface Condition

Comparing measured and predicted cladding surface corrosion and hydrogen concentration shows better agreement at cladding temperatures above 360°C. Otherwise, corrosion and hydrogen uptake are generally underpredicted by 10 to 30%. Review of currently used factors adjusting laboratory correlations for either PWR or BWR irradiation conditions seems warranted.

II. INTRODUCTION

FRAP-S2 is the second version of a steady state fuel rod analysis program. The program has been under development as part of an overall fuel behavior modeling effort in support of reactor safety analysis. The purpose of this report is to document the extent of current predictive capability in key modeling areas. Diagnosis of model performance over a range of fuel design and operating conditions is intended to identify areas of less model applicability and support further development. Other volumes describing analytical models[1] and material properties[4] have been prepared by the code developers.

The computer program itself is structured in modular form and is coupled to fuel, cladding, and gas material properties supplied by MATPRO[4]. Submodels account for surface heat transfer and corrosion, rod power and temperature distribution, sorbed and fission gas release, gas volume and temperature, fuel swelling and densification, fuel and cladding thermal expansion, and uniform cladding deformation due to creep, yield, and elastic strain. Key input to this single rod analysis code is the fuel design, system operating condition, and axial power distribution. The models are then driven by the input rod average power history. Results for the input number of rod axial segments are integrated to obtain fission gas composition, length, and void volume conditions. Unless sustained gap closure and high fuel temperature are coincident, running time and convergence are usually not limiting considerations. The program description is given in more detail elsewhere[1].

FRAP-S is intended to be a realistic analytical tool for extended burnup application. The original core of the model was used previously in industry for steady state fuel rod design analysis. A major purpose for FRAP-S now, is in supplying the transient fuel rod analysis model (FRAP-T) with initial conditions reflecting operation prior to hypothetical transients.

Importance of the steady state analysis in conjunction with FRAP-T should not be underemphasized. Feedback among cumulative burnup effects causes initial conditions for all but initial startup transients to differ considerably from beginning-of-life conditions. Main outputs of the model expected to impact transients are those which characterize initial rod temperature distribution, gap size, gas composition, rod internal void volume, gas content, clad strain accumulation, and rod surface conditions. Results of many fuel irradiations, during which these parameters were investigated, indicate that the range of foreseeable preaccident conditions is large, varying with both burnup and operating history. The number of possible output connections from FRAP-S to FRAP-T is also large due to the variety of models involved. The relative importance in different accident analyses of adequately modeling any one of the observed steady state mechanisms cannot be minimized at this stage. For this reason, different types of steady state analyses were performed in order to maximize characterization and interpretation of results.

Supporting runs were used to debug the code and evaluate the effect of changes in the model with respect to the previously documented version, FRAP-S1[3]. The main type of supporting run discussed here falls into the category of Standard Design Analyses. Input rod design and operating condition parameters for these runs are meant to benchmark full-scale application of the program to power reactor fuel from startup through end-of-life.

Several types of data comparisons were then performed to evaluate overall capabilities of the program as a predictive tool. The emphasis was necessarily placed on the ability of the code to track rod temperature, burnup mechanisms, and related dimensional effects as a function of rod operating history.

Even though large numbers of rods are more likely to represent typical fuel behavior variation in a large core, problems having to do with data scatter, volume of information processing, and result interpretation were increased by the large sample approach. A quantitative interpretation of data comparison results has not been attempted due to lack of either a basic physical model in some cases or a large enough data base in others. Trends in the relative agreement between measured and predicted comparison values can be related, however, to design and operating parameters which should have first order significance like gap size, fuel density, heat rating, burnup, and fuel temperature. These trends provide the basis for identifying, and in some cases, diagnosing lack of fit in the basic physical model.

For the most part, the relatively large number of data comparison rods considered (~400) precludes treatment of individual cases in this volume. In order to interpret FRAP-S2 results, the assumption is made throughout that the fuel rod data are explainable on the basis of parameters describing design configuration and operating conditions. Influence of fabrication parameters not considered by the model is assumed to only cause scatter in the data and not determine overall trends in data comparison results.

III. VERIFICATION RESULTS

Table I shows key predictive areas for the code and the corresponding output parameters where good performance of the models is most likely to be required. Two categories of analyses, the results of which are discussed in this section, were conducted to evaluate FRAP-S2 performance in these areas. Letters A and D indicate which modeling areas are addressed respectively by supporting analytical runs and data comparison runs. Asterisks identify data comparison indices planned for application to large sample data handling techniques now in preliminary stages of development.

Presently, the main criterion used to demonstrate adequate performance of the basic physical models is that these models be able to describe the mean measurement response over typical ranges of steady state operating conditions such as power or burnup. The fact that code capability requirements extend over different modeling areas in FRAP-S2 is based on the different feedbacks, indicated by Table II, which are expected to occur between initial conditions and off normal response.

TABLE I

FRAP-S2 COMPARATIVE PHYSICAL EFFECTS

Output Category	Output Variable	Run Series	
Rod Temperature Distribution	Fuel Center Temperature *	A	D
	Fuel Melt Radius	---	D
	Cladding Temperature	A	---
	Gap Conductance *	A	D
	Power Distribution	---	---
Cladding Stress	Rod Internal Pressure *	A	D
	Gas Content *	A	---
	Gas Composition *	A	---
	Gas Release Fraction *	A	D
	Void Volumes *	A	---
Rod Elastic Deformation	Differential Thermal Expansion *	---	D
	Cladding Pressure Deflection	A	---
Rod Permanent Deformation	Fuel Swelling *	A	D
	Stack Shortening *	A	D
	Cladding Creep *	A	D
	Cladding Yield *	---	D
Cladding Surface Condition/ Impurity Effects	Corrosion *	A	D
	Crud Buildup	---	---
	H_2 Concentration *	A	D

A Standard Design Study

D Data Comparison Study

* Potential Data Storage Application.

TABLE II

IMPACT OF FRAPS-S OUTPUT ON TRANSIENT FUEL BEHAVIOR ANALYSIS

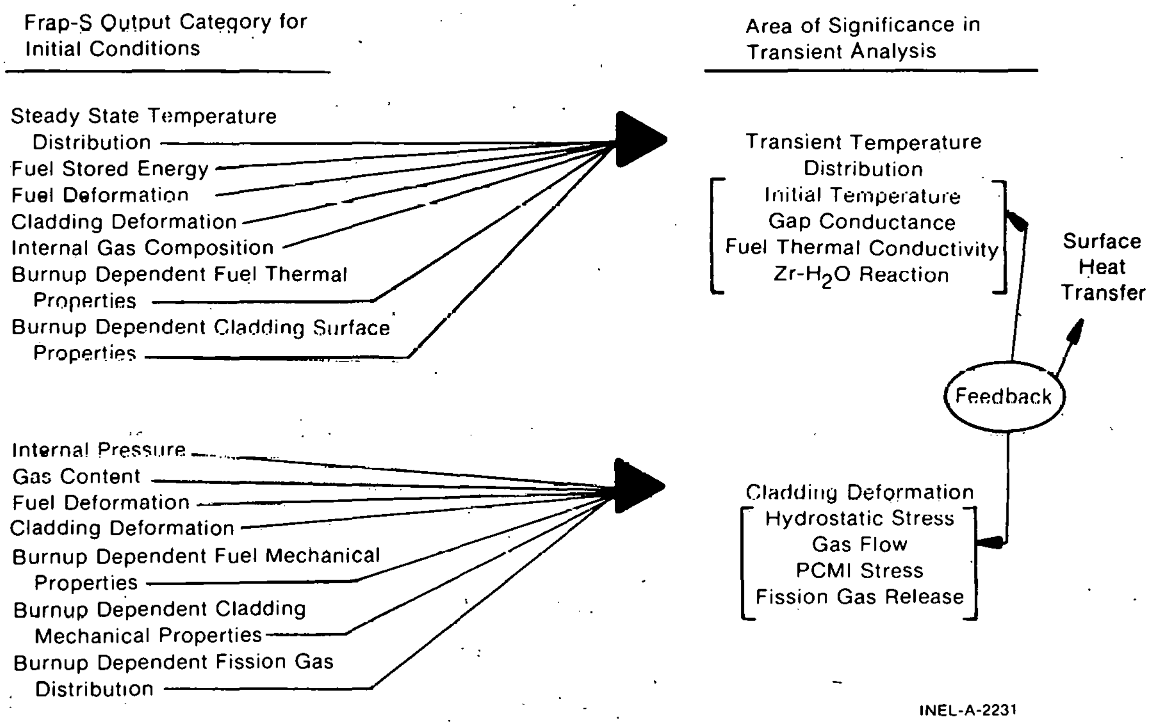

1. INPUT

For simplicity, nominal input data and references for all verification runs have been summarized in Table III. Typical values were assumed whenever full input details were not given in the reference material. Verification data processing development includes provisions for cataloging design and operating conditions on the basis of simplified code input requirements.

TABLE III

FRAP-S2 MODEL VERIFICATION -- RUN IDENTIFICATION AND NOMINAL INPUT

Run Number	Reference	Number Rods	Clad ID[a] (in.)	Diametral Gap (mils)	Fuel Density (%)	Enrichment (%)	Fill Gas[b] (psia)	Cold Plenum (in.)	Dish (%)	Fuel Length (ft)	Loop Pressure (psia)	Mass Flow (10^6lb/hr-ft^2)	Inlet Temperature (ft)	Peak Power (kW/ft)	Peak/Average (axial)	Operating Hours	Output
Standard Design Study																	
46	7 x 7	1	0.4990	12.0	94.0	2.2	15	16.0	0.0	12.0	1035	1.3	533	10.3[c]	1.4	32,000	Standard[d]
47	8 x 8	1	0.4250	9.0	95.0	2.2	15	12.0	0.0	12.3	1055	1.3	533	8.7[c]	1.4	32,000	Standard[d]
48	15 x 15	1	0.3740	7.5	94.0	2.8	345	6.8	1.5	12.0	2250	2.5	552	9.8[c]	1.4	21,000	Standard[d]
49	17 x 17	1	0.3290	6.5	95.0	2.6	300	6.3	1.5	11.9	2250	2.5	552	7.6[c]	1.4	21,000	Standard[d]
Data Comparison Study																	
1-6	HPR-80[5]	6	0.4957-0.4961	2.0-6.7	95.2-97.8	5.0	15	1.58	1.3	5.625	406	0.39	446	---	1.3	10, 4400	TC, hg
7-15	AECL-2588[6]	9	0.6701	6.7	97.1	2.75	15(Ar)	0.0098	0.0	0.230	100	0.0	127-318[e]	33.0-35.8	1.0[f]	0.25[f]	rm, ϵ_{cr}, hg
16-17, 19	AECL-2588[6]	3	0.6693	3.9	97.1	2.0	15(Ar)	0.0098	0.0	0.252	100	0.0	127-345[e]	33.0-39.5	1.0[f]	0.25[f]	rm, ϵ_{cr}, hg
18, 20	AECL-2588[6]	2	0.6693	3.9	97.1	2.0, 2.75	2(air)[f]	0.0098	0.0	0.252	100	0.0	127-345[e]	33.0-39.5	1.0[f]	0.25[f]	rm, ϵ_{cr}, hg
21, 22	AECL-2588[6]	2	0.7150	24.8	95.5, 96.1	1.5	15(Ar)	0.01	0.6	0.502	1100	2.4[f]	480	20.5, 22.0	1.0[f]	890, 640	rm, ϵ_{cr}, ϵ_{cx}, hg
23, 24	AECL-1464[7]	2	0.7510	4.0-4.5	96.7, 96.1	4.6	15(Ar)	0.006	0.6	0.506	1400	2.4[f]	480	37.1	1.0[f]	380	rm, ϵ_{cr}, hg
29, 30	AECL-4072[8]	2	0.7346	4.3	97.6, 95.8	1.4, 1.6	15	0.005	2.0	1.6, 1.2	1100	2.1	414	20.6, 20.2	1.0[f]	1810, 5.3	ϵ'_{cr}
31, 32	IFA-225[9]	2	0.4992	5.9	95.0	5.9	15	0.827	3.6, 0.0	1.736	485	0.35	463	22.6	1.2	2140	ϵ'_{cr}, ϵ'_{fx}
33-36	IFA-226[10]	4	0.3743-0.3746	7.9-9.9	91.6-95.9	7.3(U+Pu)	15	5.0-7.0	2.1	2.0-2.15	490	0.36	460, 467	12.0, 15.0	1.36, 1.07	4820	TC, P', ϵ'_{cx}
37-39	IFA-226[10]	3	0.3737-0.3741	3.6-7.8	94.5	7.3(U+Pu)	15	7.0-7.1	0.9	2.0	490	0.36	460	15.6	1.1	4820	ϵ'_{cx}
50-52	IFA-226[10]	3	0.3743-0.3746	8.2-8.4	90.6-95.1	7.3(U+Pu)	15	4.8-5.3	0.9	2.14-2.18	490	0.36	467	11.8	1.4	4820	P'
40	HPR-107[11]	1	0.4922	5.9	95.0	5.8	15	1.43	0.0	1.77	490	0.27	467	17.8	1.26	14	ϵ'_{fx}, ϵ_{cx}
41, 42	HPR-107[11]	2	0.4921	7.5	95.7	5.8	15	0.57	1.0, 0.0	1.76	490	0.33	467	15.8	1.26	14	ϵ'_{fx}
43-45	HPR-107[11]	3	0.5535	8.4	96.9, 91.3	6.0	15	0.39, 1.46	1.4	1.77	485	0.32	460	14.7-16.3	1.07	14	TC, ϵ'_{cx}
53	RISO-269[12]	1	0.6929(SS)	3.9	95.7	1.35	15	0.42	0.0	0.46	2000[f]	0.0	375-813[e]	14.1	1.0[f]	3830	TC
54, 55	RISO-415[13]	2	0.5043	7.1	94.0	1.45	15	1.14	2.2	1.64	1000	0.0	563[e]	20.8	1.2[f]	1692	TC
57, 59-60	IFA-223[14]	3	0.4988, 0.4992	5.9, 6.3	94.7	6.0	15	3.66	2.0, 0.0	1.98	490	0.36	467, 460	21.5, 23.8	1.4, 1.3	6450, 20	TC, ϵ'_{fx}, ϵ'_{cx}
58, 61	IFA-223[14]	2	0.4992, 0.4994	6.5, 6.3	94.7	6.0	15	3.66	2.0, 0.0	1.98	490	0.36	467, 460	21.5, 23.8	1.4, 1.3	20	ϵ'_{fx}, ϵ'_{cx}
62-64	WCAP-2923[15]	3	1.2745(SS)	24.5	95.0	0.6, 0.8	15	0.5	0.0	0.37	15[f]	0.0	150-290[e]	22.9, 25.7	1.0[f]	24, 30	TC, hg
65-69	IFA-130, 131[16]	5	0.5024-0.5035	5.9-12.3	90.0-94.0	6.0	15	1.69	0.0	1.52	485	0.39	464	19.4	1.5	20, 1500	TC
70, 71	IFA-132[16]	2	0.5512	9.9	94.7, 94.9	10.0	15	9.45	0.0	1.8	485	0.46	464	32.0, 40.3	1.5[f]	2740, 130	P', ϵ'_{cx}
72-87	B&W[17]	16	0.370	4.0, 8.0	93.5	3.0	15	1.62	0.0	0.24	0	0.0	650[e]	14.0-26.0	1.02-1.05	1800-18,000	ϵ_{cr}, GR, ϵ_{fx}
88-89	KWO[18]	2	0.3661	8.6	94.3	2.8, 3.1	15, 329	5.1, 9.1	1.5	9.0, 8.7	2360	2.5[f]	550	7.4[f]	1.4[f]	20,000	ϵ_{cr}, ϵ_{fx}
90-94	Saxton I[19]	5	0.3435	6.5	95.0	6.1-7.3	15(0.1N)	0.8	1.9	2.9-3.05	2000	2.8	515	4.2-8.4	1.32	1200-7800	ZrO_2, H_2
95-107	Saxton II[20]	13	0.3444	7.1	94.0	5.9(U+Pu)	15(0.1N)	0.8	1.9	3.05	2000, 2250	2.7	515, 480	8.4-18.3	1.32	2200-10,400	ϵ_{cr}, ϵ_{cx}, GR, ZrO_2, H_2
108-123	Saxton III[21]	16	0.3444	7.1	94.0	5.9(U+Pu)	15(0.1N)	0.8	1.9	3.05	2000, 2250	2.7	515, 480	7.2-24.3	1.32	12,600-18,000	ϵ_{cr}; ϵ_{cx}, GR, ZrO_2, H_2
124-152	HPR-132[22]	29	0.574-0.5745	5.1-9.5	95.9-97.0	7.0	15	1.86, 1.99	2.4	5.5	406	0.39-0.51	440	8.2-16.8	1.24	900-7700	ϵ_{cr}, ϵ_{cx}, GR, ZrO_2, H_2
153-204	AECL-1192[23]	52	0.669-0.672(SS)	3.0-17.0	96.2-97.6	4.0-4.9	15(Ar)	0.0-0.05	0.8, 0.0	0.23	100	0.0	126-355[e]	32.9-41.1	1,0	0.06-0.67	rm, ϵ_{cx}, ϵ_{cr}
205-212	AECL-1676[24]	8	0.7811	33.1	96.6	4.34	15(air)[f]	0.01	1.8	0.52	1407	0.0	126-324[e]	19.6-36.6	1.0-1.13	600	rm, ϵ_{cr}, ϵ_{cx}, GR ∼
213-217	AECL-1685[25]	5	0.8005-0.8044	4.0-8.0	93.1-95.0	1.85	15(Ar)	0.01-0.16	0.0	0.51-1.01	1421	0.0	100-177[e]	9.5-16.8	1.0	14,000	ϵ_{cr}, ϵ_{cx}, GR
219-221	AE-318[26]	3	0.5024, 0.4969	6.0-6.7	96.0-96.3	1.5-6.0	15	0.51-0.54	1.5, 0.0	2.6-5.6	406	0.3-0.48	440	9.3-18.8	1.28	500-1900	TC
218	GEAP-5100[27]	1	0.500	6.0	92.5	3.9	15	1.38	0.0	2.47	1200	1.2[f]	340	60.0	1.15	5000	rm
222-231	AECL-2588[6]	10	0.6654, 0.6693(SS)	6.0-7.9	95.3-95.7	4.0, 4.8	15(Ar)	0.0-0.02	0.0	0.23	100	0.0	127-345[e]	13.9-16.4	1.0	0.67	rm, hg, ϵ_{cr}, ϵ_{cx}
232-239	AECL-2230[28]	8	0.6497-0.6505	7.2-8.0	95.0-97.9	2.4	15(air)[f]	0.002	0.0	0.50	1180	2.4	480	16.6-17.4	1.0	2800	ϵ_{cr}, ϵ_{cx}, GR
240-250	AECL-2662[29]	11	0.7685(SS)	4.7	93.4-98.0	2.4	15(Ar)	0.004	0.0	0.80	995	2.4	410	17.2-24.9	1.07-1.15	3800	P', rm, GR, ϵ_{cr}, ϵ_{cx}
251-270	GEAP-4264[30]	20	0.5003-0.5103	4.3-8.9	94.8	1.5-3.8	15	2.1-7.5	---	2.46-2.85	1000	3.2-6.8	344	27.4-47.3	1.3-1.5	480-1560	rm, GR, ϵ_{cr}
273-275 277-278	PBF[31-35]	4	0.374	8.0	93.0, 94.0	20.0	550.0, 375.0	2.0	2.3	3.0	2080-2200	0.94-2.0	590, 620	19.9-24.9	1.35	10	TF, ϵ'_{cx}, P, hg', ZrO_2, ϵ_{cr}
276, 279-281	PBF[36,37]	3	0.346	9.9	92.0	9.5	380(He, Ar)	3.0	4.1	2.89	2160	0.61-2.6	540-620	19.2-20.3	1.32, 1.34	23, 33	TF, ϵ_{cx}, P, hg'
282-284	EPRI[38]	4	0.370	6.0	90.0-97.5	3.5, 3.9	15.0, 780.0	2.7, 1.8	2.2, 1.8	3.0	1050[f]	1.3[f]	532[f]	8.0-9.2	1.52-1.59	450, 1630	---
286-288	PRTR[39]	3	0.5078	12.0	94.5	1.2	15.0	7.0[f]	1.1[f]	7.38	1050	1.5[f]	500	9.5-12.1	1.28	5500-7900	GR, GRMOL, GCOMP
289-298	PRTR[39]	10	0.505, 0.5078	12.0	94.5	2.4, 2.6	15.0	7.0	1.0, 1.1[f]	4.89	1050	1.5[f]	500	12.1-21.4	1.28	500-3260	GR, GRMOL, GCOMP, ϵ_{cx}, ϵ_{cr}
299-304	HP(PIE)[40]	6	0.7472	3.5, 5.1	94.0	4.0	15.0	0.13	1.8	1.56	490	0.96	454, 464	13.2-19.4	1.08-1.39	5060	GR
305, 306	HP(PIE)[40]	2	0.7441	6.3	94.0	4.0	15.0	0.13	2.6	1.58	490	0.96	454, 464	18.6, 19.8	1.04, 1.18	7070	GR
307-309	HP(PIE)[40]	3	0.4264	11.7	95.1	10.1	15.0	5.6	1.8	4.81	490	0.26	454	11.3	1.28	5500	GR
300-313	HP(PIE)[40]	4	0.4264	5.8-11.8	95.1	10.1	15.0	5.6	1.8, 1.9	4.81	490	0.26	454	11.4, 11.6	1.28	9700	GR
314, 315	HP(PIE)[40,41]		0.4922	3.9, 5.9	95.0	5.76	15.0[f]	1.4	0.0, 1.2	1.66	490	0.27	454	20.2, 21.0	1.11	2100	GR, P

TABLE III (continued)

Run Number	Reference	Number Rods	Clad ID[a] (in.)	Diametral Gap (mils)	Fuel Density (%)	Enrichment (%)	Fill Gas[b] (psia)	Cold Plenum (in.)	Dish (%)	Fuel Length (ft)	Loop Pressure (psia)	Mass Flow (10^6lb/hr-ft^2)	Inlet Temperature (ft)	Peak Power (kW/ft)	Peak/Average (axial)	Operating Hours	Output
316-318	IFA-208[42]	3	0.4922	11.8	94.9	7.0	15.0[f]	3.2	0.0, 1.8	4.82	490	0.33	454	22.8-24.9	1.34	3200	ε_{cx}, ε_{cr}, ε'_{fx}, ε'_{cx}
319, 320	IFA-116[43-46]	2	0.5537, 0.5538	8.6, 8.7	96.9, 91.3	6.0	5.7, 11.4[f]	0.96, 1.01	1.1	1.64	490	0.32	454	24.1	1.04	4000	P, TF
321-324	IFA-117[44-46]	4	0.5531-0.5539	8.0-8.8	96.9, 91.3	6.0	11.4[f]	1.06-1.41	1.1	1.64	490	0.32	454	21.7-26.0	1.04-1.27	4450	P, TF
325	HP(P)[45,46]	1	0.6309	8.5	95.9	9.65	15.0	5.5[f]	2.1[f]	1.64	490	0.36	454	41.8	1.14	1650	GR
326, 327	HP(P)[45,46]	2	0.5034, 0.5036	9.0, 12.2	94.0	6.0	15.0	1.68	0.0	1.52	490	0.39	454	20.4	1.03	5440	GR
328	HP(P)[45,46]	1	0.5512	9.9	95.0	10.0	15.0	5.0	0.0	2.21	490	0.90	464	25.2	1.32	4250	GR
331-334	IFA-178[47]	4	0.5189	11.0	93.8	6.0	15.0	1.77	0.0	1.71	490	0.30	454, 464	16.3-17.1	1.11, 1.15	7400	P
335-339	IFA-181[48]	5	0.4921	11.2	94.0	11.01	15.0	2.7, 3.2	2.5	4.83	490	0.28	454	18.5	1.25	5790	P, ε'_{fx}, ε'_{cx}
340-345	IFA-162[49,60]	6	0.5059	7.5-13.0	94.8	5.1	15.0	3.9	0.1, 1.4, 1.8	5.48	490	0.32	464	16.0	1.25	5280	ε_{fx}
346, 347	IFA-150[51]	2	0.4264	5.9, 11.8	95.1	10.1	15.0	5.6	1.8	4.81	490	0.26	454	13.8	1.28	9700	ε'_{cx}
348	IFA-208[42]	1	0.4992	11.8	94.9	7.0	15.0	3.2	0.0	4.82	490	0.33	454	21.7	1.34	3180	ε_{fx}
351	IFA-224[42]	1	0.4992	11.8	90.1	7.0	15.0	3.2	3.7	4.82	490	0.34	454	17.6	1.34	150	ε'_{fx}
352, 353	IFA-230[42,49]	2	0.4992	9.8, 13.8	94.9	6.0	15.0	3.2	0.0, 3.3	4.92	490	0.34	454	16.3	1.34	60	ε'_{cx}, ε'_{fx}
354-358	SGHWR[52]	5	0.5756	4.9-14.8	96.3-97.1	3.7	15.0	7.8	0.0	12.0	943	2.4	525	5.3-17.7	1.42	8700	---
359-362	WEST[53]	4	0.374	7.5	92.0	2.8	345.0	6.8	1.5	12.0	2250	2.5	552	5.9, 13.7	1.40	5000, 10,000	ε_{fx}
363-366	B&W[54]	4	0.380	10.0-13.0	92.5-96.5	5.0[f]	15.0	2.0[f]	2.2	0.33	500[f]	0.0	400	4.5	1.12	1200, 2000	ε'_{fx}
367	IFA-166[49]	1	0.4922	5.9	95.0	5.8	15.0	1.42	0.0	1.66	490	0.27	454	18.0	1.11	12	ε'_{fx}
370, 371	IFA-116[43]	2	0.5530, 0.5539	7.9, 8.8	91.3, 96.9	6.01	15.0[f]	1.06, 2.04	1.1	1.64	490	0.32	464	13.5, 14.5	1.26	15	TF
372, 373	IFA-142[47]	2	0.7480	4.7	94.3	3.0	15.0[f]	0.12	2.0, 2.2	1.57	490	0.31	464	20.3	1.14	4180	P
380, 381	IFA-180[55]	2	0.5531	9.2	87.3, 91.3	11.0	15.0[f]	1.05	0.0	1.74	490	0.30	454	20.0, 20.4	1.11	1070, 10,400	GRMOL, GR
386	IFA-181[48]	1	0.4921	11.2	94.0	11.0	15.0[f]	2.73	2.5	4.83	490	0.28	454	18.5	1.25	5790	ε'_{fx}, ε'_{cx}, P
387-389	IFA-225[56]	3	0.4992	11.8	95.0	5.9	15.0[f]	0.84	3.7	1.60	490	0.35	464	15.2	1.27	39	P
390 401	IFA-401II[57]	11	0.5000	2.8, 13.8	86.8-94.5	7.0	15.0	1.4[f]	2.4	0.82	490	0.34	454, 464	12.9, 17.5	1.04, 1.14	7170	ε'_{fx}
402-404	IFA-404I[58]	3	0.5000	2.4-3.9	94.8	7.0	15.0[f]	2.8[f]	2.4	1.64	490	0.17	454	17.9	1.08	1640	ε'_{cr}
405, 406	IFA-414[59,60]	1	0.3933	2.0 8.7	95.0	7.0	15.0[f]	1.0[f]	2.7[f]	1.31	2000	0.12	491[f]	14.0	1.20	810	ε'_{fx}, ε'_{cr}
407	IFA-173[49]	1	0.4921	10.6	91.9	6.1	15.0[f]	0.90	1.8[f]	1.66	490	0.34	464	12.9	1.16	36	ε'_{fx}
408-410	IFA-404II[68]	3	0.4988	2.4	90.1-95.8	7.0	15.0[f]	2.8[f]	2.4	1.64	490	0.17	454	16.3	1.08	3900	ε'_{cr}
411-414	MIR[61,62]	4	0.2483-0.2498	0.3, 1.0	95.7-97.4	43.0-49.9	15.0	0.04-0.06	10.2, 11.9	0.41	2000	0.39	518	13.0-15.6	1.23	285, 320	ε'_{cx}, ε'_{cr}, ε_{cx}, ε'_{cr}
415-423	IFA-429[63]	9	0.374	8.0	91.0-95.0	13.0	375.0	1.0	1.1	0.80	490	0.56	464	7.2-12.0	1.02-1.30	960	TF, P
424-429	IFA-431[64,65]	6	0.4291	1.9-14.9	92.0, 95.0	10.0	15.0	0.59-0.94	0.0	1.86-1.89	490	0.36	464	5.6-8.2	1.08	17	TF, hg'

NOTE:
- TF - fuel centerline temperature
- rm - fractional melt radius
- ε_{cr} - clad circumferential deformation
- ε_{cx} - clad axial deformation
- GR - gas release fraction
- P - rod internal pressure
- hg - gap conductance
- GRMOL - gas content
- GCOMP - gas composition
- ε_{fx} - fuel axial deformation
- ZrO_2 - clad corrosion thickness
- H_2 - clad hydrogen concentration
- (') - prime indicates instrumented rod data

[a] Zircaloy unless otherwise noted.
[b] Helium unless otherwise noted.
[c] Core average rod power.
[d] Standard Design Package (versus time): centerline temperature, gas release fraction, h_{gap}, internal pressure, void volume gas abundance, gap size, gas helium fraction.
[e] Clad surface temperature specified.
[f] Assumed.

2. STANDARD DESIGN STUDY

Calculations of steady state fuel behavior were performed with FRAP-S2 for standard design commercial fuel rods. Previously reported FRAP-S1 Standard Design results showed that expected variation in design, operating, and model parameters had significant impact on initial conditions for transients. Two different PWR (15 x 15, 17 x 17) and BWR (7 x 7, 8 x 8) fuel designs were analyzed. Results for the main output parameters as a function of operating time are discussed for the core average 15 x 15 and 7 x 7 rod. Trends seen in the 17 x 17 and 8 x 8 results are consistent with those identified for 15 x 15 and 7 x 7 rods, differing only in magnitude due to lower heat rating and fuel temperature. Results for different power histories with the same discharge burnup are presented but have not been analyzed in detail.

One objective of the Standard Design Study was to benchmark FRAP-S2 output characteristics for extended burnup, full-scale application. Establishing steady state output ranges for power reactor conditions is a prerequisite for investigating typical fuel behavior variation for transients. Another objective of Standard Design runs was to relate FRAP-S2 results with previously generated results so as to establish the cumulative effect of changes in models and material properties.

The relative power histories used in the standard design study are shown in Figures 1 and 2 for PWR (3 cycles) and BWR (4 cycles) rods, respectively. Rod average discharge burnup is about 32,000 MWd/t in all cases. The axial peaking factor is 1.4. Rod average heat rating has been normalized to the core average value at 100% power, respectively 7.05, 5.45, 7.3, and 6.3 kW/ft for 15 x 15, 17 x 17, 7 x 7, and 8 x 8 fuel designs. All local results presented here, such as fuel temperature, gap size, and cladding deformation, will correspond to the axial peak power location.

The nominal (Case A) run represents steady power operation of the core average rod at 100% core power. Most of the results to be discussed

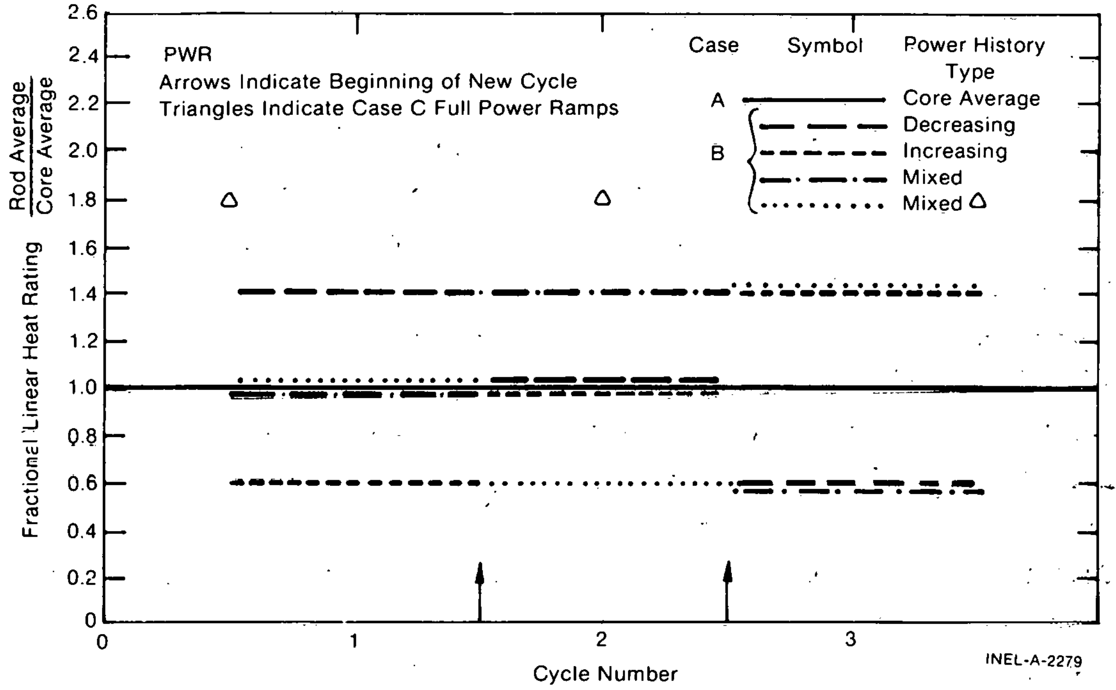

Fig. 1 Power history for PWR standard design rods.

in detail here relate to the Case A power history and correspond to typical output characteristics of the code. Case A results are used as an indication of what differences exist between FRAP-S1 and FRAP-S2.

The different Case B power histories (increasing, decreasing, and mixed) represent steady operation over each cycle at various normalized power levels between 0.6 and 1.4. Different power levels will be encountered in the course of achieving high burnup due to fuel management activity. Normally about 70% of the rods in the core fall within this operating range (i.e., core average heat rating ±40%) at any given time.

Case C represents the lead rod at different burnup conditions. In this case, core average burnup conditions are combined with full power ramps at beginning-, middle-, and end-of-life.

FRAP-S2 results for Case B and Case C power histories are shown only for purposes of illustration in Figures 3 through 20. What is shown is the contribution of power history to variation in initial

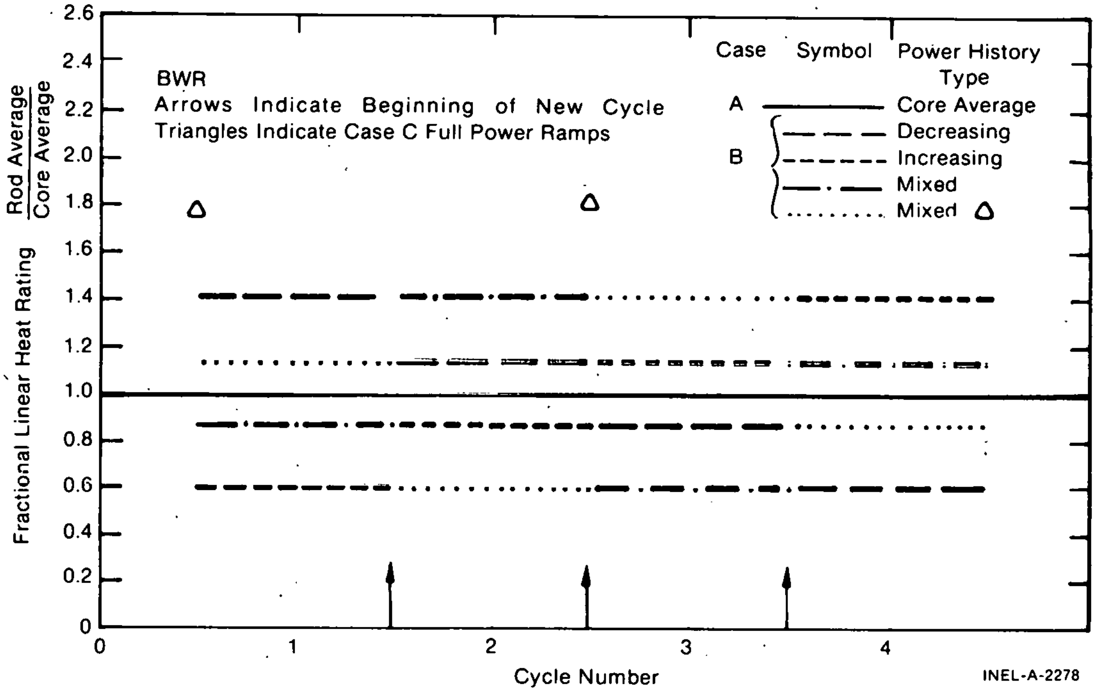

Fig. 2 Power history for BWR standard design rods.

conditions for transients. These results generally indicate that differences between FRAP-S1 and FRAP-S2 results are small compared to the effect of core power distribution or input power history assumed by the user.

Figure 3 shows predicted fuel center temperature for the 7 x 7 BWR design. Horizontal curves correspond to results from three different Case A power history runs. These are runs whose input power history corresponds to steady core average rod operating conditions. Results are discussed for FRAP-S2 with and without fuel densification and FRAP-S1 which had no densification model. The FRAP-S2 power history effect is only shown to illustrate the relative effect due to variable operating conditions across the core as opposed to variation in models.

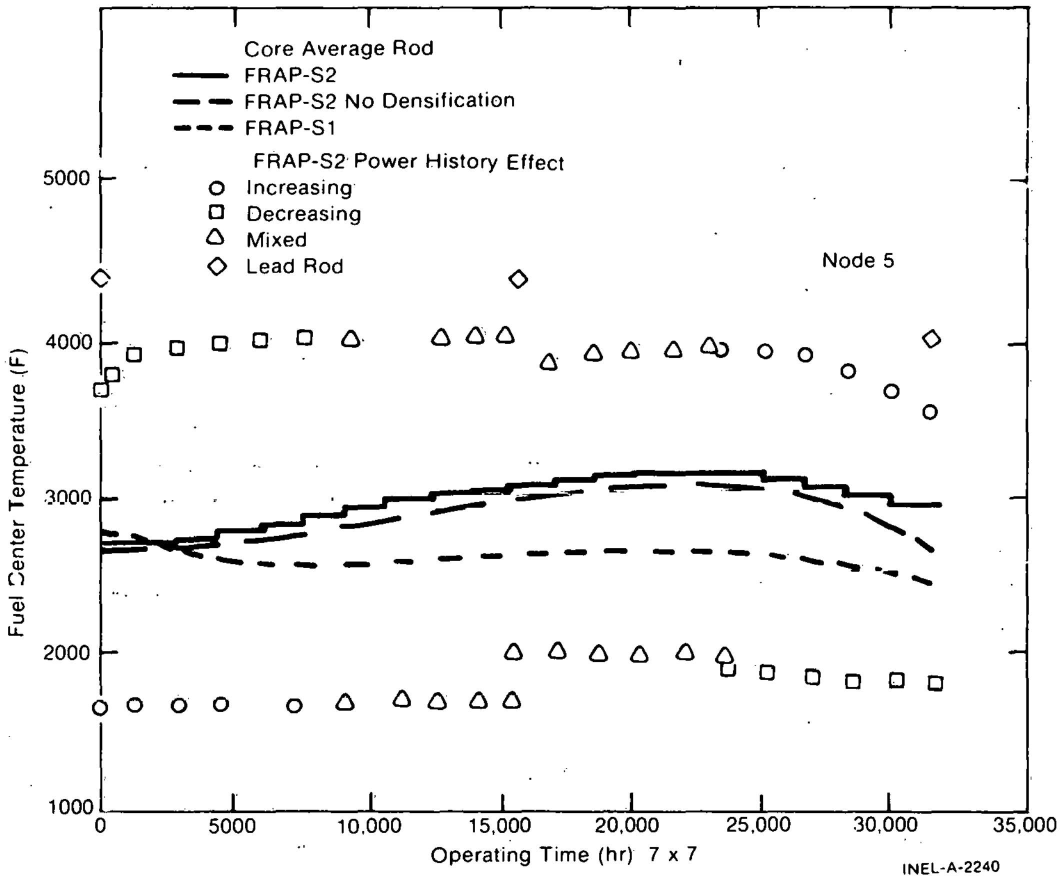

Fig. 3 FRAP-S standard design study, 7 x 7 fuel center temperature versus irradiation time.

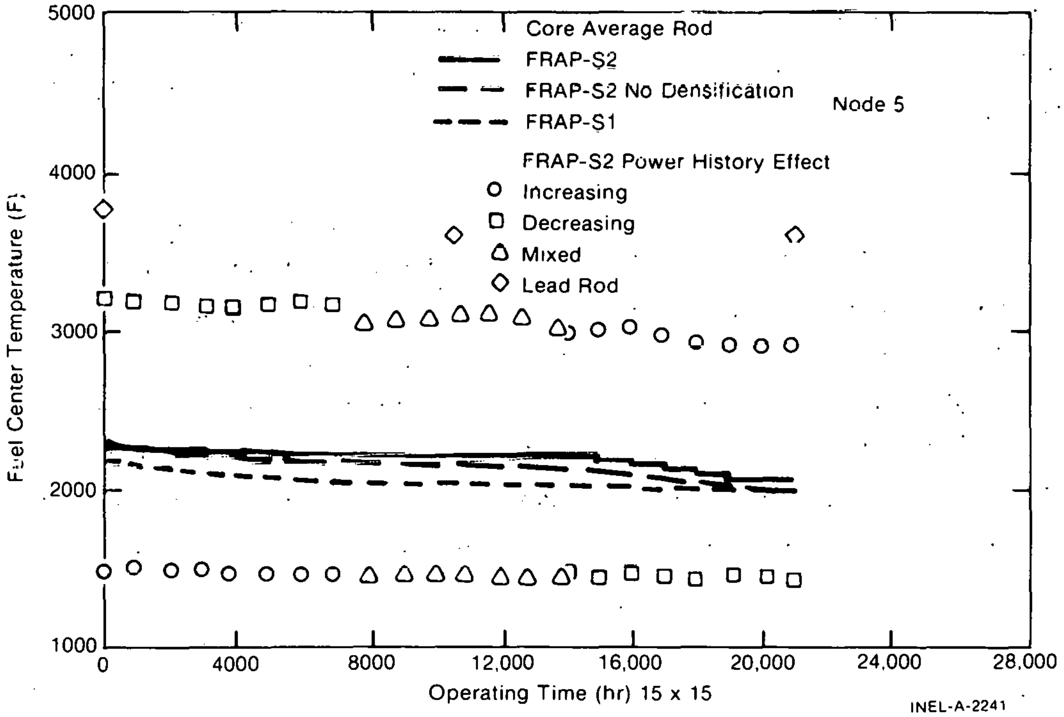

Fig. 4 FRAP-S2 standard design study, 15 x 15 fuel center temperature versus irradiation time.

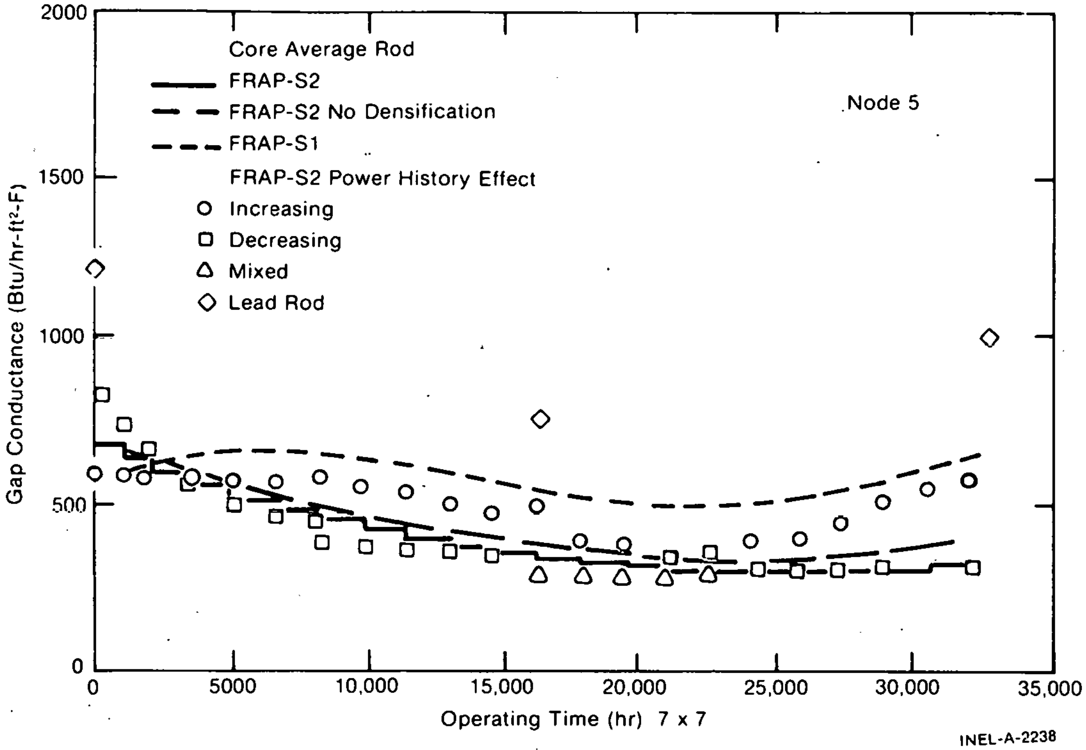

Fig. 5 FRAP-S2 standard design study, 7 x 7 gap conductance versus irradiation time.

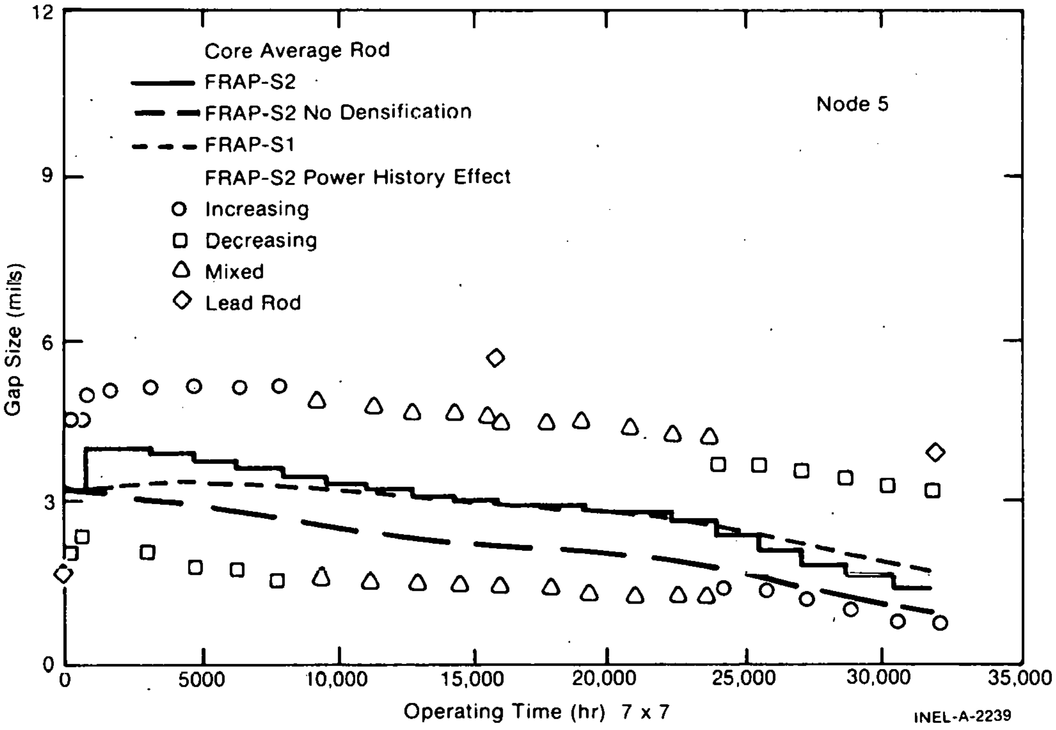

Fig. 6 FRAP-S2 standard design study, 7 x 7 radial gap size versus irradiation time.

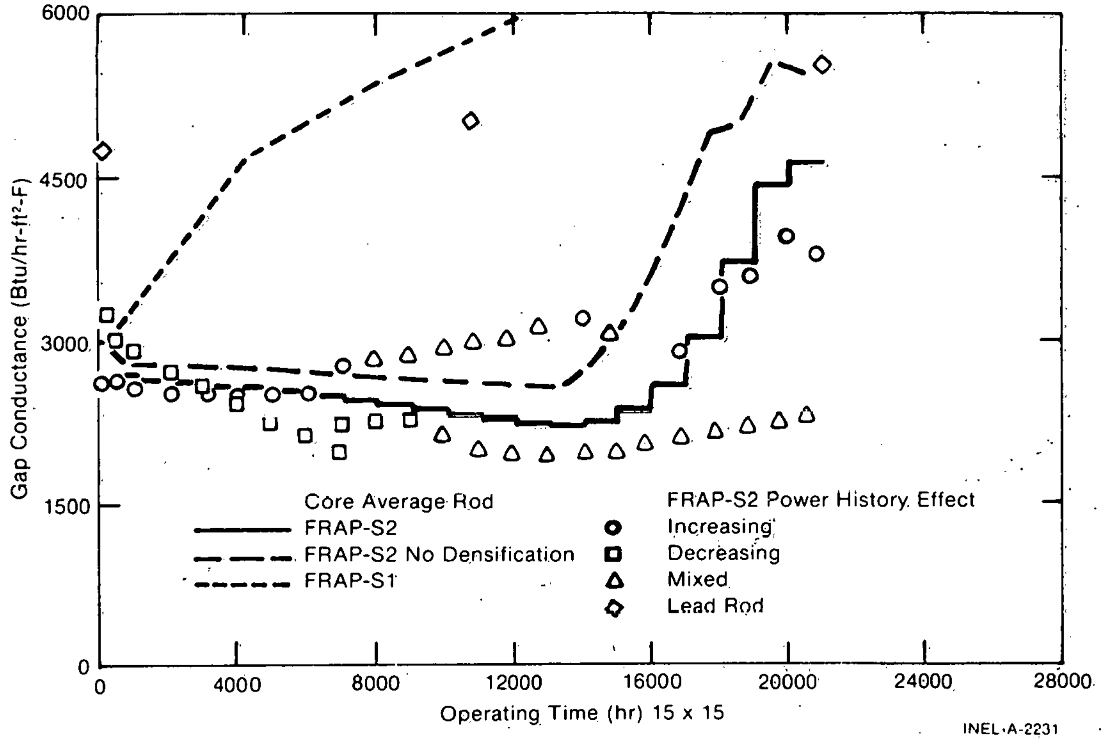

Fig. 7 FRAP-S2 standard design study, 15 x 15 gap conductance versus irradiation time.

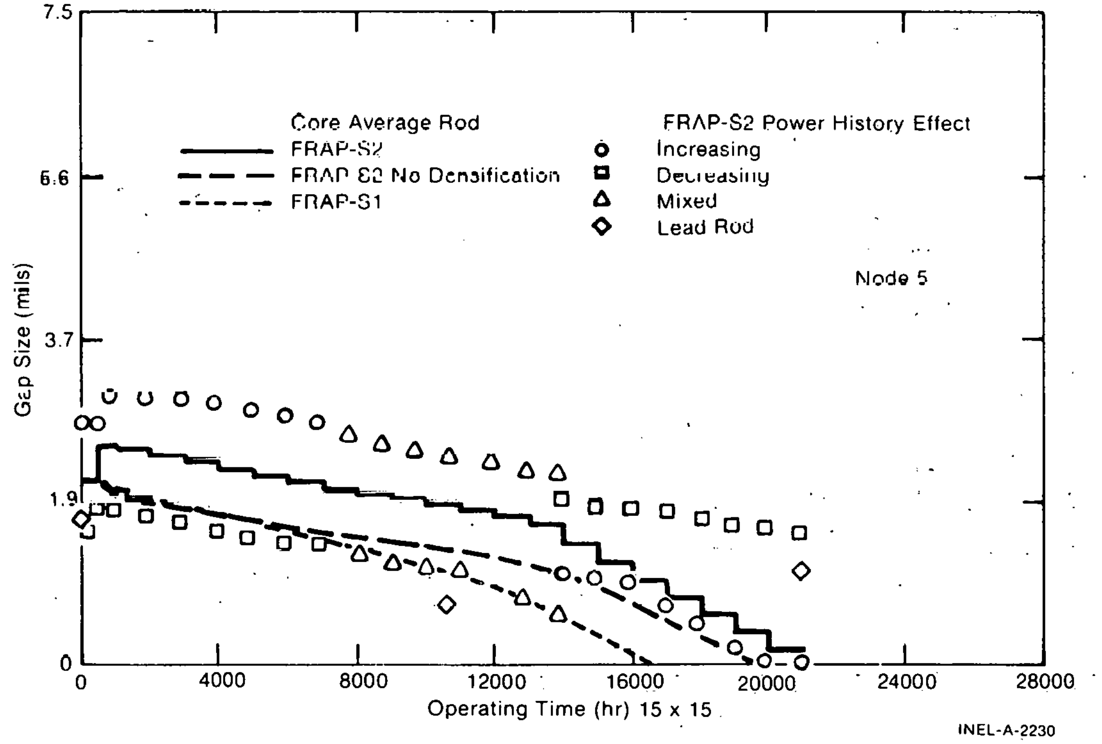

Fig. 8 FRAP-S2 standard design study, 15 x 15 radial gap size versus irradiation time.

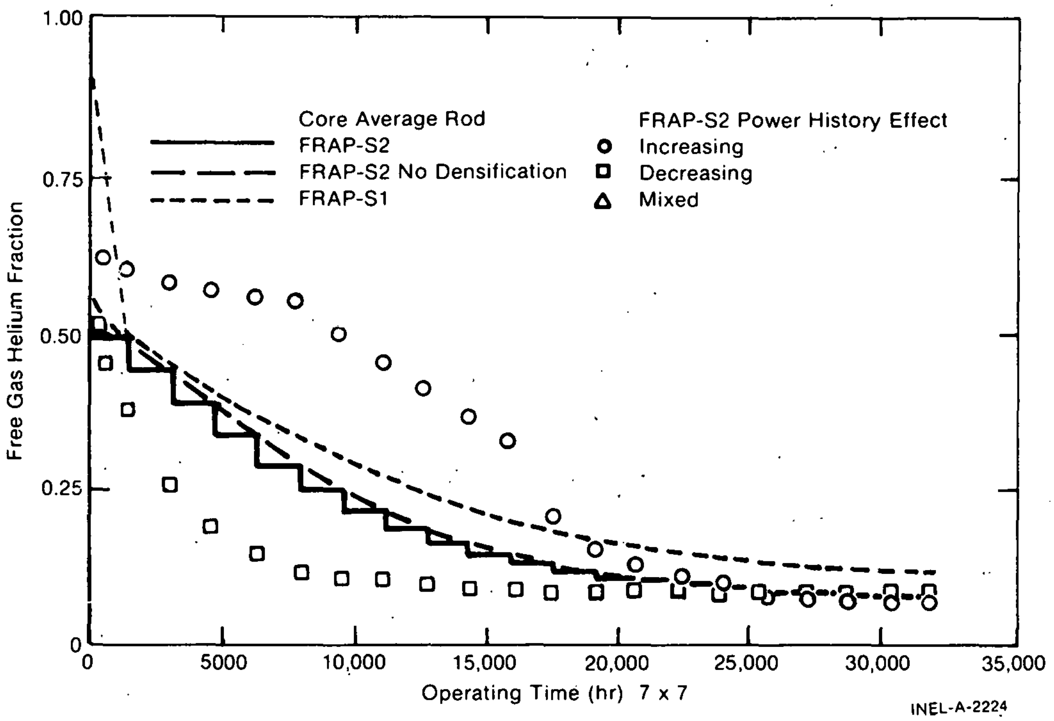

Fig. 9 FRAP-S2 standard design study, 7 x 7 free gas helium fraction versus irradiation time.

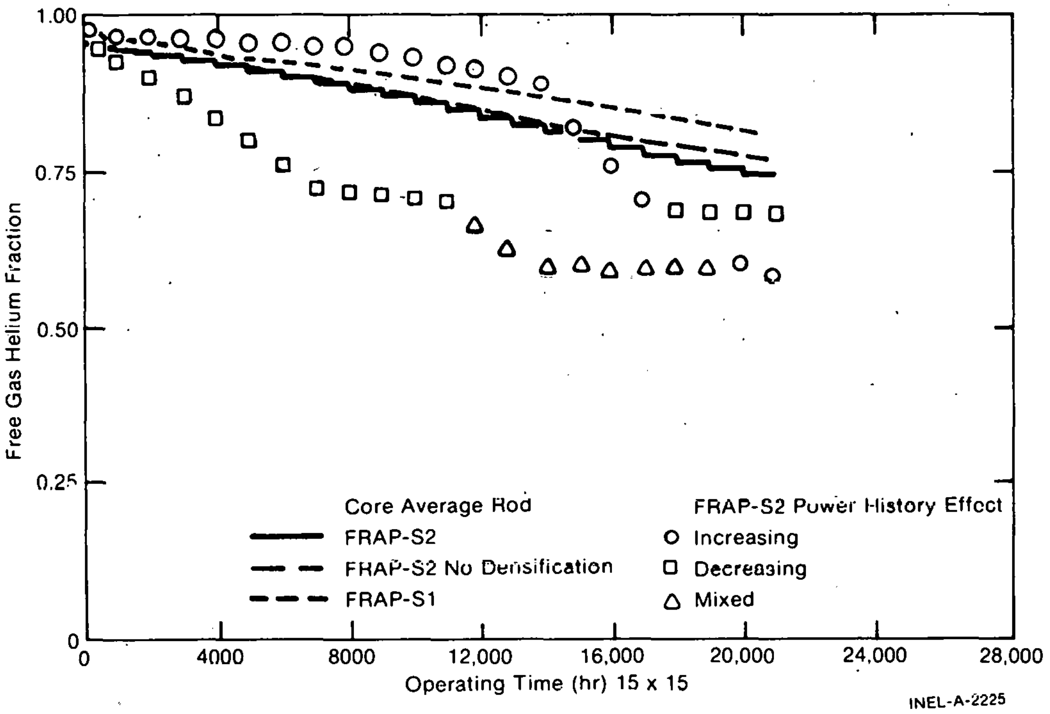

Fig. 10 FRAP-S2 standard design study, 15 x 15 free gas helium fraction versus irradiation time.

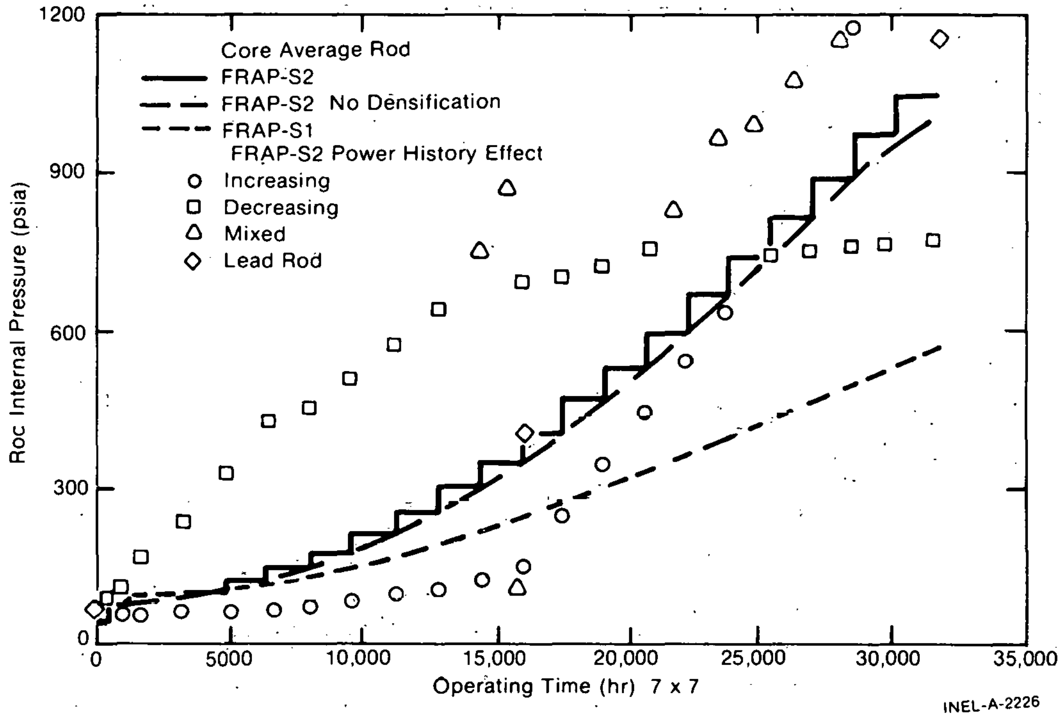

Fig. 11 FRAP-S2 standard design study, 7 x 7 rod internal pressure versus irradiation time.

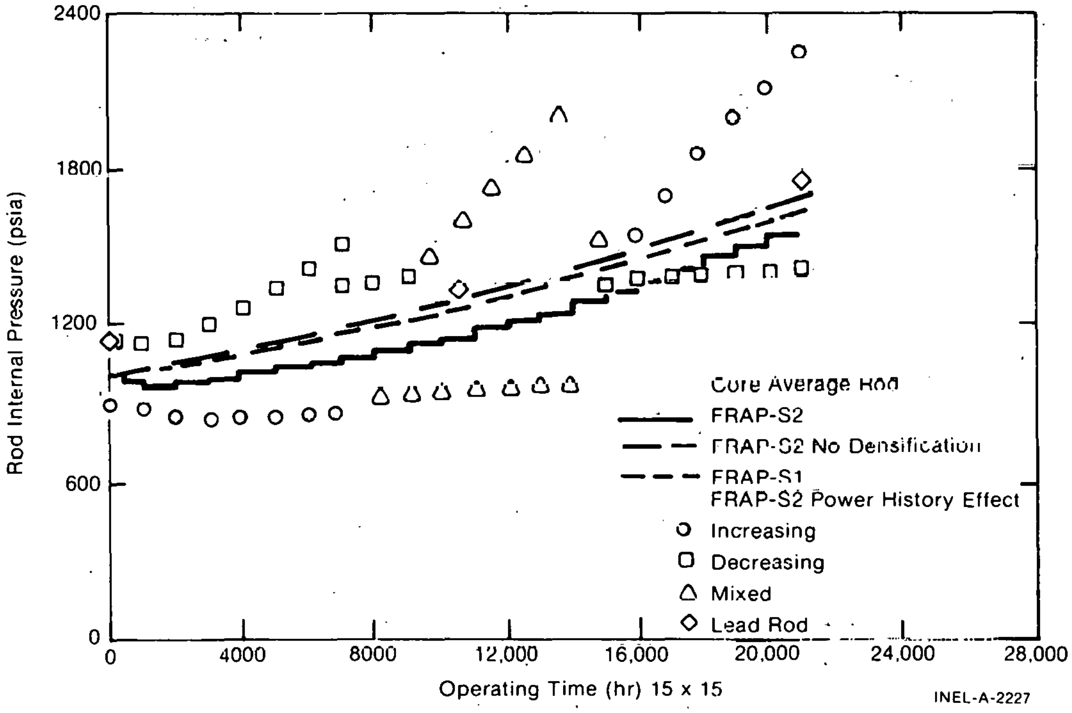

Fig. 12 FRAP-S2 standard design study, 15 x 15 rod internal pressure versus irradiation time.

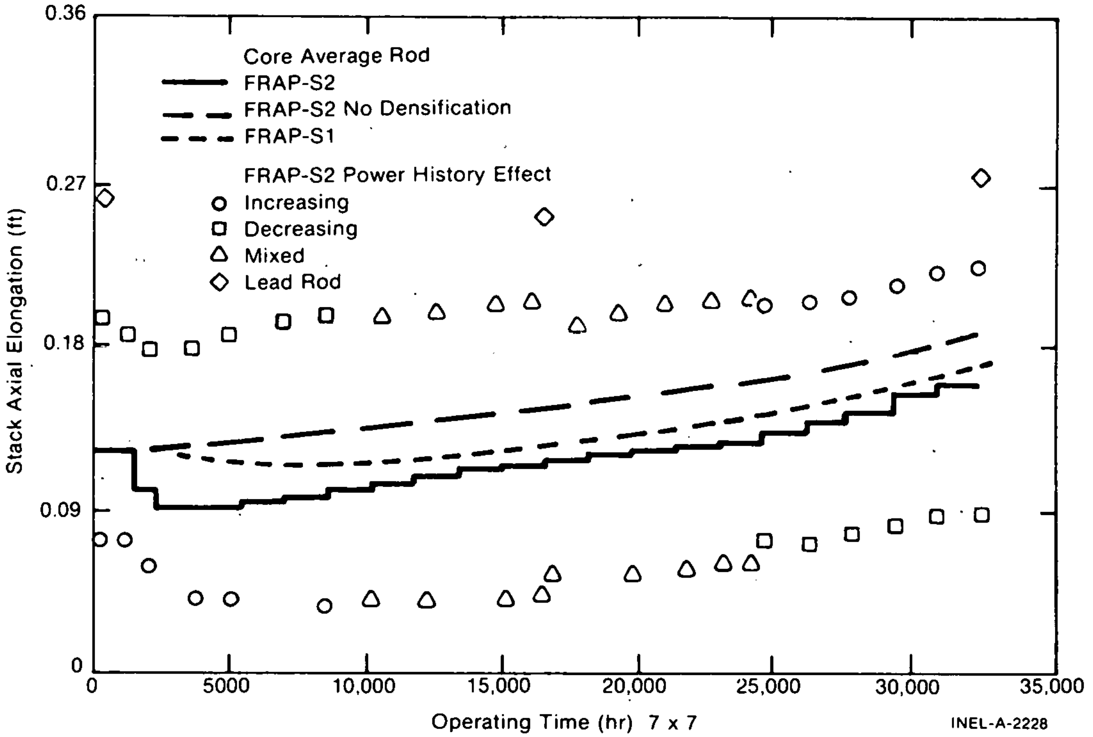

Fig. 13 FRAP-S2 standard design study, 7 x 7 stack axial elongation versus irradiation time.

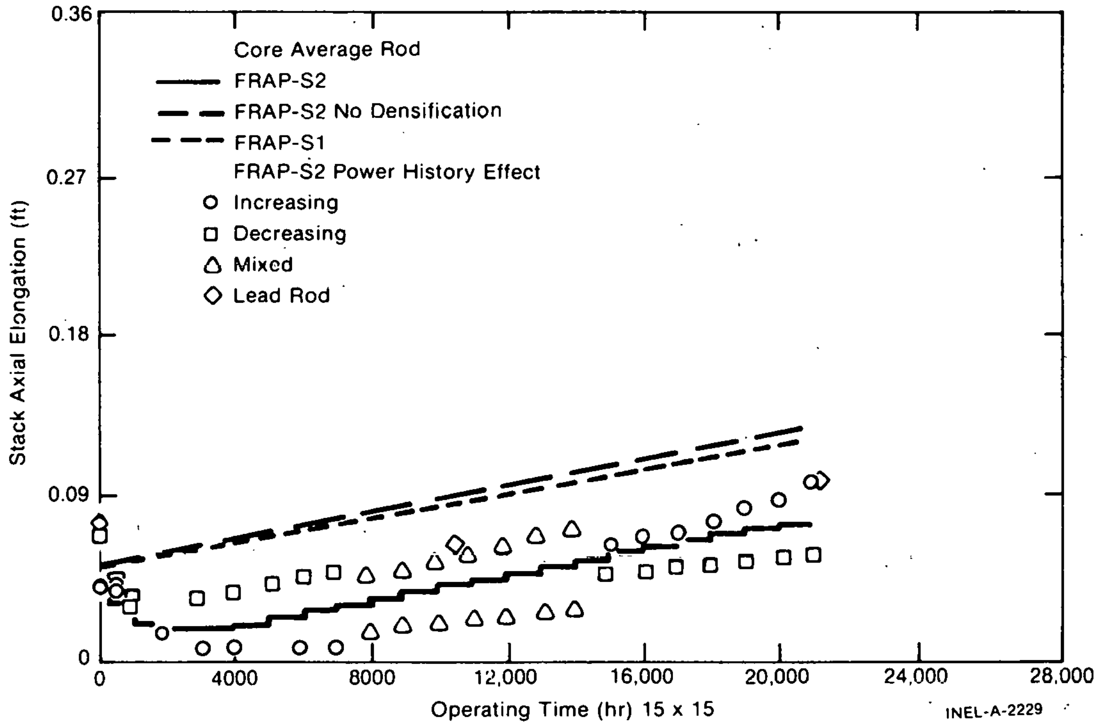

Fig. 14 FRAP-S2 standard design study, 15 x 15 stack axial elongation versus irradiation time.

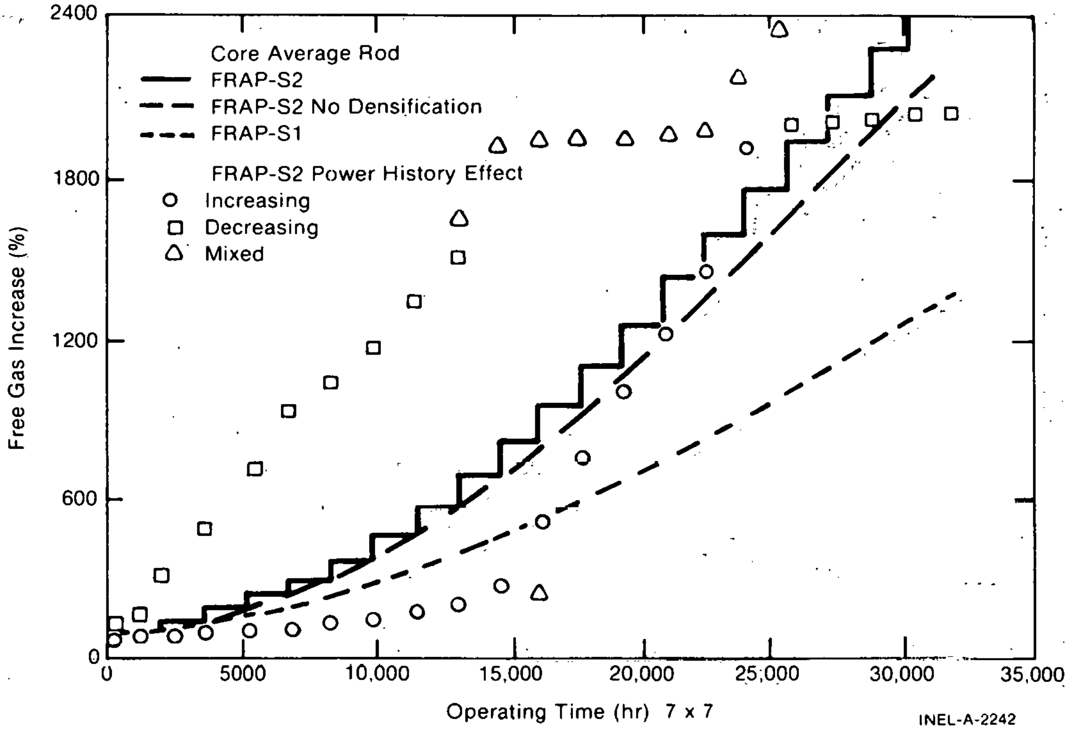

Fig. 15 FRAP-S2 standard design study, 7 x 7 free gas increase versus irradiation time.

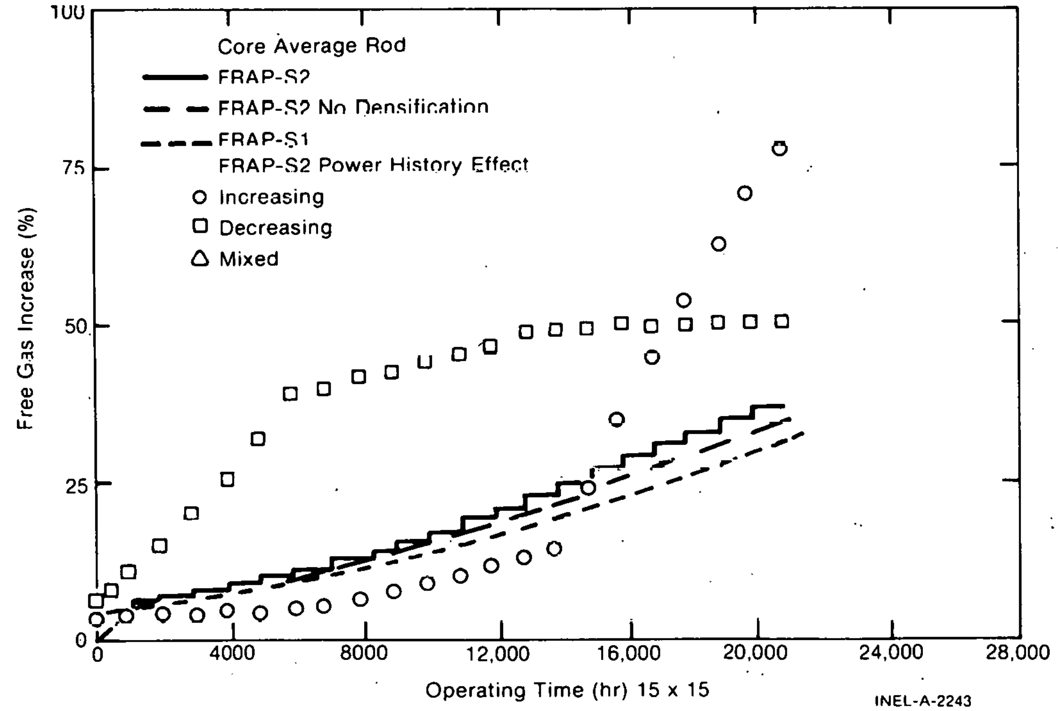

Fig. 16 FRAP-S2 standard design study, 15 x 15 free gas increase versus irradiation time.

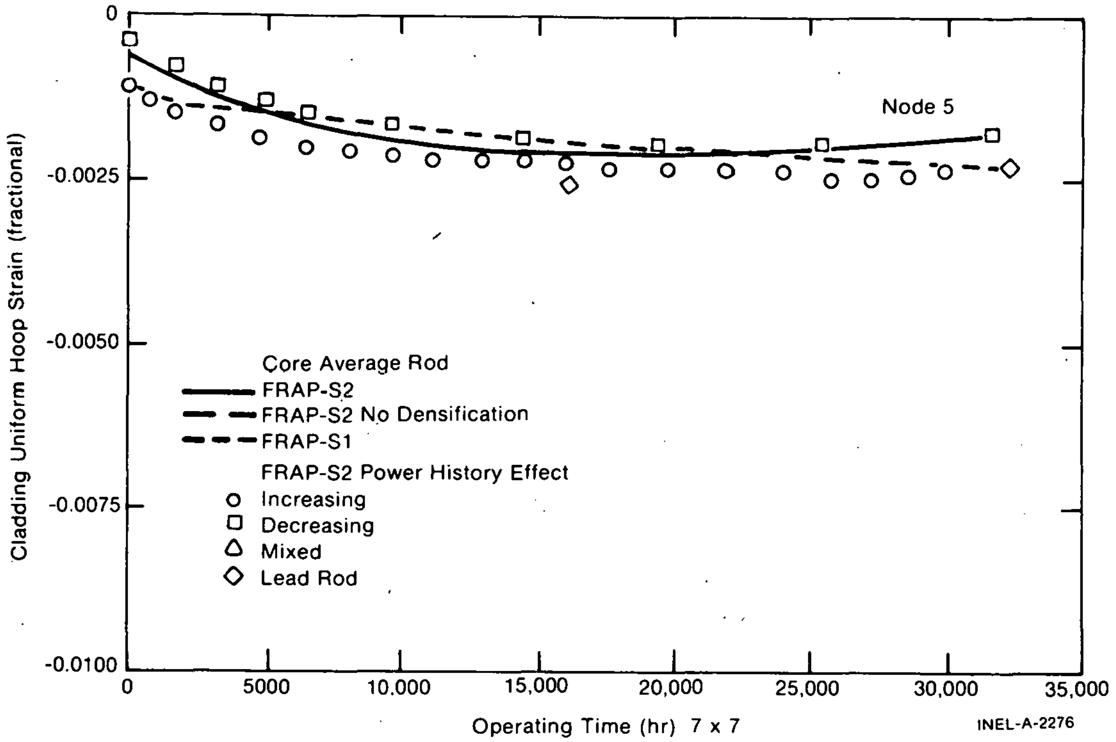

Fig. 17 FRAP-S2 standard design study, 7 x 7 clad uniform hoop strain versus irradiation time.

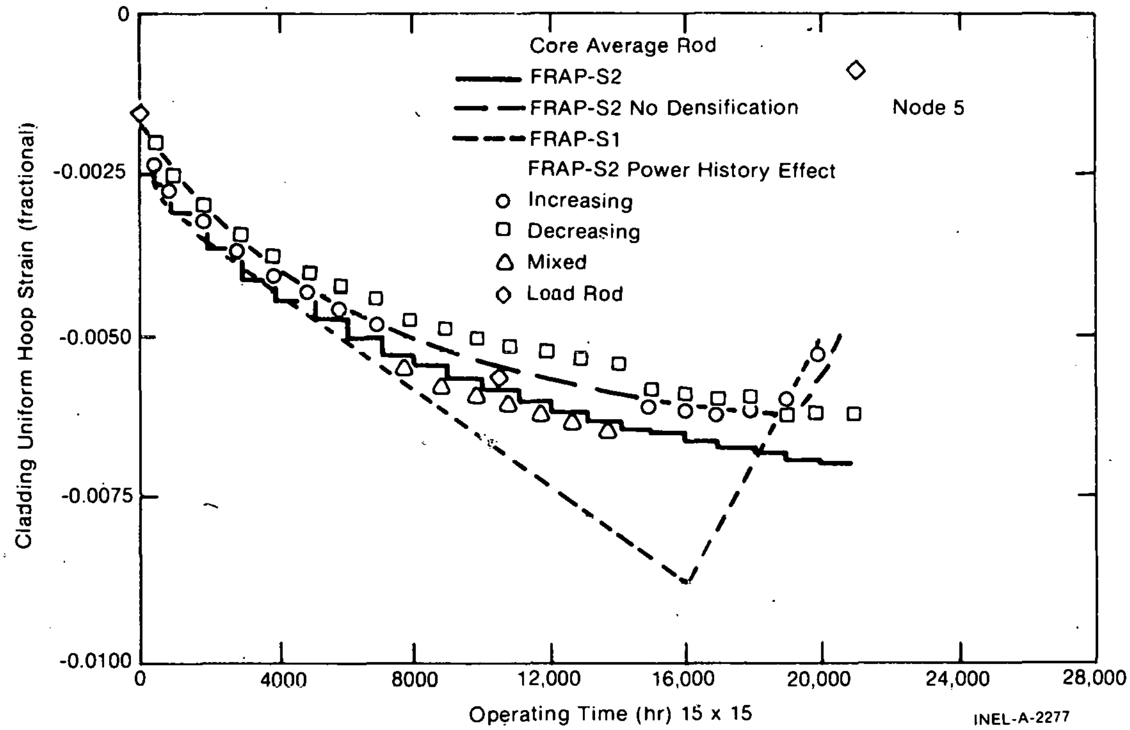

Fig. 18 FRAP-S2 standard design study, 15 x 15 clad uniform hoop strain versus irradiation time.

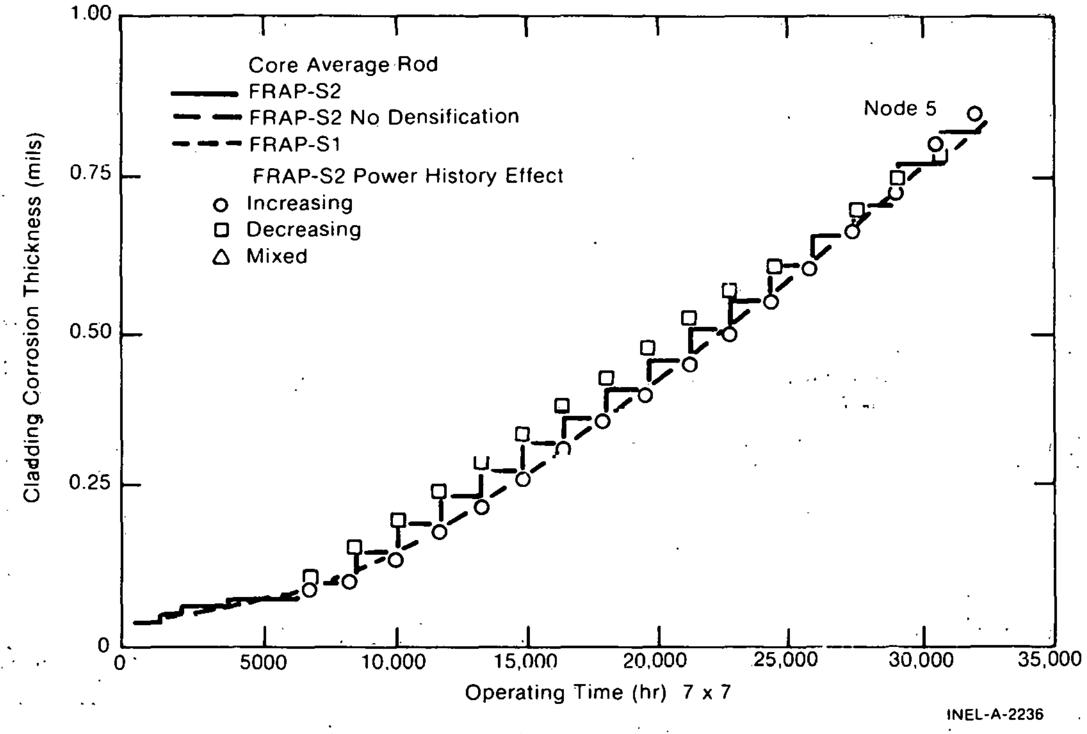

Fig. 19 FRAP-S2 standard design study, 7 x 7 clad corrosion thickness versus irradiation time.

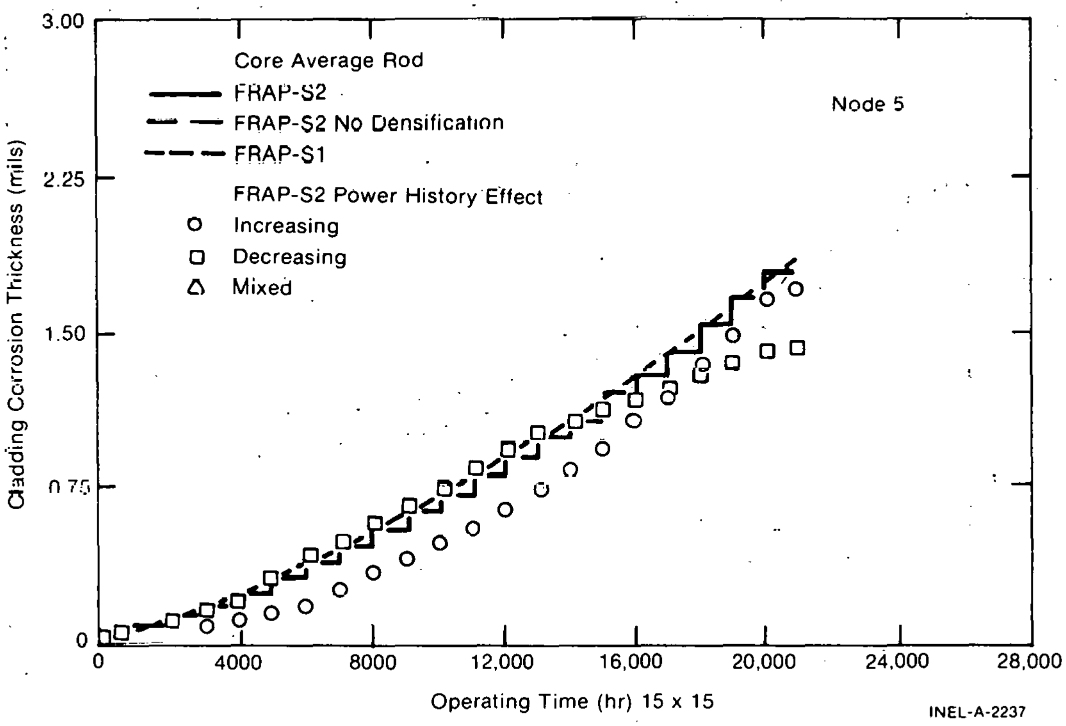

Fig. 20 FRAP-S2 standard design study, 15 x 15 clad corrosion thickness versus irradiation time.

Figure 3 shows that initially comparable core average rod results from both FRAP-S1 and FRAP-S2 begin to diverge early in the operating history. The nominal FRAP-S2 results give central fuel temperatures as much as 500°F higher than FRAP-S1. Fuel densification is responsible for only a small part of the temperature increase as indicated by the FRAP-S2 run without densification. Both FRAP-S2 and FRAP-S1 predict a fuel temperature decrease, occurring at high burnup and associated with gap closure from fuel swelling.

Similar trends are seen in the 15 x 15 curves in Figure 4 but the magnitude of temperature differences between FRAP-S1 and FRAP-S2 is much less than for the BWR design. The relatively small temperature effect is due to consistently high gap heat transfer calculated by both codes for pressurized rods.

Figures 5 and 6 show steady power burnup effects on gap conductance and gap size, respectively, versus operating time for the 7 x 7 design. Results are consistent with temperature trends shown in Figure 3. Runs having lower gap conductance are associated with higher fuel temperature and vice versa. Both FRAP-S2 runs (with and without densification) predict significantly lower gap conductance compared with FRAP-S1. On the basis of Figure 6, this result is not unexpected given the larger hot gap size predicted by FRAP-S2 with densification. The combination of smaller gap size and lower gap conductance for FRAP-S2 without densification warrants additional investigation. Current results may only reflect sensitivity of unpressurized rod burnup condition to gas release during early time steps. The pressure and gas release comparison is shown further on.

Figures 7 and 8 compare gap conductance and gap size burnup effects between FRAP-S1 and FRAP-S2 for the 15 x 15 design. Again FRAP-S2 predicts lower gap heat transfer than FRAP-S1. This is considered to be a desirable result since limited FRAP-S1 verification runs for pressurized rods had indicated that the effective gas conductivity used in the gap conductance model was being overestimated at high helium pressure. Large gap conductance values, characteristic of hard pellet-cladding contact, were predicted by the previous model, even for open gap conditions. Trends in PWR gap size results shown in Figure 8 are consistent with the relatively small temperature differences seen in Figure 4. The effects of considering fuel densification and using a different cladding creep model are more evident with less temperature change between runs. The nominal FRAP-S2 curve maintains a larger gap resulting from densification which is mainly predicted to occur during the first few thousand hours, consistent with most measurements. FRAP-S2 without densification initially predicts gap sizes comparable with FRAP-S1 as expected. As burnup progresses, however, the FRAP-S2 curve indicates an increasing (cumulative) gap size effect due to less cladding creepdown. The slower FRAP-S2 collapse rate occurs because of higher internal pressure calculated by the model and the higher creep activation energy used by revised cladding properties in the current MATPRO.

Figures 9 and 10 show, for 7 x 7 and 15 x 15 designs, the expected effect on gas composition of higher fuel temperature in FRAP-S2 relative to FRAP-S1. In Figure 9 the end-of-life difference in free gas helium fraction between the current and previous code versions seems less than that expected on the basis of the relatively large fuel temperature difference. This may be due to physical limits on the amount of retained gas left to be released in different fuel temperature regions after prior and extended operation under high release conditions. In any event, unpressurized rod thermal conditions were seen earlier to be sensitive to the cumulative effects of calculated differences in gas composition between FRAP-S1 and FRAP-S2.

Figures 11 and 12 give the rod internal pressure history for 7 x 7 and 15 x 15 rods, respectively. Here again is seen marked differences between trends for unprepressurized and pressurized rods. Both FRAP-S2 pressure histories are markedly higher than that predicted by FRAP-S1 for the BWR design in Figure 11. It is not considered reasonable for the core average rod analysis to result in end-of-life internal pressure exceeding the system value in violation of accepted design criteria. Higher fuel temperature, thermal expansion, and gas release dominate the results, regardless of whether fuel densification is considered. For the PWR cases shown in Figure 12, FRAP-S2 with densification predicts lower internal pressure than FRAP-S1. Removing densification results in close agreement between FRAP-S2 and FRAP-S1. In the PWR analysis, more void volume from densification and less cladding creepdown determines the pressure history more than the marginally higher fuel temperature and gas release predicted by FRAP-S2. The effects of any differences in center temperature on fuel thermal expansion and rod void volume are moderated for the dished PWR fuel which is calculated to expand axially based on pellet shoulder temperature.

The point in regard to governing influence of fuel temperature over other models is again illustrated by the 7 x 7 and 15 x 15 fuel stack elongation results shown in Figures 13 and 14. The addition of a densification model in FRAP-S2 is seen to have less effect on the BWR results due to influence of other modeling differences on fuel temperature.

With regard to the key modeling output of free gas abundance, it is a design rather than any modeling difference which mainly controls the results. The amount of free gas in the core average BWR rod at end-of-life ranges in Figure 15 between 13 and 25 times the as-built value, depending on whether predictions are based on core average rod FRAP-S1 or FRAP-S2 runs. Results for the prepressurized rod shown in Figure 16 show that burnup causes rod gas content to build up to a value only 30 to 35% in excess of the as-built amount.

Figures 17 and 18 show cladding hoop strain versus operating time for the 7 x 7 and 15 x 15 design. For this output parameter, differences in operating system condition have strong influence on determining trends in the results, regardless of whether FRAP-S1 or FRAP-S2 is used. The 7 x 7 curves are all quite similar since the creep rate is small with relatively low cladding temperature and pressure difference. Diameter increases are predicted by FRAP-S2 beginning late in life due to excessive internal pressure buildup previously shown in Figure 11. For the 15 x 15 rod in Figure 18, FRAP-S2 predicts less cladding collapse than FRAP-S1 due to use of a revised creep correlation with higher activation energy in the temperature dependent creep term[4].

Figures 19 and 20 show the buildup of cladding surface corrosion with time again for 7 x 7 and 15 x 15 rods, respectively. FRAP-S1 and FRAP-S2 results are seen to be very comparable since the corrosion model is nominally unchanged. For both fuel types, significant differences in rod internal conditions between current and previous code versions have no impact on cladding surface conditions given consistently high surface heat transfer.

3. DATA COMPARISONS

The data base used for fuel behavior model verification has been expanding with each new version of the Fuel Rod Analysis Program. Additional tests of the physical model are performed to enable verification runs to have continued significance in evaluating successively fine-tuned code versions. Also, most data types are characterized by significant scatter reflecting differences in design configuration, operating condition, and data reproducibility itself. This measurement variation necessitates a maximum sample size approach to facilitate interpretation of results. Data comparison runs, in addition to those considered during FRAP-S1 verification, were added as time allowed. Continued representation of various research programs and facilities was actively pursued. This approach minimizes the effect of variation in measurement reproducibility and systematic error on interpretation of results.

Identifying the mean, range, and distribution of fuel behavior measurements is dependent on having many data points applicable to a given design configuration and range of operation conditions. Reporting of replicate measurements for instrumented rods, even for subsequent power cycles of the same rod, is generally not the practice. Local operating conditions reflecting nonuniform power distribution were not always well characterized in the reference material. Fabrication data reflecting as-built dimensional tolerances and details about material preparation was usually not reported. Much of the data, in particular from relatively high power tests with fuel melting, center voids, fuel plasticity, or clad ridging, may reflect to a greater or lesser degree, mechanisms not expressly treated by the current physical model. It is felt, however, that influence of unaccounted for effects on applicability of data comparison results is usually not larger than the range of data reproducibility itself. Anomalous or outlying data points are more readily identified then, among relatively large sample populations.

Data processing functions used in verification are being expanded beyond the current large sample input procedures. This expansion promotes the capability for evaluating results of many different experiments as well as making more quantitative interpretations of model accuracy. Table IV summarizes the number of runs, types of data, and main sources of information for each comparison index investigated with FRAP-S2. Comparing FRAP-S1 and FRAP-S2 sample sizes, it is observed that significantly more fuel behavior measurements have been considered in the current effort.

3.1 Thermal Model

3.1.1 Fuel Centerline Temperature. Discussion of fuel temperature results will be given first since this parameter strongly influences other models in FRAP-S2. It has not normally been verification practice to base conclusions on results of individual comparisons. As previously stated, there is too much variation in reproducibility of fuel rod measurements to permit more than establishment of isolated trends (i.e., applicable to only 1 design and operating condition) when single rod results are shown. Identifying these trends is useful, however, for interpreting the summary results discussed later on.

TABLE IV

FRAP-S2 MODEL VERIFICATION: SCOPE OF DATA COMPARISON STUDY

		Sample Size			
Comparison Index	Data Category	S1	S2	Maximum Operating Hours	Test Program
Fuel Temperature	*	30	52	8800	HPR, RISO, WCAP, PBF
Gap Conductance	Δ/PIE	-/27	18/27	BOL/900	AECL, HPR, PBF
Fuel Melt Radius	PIE	94	94	2500	AECL, GEAP
Fuel Axial Elongation	*/PIE	8/18	35/22	9000/19,000	HPR, KWU, B&W, W
Rod Internal Pressure	*	17	50	12,000	HPR, AECL, PBF
Gas Release Fraction	PIE	104	159	18,000	HPR, SAXTON, B&W, W, AECL, PRTR
Gas Composition	PIE	---	8	6600	PRTR
Gas Content	PIE	---	10	10,000	HPR, PRTR
Cladding Axial Elongation	*/PIE	13/82	28/92	9500/18,000	HPR, SAXTON, AECL, PRTR, MTR, PBF
Cladding Circumferential ϵ	*/PIE	4/123	16/132	2100/18,000	HPR, AECL, GEAP, SAXTON, KWU, PRTR, MTR
Cladding Corrosion	PIE	30	30	18,000	HPR, SAXTON
Cladding H_2 Concentration	PIE	30	36	18,000	HPR, SAXTON

* Instrumented rod data.

Δ Inferred from instrumented rod data.

PIE Postirradiation examination.

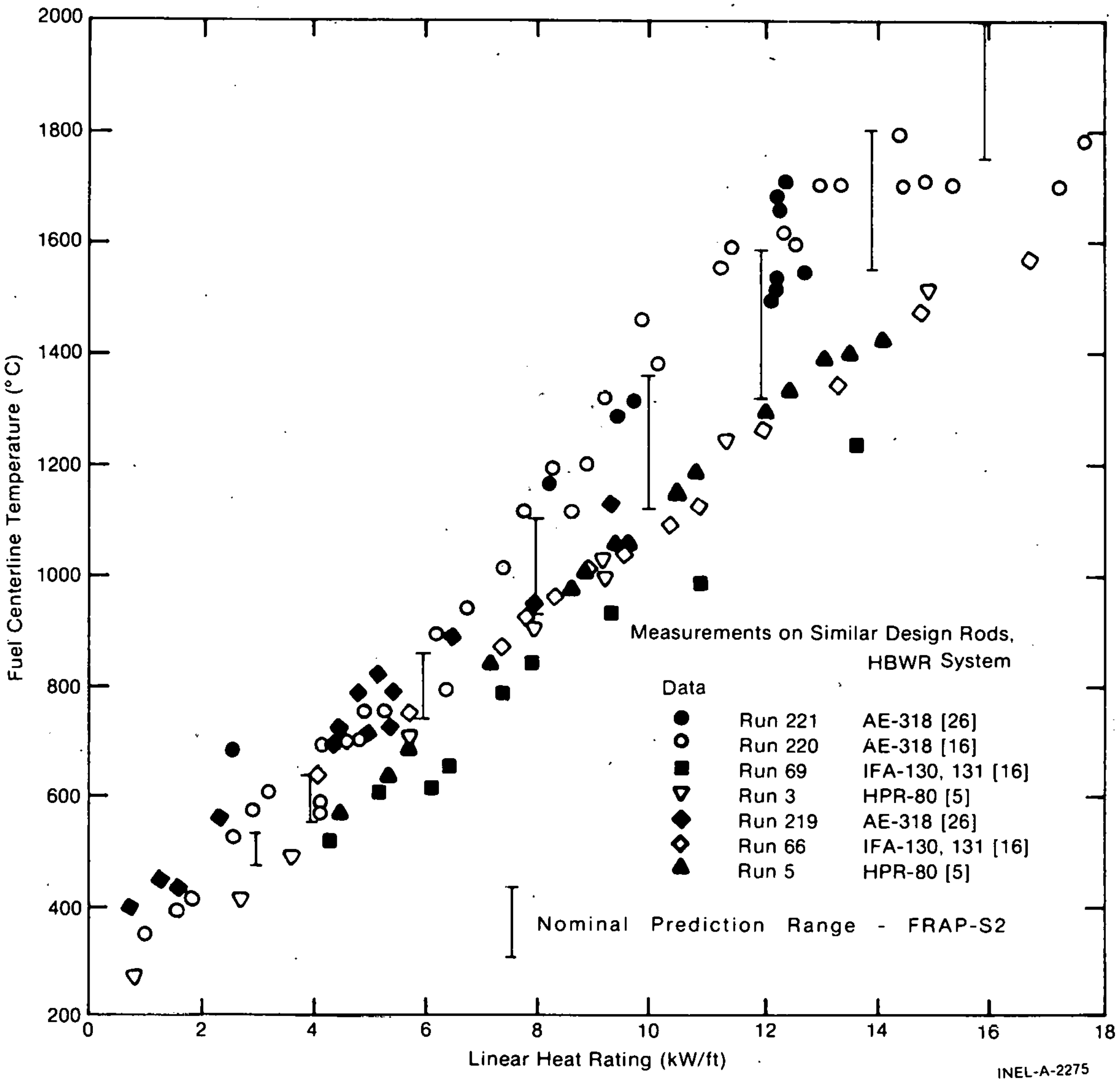

Fig. 21 Reproducibility of BWR fuel centerline temperature versus power.

Figures 21 and 22, for example, respectively summarize startup temperature measurements from 7 BWR[5,16,26] and 4 PWR[31,32,34,35] rods with almost identical design, fuel form, and surface heat transfer. Gap size and fuel density for the BWR rods ranged respectively from 6 to 7 mils and from 94 to 96%. Enrichment was either 5 or 6% U-235 with 1 atmosphere helium backfill. The PWR rods all had 8-mil gaps, 93% fuel density, 20% enrichment, and initial helium pressurization of either 375 or 550 psia. With these similarities, the total range of predicted fuel temperatures for the BWR and PWR rods spans no more than 250 and 10°C, respectively, for a given heat rating. Observed variation in the data, however, is larger than that attributable to known differences between

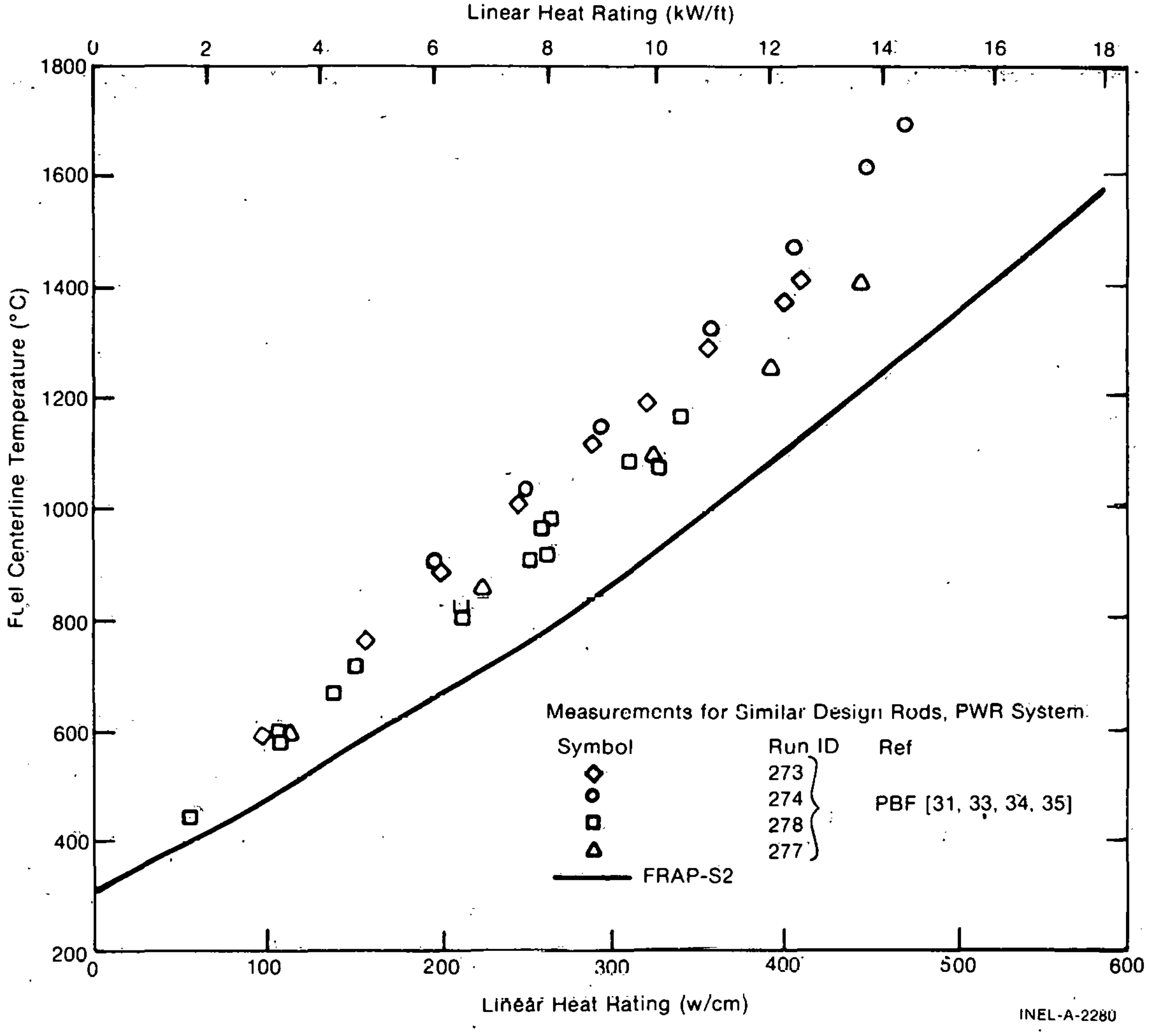

Fig. 22 Reproducibility of PWR fuel centerline temperature versus power.

the rods. The measurement range at a given power level is as high as 600°C for the BWR rods and 200°C for the PWR rods. Even for predictions which lie inside the measurement envelope, it may be unfounded to conclude that the code is adequate and only the data are in need of improved characterization. There are uncertainties in the fuel design parameters and differences in fabrication tolerances and procedures, which are not considered in the prediction and therefore only affect the data in this case. On the other hand, error in determining local power at instrument locations, together with thermocouple decalibration and placement, have an effect on the apparent relationship between temperature and heat rating. FRAP-S2 is generally observed to overpredict the BWR fuel temperatures and underpredict the PWR fuel temperatures.

Another point with regard to the effect of relative measurement reproducibility on data comparison results can be illustrated by Figures 23 and 24. Figure 23 shows fuel temperature behavior for two initial power cycles involving an 8-mil gap, PWR size rod without prepressurization[10]. Error in calculated power distribution for this mixed oxide fuel type is partly responsible for the overall model's apparent tendency to overpredict fuel temperature. In any event, the prediction changes very little from ramp 1 to ramp 2, only 50 hours later. The observed temperatures show considerable increase for the second ramp, however, reaching a level which is then maintained for ramps over several thousand MWd/MtU. One conclusion might be that the code properly represents the fuel temperature, except for the startup period when all of the fuel and instrument accommodates seem to take place. Alternately, the data indicate that most of the burnup effect on fuel temperature is exhibited in the first 50 hours of irradiation. Neither conclusion, however, seems entirely reasonable on physical grounds.

Figure 24 gives beginning-of-life results from a BWR size 8-mil gap rod from another experiment[11]. In this case it has not been reported whether a similar temperature change from one early life ramp to the next had occurred. Use of annular design pellets further complicates interpretation due to uncertainties in calculated power distribution. The code, in other words, could be doing a better or worse job than isolated results indicate. It seems reasonable to put more emphasis on nonstartup ramps or average measurement response, the net result being an emphasis on the most typical behavior. Continued reporting of experiment details through postirradiation examination (PIE) is necessary for good characterization of verification instrumented rod data.

Figure 25 compares measured and predicted fuel center temperature for the data sample considered (52 rods). Most of the data points reflect initial startup or relatively low burnup conditions (<100 operating hours). The fuel diameter was BWR size (0.500 in.) or larger for 34 rods. Of the remaining 18 rods with PWR size fuel, only 8 were prepressurized.

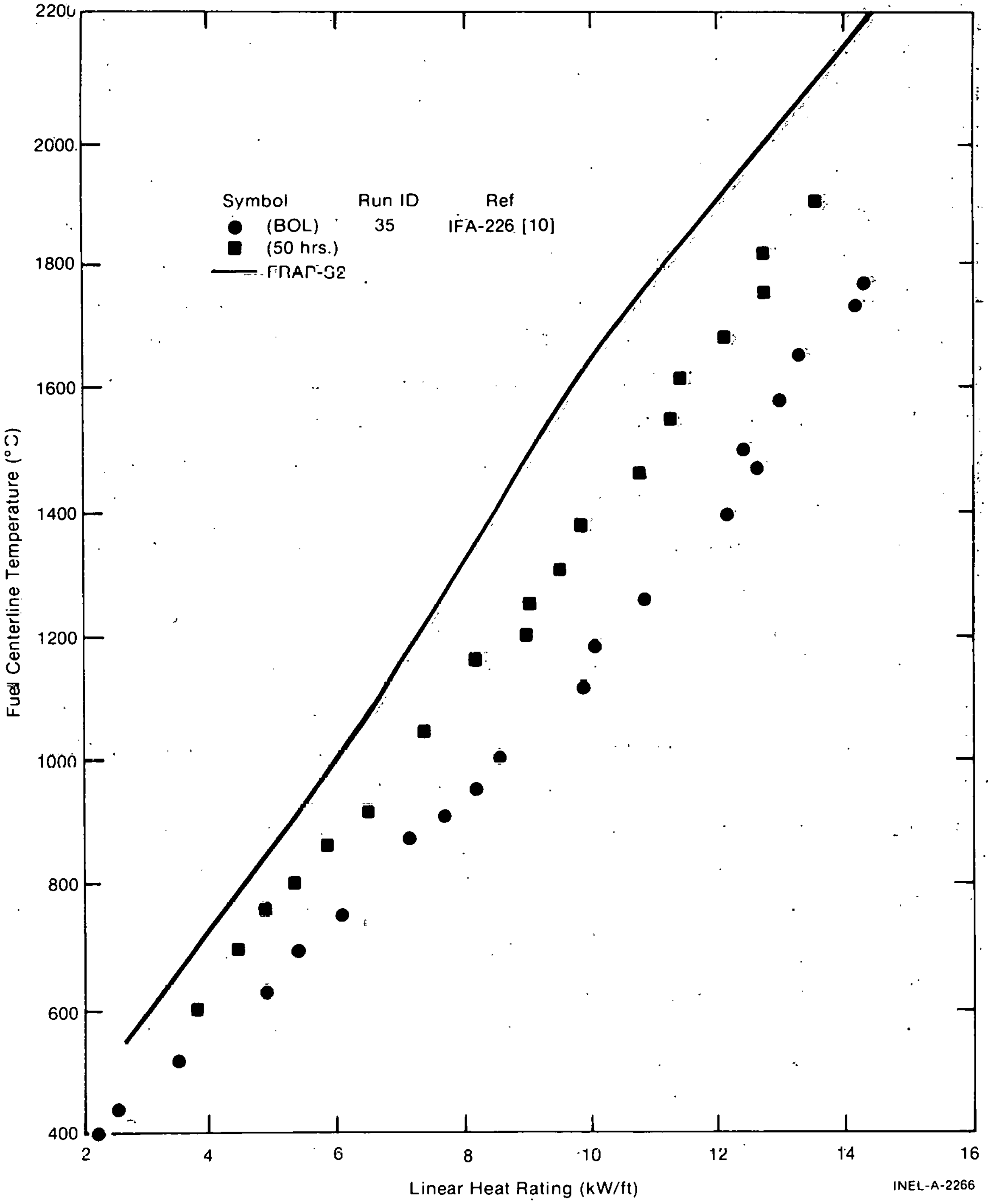

Fig. 23 Fuel temperature versus power for mixed oxide rod.

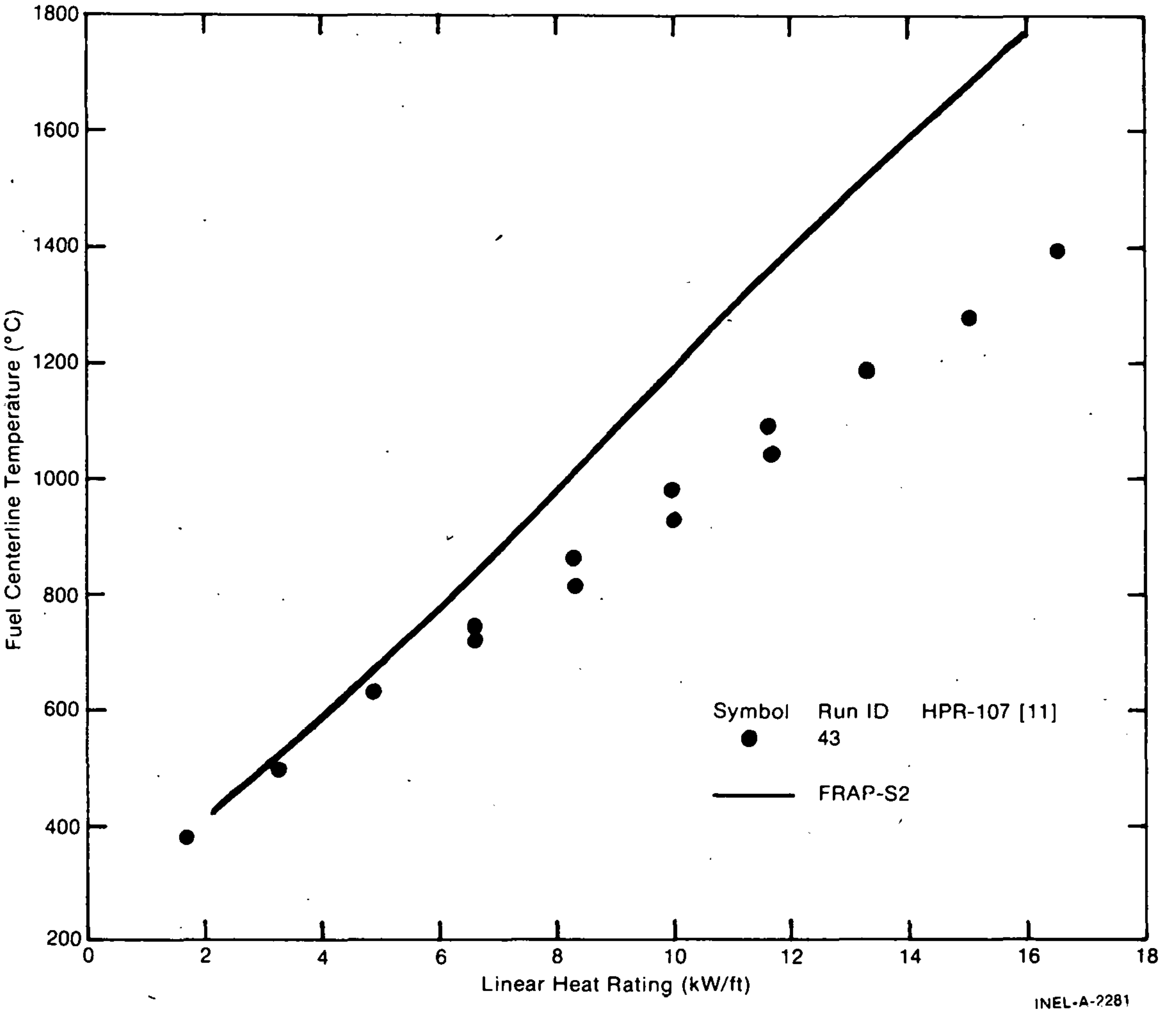

Fig. 24 Fuel centerline temperature versus power for annular pellet rod.

Ranges of fuel density (90 to 98%) and gap size (diametral gap/fuel diameter 0.40 to 3.55%) are represented on the figure.

A general trend toward overestimating fuel temperature is observed especially above calculated fuel temperatures of 1000°C. Highlighting burnup data in Figure 26 suggests that the predicted gas conductivity effect on gap conductance is too strong. The main calculated burnup effect in these cases is the variation from the initially pure helium gas composition. Figure 27 shows this point in terms of fractional temperature agreement versus the relative helium content of the internal gas mixture. A gradual increase in the amount of temperature overprediction is seen to accompany dilution of the helium fill gas due

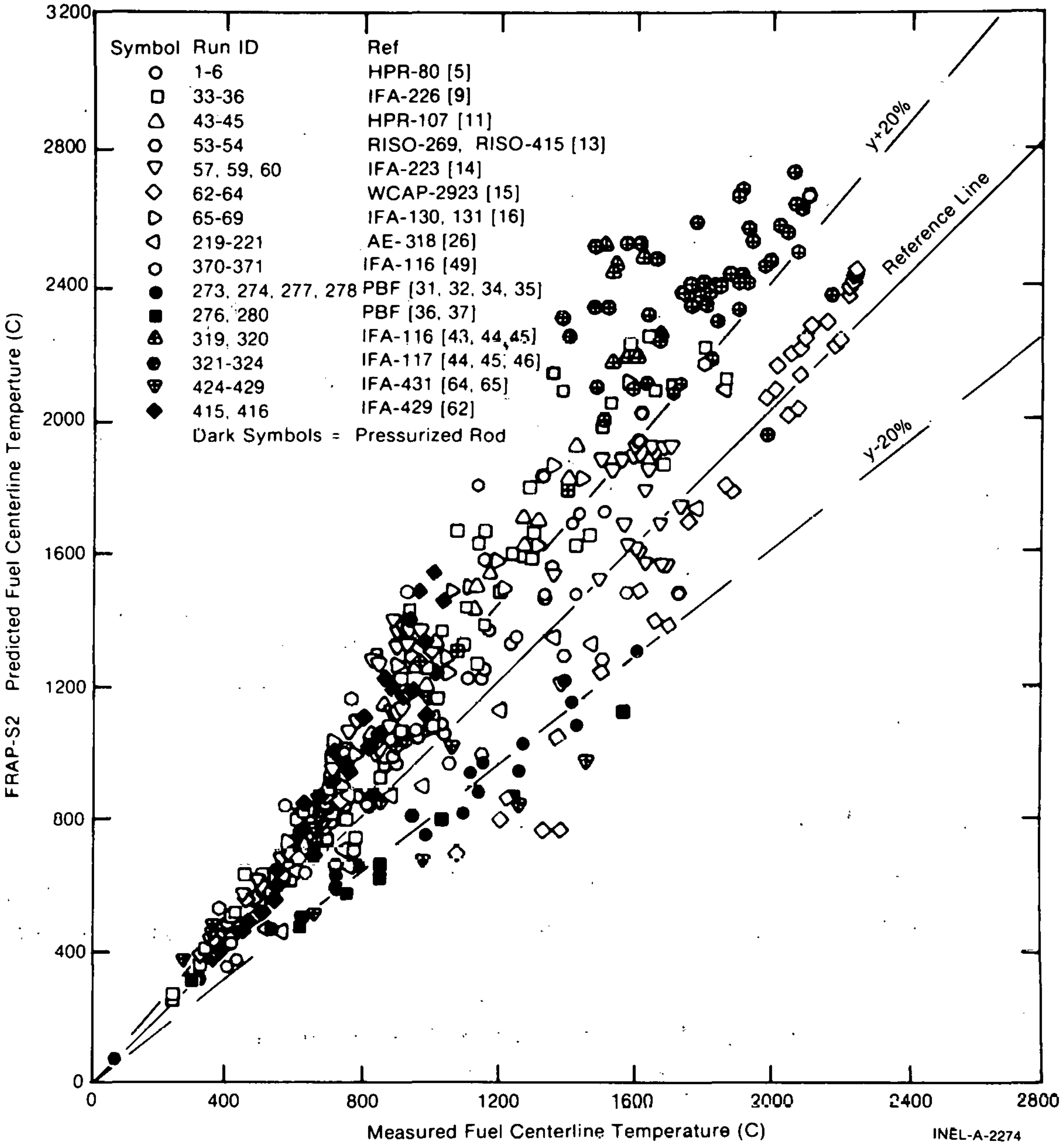

Fig. 25 Predicted versus measured fuel centerline temperature - summary results.

to gas release from the fuel. This trend is consistent with Standard Design results discussed in a previous section.

Some exceptions are noted relative to the generally observed effect of gas composition on relative model agreement. In these cases, the

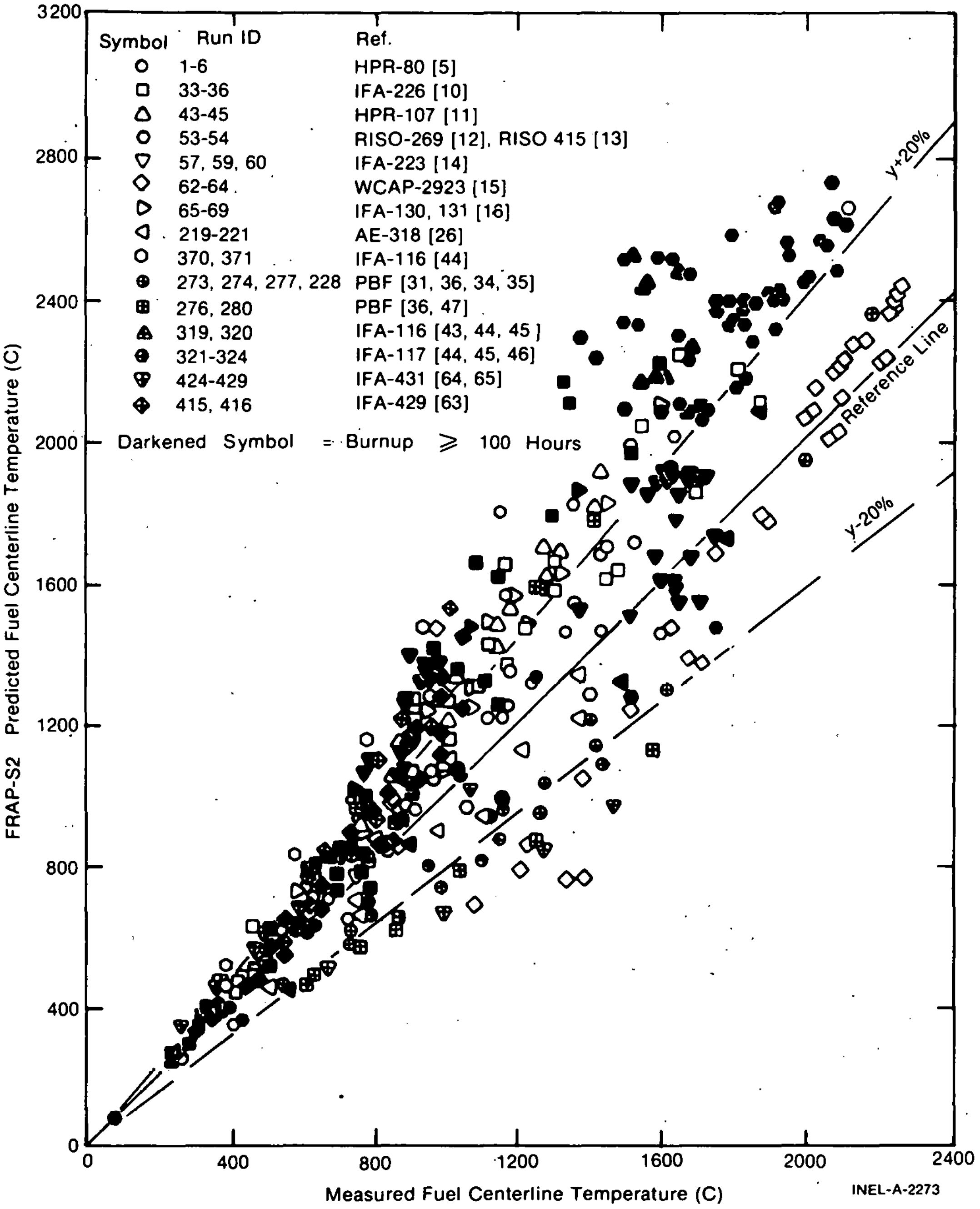

Fig. 26 Predicted versus measured fuel centerline temperature - burnup data.

rods were prepressurized, and/or were fabricated with a relatively large amount of gas other than helium in the fill gas mixture, and/or had large diameter gaps. The fill gas effect is not really amenable

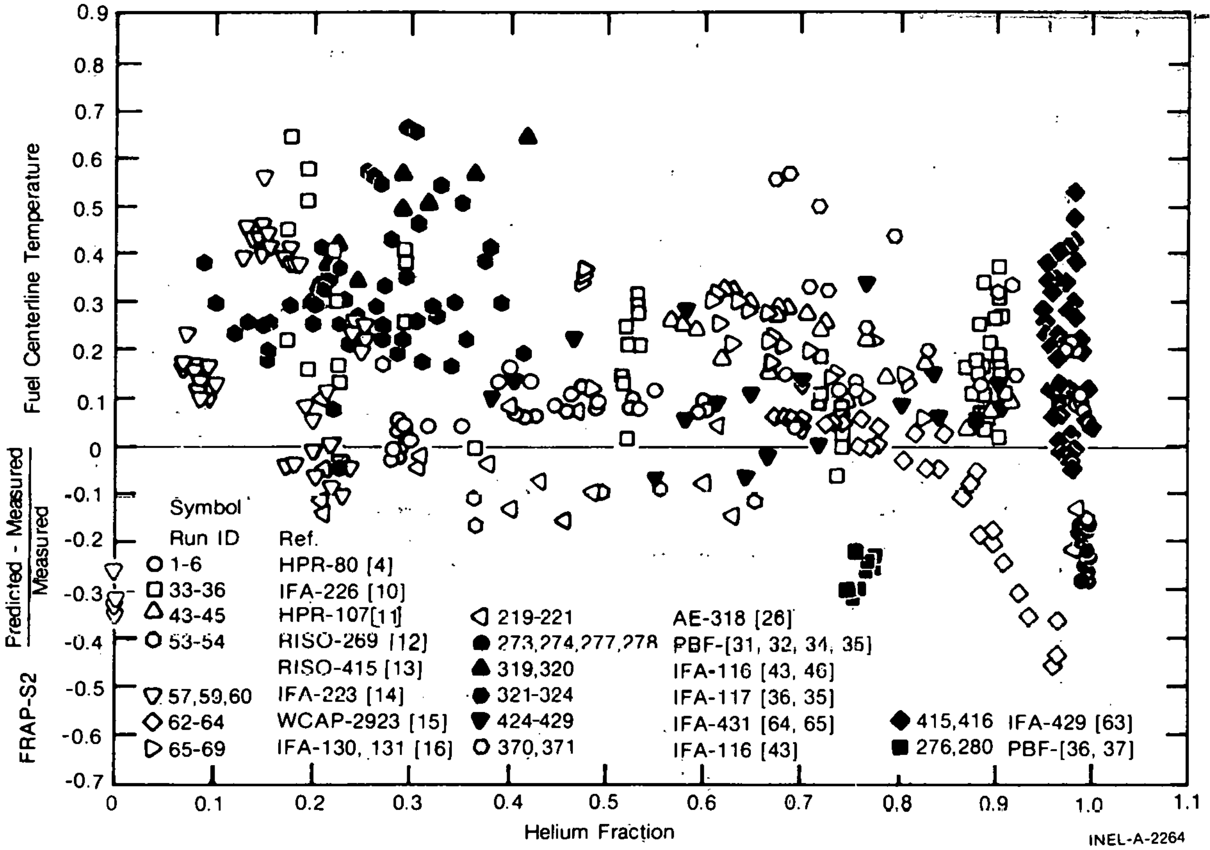

Fig. 27 Relative fuel centerline temperature model agreement versus helium fraction.

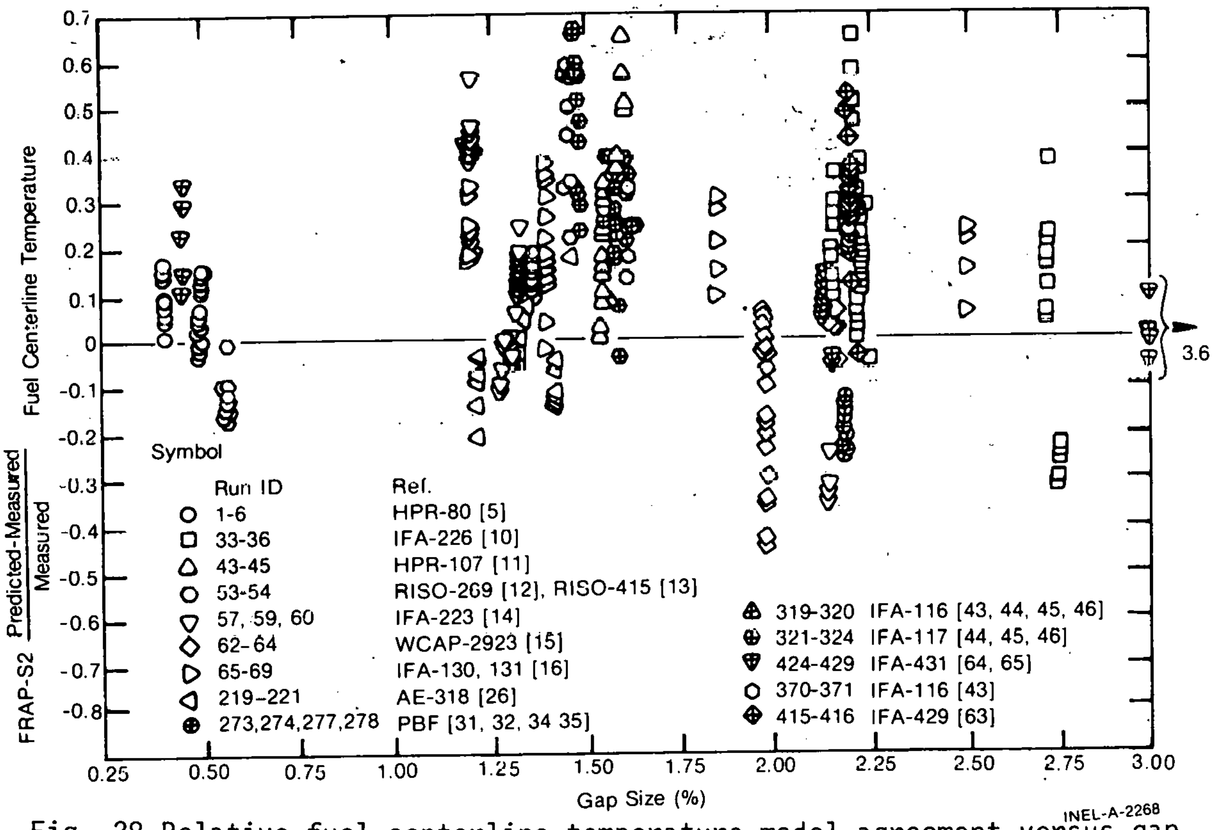

Fig. 28 Relative fuel centerline temperature model agreement versus gap size.

to further definition due to conflicting trends among the limited number of rods available. Figure 28 indicates there is less tendency to overpredict fuel temperature for very small and very large gaps. This trend supports the high contact fraction assumed in the model for small gaps as well as the assumption that at least 30% of the pellet surface will always be in contact with the cladding, even for relatively large hot gaps. Modeling attention seems warranted for the cracking and soft contact conditions expected for power reactor designs with gaps between 1.5 and 2.5%.

The fact that lack of fit in fuel cracking models has an effect on relative model agreement is indicated by Figure 29. Fuel temperatures are overpredicted more consistently at low fuel density indicating some tendency to underestimate heat transfer. Rather than pointing to an influence on the part of fuel thermal conductivity, the fuel density trend suggests that the amount of fuel cracking may be underpredicted at low density. Fuel density is a parameter whose possible structural significance is currently not considered by the pellet cracking model.

The fact that enrichment has a slight overall effect on relative temperature agreement as seen in Figure 30 may indicate that verification input is in need of some improvement. The amount of flux depression for a 5 to 9% enriched pellet rod is probably underestimated since the built-in (LASER) power distribution model is limited to the effect of 4% enrichment. This overprediction of centerline heat generation (<10%) is balanced in part by not accounting for the center instrument hole in the calculated power distribution, an effect which would tend to underpredict central heat generation by a comparable amount (<10%). An externally supplied power distribution factor[66] was used in the predictions for enrichment levels greater than 9%. Figure 30 does indicate that flux distribution input conventions do not cause any overriding effect which invalidates further interpretation of data comparison trends on the basis of design or operating conditions.

3.1.2 Gap Conductance.

For several experiments with measured fuel temperature, gap conductance values were inferred analytically (see References 5, 15, 31-37, 64, 65). In a few other cases[6,7], derived gap

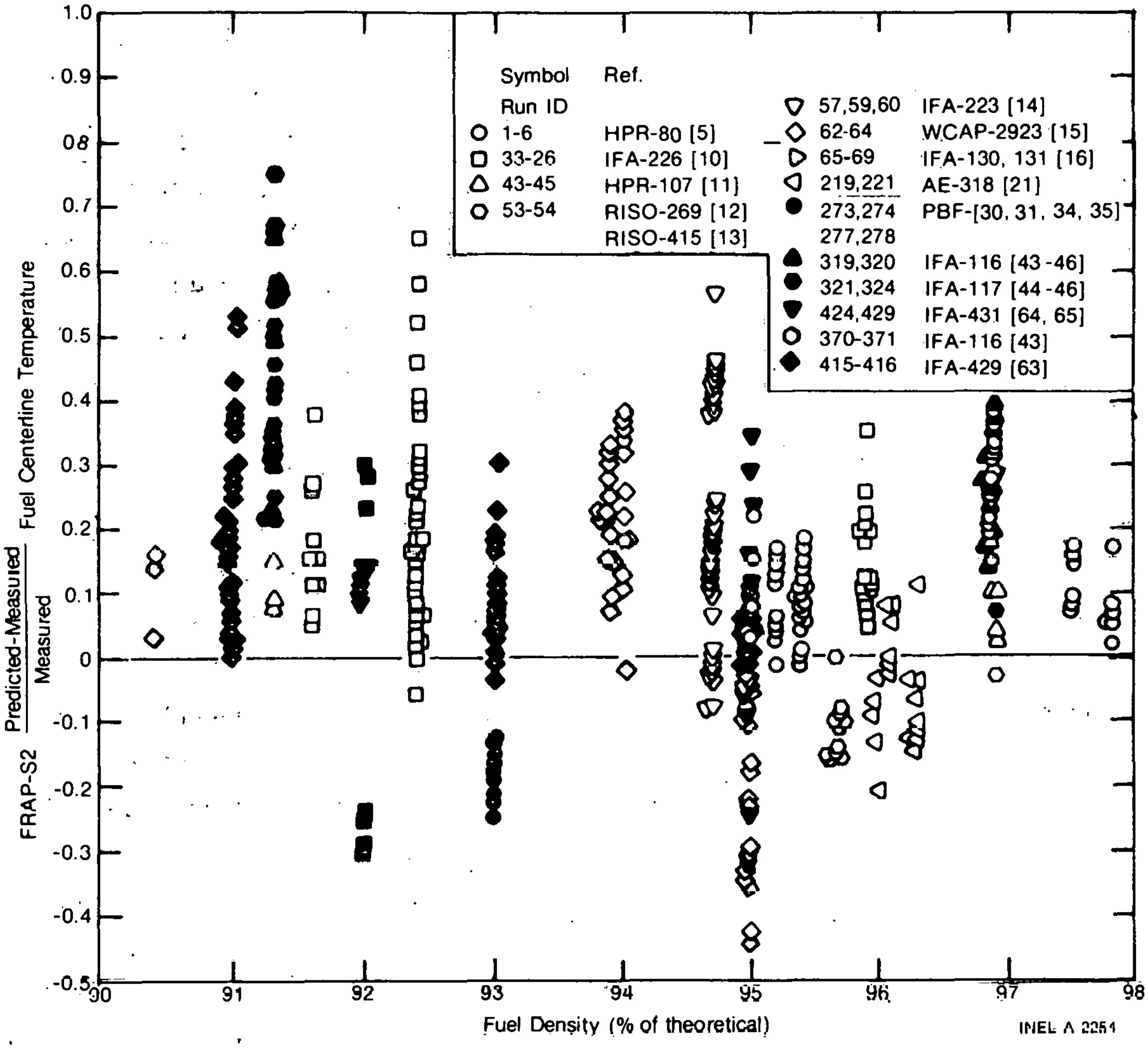

Fig. 29 Relative fuel centerline temperature model agreement versus fuel density.

conductance was based on temperature markers provided by postirradiation pellet metallography. Significant data scatter arises due to the geometric boundary nature of the mechanism (with an accompanying steep temperature gradient), together with the fact that consistent analytical methods have not been applied among test programs. Agreement between FRAP-S2 results and inferred experimental values is in this case strongly affected by similarity in material properties and analytical assumptions. For this reason, the primary gap conductance data comparisons were those which could also be associated with demonstrated fuel temperature consistency.

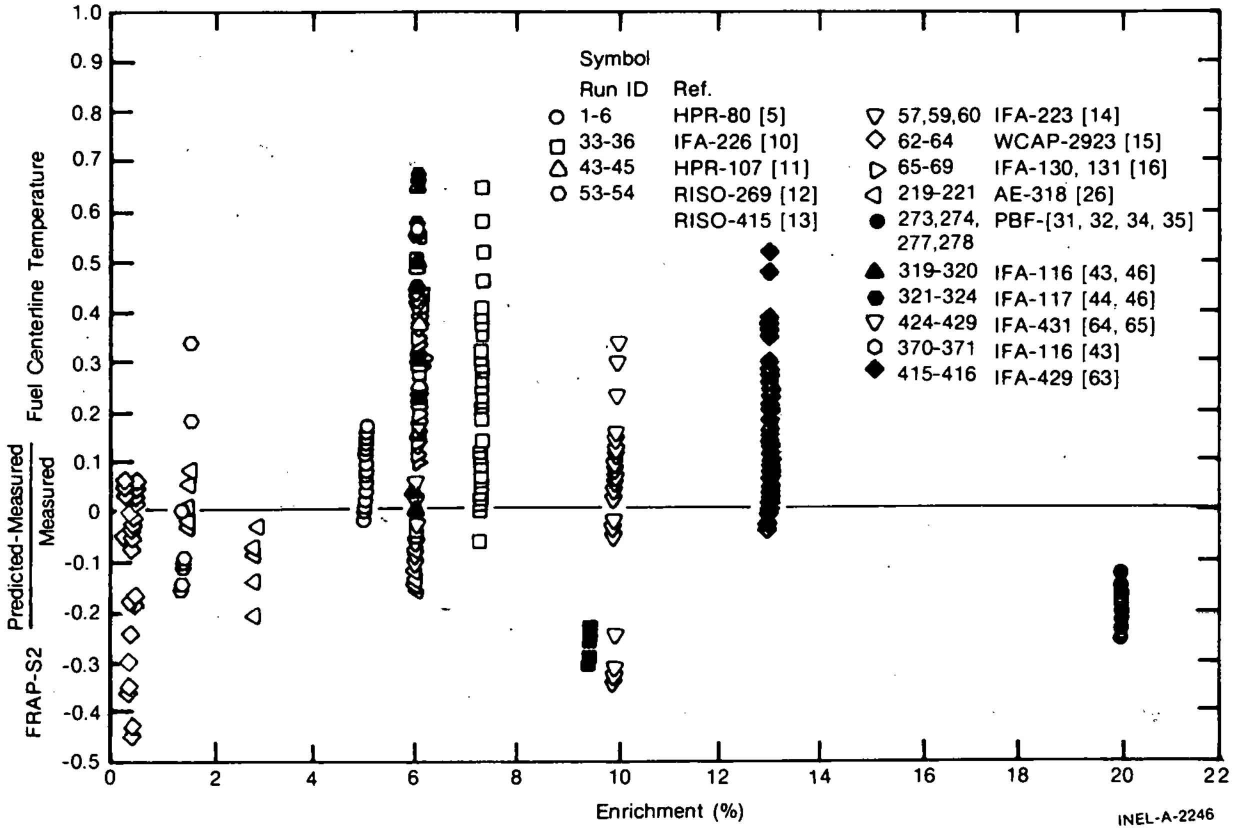

Fig. 30 Relative fuel centerline temperature model agreement versus enrichment.

Measured and predicted steady state gap conductance is shown in Figure 31 for 45 rods, 18 with fuel thermocouples and 27 with data based on postirradiation exam (darkened). Contact conductance for argon filled melt rods is better represented by the model as shown by a more uniform distribution of the PIE results about the reference line. Accuracy of models for gap closure or those contributing to gas conductivity changes do not compromise these data comparison results since the gap is definitely closed at high temperature and the gas conductivity is definitely low to begin with. Many predicted values above the (Y + 100%) line are found to correspond to rods with relatively large gaps and/or helium prepressurization.

Applicability of the gap closure model seems to have some influence on relative gap conductance agreement as shown in Figure 32. The observed trend of matching the unpressurized rod thermal data better for

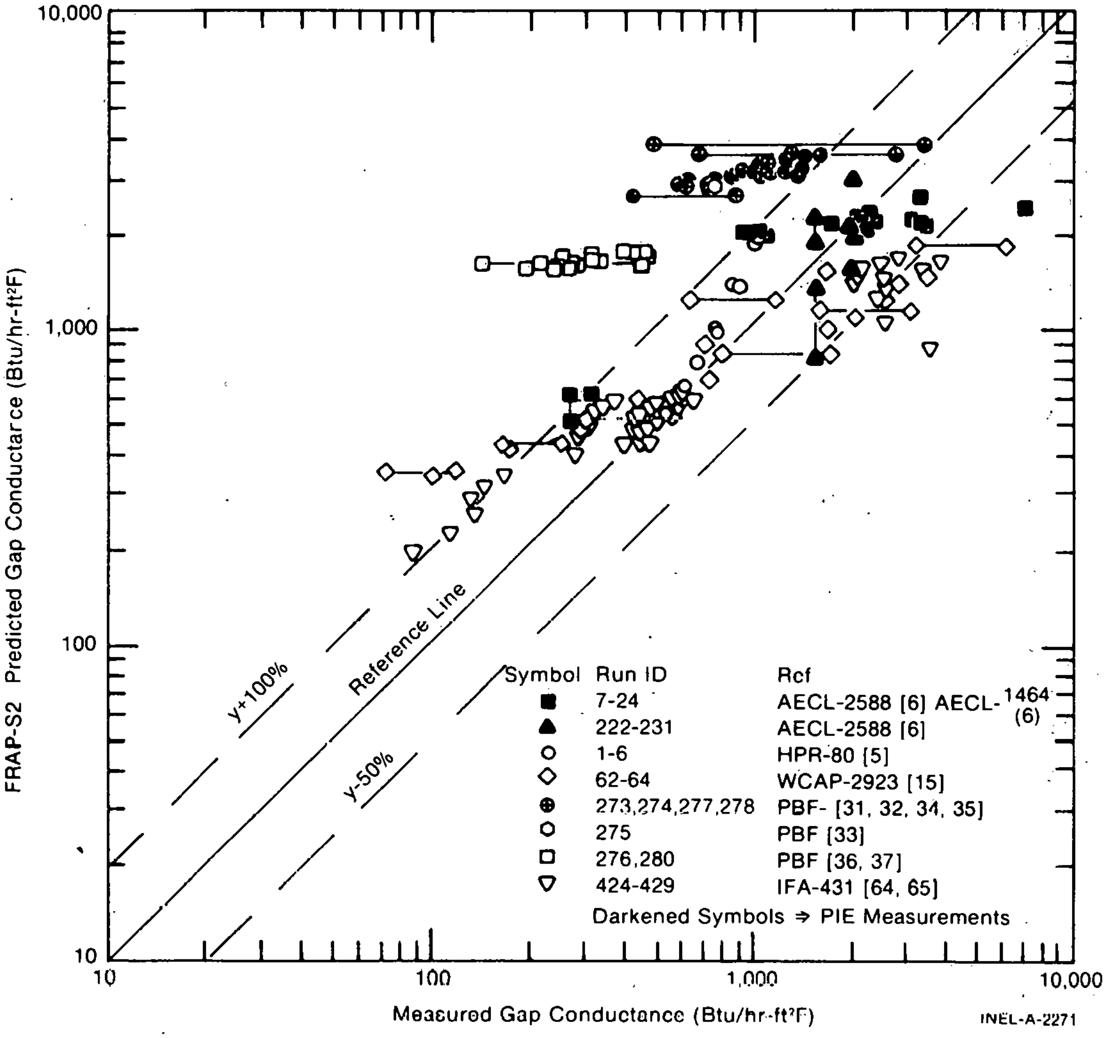

Fig. 31 Measured versus predicted gap conductance - summary results.

small and large gaps is consistent with previously discussed fuel temperature comparisons. There is also consistency between fuel temperature results and the fuel density trend shown in Figure 33. The cracking model is more supported for high density fuel in terms of closer gap conductance agreement in this range.

The fact that FRAP-S2 generally overpredicts gap conductance for this data sample is not inconsistent with the previously identified overprediction of fuel temperature for unpressurized rods. Data points available for the gap conductance comparison include a relatively larger representation of instrumented helium prepressurized rods compared with

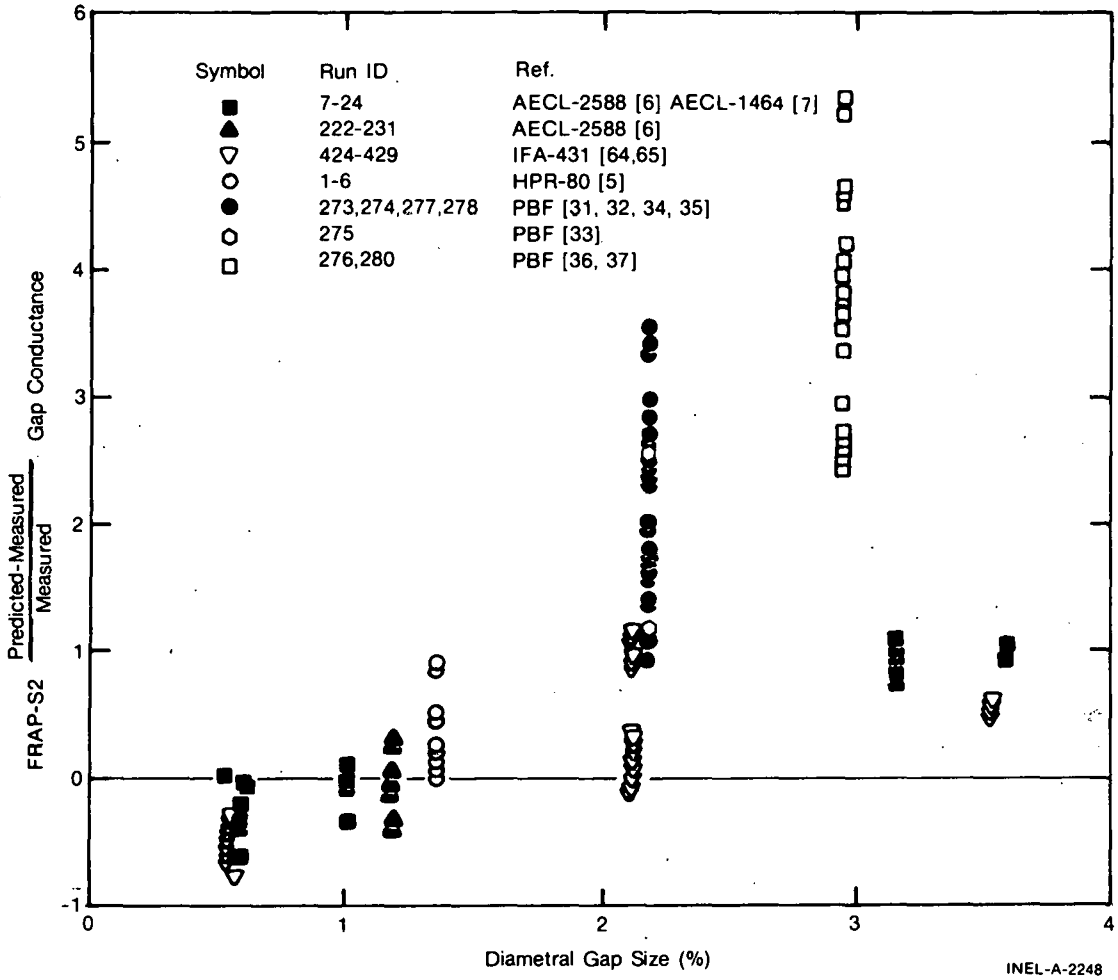

Fig. 32 Relative gap conductance model agreement versus diametral gap size.

data used for center temperature comparisons. With the exception of 2 IFA-429 rods[63], fuel temperature was shown earlier to be underpredicted for helium prepressurized rods.

Cross comparisons for instrumented rods indicated consistency in thermal model results. Overpredicting gap conductance, in other words, is most often associated with underpredicting fuel temperature, and vice versa. This correspondence indicates overall agreement in fuel thermal conductivity models between FRAP-S2 and those derived through various experimental efforts whose analytical tools provide the gap conductance data used here.

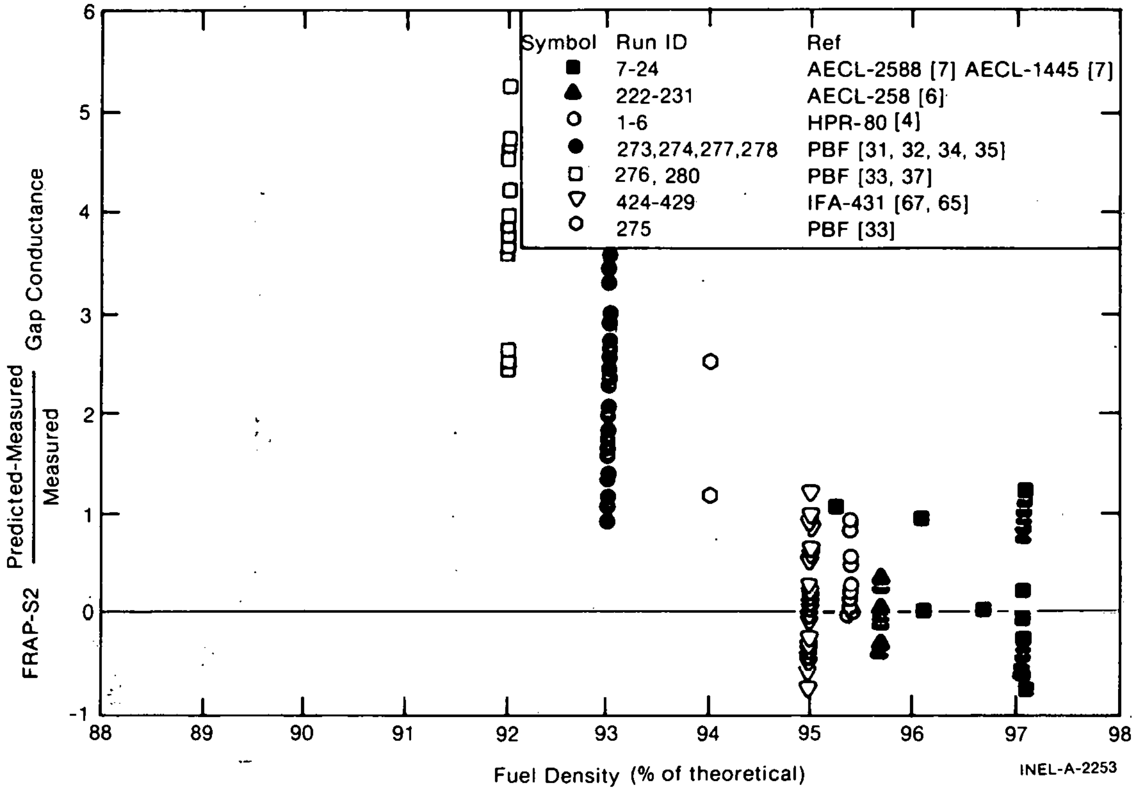

Fig. 33 Relative gap conductance model agreement versus fuel density.

3.1.3 Fuel Melt Radius. Steady power experiments with fuel melting were included in the data comparison study[6,7,23,24,27,29,30]. The intent was to characterize fuel conductivity, thermal expansion, and contact conductance models at their upper limit of application. In setting up the melt radius study, advantage was taken of an input option for allowing the code to specify stainless cladding properties. This flexibility allowed more of the available melt data[23,29] to be included in the analysis.

Due in part to the severity of test conditions, associated large data scatter, and power uncertainty, the objective of diagnosing any lack of fit in the thermal model is not achieved with good definition. Since melt cross section itself is a local measurement, the ability to characterize local power had a strong influence on results. There is also difficulty in determining the difference between operating conditions governing relatively rapid, as opposed to time-dependent, structure changes accompanying high fuel temperature. Even for relatively short-term irradiations, the different measurement techniques indicate considerable uncertainty (estimated ±20%) in the melt radius data itself.

Figure 34 shows predicted versus measured fractional melt radius from several experiments. Vertical lines show the influence of ±10% input power uncertainty on the prediction for selected points. Horizontal lines give the measurement range for cases where data based on both autoradiography and metallography are reported for the same fuel cross section. All but 5 of the 94 rods considered were large diameter specimens with argon fill gas. Most of these rods (66) were stainless clad. Measured heat ratings ranged from 13 to 40 kW/ft. Cold diametral

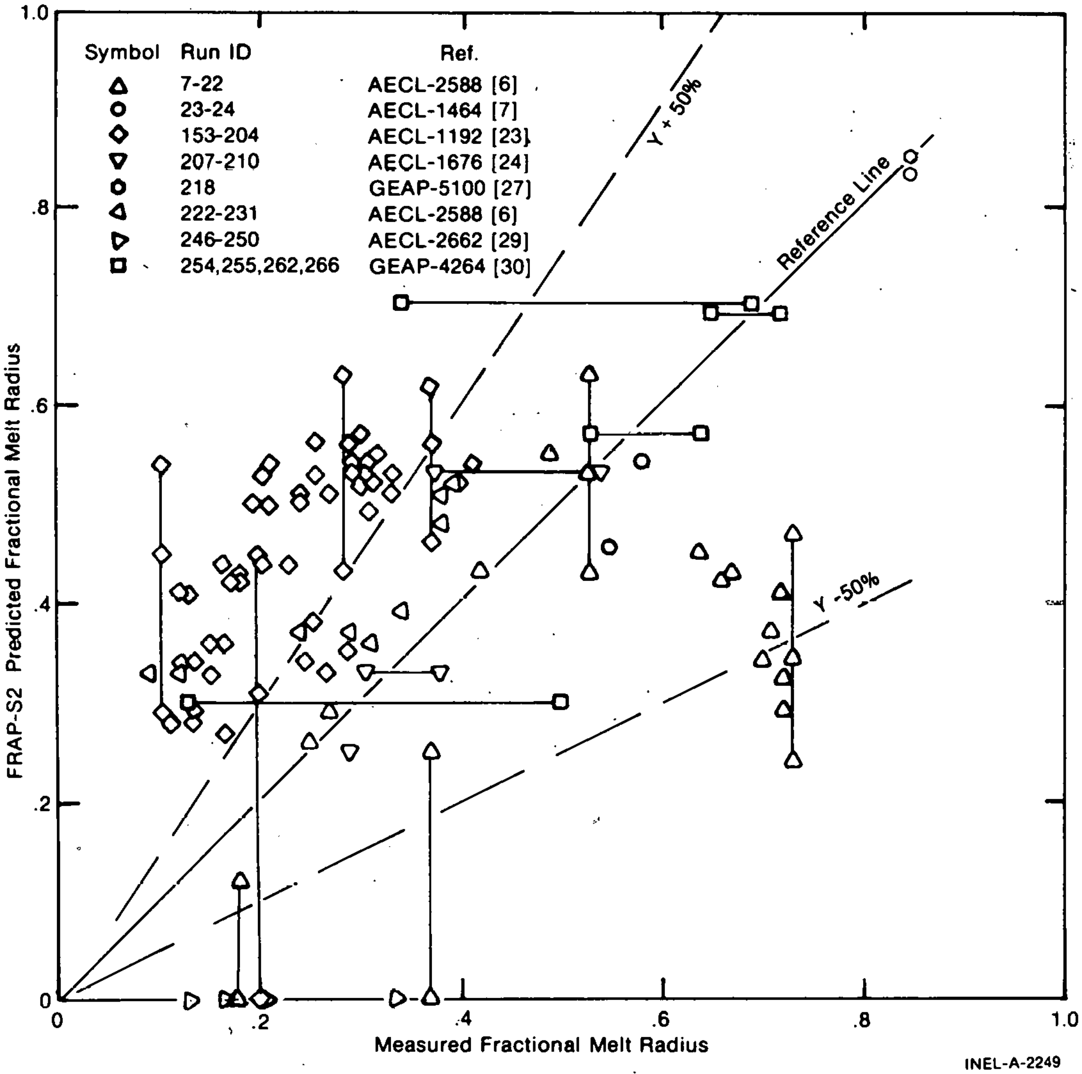

Fig. 34 Measured versus predicted fractional melt radius - summary results.

gap was between 0.8 and 33 mils with fuel density between 92 and 98%. Maximum operating time at high temperature was about 2500 hours. This range of conditions produced observed melt structures extending over from 10 to 85% of the fuel radius.

Figure 34 indicates that incipient melt conditions are not fully characterized by the code. There is only one nonzero prediction of less than 0.2 fractional melt radius. The trend of calculated values has its effective origin then at location (0, 0.2). The main reason for this is built-in nodalization for 10 equal area fuel rings in the model. The innermost mesh interval spans a pellet fractional radius near 0.3. More definition is needed over the center fuel annulus. This need arises because even the most limiting steady state overpower operation for LWR fuel is not expected to cause any extent of melting beyond incipient conditions. FRAP-T2 analysis using the same data and the same fuel thermal conductivity, power distribution, and gap conductance models showed calculated values to be within measurement reproducibility of the data[67].

No consistent trend was found relating agreement of the model with gap size, burnup, or fuel density for the melt data taken as a whole. The calculated result is more dominated by large pellet expansion, contact conductance, and nodalization regardless of design or exposure. Omitting all but zircaloy clad rods in Figure 35 does give a different distribution about the reference line. This change is mainly a consequence of eliminating short-term (3 to 40 min), hydraulic rabbit tests[23] where mainly small (<30%) melt radii were observed, i.e., beyond the nodalization capability. Underpredictions for large observed melt radius cases are associated with relatively big gaps on the order of 3%.

3.2 Fission Gas Model

Varying amount and composition of internal gas was shown in the Standard Design section to have strong influence on uniform clad strain, gap size, and fuel thermal conditions. Two types of data comparisons

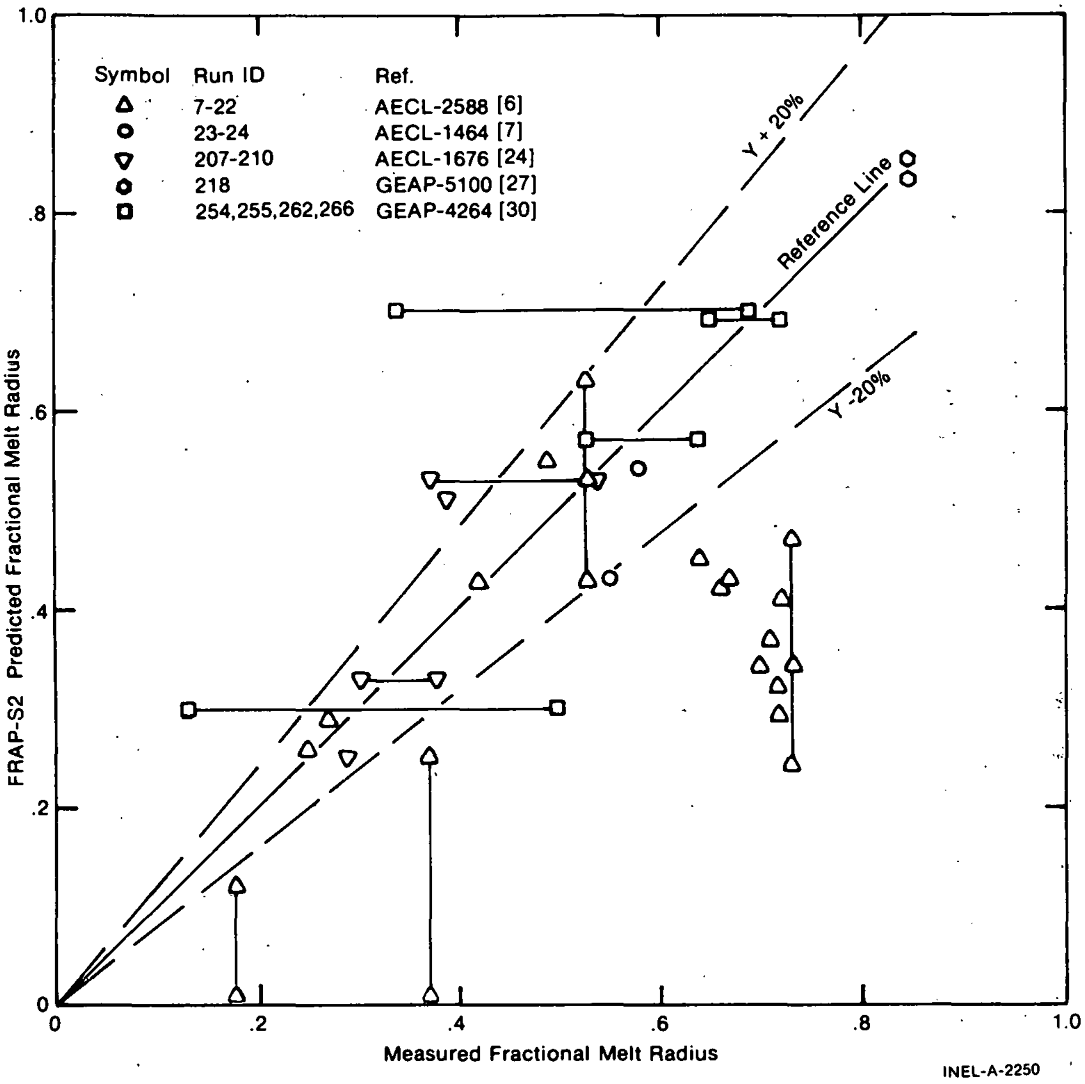

Fig. 35 Measured versus predicted fractional melt radius (Zr-clad rods).

were performed to characterize ability of the code to track buildup of fission gas and internal pressure. The mechanisms are important for determining cladding stress conditions, rupture behavior, and fission product release for accidents involving core depressurization.

3.2.1 Gas Release Fraction. Fractional gas release will be discussed first since interpretation of results is less dependent on being able to model rod internal void volume changes. Predicted versus measured fractional release is shown for several groups of rods in Figure 36. The rods represent nonpressurized PWR, BWR, HBWR, and NRX (AECL) fuel types operated at various steady state power levels with

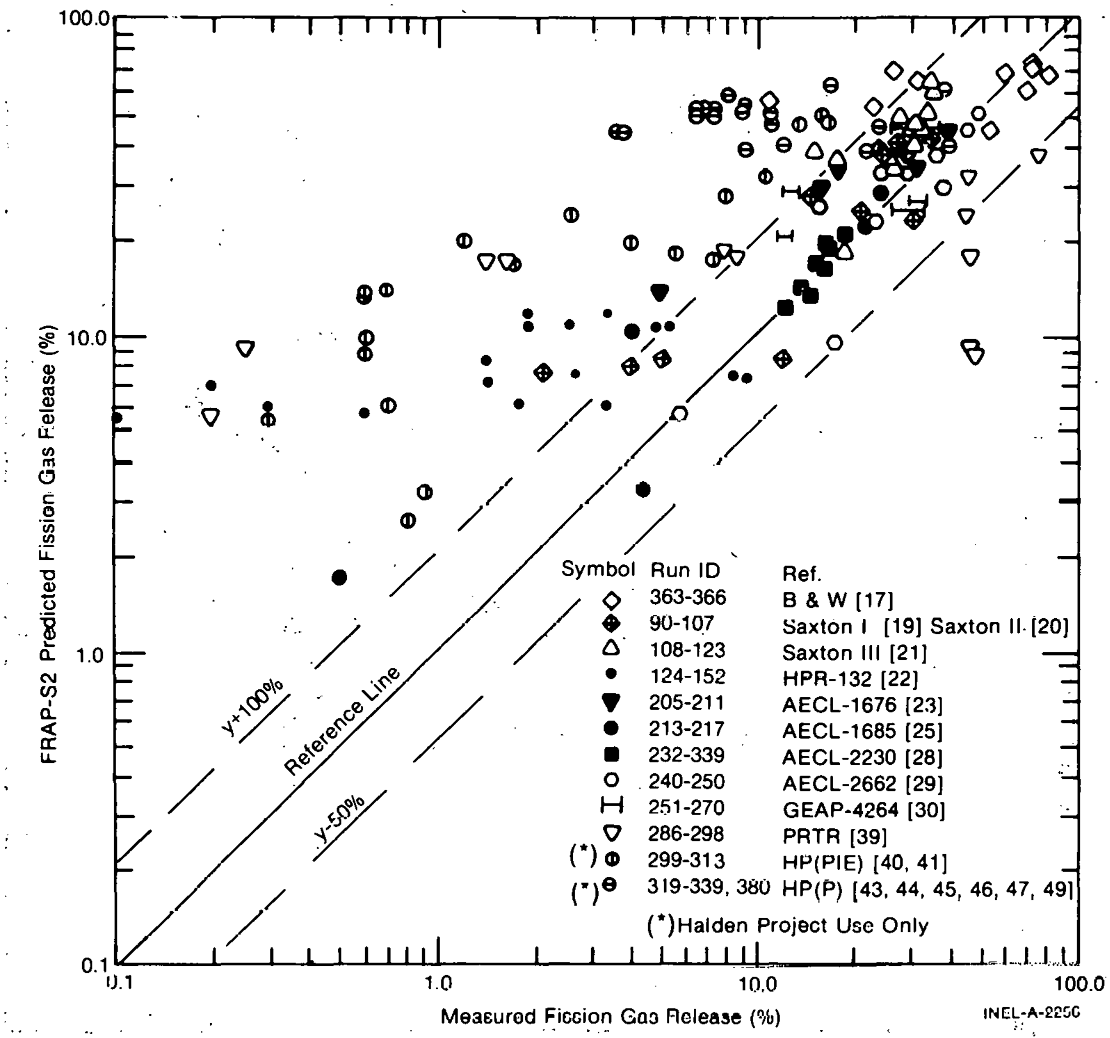

Fig. 36 Measured versus prediction fission gas release - summary results.

surplus cooling and periodic shutdowns over a range from low temperature to gross melt conditions.

The comparison indicates that gas release is generally overpredicted, consistent with the general overprediction of fuel temperature shown earlier for unpressurized rods. The gas release model is itself dominated by strong fuel temperature dependence as shown in Figure 37.

It is observed that the model better represents the relatively high temperature experiments[17,24,25,28-30] with observed release fractions greater than 10%. Rod power history for these cases is usually based on time averaged heat rating with few details available concerning the

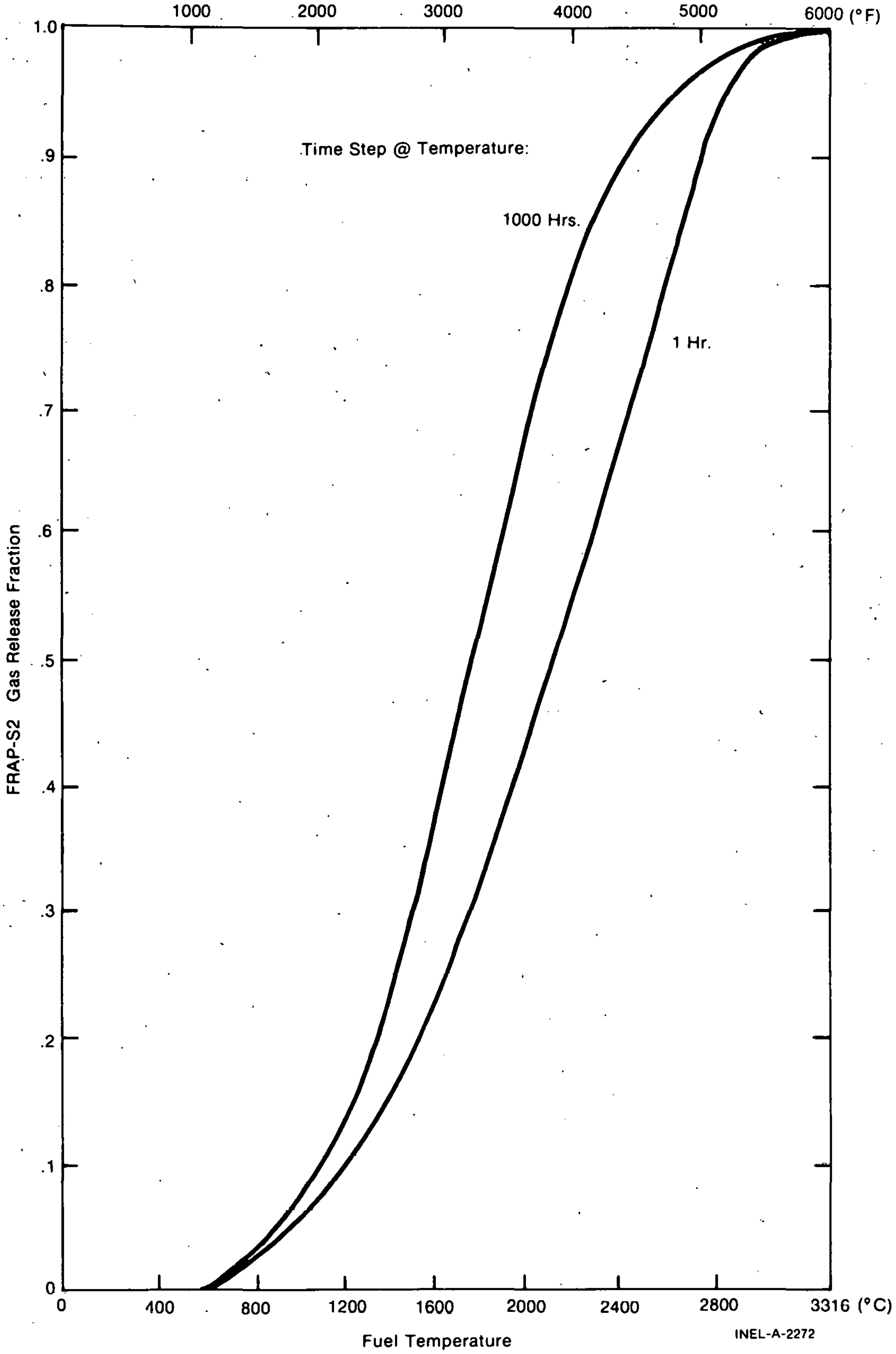

Fig. 37 Calculated gas release fraction versus fuel temperature.

relatively short-term power changes which undoubtedly occurred. Nevertheless, relatively sustained high fuel temperatures dominates these cases and causes significant gas release to be both observed and predicted.

Gas release for experiments having more detailed power history input and more moderate operating conditions[19-22,39,40,45,46] seems to be overpredicted at low and moderate burnup and better characterized by the model at high burnup. This trend indicates that the assumption of instantaneous gas bubble equilibrium implied by the model may not always be applicable to rods experiencing occasional short-term periods of high power during a longer term irradiation. For many of the Halden rods[22,40,45,46] (maximum irradiation time 9500 hours), preferential release of previously generated gas during peak power operation is predicted on the basis of fuel temperature alone. The data indicate that it is possible for periodic fuel temperatures above 2000°C to have relatively little effect on cumulative gas content. Low observed gas release for these moderate burnup conditions may be due to some combination of pellet structural properties, porosity distribution, incomplete gas bubble coalescence, or relative abundance of gas bubble trapping sites. Higher burnup Saxton data[20,21], on the other hand, for rods with late life (15 to 18,000 hours) power increases, show gas release greater than 10%. This observation is consistent with enhanced fuel damage and gas bubble channeling at high burnup. In this case, the physical condition of the fuel can be more associated with the instantaneous release assumed by the model. Retained fission gas is able to quickly respond to current fuel temperature conditions because gas bubbles already occupy preferential release locations at grain boundaries.

Figure 38 shows that the tendency to overpredict gas release is more pronounced when the calculated peak fuel temperature is between 1400 and 2400°C. This temperature range corresponds to the rapid transition from low to high gas release used by the current model (Figure 37). The effect of fuel temperature on the calculation may be too strong since the empirically derived gas release model incorporates data reflecting dependence of gas release on parameters other than fuel temperature, for example the coupling between bubble diffusion processes and fuel structure.

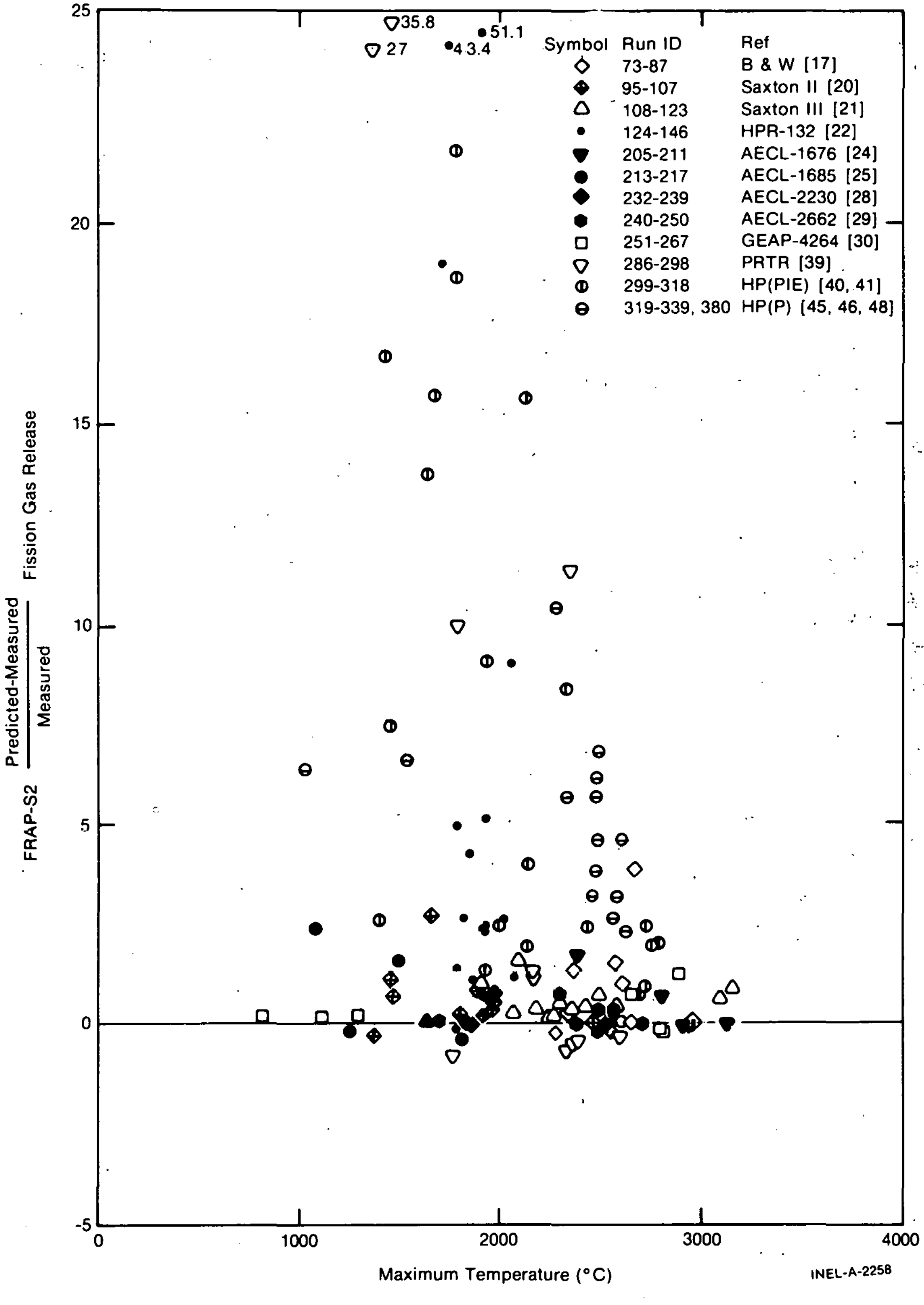

Fig. 38 Relative fission gas release model agreement versus maximum fuel temperature.

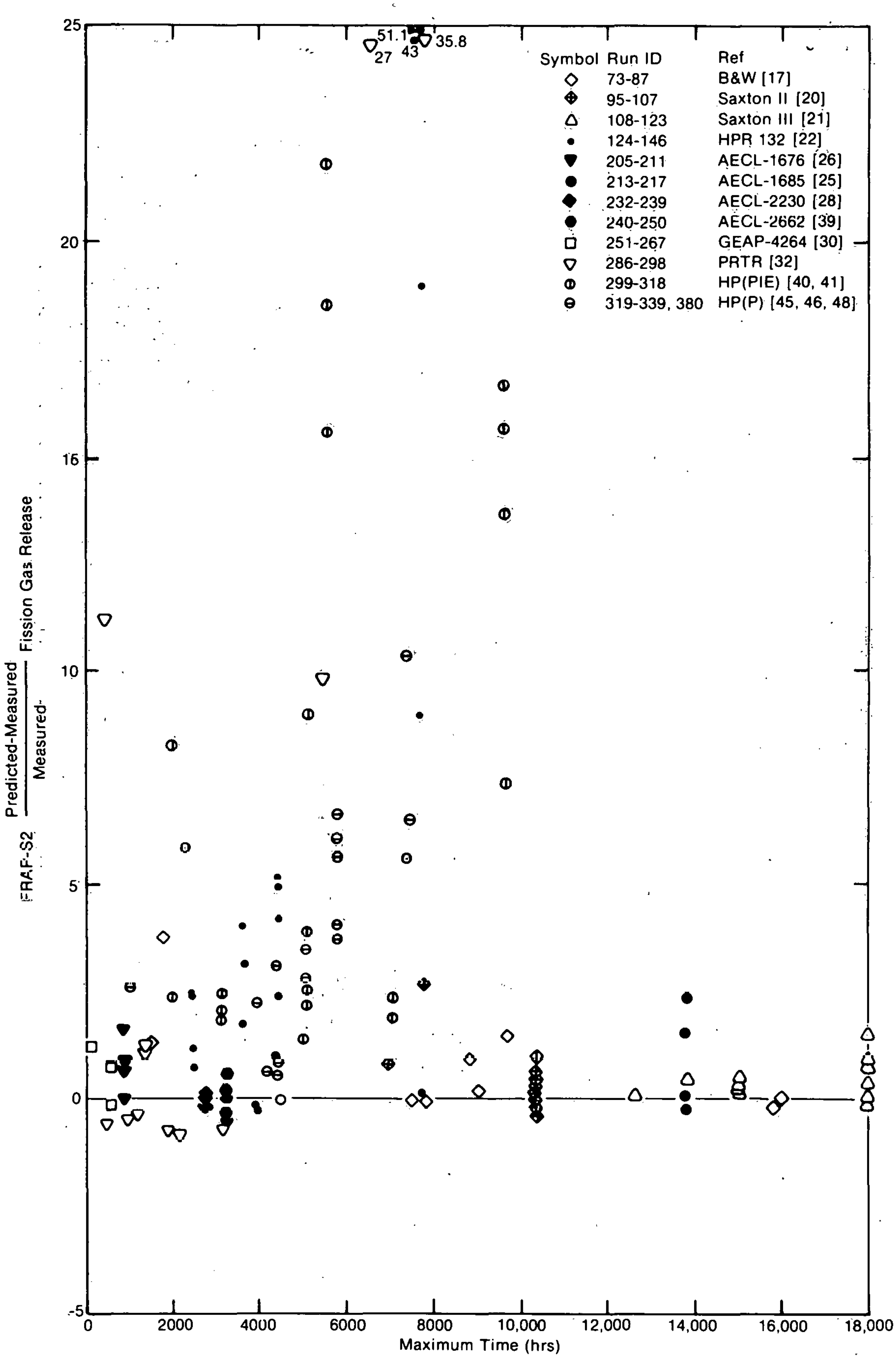

INEL-A-2259

Fig. 39 Relative fission gas release model agreement versus maximum irradiation time.

Figure 39 supports the contention that lack of a mechanistic treatment of fuel cracking and bubble disposition in the gas release model affects the relative agreement in spite of strong influence on the part of calculated fuel temperature. This is said because there is a trend of decreasing overprediction versus operating time. Operating time should be at least roughly proportional to the number of shutdown and startup periods during which fuel cracking and discontinuous gas release are likely to add to the temperature dependent release. Relative overprediction of temperature dependent release by the model is seen to decrease as the influence of burnup and load-follow dependent release (not considered by the model, but manifest in the data) increases.

Figure 40 shows relative model agreement versus fuel density, a design parameter which should have some mechanistic significance in terms of fission gas retention within the fuel matrix. In this case, either overestimation of fuel temperature or the overly strong sensitivity of calculated gas release to fuel temperature precludes further diagnosis of this modeling effect. Without more low density data being considered, their seems to be no physical basis for density alone to cause the observed trend in relative gas release overprediction.

3.2.2 Rod Internal Pressure. Mixed results were obtained when operating pressure measurements were compared with FRAP-S1 predictions for various[10,16,29,31-37,44,47,56,63,65] experiments. Ability of the code to track fission gas behavior is strongly dependent on the calculated fuel temperature distribution. Also, even if plenum temperature is well characterized by knowing external system conditions, comparisons are confounded by unknown differences between predicted and actual plenum void volume changes. Another factor affecting pressure results is that fuel stack volume changes resulting from mechanical deformation are not considered by the model, nor are gas absorption or evolution by mechanisms other than temperature dependent release.

Sample size has been expanded for rod internal pressure measurements. Relative agreement between early life data and calculated

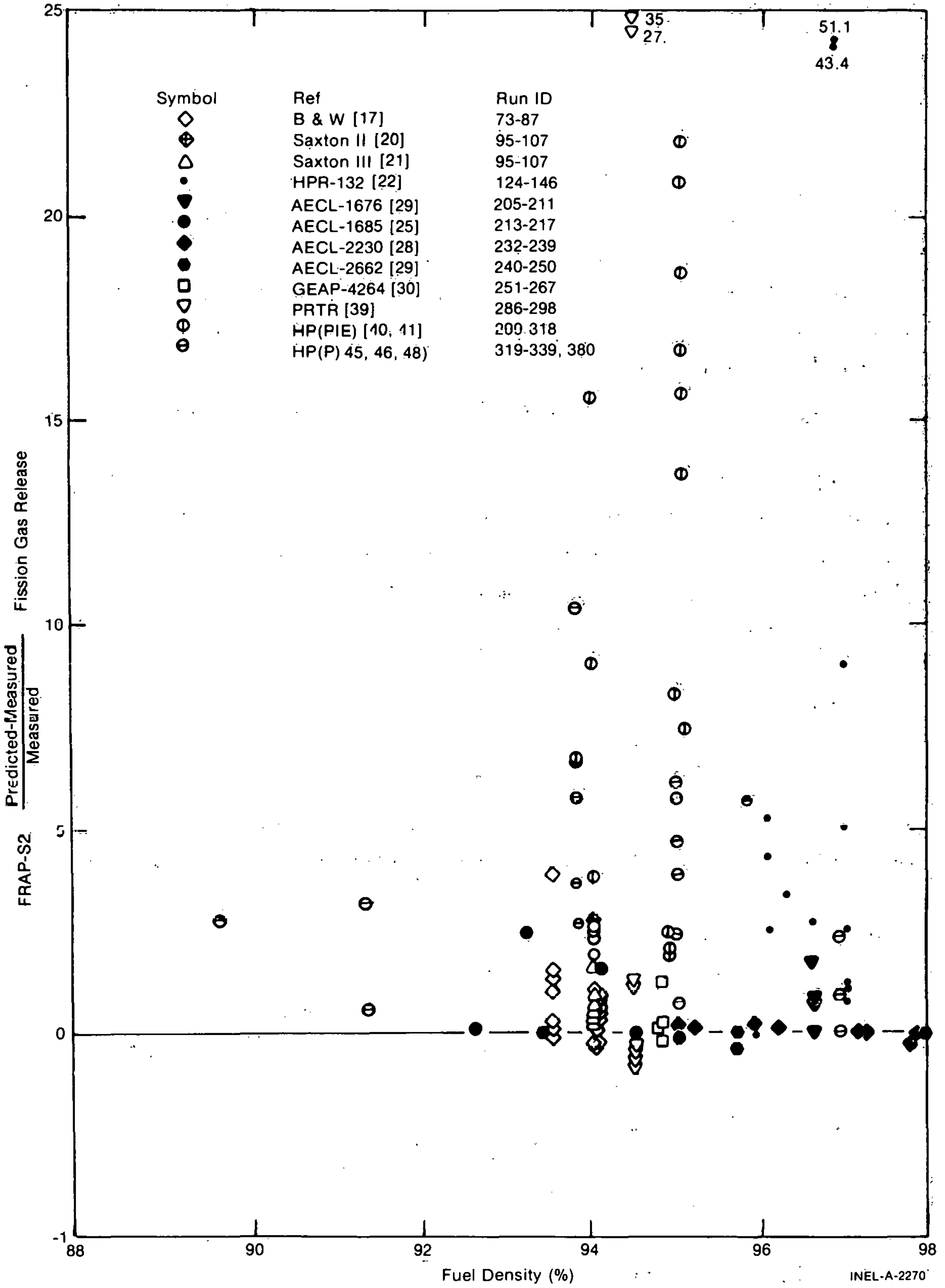

Fig. 40 Relative fission gas release model agreement versus fuel density.

pressure is evaluated separately in order to benchmark the fuel heatup effect on void volume and gas temperature. Basic gas volume and temperature response at startup initially establishes the rod operating pressure. Interpretation of higher burnup comparisons reflects additional dependence of the results on performance of the gas release model.

Figure 41 shows measured versus predicted rod internal pressure for all of the data considered. The results are scattered since the effects of heatup alone on gas volume and temperature should be separated from the effects of prepressurization and gas release on the amount of gas considered by the model. Darkening symbols reflecting heatup only[10,31-37,56,63] reveal the general trend that operating pressure is better characterized by the model at beginning-of-life, regardless of fill gas pressure. Importance of active length void volume and temperature assumptions used by FRAP-S2 is better illustrated in Figure 42, which shows relative model agreement versus plenum volume fraction for the heatup data. Increasing sensitivity of relative model agreement is observed as the plenum volume fraction decreases, i.e., as the model result becomes more governed by the active length contribution to temperature-to-volume ratio terms in the ideal gas law. This sensitivity indicates relatively strong pressure effects due to gas void volume and temperature assumptions for rods in the commercial design range between 5 and 10%.

As shown in Figure 43, relative agreement for burnup data versus irradiation time shows more tendency to overpredict pressure for rods with plenums and underpredict pressure for rods without plenums (darkened symbols). The plenum rod results are dominated by overprediction of fuel temperature and gas release for unpressurized designs. Calculated release of large amounts of gas during periodic high power operation is responsible for the highest overpredictions. Limited data beyond 11,000 hours of operation indicates that the instantaneous release model (i.e., solely dependent on temperature) is better applied at higher burnup. This observation, based on pressure comparisons, is consistent with gas release trends discussed earlier. Comparison

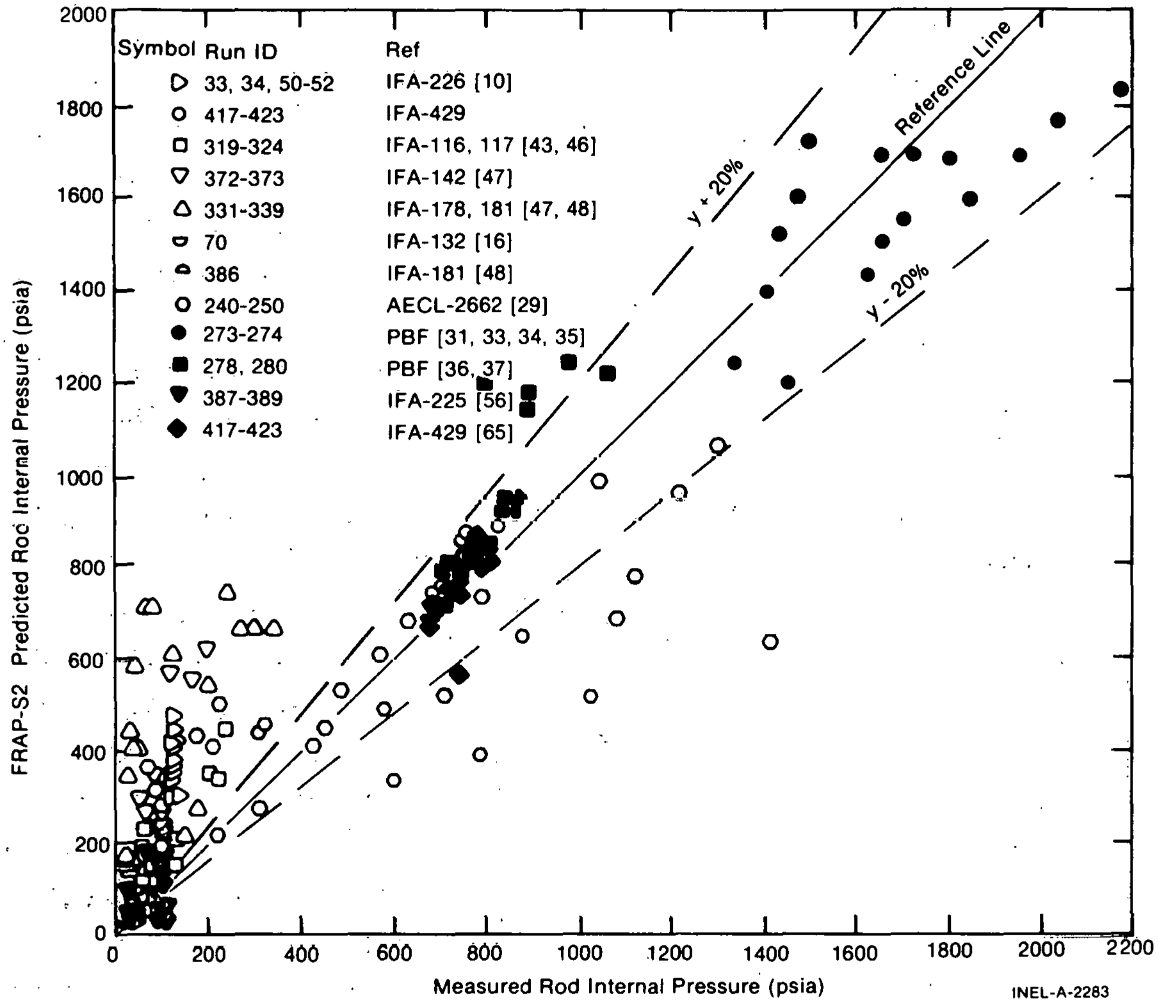

Fig. 41 Measured versus predicted rod internal pressure - summary results.

results for rods without plenums show the expected influence (underprediction of pressure) of applying the relatively low fuel surface temperature value to active length void volumes.

3.3 Rod Deformation Model

Various comparisons were performed to determine capability of FRAP-S2 in account for steady state fuel and cladding deformation. Previous results from high burnup Standard Design runs[3] indicated that representing fuel thermal expansion in the current model accounts for much of the through-life volume change in full-size rods. Other Standard Design results have shown that PCMI and creep deformation of the cladding have strong influence on gap size at initiation of a transient. Fuel

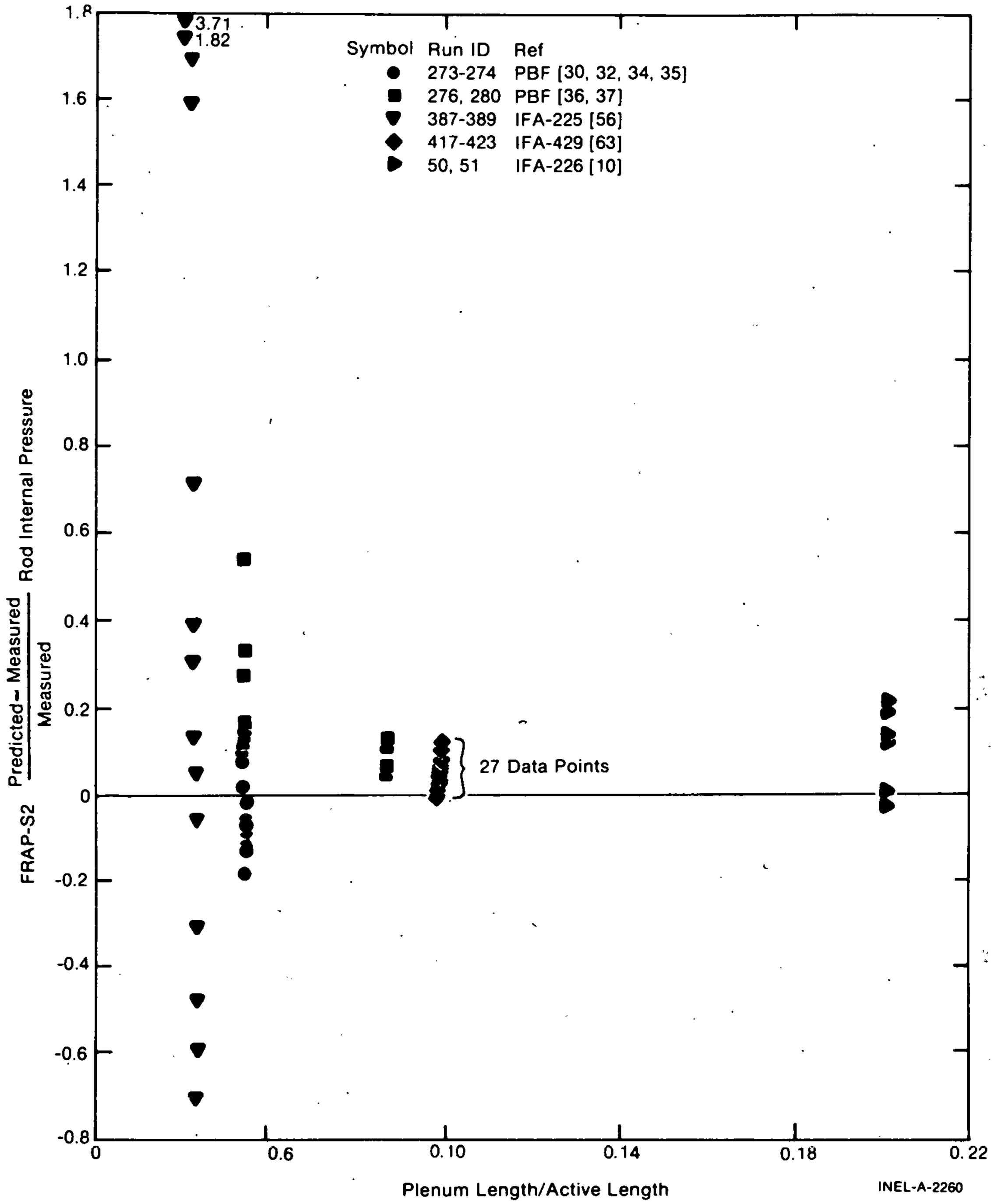

Fig. 42 Relative rod internal pressure model agreement versus plenum volume fraction - heatup data.

thermal expansion results are shown first, followed by discussion of fuel permanent deformation and then cladding axial and circumferential strain.

3.3.1 <u>Fuel Stack Thermal Expansion</u>. Figure 44 shows measured versus predicted fuel stack axial expansion relative to the cladding

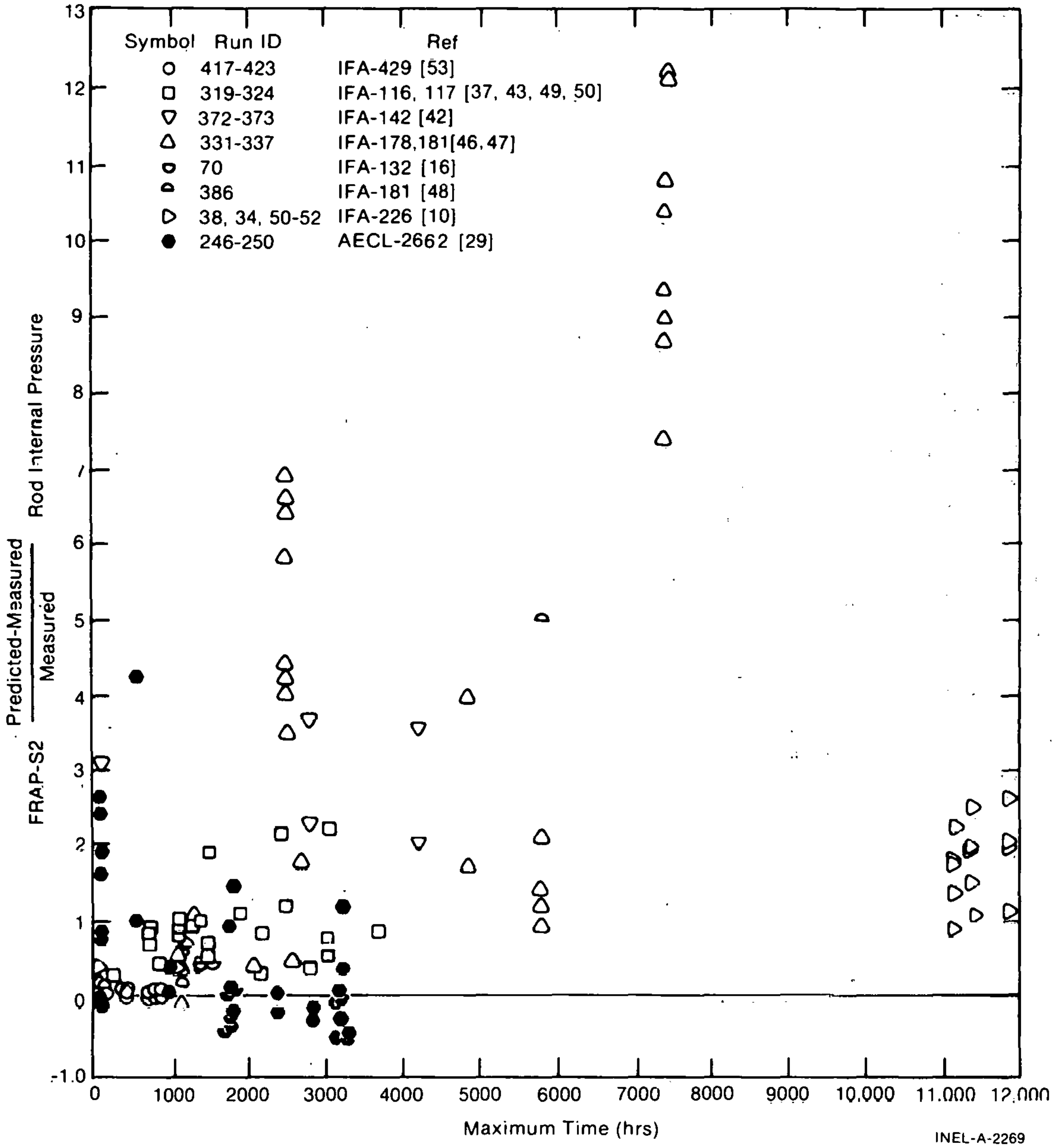

Fig. 43 Relative rod internal pressure model agreement versus maximum irradiation time.

during startup power ramps for 6 dished and 2 flat pellet rods[11,42,48,49]. For dished and flat pellet rods the governing temperature for predicted axial expansion is set respectively at the fuel shoulder and centerline. Thermal expansion is better represented by the model below about 0.3%, i.e., at relatively low power levels when PCMI is less likely to affect the data. Beyond this point, axial expansion is overpredicted since the often observed mechanism of nonuniform gap closure at relatively low power is not predicted by the annular gap model in FRAP-S2. Since the

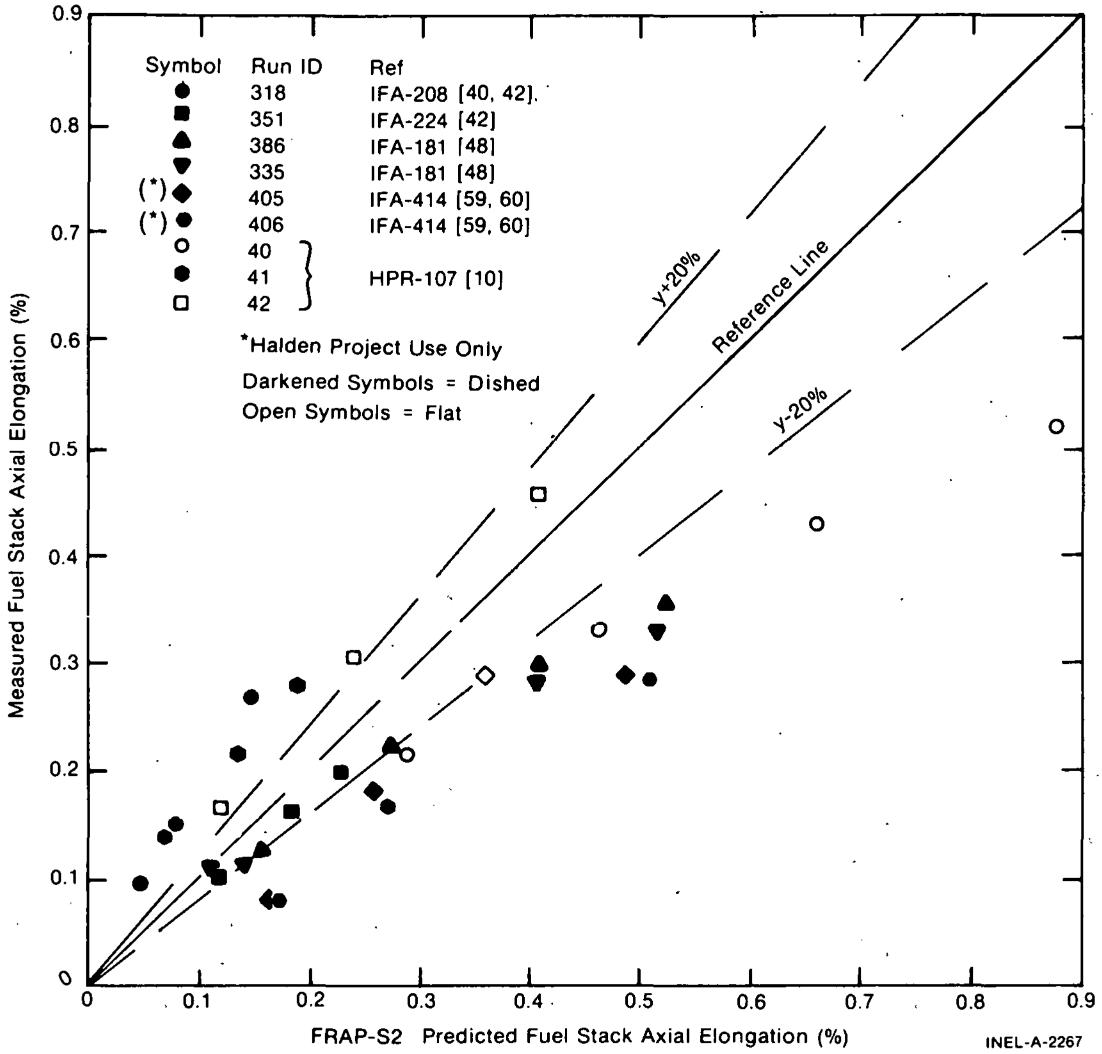

Fig. 44 Measured versus predicted fuel axial elongation - heatup data.

instruments in these cases monitor fuel expansion relative to the cladding, the data affected by PCMI show a decreasing fuel expansion rate and an increasing cladding expansion rate after the onset of gap closure. Lack of fit in gap closure mechanics obscured quantitative trends in relative model agreement with respect to rod design or validity of the governing temperature assumption for dished or flat pellet designs. Larger expansion is both measured and predicted for the undished fuel.

3.3.2 Fuel Stack Permanent Deformation. The main burnup effects contributing to permanent stack volume changes are some combination of swelling, densification, and creep/hot pressing. The latter two mechanisms can compete with swelling until the extent of their influence decreases due to saturation of porosity and stress accommodation in the fuel. FRAP-S1 had a swelling model but did not include fuel mechanical deformation or densification models. FRAP-S2 has both fuel swelling and densification but no mechanical deformation model.

Figure 45 compares measured and predicted permanent fuel stack length changes[18,50,53,54,57,59]. Most of the data points are from

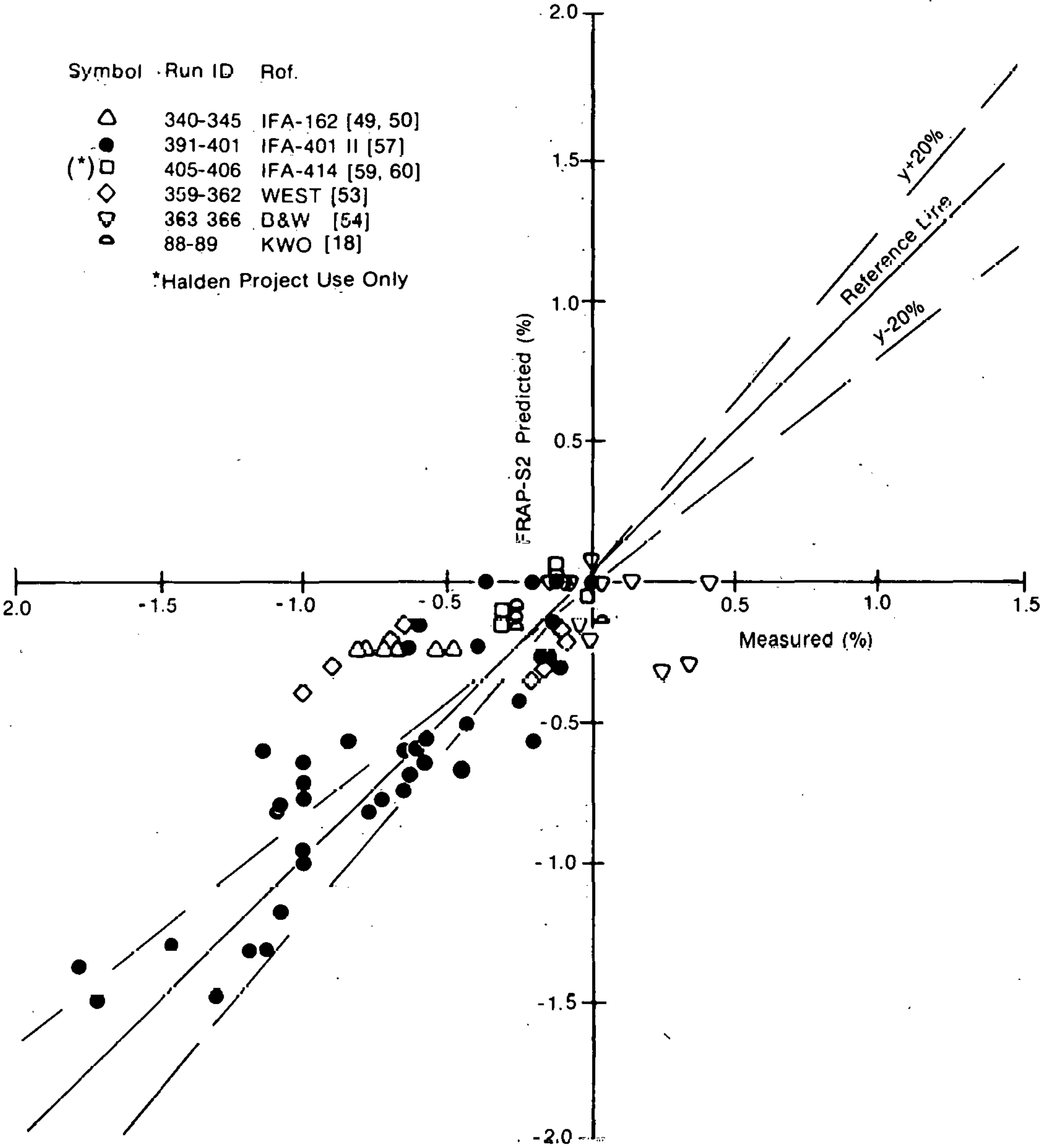

Fig. 45 Measured versus predicted fuel stack permanent elongation - summary results.

experiments[54,57] intended to investigate the magnitude of fuel densification and thermal stability effects on axial gap formation. In these cases, operating conditions and rod design were chosen to minimize influence of PCMI on experiment results. Few rods had high enough burnup to result in enough fuel swelling to produce net positive length changes.

The model result is seen to be somewhat more consistent with those measurements corresponding to its own densification data base[57] (darkened symbols). At least some stack shortening then, is always predicted to occur using the nominal model which is based on sintering temperature, fuel density, and irradiation time. For other experiments where PCMI was actually observed[50] or was more likely to have occurred[18,53,59] due to differences in gap size and power history, stack length change is underestimated. This coincidence indicates that at least some amount of stack shortening is dependent on stress in addition to irradiation induced densification. This fact is illustrated when relative model agreement is plotted versus gap size in Figure 46. With increasing gap, the relative number of individual rod comparison points below the reference line suggests that there is additional tendency for stack shortening to be underpredicted. This observation is consistent with less applicability of the uniform gap closure model as gap dimension increases. Since the correspondence between stack axial length change and fuel density change is not treated by the model, direct densification measurements available for two other experiments[38,52] have not been compared with code predictions.

3.3.3 Cladding Deformation. It has not been well established how prior cladding deformation affects high temperature transient performance. Some rod bowing was seen in early fuel designs under normal operation where inadequate assembly clearance was provided. For test rods, maximum total and permanent cladding axial elongation beyond thermal expansion is typically very small, (respectively less than 0.5 and 0.2%) with considerable slip evident during mechanical interaction. It is also observed that stack shortening is a competing mechanism when gap closure during power increase results in axial compression of fuel.

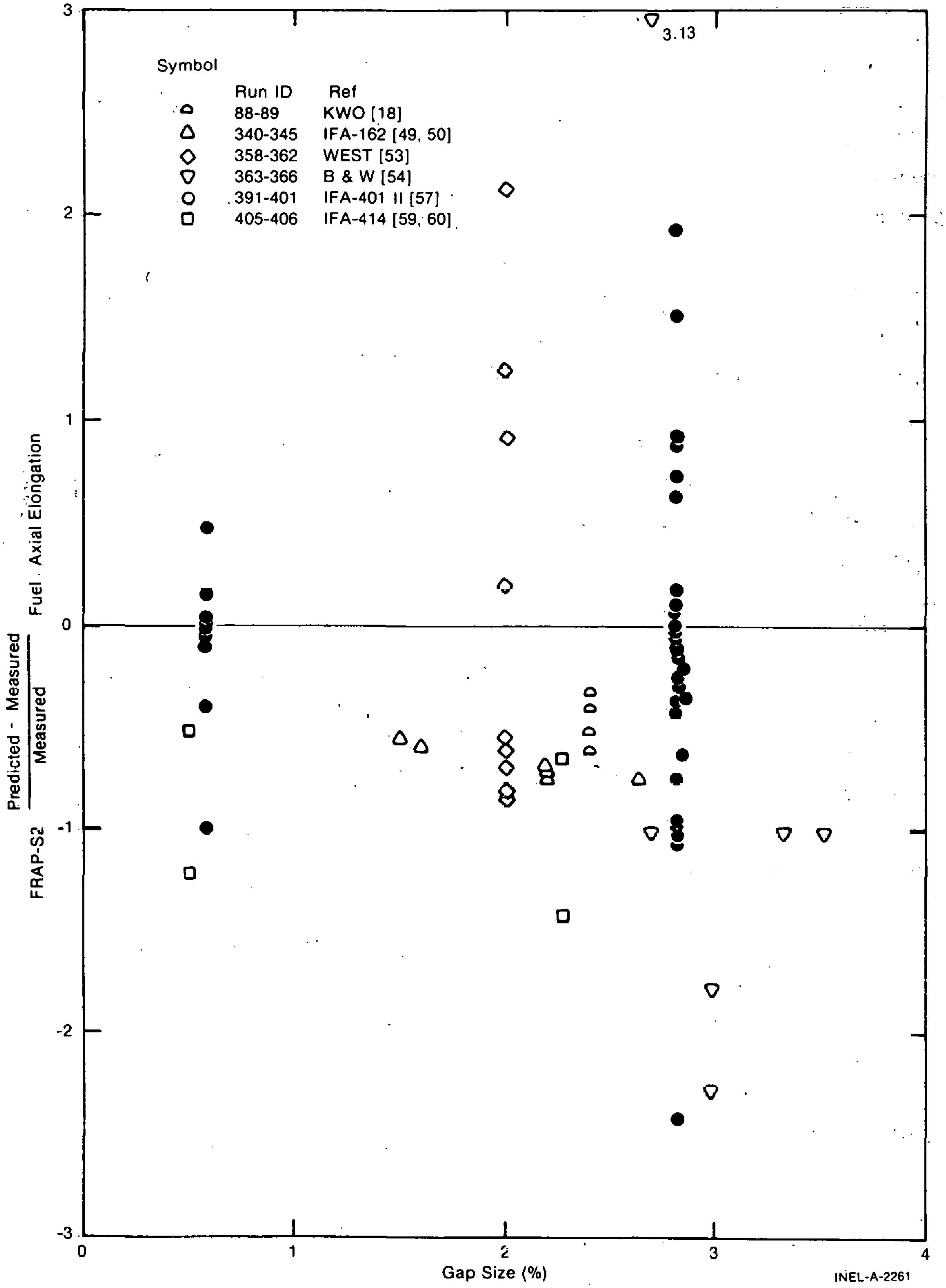

Fig. 46 Relative fuel stack permanent elongation model agreement versus gap size.

In the more limiting hoop direction, strain concentration in rods which have been power cycled under normal conditions without adequate break-in has been observed to increase failure probability from nonuniform mechanical interaction. Based on uniform mechanial considerations[67], some interaction failures apparently involve other mechanisms of the stress corrosion type. Where rods experience extended operation without long-term tensile stresses from local gap closure, permanent decreases in diameter occur from compressive creep strain.

It is desirable for FRAP-S to be able to characterize initial gap size for transients from the standpoint of gap heat transfer, mechanical interaction, and gas flow. Cladding deformation input to the transient code accounting for prior strain hardening or accumulation of mechanical damage may also be needed in subsequent code versions. The efficiency with which high temperature annealing can consolidate mechanical properties under accident conditions for rods with prior operation is not well known.

(1) Cladding Axial Strain. The two main contributors to permanent cladding axial deformation are PCMI and irradiation induced growth. PCMI is the dominant mechanism when it occurs. Correlation data[4] indicate that irradiation normally causes rod length changes less than 0.05%. Instrumented rod elongation data suggests that ratchetting preferentially occurs at startup or when prior heat rating is exceeded.

Figure 47 compares measured and predicted permanent length change for zircaloy clad rods. The figure shows that there is no measurement greater than 0.5% even though experiment conditions span a range from low fuel temperature to observed central melting. Predicted elongation is normally observed to be very small, in the narrow range between 0 and ±0.025%. A much larger range of elongations are calculated for a few cases however. These cases correspond to rods with small gaps (<0.5%) and/or high enough fuel temperatures to finally result in calculated

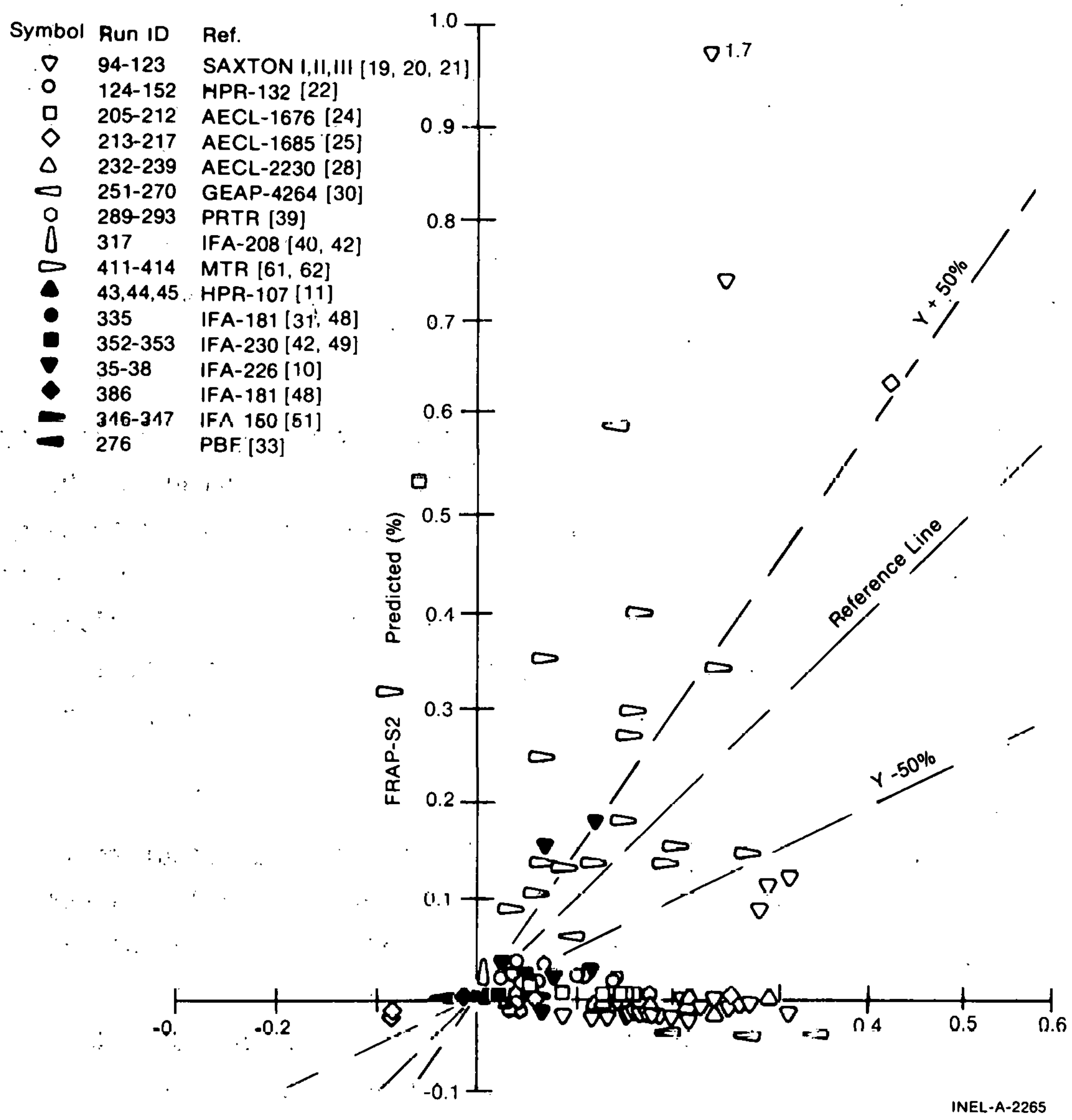

Fig. 47 Measured versus predicted permanent cladding elongation - summary results.

PCMI. It is the extent of mechanical interaction then which is underestimated by the annular gap closure model for rods in the small prediction range near zero.

As shown in Figure 48 by the distribution of points above the reference line, PCMI effects are overpredicted by the model for gap sizes <0.5%. Otherwise, axial strain was more frequently underestimated with increasing gap size, the exceptions corresponding to fuel temperatures above 2000°C (darkened). This is not an unexpected trend given

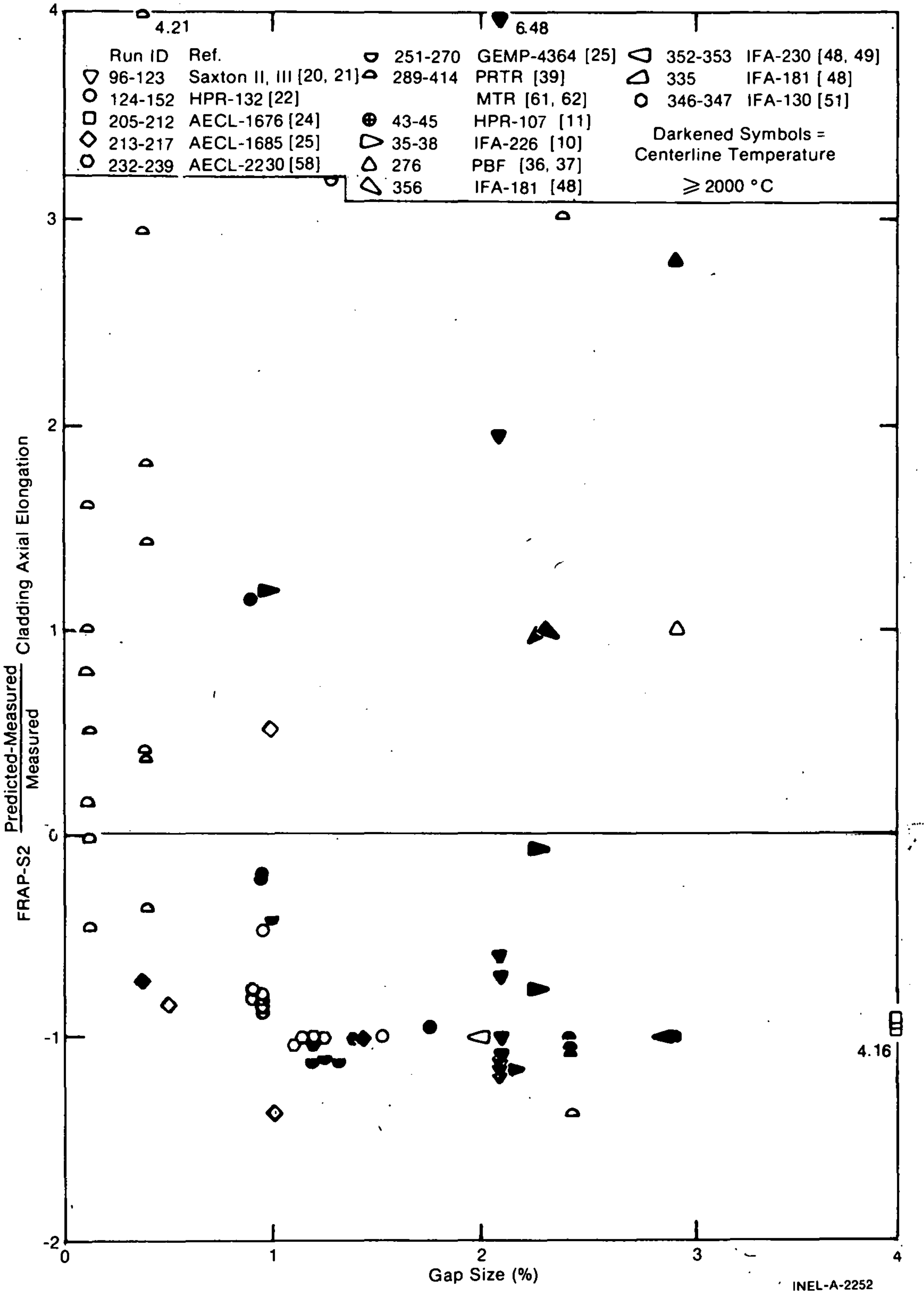

Fig. 48 Relative cladding permanent elongation model agreement versus gap size.

that relative error introduced by the annular gap closure model would increase as gap size went in the direction of allowing more space for nonuniform fuel relocation to occur.

Figure 49 suggests that in the axial direction, gap closure rather than fuel temperature or lack of fuel mechanical deformation has more influence on the relative model agreement. The tendency of the model to underpredict PCMI continues to be evident, even to some extent beyond 2000°C. If gap closure were calculated in this temperature range, cladding strain would be overpredicted due to coincidence of high thermal expansion and lack of modeling fuel mechanical deformation. The few cases for which cladding strain is overpredicted are in fact observed in Figure 49 to correspond with rods having gap sizes $\leq$0.5% (darkened) or rods with fuel temperature $\geq$2000°C. The model, in other words, underpredicts the extent of gap closure, but once calculated, overpredicts the consequences of gap closure. The effect of large fuel thermal expansion on the cladding strain is not appreciably moderated by deformation of the fuel imposed by cladding restraint.

(2) Cladding Circumferential Strain. Many permanent hoop strain data comparisons were performed using FRAP-S2. The source for most of the data is postirradiation exam. Comparing instrumented rod data between strain gauges mounted over pellet midplanes and interfaces shows strong localization of mechanical effects leading to ridge formation at the interfaces. The model, on the other hand, treats each axial interval of active length uniformly. All the difference between calculated hoop strain then at various elevations is attributable to axial power distribution and not fuel relocation. As such, the model is more representative of average cladding deformation associated with pellet midplane locations.

Figure 50 shows measured versus predicted permanent cladding hoop strain for zircaloy rods. Again, wide variation in experiment conditions is responsible for occurrence of a range of measurements between -1 and +6.5%. Negative strain measurements correspond to relative lack of extended PCMI and dominance of compressive creep mechanisms. Strain

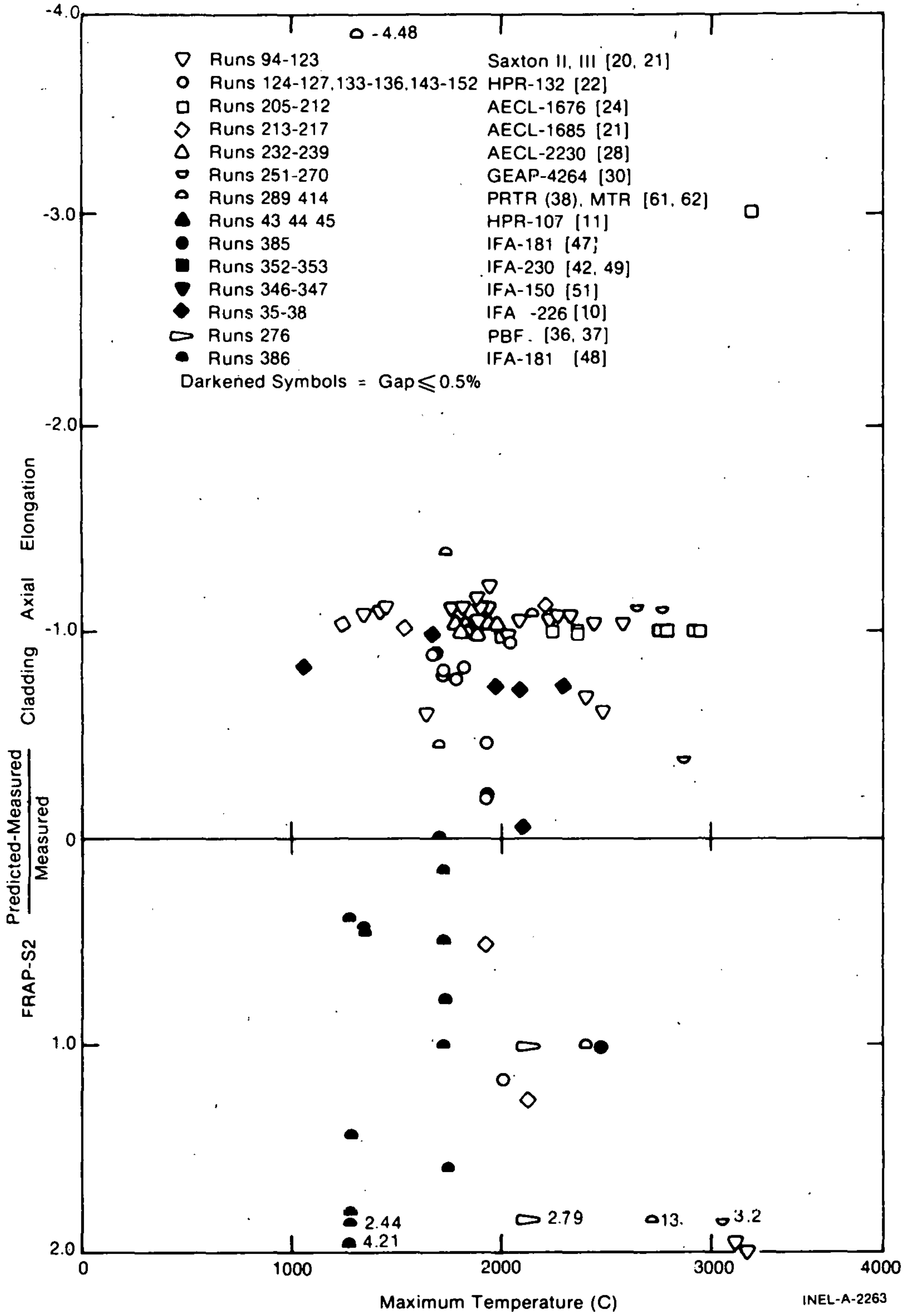

Fig. 49 Relative cladding permanent elongation model agreement versus maximum fuel temperature.

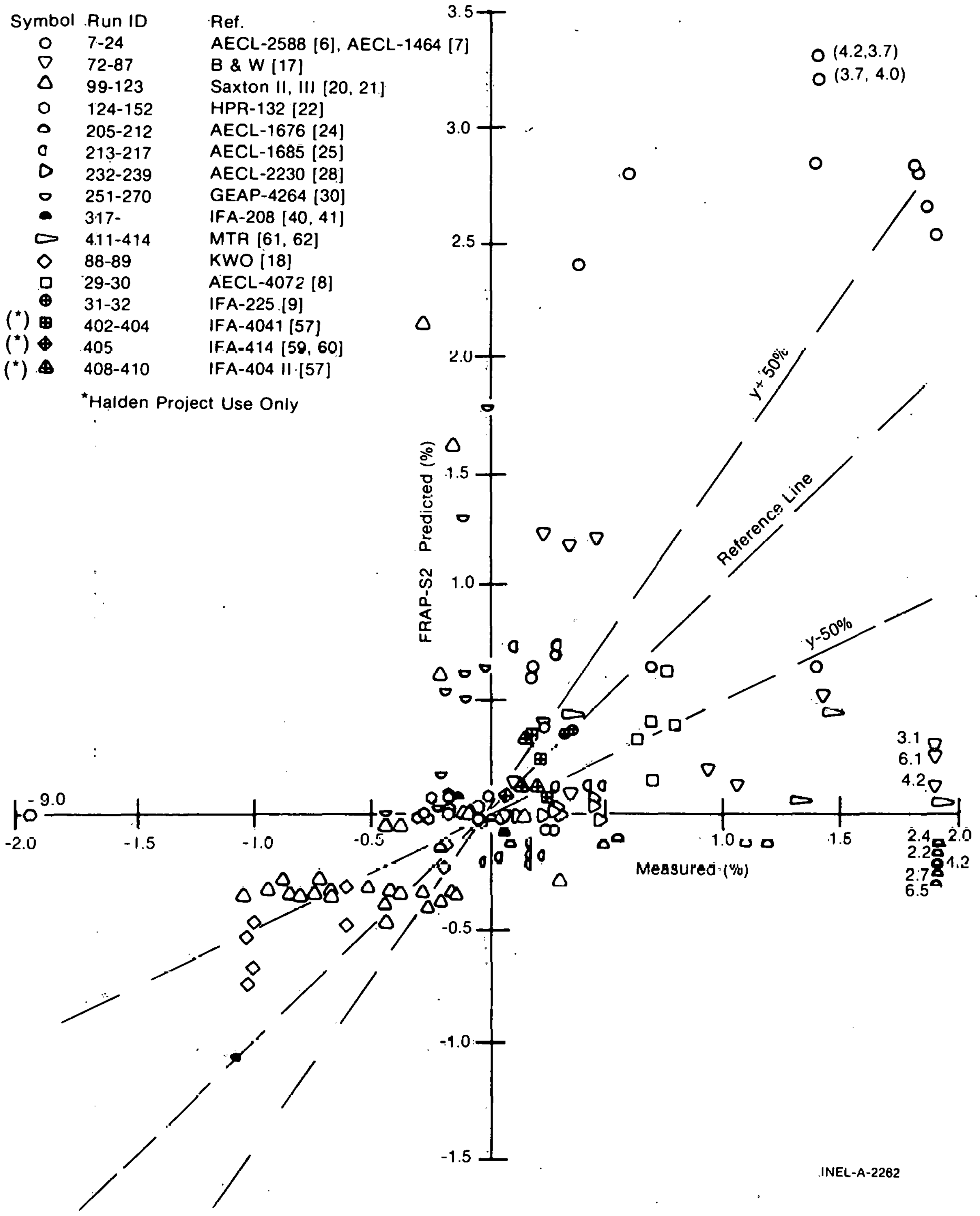

Fig. 50 Measured versus predicted permanent cladding circumferential strain - summary results.

data between -0.5 and +0.5% tend to indicate competition between creep and mechanical interaction. Deformations larger than ±0.5% mainly correspond to high power experiments where consequences of hard gap closure tend to dominate the measurements.

Comparison points in quadrant III show some trend towards underpredicting cladding creepdown. This behavior is expected given the previously identified overprediction of rod internal pressure for rods with low helium backfill and the relatively low creep rates used by FRAP-S2. Comparison points in quadrant I, or those points lying along both positive axes, show that the model can either underestimate or overestimate cladding tensile hoop strain. This behavior is consistent with prior axial elongation results, but more scattered due to more direct influence of PCMI assumptions on calculated hoop strain. Underpredictions again seem attributable to lack of fit in annular gap closure mechanics. This point is shown in Figure 51 by the overall distribution of relative model agreement versus gap size. With increasing gap size, circumferential strain is underpredicted more often, the exceptions being rods with fuel temperature >2000°C (darkened symbols). Again, the gap trend follows from coexistence of lack of fuel relocation models and increasing influence of fuel relocation effects on the data as gaps get larger. Overprediction of cladding hoop strain is shown in Figure 52 to be associated with those fuel temperatures in excess of 1800 to 2000°C. For these cases, lack of fuel mechanical deformation in the model again has the effect of limiting calculational accuracy at temperatures associated with fuel plasticity. Once gap closure is calculated to occur, the result of a nondeformable pellet model is the observed coincidence of strain overprediction and high fuel temperature. This is not felt to be a severe modeling limitation under normal operating conditions when most of the core experiences fuel temperature <1500°C, low contact pressures, and negative cladding strain.

3.4 Cladding Surface and Impurity Effects

Data comparisons were made to determine ability of FRAP-S2 to predict buildup of cladding surface corrosion and associated hydrogen

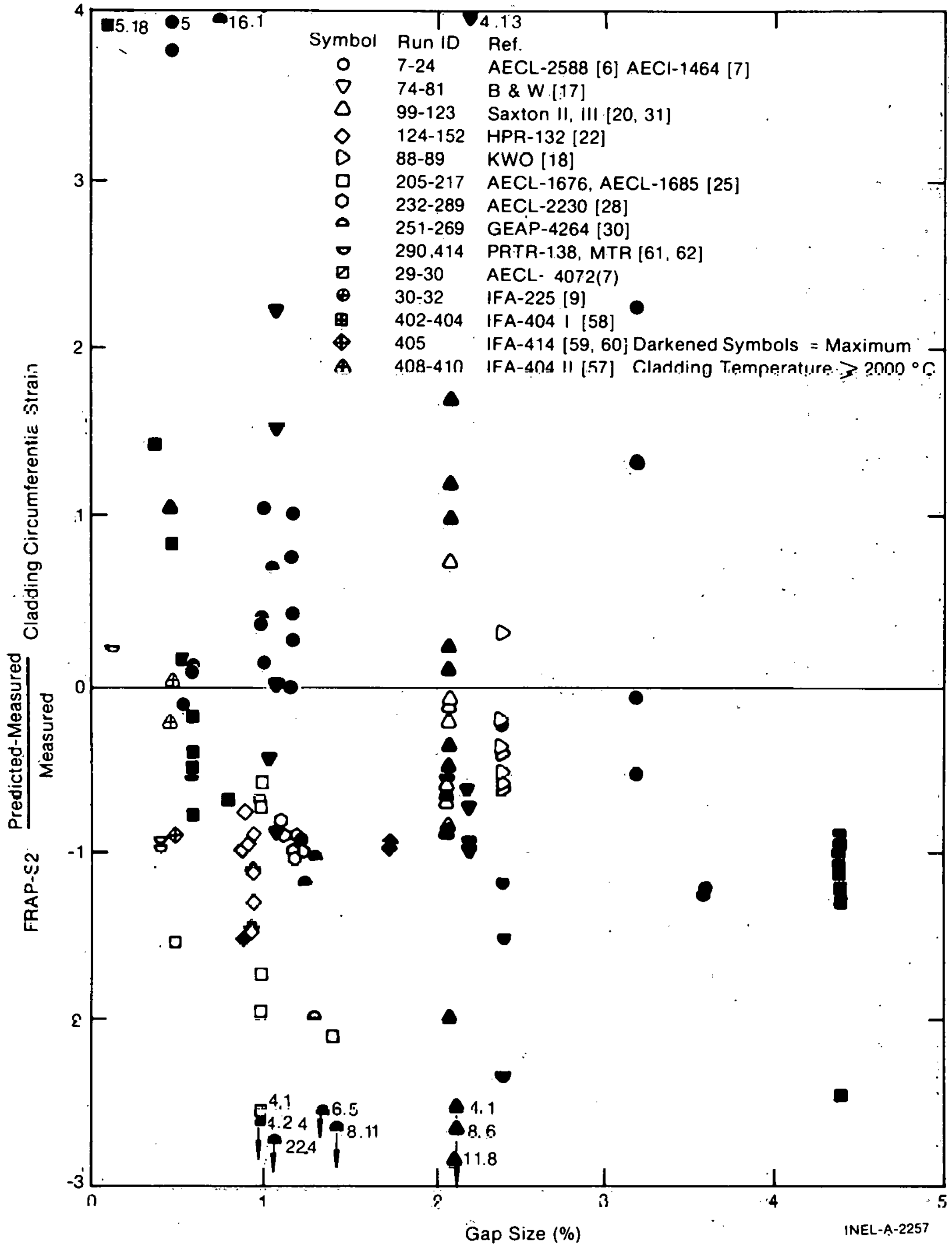

Fig. 51 Relative permanent cladding circumferential strain model agreement versus gap size.

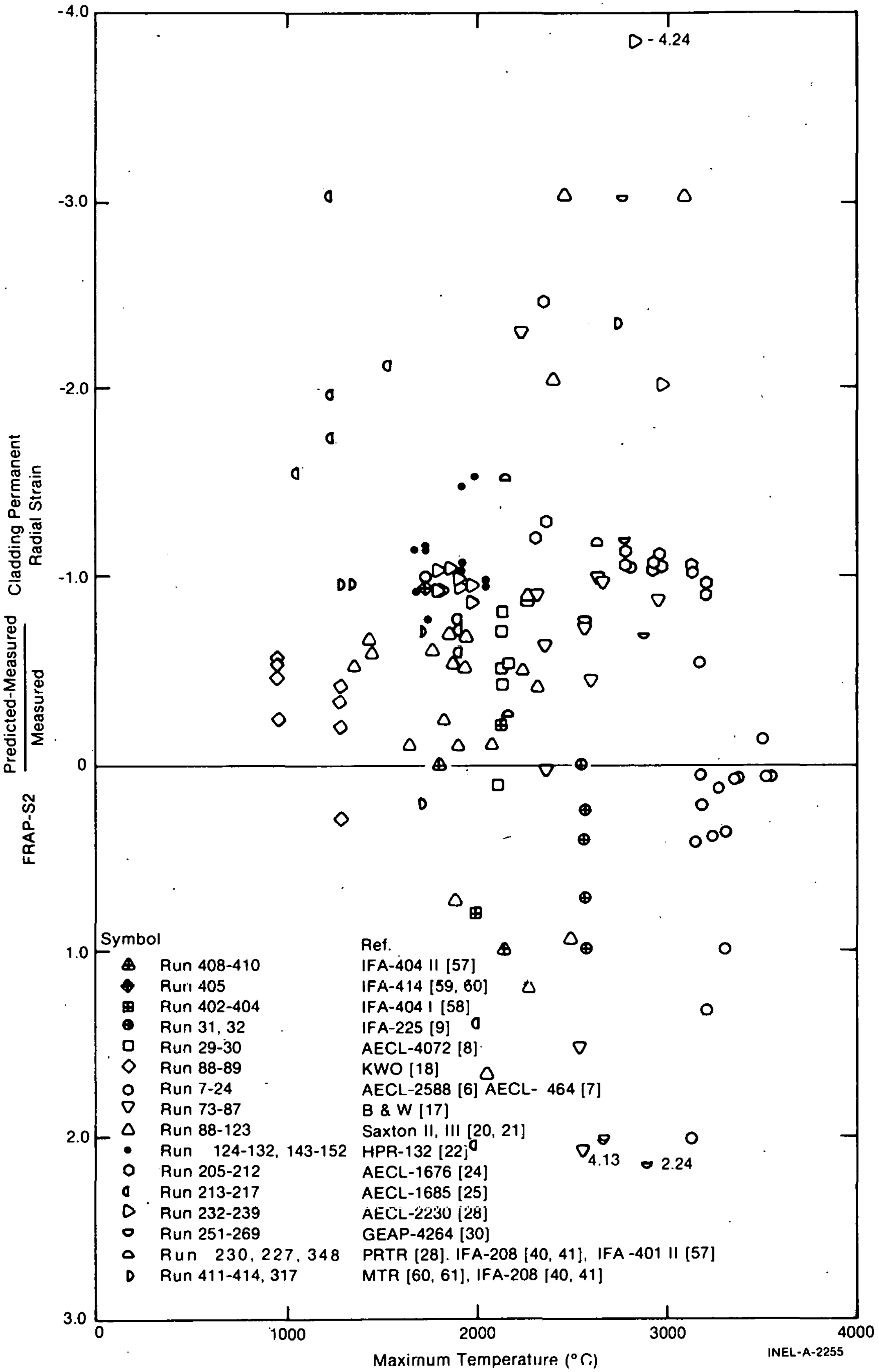

Fig. 52 Relative permanent cladding circumferential strain model agreement versus maximum fuel temperature.

concentration. There is currently no communication of these outputs to the transient model, although such a coupling may be necessary. The actual effects of these initial conditions on high temperature cladding reaction rates, mechanical properties, and deformation are among the subjects of current experimental programs.

3.4.1 Corrosion. The metal water reaction rates predicted by FRAP-T2 are sensitive to initial oxide thickness when the reaction commences at high LOCA temperatures. The current FRAP-T2 model uses a constant initial oxide thickness which is not affected by the initial surface condition output from FRAP-S2. Many of the rods affected by accidents will have accumulated varying amounts of corrosion over long-term operation, prior to the transient however. It is relevant then to evaluate model capability in this area.

The corrosion mechanism itself is affected by cladding surface temperature and radiolytic decomposition of the coolant. Differences in system temperature and chemistry conditions are such that the suggested corrosion rate acceleration factor for BWR and PWR conditions is, respectively, 10 and 3[1]. This factor is intended to account for variation in corrosion behavior observed between the in-pile and out-of-pile test[4].

Figure 53 shows measured versus predicted cladding surface corrosion for two sets of experiment conditions. Bar figures on the predictions account for variation due to undocumented surface treatment effects which typically result in an as-built corrosion layer thickness between 0 and 0.1 mil. Both measured and predicted ranges show strong combined influence of cladding temperature and reactor system environment. Perhaps the largest statistical variation in the data is due to grid-induced flow patterns not considered by the model.

Low value predictions correspond to rods tested in a low pressure (460 psia) HBWR system. Moderate and high value predictions relate to moderate and high power irradiation in a high pressure (2200 psia) PWR system. Low temperature data is generally underpredicted by the model,

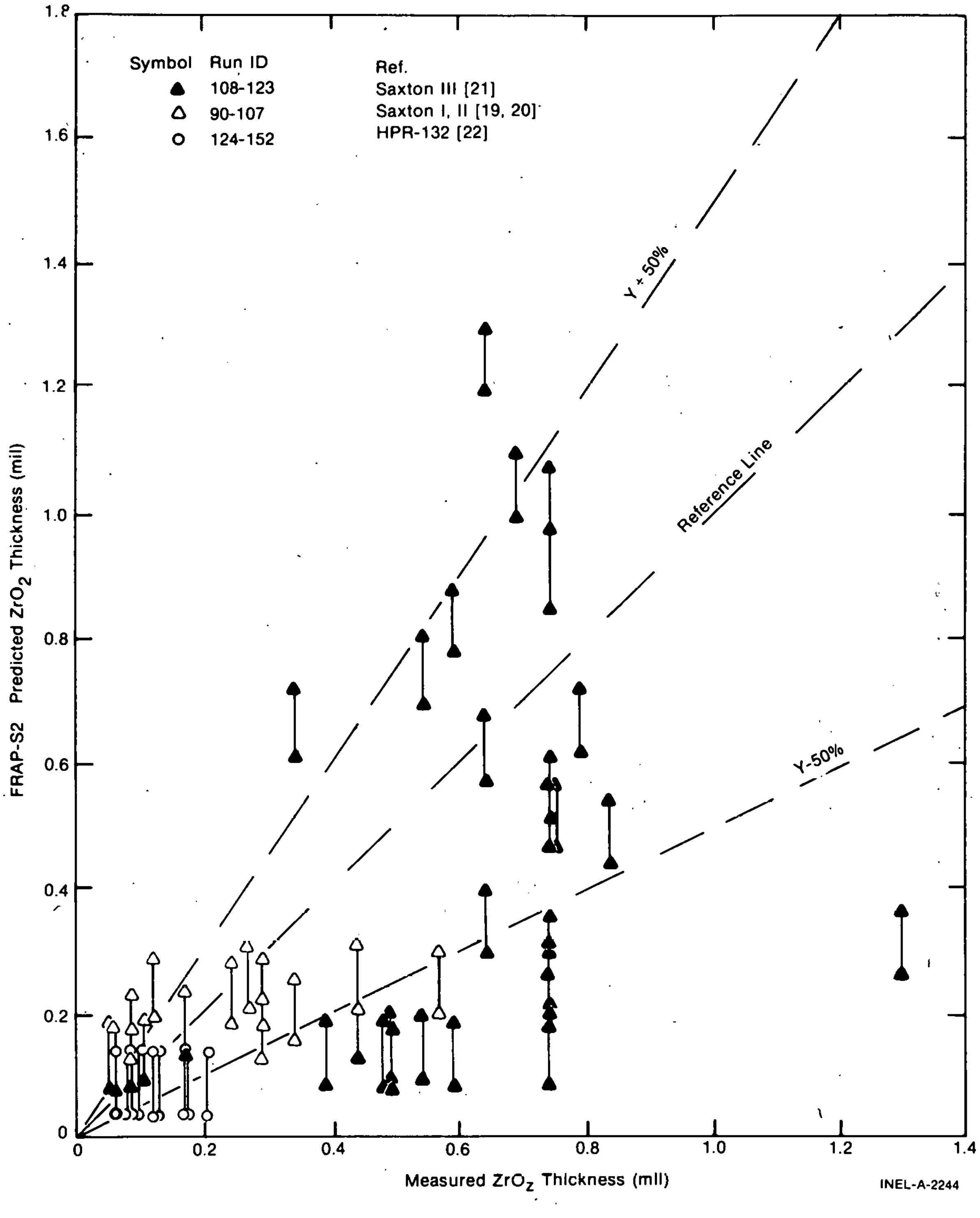

Fig. 53 Measured versus predicted cladding corrosion thickness - summary results.

as is the case for the moderate power PWR rods with predicted corrosion thickness less than 0.4 mil. Corrosion for high power PWR rods generally seems better represented by the model, the predictions in these cases being greater than 0.5 mil.

The influence of temperature on accuracy of the corrosion model is shown somewhat more clearly in Figure 54 by the trend of mean relative agreement versus maximum steady state cladding temperature. The number of comparison points above and below the reference line for different temperature intervals indicate that the current irradiation enhancement factors (BWR 10, PWR 3) seem better applied at cladding temperatures above 350°C. More recent MATPRO development[68] has begun to identify more detailed aspects of corrosion kinetics and temperature dependence of the associated irradiation effect.

3.4.2 Hydrogen Pickup. Pickup and diffusion of hydrogen occurs through the cladding wall as a by-product of the oxidation process. Orientation of zirconium hydride platelets seems to have more influence on cladding mechanical properties than overall hydrogen concentration below about 200 PPM. Rods operated under normal conditions with internal hydrogen contamination problems show areas of high concentration (>600 PPM) and degraded mechanical properties near the failures[21]. Normally, internal sources of hydrogen do not raise the as-fabricated hydrogen content to limiting levels. For accident behavior however, the impact of as much as 300 PPM hydrogen content in high burnup cladding may influence mechanical properties. Current understanding of the disposition and effect of accumulated chemical impurities on the behavior of zircaloy at high temperature is not conclusive. Initial hydrogen concentration may reduce maximum ballooning for some rods through a loss of ductility.

Figure 55 shows measured versus predicted cladding hydrogen concentration for the same set of rods used for corrosion data comparisons. With the exception of rods contaminated with water or hydrocarbons, surface corrosion is the main source of hydrogen pickup by the

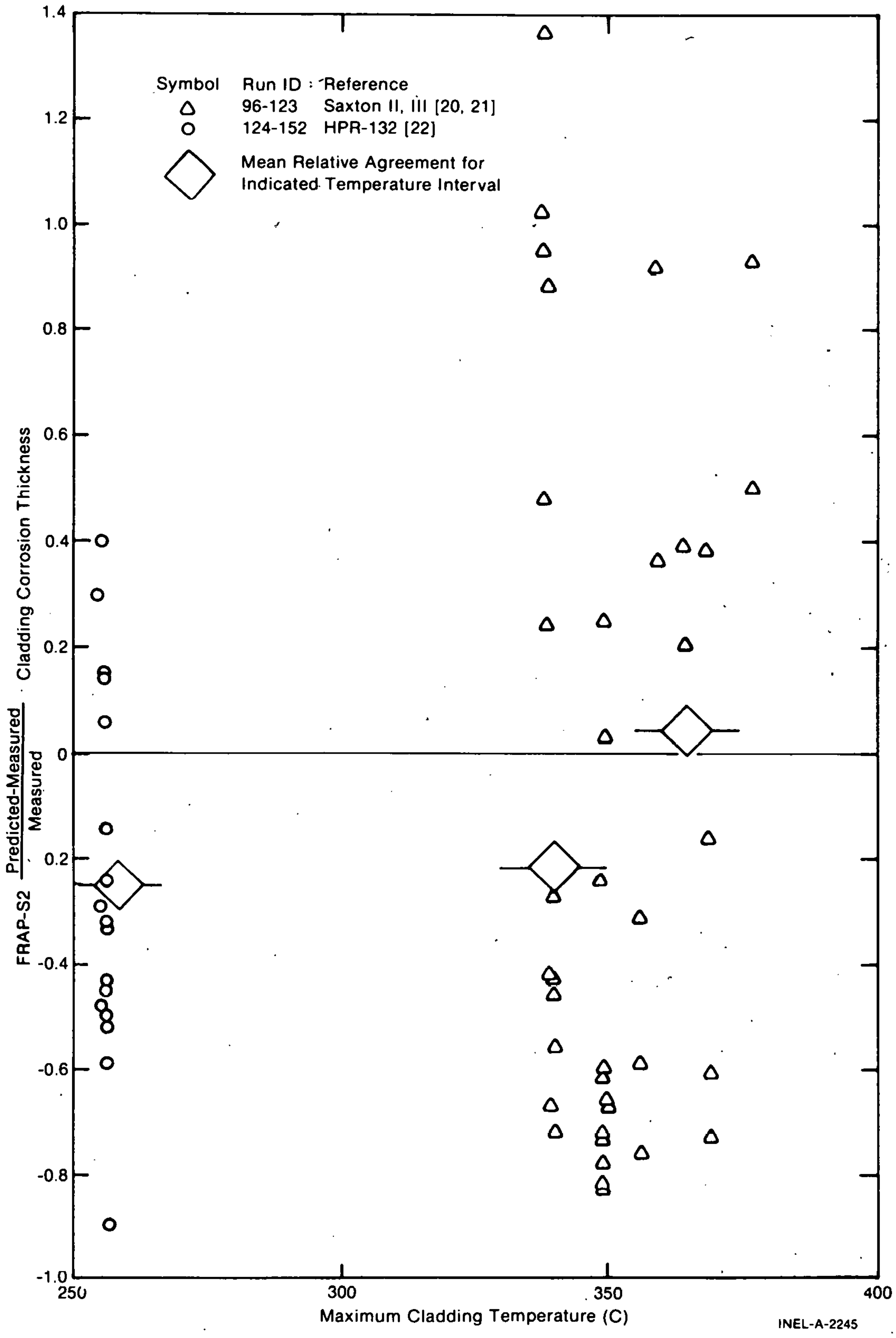

Fig. 54 Relative cladding corrosion thickness model agreement versus maximum clad temperature.

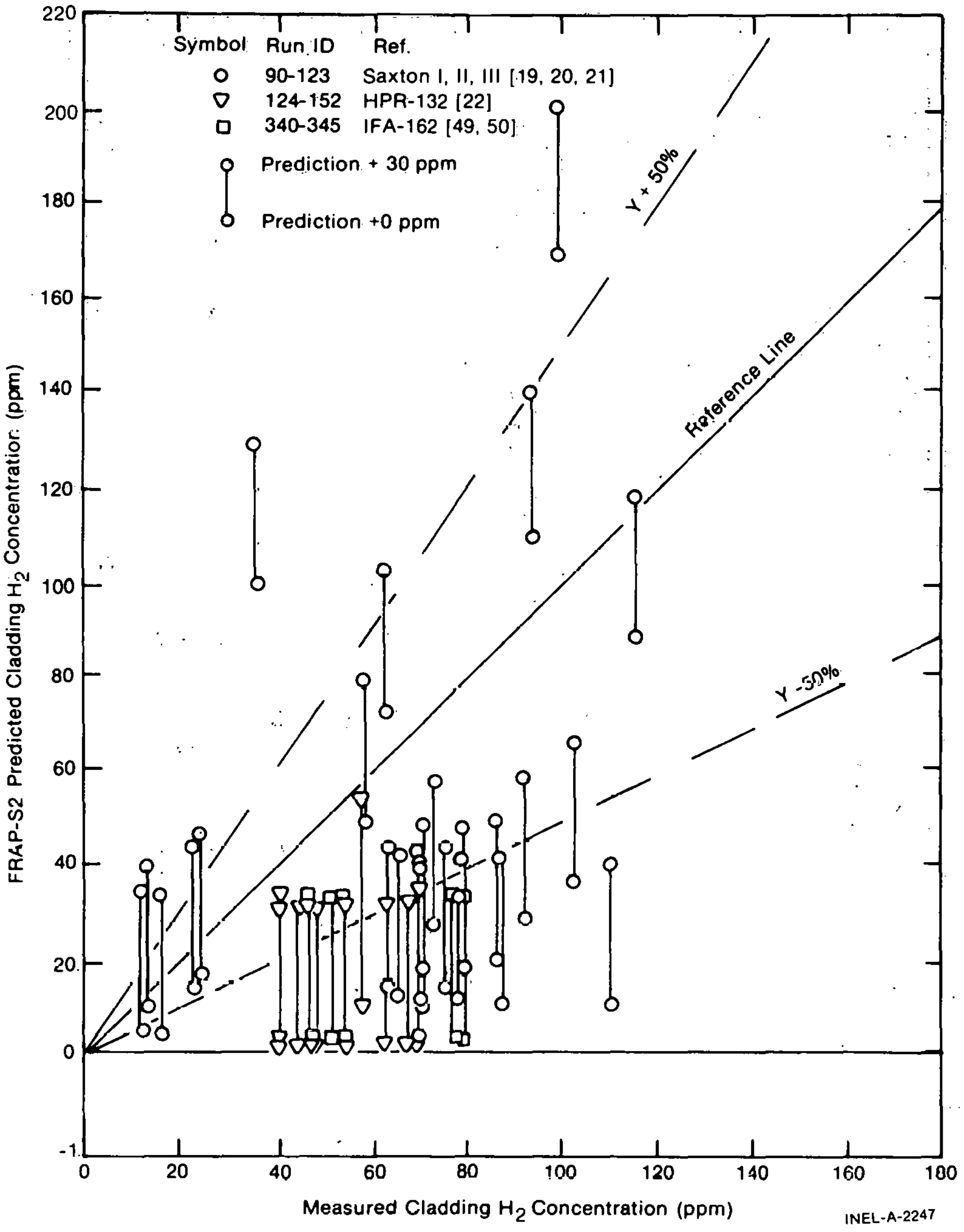

Fig. 55 Measured versus predicted cladding hydrogen concentration - summary results.

cladding. It is not unexpected then that observations made with respect to corrosion results can be applied to hydrogen concentration. In this case, bar symbols are intended to allow for up to 30 PPM hydrogen content in the as-built condition. Trends in the distribution of results can again be related to system conditions and cladding temperature. Figure 56 shows that the mean relative model agreement tends to

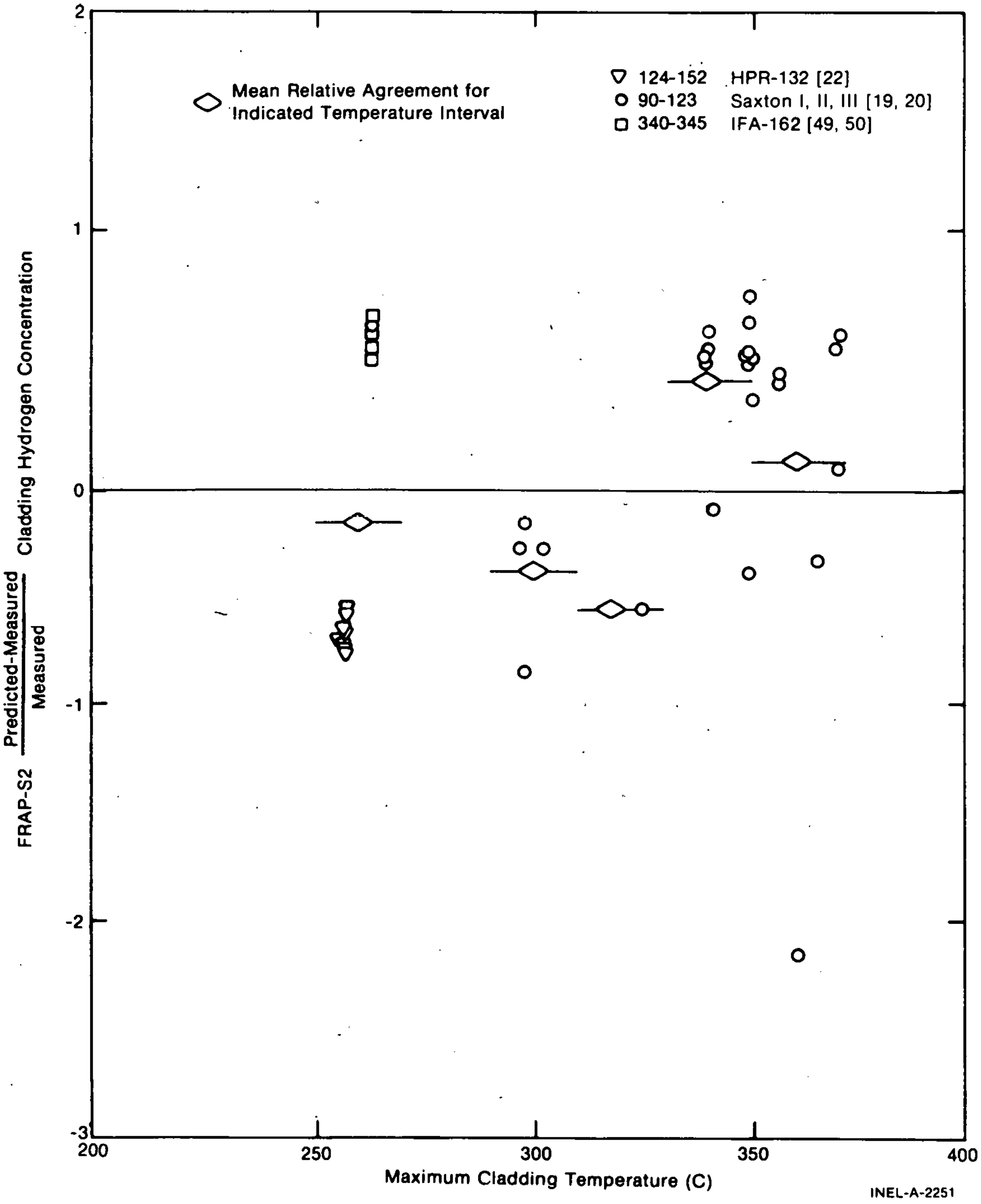

Fig. 56 Relative cladding hydrogen concentration model agreement versus maximum clad temperature.

be below the reference line for the lower temperature data and above the reference line for the higher temperature data. This overall trend is consistent with previously discussed corrosion results.

THIS PAGE

WAS INTENTIONALLY

LEFT BLANK

IV. REFERENCES

1. J. A. Dearien et al, *FRAP-S: A Computer Code for Steady State Analysis of Oxide Fuel Rods - Report I, FRAP-S2 Analytical Models and Input Manual*, TREE-NUREG-1107 (May 1977).

2. J. A. Dearien et al, *FRAP-T - A Computer Code for Transient Analysis of Oxide Fuel Rods - Report I, FRAP-T2 Analytical Models and Input Manual*, TREE-NUREG-1040 (April 1977).

3. D. R. Coleman, *FRAP-S1: A Computer Code for Steady State Analysis of Oxide Fuel Rods, Vol. 3 - Model Verification Report*, SSRD-6-76 (September 1975).

4. P. E. MacDonald and L. B. Thompson, *MATPRO - A Handbook of Materials Properties for Use in the Analysis of Light Water Reactor Fuel Rod Behavior*, ANCR-1263 (February 1976).

5. G. Kjaerheim and E. Rolstad, *In-Pile Determination of UO_2 Thermal Conductivity, Density Effects and Gap Conductance*, HPR-80 (1967).

6. A. S. Bain, *Microscopic, Autoradiographic, and Fuel Sheath Heat Transfer Studies on UO_2 Fuel Elements*, AECL-2588 (1966).

7. A. S. Bain, *Irradiation of UO_2 Specimens with Molten Core in a Pressurized Water Loop*, AECL-1464 (1961).

8. M. J. F. Notley et al, *Measurements of the Circumferential Strains of the Sheathing of UO_2 Fuel Elements During Reactor Operation*, AECL-4072 (1972).

9. M. J. Brakas, "Cladding Strain Measurements Using Strain Gauges," *Paper F-7 Presented at the Enlarged Halden Programme Group Meeting, Sanderstolen, Norway, March 18-23, 1973*.

10. E. T. Laats et al, USNRC-OECD Halden Project Fuel Behavior Test Program - Experimental Data Report for Test Assemblies IFA-226 and IFA-239, ANCR-1270 (December 1975).

11. G. Kjaerheim and E. Rolstad, In-Core Study of Fuel/Clad Interaction and Fuel Centre Temperature, HPR-107 (1969).

12. G. Fayl and K. Hansen, In-Reactor Determination of the Thermal Conductivity of UO_2-Pellets up to 2200 C, RISO Report No. 269 (July 1972).[a]

13. G. Fayl and K. Hansen, Observations of Increase in Fuel Centre Temperature with Burn-Up in UO_2/ZR 2 Fuel Rods, RISO Report No. 415 (May 1974).[a]

14. Y. Iwano et al, "Irradiation Behavior of Fuel Assembly IFA-223," Paper Presented at the Enlarged Halden Programme Group Meeting, Sanderstolen, Norway, March 19-23, 1973.

15. M. G. Balfour, J. A. Christensen, and H. M. Ferrari, Final Report on In-Pile Measurement of UO_2 Thermal Conductivity, WCAP-2923 (March 1966).

16. G. Testa et al, "In-Pile Fuel Studies for Design Purposes," Nuclear Applications and Technology, 7 (December 1969).

17. C. J. Baroch and M. A. Rigdon, "Irradiation Behavior of UO_2 at Burn-Ups from 10 to 80 GWD/tonne U," Paper No. 58 Presented at Conference BNES, London 1973.

18. D. Knodler and H. Stehle, "PWR Fuel Reliability and Quality Assurance KWU Experience," Paper No. 87 Presented at Conference BNES, London, 1973.

---

[a] Halden project use only.

19. E. A. Bassler et al, Saxton Core I Performance Summary, WCAP-3269-43 (1965).

20. W. R. Smalley, Saxton Core II Fuel Performance Evaluation, WCAP-3385-56 (September 1971).

21. R. Goodspeed, Saxton Core III Materials Evaluation, WCAP-3385-57 (1973).

22. D. G. Bridge et al, UKAEA Fuel Test Assemblies Irradiated in HBWR 1964-1966, HPR-132 (1970).

23. A. S. Bain et al, UO_2 Irradiation of Short Duration, Part II, AECL-1192 (1961).

24. M. J. F. Notley et al, Zircaloy Sheathed UO_2 Fuel Elements Irradiated at Values of $\int k d\theta$ Between 40 and 83 W/cm, AECL-1676 (1962).

25. R. D. MacDonald and A. S. Bain, Irradiation of Zircaloy-2 Clad UO_2 to Study Sheath Deformation, AECL-1685 (1962).

26. I. Devold, A Study of the Temperature Distribution in UO_2 Reactor Fuel Elements, AE-318 (1968).

27. M. F. Lyons et al, High Performance UO_2 Program, Molten Fuel Rod Operation to High Burn-Up, GEAP-5100-2 (1966).

28. M. J. F. Notley and J. R. MacEwan, The Effect of UO_2 Density on Fission Product Gas Release and Sheath Expansion, AECL-2230 (1965).

29. M. J. F. Notley et al, Measurements of the Fission Product Gas Pressures Developed in UO_2 Fuel Elements During Operation, AECL-2662 (1966).

30. M. F. Lyons et al, UO_2 Fuel Rod Operation with Gross Central Melting, GEAP-4264 (1963).

31. Z. R. Martinson et al, Power-Coolant-Mismatch Test Series, 8-1 Reduced Shroud Test, TFBP-TR-109 (October 1975).

32. J. R. Larson et al, Power-Cooling-Mismatch Test Series, CHF Scoping Test, TFBP-TR-114 (March 1976).

33. R. W. Garner et al, Gap Conductance Thermal Oscillator Feasibility Test 1-1, TFBP-TR-108, (September 1975).

34. Z. R. Martinson et al, Power-Cooling-Mismatch Test Series, Test PCM 8-1 RF Test Results Report, TFBP-TR-119 (June 1976).

35. Z. R. Martinson and G. W. Cawood, PCM-2A Test Quick Look Report, TFBP-TR-133 (January 1976).

36. W. J. Quapp et al, Irradiation Effects Test Series, Scoping Test 1, TFBP-TR-110 (January 1976).

37. C. M. Allison et al, Irradiation Effects Scoping Test 2 Quick Look Report, TFBP-TR-169 (April 1976).

38. D. W. Brite et al, EEI/EPRI Fuel Densification Project, Research Project 131, Final Report, (March 1975, Revised June 1975).

39. M. D. Freshly, Mixed-Oxide Fuel Irradiations in the Plutonium Recycle Test Reactor, Nuclear Technology, 15 (August 1972) pp 138-173.

40. K. Joon, "Verification of Four Models for Fission Gas Release," Paper Presented at Enlarged Halden Programme Group Meeting, Geilo, Norway, March 16-21, 1975.[a]

41. M Hurme, Observation of Fuel Pin Internal Pressure, HPR-110 (June 1969).

---

[a] Halden project use only.

42. K. Taketani and M. Ichikawa, "Fuel Irradiation Experiments by JAERI for Light Water Reactors," Contribution to Crest Specialist Meeting, Sacley, France, October 21-24, 1973

43. OECD Halden Reactor Project Quarterly Progress Report, January to March 1968, HPR-099 (May 1968).

44. J. B. Ainscough, An Assessment of the IFA-116 and 117 Irradiations from Data Obtained from the In-Reactor Instrumentation, HPR-129 (April 1971).

45. OECD Halden Reactor Project Quarterly Progress Report, October to December 1973, HPR-167 (February 1974).[a]

46. H. Christensen et al, Iodine Release from Defect Fuel Elements in the HBWR, HPR-169 (March 1974).[a]

47. OECD Halden Reactor Project Quarterly Progress Report, July to September 1970, HPR-128 (November 1970).

48. OECD Halden Reactor Project Quarterly Progress Report, April to June 1971, HPR-140 (August 1971).

49. OECD Halden Reactor Project Quarterly Progress Report, January to March 1972, HPR-150 (May 1972).

50. F. List et al, "Fuel Column Shortening in Irradiation UO_2-Zr Fuel Pins," Paper No. 75, Presented at Conference BNES-73, London, 1975.

51. M. Ichikawa et al, "Uranium Oxide Fuel Pin Elongation Behavior Under Irradiation," Journal of Nuclear Science and Technology, 8 9 (September 1971) pp 52-54.

---

[a] Halden project use only.

52. D. A. Banks, "Some Observations of Density and Porosity Changes in UO_2 Fuel Irradiated in Water-Cooled Reactors," Journal of Nuclear Materials, 54, (1974) pp 97-107.

53. H. M. Ferrari et al, "Fuel Densification Experience in Westinghouse Pressurized Water Reactors," Paper No. 54 Presented at Conference BNES, London, 1973.

54. M. A. Rigdon et al, "Babcock and Wilcox's Irradiation Program on Fuel Densification," Paper No. 59, Presented at Conference BNES, London, 1973.

55. OECD Halden Reactor Project Quarterly Progress Report, October to December 1970, HPR-130 (February 1971).

56. OECD Halden Reactor Project Quarterly Progress Report, April to June 1972, HPR-152 (August 1972).[a]

57. A. Hanevik et al, "In-Reactor Measurements of Fuel Stack Shortening," Paper No. 89, Presented at Conference BNES, London, 1973.

58. E. Kolstad, "The 3-Rod Diameter Rig Experiment IFA-404 I (HP) and IFA-404 II (HP)," Paper Presented at the Enlarged Halden Programme Group Meeting, Geilo, Norway, March 16-21, 1975.[a]

59. E. Kolstad and E. Rolstad, "The High Pressure Rig Experiment IFA-414 (N) In-Pile Results Obtained with First Test Rod," Paper Presented at the Enlarged Halden Programme Group Meeting, Geilo, Norway, March 16-21, 1975.[a]

60. E. Kolstad et al, "The High Pressure PWR Rig IFA-414 (N), A Short Description of the Design and the Performance Characteristics," Paper Presented at the Enlarged Halden Programme Group Meeting, Geilo, Norway, March 16-21, 1975.[a]

---

[a] Halden project use only.

61. R. M. Berman et al, Irradiation Bahavior of Zircaloy-Clad Fuel Rods Containing Dished End UO_2 Pellets, WAPD-TM-629 (July 1967).

62. J. T. Engle and H. B. Meieran, Performance of Fuel Rods Having 97 Percent Theoretical Density UO_2 Pellets Sheathed in Zircaloy-4 and Irradiated at Low Thermal Ratings, WAPD-TM-631 (July 1968).

63. W. F. Domenico, Preliminary Test Results for Halden Instrumented Assembly (IFA) 429, WFD-11-76, SRD-72-76 (March 1976).

64. C. R. Hann et al, "Experimental Verification of Nuclear Fuel Rod Stored Energy Calculations," Paper Presented at the Enlarged Halden Programme Group Meeting, Sanderstolen, Norway, March 8-12, 1976.

65. OECD Halden Reactor Project Quarterly Progress Report, April to June 1975, HPR-187 (September 1975)[a].

66. L. S. Tong and J. Weisman, Thermal Analysis of Pressurized Water Reactors, Hinsdale, Illinois: American Nuclear Society, 1970.

67. D. R. Coleman and E. T. Laats, FRAP-T - A Computer Code for Transient Analysis of Oxide Fuel Rods - Report II, FRAP-T2 Model Verification Report, TREE-NUREG-1040 (April 1977).

68. Personal Communication with D. L. Hagrman, ANC, (August 1976).

---

[a] Halden project use only.

DISTRIBUTION RECORD FOR TREE-NUREG 1107

Internal Distribution

1 - Chicago Patent Group - ERDA
9800 South Cass Avenue
Argonne, Illinois 60439

2 - CA Benson
Idaho Operations Office-ERDA
Idaho Falls, ID 83401

3 - RJ Beers, ID

4 - PE Litteneker, ID

5 - RE Tiller, ID

6 - RE Wood

7 - HP Pearson, Supervisor
Technical Information

8-18 - INEL Technical Library

19-39 - Authors

40-77 - Special Internal

External Distribution

78-79 - Saul Levine, Director
Office of Nuclear Regulatory Research, NRC
Washington, DC 20555

80-391 - Distribution under NRC-4, Water Reactor Safety Research
Analysis Development